Tailoring Perovskite Quantum Dot Surface Chemistry for Single Photon Emission

Jessica Kline

A dissertation

submitted in partial fulfillment of the

requirements for the degree of

Doctor of Philosophy

University of Washington

2025

Reading Committee:

David Ginger, Chair

Brandi Cossairt

Stefan Stoll

Program Authorized to Offer Degree:

Chemistry

University of Washington

Abstract

Tailoring Perovskite Quantum Dot Surface Chemistry for Single Photon Emission

Jessica Kline

Chair of the Supervisory Committee:

David Ginger

Chemistry

Perovskite quantum dots are one of the most promising colloidal materials for use as a single photon source. However, despite their remarkable performance so far, perovskite quantum dots have long way to go to be a deterministically positionable, scalable single photon source. To improve the performance of perovskite quantum dots as single photon emitters we must optimize the surface chemistry. In this thesis we have studied the difference between monodentate and zwitterionic ligands, spheroidal and cubic morphologies and hydrocarbon and cross-linked siloxane tails. We have found that zwitterionic ligands bind more strongly to the quantum dot surface than monodentate ligands resulting in better performing single quantum dots. We have also found that spheroidal quantum dots have a small population of emissive traps, resulting in asymmetrical line shapes suggesting that cubic quantum dots will perform better as single emitters. Finally, we found that ligands with a cross-linked siloxane tail result in better performance than ligands with hydrocarbon tails at room temperature, however this trend reverses at low temperatures with poor performance from quantum dots passivated using ligands with a cross-linked siloxane tail due to increased trion formation.

Chapter 1: Introduction

Table of Contents

1.1 Introduction to Perovskite Quantum Dots

First synthesized in 2015 by Protesecu et al[1], perovskite quantum dots are a unique class of materials that have great potential for a variety of optoelectronic applications. Perovskite quantum dots have an ABX_3 crystal lattice where A is a monovalent cation, most often Cs^+, formadinium (FA^+) or methylammonium (MA^+), B is a divalent cation such as Pb^{2+} or Sn^{2+} and X is a halide such as Cl^-, Br^- or I^-. These quantum dots have large absorption coefficients, tunable emission in the visible range[2], narrow linewidths[3] and high quantum yields (PLQY)[4] which have made them attractive for classical optoelectronics such as light emitting diodes (LEDs)[5], photovoltaics[6] and photodetectors[7]. In the years since the first synthesis, perovskite quantum dots have also seen significant interest for quantum optoelectronic applications – namely as a single photon source.

Single photon sources are considered a fundamental building block for quantum information science. The ideal single photon source has a high PLQY, narrow linewidth, short radiative lifetime, and high single photon purity. At 4K the best performing perovskite quantum dots have linewidths of less than 5 meV and lifetimes of approximately 200 ps. [8,9] High performing perovskite quantum dots also have a zero phonon line fraction of approximately 0.5-0.8 and biexciton emission is spectrally distinct (ie filters can be used to eliminate biexciton emission). [8,9] With this kind of performance, perovskite quantum dots represent one of the best options for a colloidal single photon source, out-performing both colloidal and epitaxial II-VI and III-V quantum dots.[9,10]

Despite these remarkable benchmarks, perovskite quantum dots have a long way to go to be applied as a deterministically positionable, scalable single photon source. The main challenges to scaling perovskite quantum dots can be split into two categories – synthesis and surface. While these two categories are intertwined, here we consider synthesis to be the process of making the quantum dots and surface to be all factors impacting the passivation of the quantum dots. Understanding the interactions between surface, synthesis and performance will allow us to tailor perovskite quantum dots for single photon emission applications.

1.2 Perovskite Quantum Dot Synthesis

Like most quantum dots, perovskite quantum dots were first synthesized *via* hot-injection[1] – a technique where two precursor solutions are prepared and one is injected into the other at high temperatures to start quantum dot nucleation and growth. For perovskite quantum dots these two solutions are traditionally $[PbX_3^-][OAm^+]$ and A-oleate.[1] However, unlike in II-VI and III-V quantum dots, nucleation and growth occur near simultaneously in perovskite quantum dots.[1] Practically, this means that the size of perovskite quantum dots depends strongly on the temperature of the reaction and that perovskite quantum dots tend to have a rather large size distribution.[1] Large size distributions are bad because they broaden the ensemble linewidth and increase the possibility that the photons from two quantum dots are distinguishable. Thus, it is important to depart from the traditional hot-injection synthesis and separate nucleation and growth for precise size control.

To separate perovskite quantum dot nucleation and growth, we have to change the kinetics of the synthesis. The key chemical reactions for perovskite quantum dot nucleation and growth are (1) the formation of PbX_3^- from PbX_2 and (2) the reaction of PbX_3^- with A^+ which both strongly depend on the coordinating ligands for PbX_3^- and A^+.[11–13] In a traditional hot-injection PbX_2 is first solubilized using oleylamine (OAm) and oleic acid (OA) forming $[PbX_3^-][OAm^+]$ and $Pb(OA)_2$.[14] A(OA) is then added to

the solution providing a source of A^+ which quickly reacts with all available PbX_3^-.[14] This means that there is no sustained growth phase because all of the precursors have been consumed in the first few seconds of the reaction.

The trioctlyphosphine oxide (TOPO)/$PbBr_2$ method, pioneered by Akkerman et al[11], changes the precursor coordinating ligands to change the kinetics of perovskite quantum dot synthesis and separate nucleation and growth. The TOPO/$PbBr_2$ method makes two important changes: first TOPO is used to dissolve $PbBr_2$ and second diisooctlyphosphinic acid (DOPA) is used as the A+ coordinating ligand. [11] TOPO is a neutral coordinating agent and thus dissolves $PbBr_2$ by forming a [TOPO][$PbBr_2$] complex preventing the premature formation of $PbBr_3^-$.[11] In this reaction $PbBr_3^-$ cannot form until the addition of A(DOPA) provides a counter-ion allowing the formation of an equilibrium between the monomeric precursors and a [A^+][$PbBr_3^-$] intermediate.[11] This self-limiting equilibrium requires the presence of both TOPO and DOPA; OAm or OA substitutions destroy this equilibrium by creating $PbBr_3^-$ and increasing the stability of the $Pb(acid)_2$ product respectively.[11,12] Due to this equilibrium a limited amount of $PbBr_3^-$ is available for growth and nucleation – separating the two processes. Nucleation occurs on the time scale of a few seconds as the initial population of [A^+][$PbBr_3^-$] converts to $APbBr_3$ and growth is controlled by the slow conversion of the remaining monomers to [A^+][$PbBr_3^-$] to $APbBr_3$ over the course of minutes.[12] In total, the TOPO/$PbBr_2$ method extends perovskite quantum dot growth time to 30 minutes, hundreds of times slower than the few seconds required for complete growth in a hot-injection synthesis.[11]

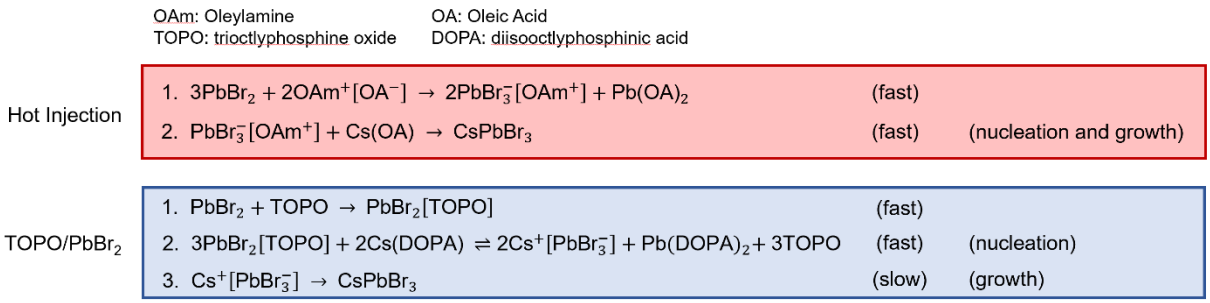

Figure 1.1: Separating Perovskite Quantum Dot Nucleation and Growth via Kinetic Control. A hot-injection synthesis completely converts $PbBr_2$ to $PbBr_3^-$ which results in fast nucleation and growth after the addition of Cs(OA). In contrast the TOPO/$PbBr_2$ synthesis can only form $PbBr_3^-$ after the addition of Cs(DOPA) creating a self-limiting equilibrium which separates nucleation and growth.

The TOPO/$PbBr_2$ synthesis provides many benefits over the traditional hot-injection synthesis. The TOPO/$PbBr_2$ synthesis requires less technique as it takes place under ambient conditions at room temperature, greatly reduces the dependence of high-quality quantum dots on high quality reagents, results in a 2x narrower size distribution and opens the door for efficiently screening a variety of passivation methods.[11,15] The ability of this synthesis to screen passivation methods is one of its most unique features. Since this synthesis produces quantum dots passivated by very weak ligands (TOPO and DOPA) they are easily replaced by most ligand candidates at room temperature, opening the door for a variety of ligands which have previously been discounted for hot-injection syntheses over temperature and colloidal stability concerns.[11]

However, there are lingering questions which affect the potential utility of quantum dots synthesized by the TOPO/$PbBr_2$ method. The delicate equilibrium kinetics of this synthesis method mean

that only $APbBr_3$ quantum dots can be synthesized natively. $APbCl_3$ and $APbI_3$ quantum dots can only be synthesized *via* halide exchange – which can occur during quantum dot growth, after quantum dot growth or after ligand exchange.[15] Each halide exchange option has its own benefits and drawbacks, but the overarching concern is halide exchanged quantum dots typically perform worse than their as-grown counterparts.[16] The other open question about quantum dots synthesized *via* the TOPO/$PbBr_2$ method involves the morphology – namely that quantum dots synthesized *via* hot-injection have a cubic morphology while quantum dots synthesized *via* the TOPO/$PbBr_2$ method have a spheroidal morphology.[1,11] This change in quantum dot morphology arises from changing the PbX_2 coordinating ligand from oleylammonium to TOPO. Ammonium preferentially encourages quantum dot growth along the {100} crystal axis – forming cubic quantum dots. In contrast phosphines favor crystal growth along the {100} and {110} axes equally – resulting in quantum dots with a spheroidal morphology.[11,17] Quantum dot morphology changes have been linked to both increases and decreases in performance[18–20] – and so the question remains how this specific morphology change impacts the performance of perovskite quantum dots.

1.3 Perovskite Quantum Dot Surface Passivation

Like all quantum dots, perovskite quantum dots require surface passivation for optimal performance. There are two common passivation approaches for quantum dots – ligands and shells. Ligand passivation refers to organic molecules with two key components – head groups and tail groups. The head groups (positively and negatively charged functional groups) are designed to fill vacancies by binding to under coordinated atoms. The tail groups (most commonly long hydrocarbon chains) are designed to solubilize quantum dots in a chosen solvent. Ligands can be classified by the number of binding sites (monodentate, bidentate ect) and the identity of the head groups. For perovskite quantum dots ammonium is the most common cationic head group, while carboxylates, phosphates and sulfonates are the most common anionic head groups.[1,15,21,22] Cationic head groups can fill A site vacancies, while anionic head groups fill X site vacancies. Shell passivation refers to layers of a higher-bandgap material grown on top of the quantum dot core. Shells are the most prevalent passivation for II-VI and III-V quantum dots where materials like CdS, ZnS and ZnSe can easily be grown on top of the cores. Shell passivation is ideal for quantum dots since it creates an impermeable layer that both passivates the core and protects it from the surrounding environment. However, developing shells for perovskite quantum dots is an ongoing synthetic challenge due to the soft nature of the perovskite lattice.[23] As such, most perovskite quantum dots use ligands for passivation.

The first set of ligands used for perovskite quantum dots was a mixture of two monodentate ligands- oleylammonium and oleate.[1] The chemistry of these two ligands is complex and depends on the acid-base equilibrium between the two – as the charged species are formed in-situ from oleylamine and oleic acid.[14] The charged ligand species are primarily responsible for passivating the quantum dot by binding to the surface, although the neutral ligand species may play a role in passivation through hydrogen bonding.[24] While oleylammonium and oleate passivated perovskite quantum dots perform reasonably well with initial PLQYs over 80%, their shelf stability is limited.[24] Over the years other ligand candidates with high PLQYs and increased storage stability have emerged. Currently, some of the most common ligand choices for perovskite quantum dot passivation include: didodecylammonium bromide (DDAB),[25] sulfobetaine (also called ASC18),[21] lecithin[22] and phosphoethylammonium derivatives.[15] While the effect of different ligands is well studied in QLEDs, good ligands for QLEDs rarely translate

into good ligands for single photon emission. As such it is important to study the impact of ligands focusing on single photon emission applications.

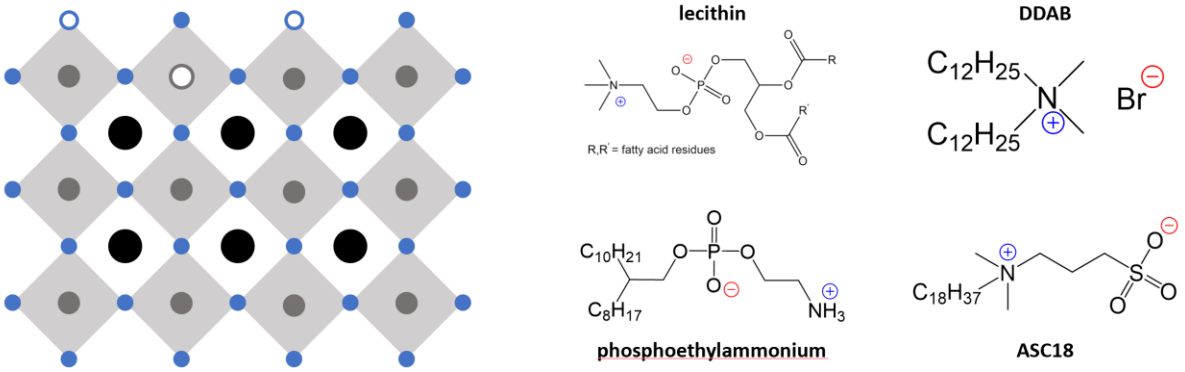

Figure 1.2: Perovskite Crystal Structure and Selected Ligands. (right) ABX_3 crystal structure of the perovskite with atoms represented by the black, grey and blue circles respectively. (left) Chemical structures of selected common ligands used for perovskite quantum dot passivation.

1.4 Quantum Dot Characterization

There are a variety of ways to characterize the optical performance of quantum dots. They can be characterized in solutions and films and in ensembles or as single emitters. The choice of characterization medium determines the observed properties. For instance, quantum dots often have higher PLQYs and narrower linewidths in solution since film deposition introduces variables such as charge transfer/delocalization, quantum dot packing and increases atmospheric exposure. Ensemble characterization techniques are much faster and more representative than single emitter characterization techniques – but they contain less information. However, single quantum dot characterization techniques are time-consuming and the process of characterizing enough single quantum dots to accurately represent a sample takes weeks to months. While large volume single emitter characterization techniques exist, they often sacrifice full characterization to focus on one metric[26,27] and one of the most important metrics (single photon purity) is impossible to do using current large volume single emitter characterization techniques. This means that carefully designed experiments which mix ensemble and single emitter characterization techniques are a necessity for understanding the impact of different passivation methods on the performance of quantum dots as single photon sources.

1.5 Characterizing a Single Quantum Dot

While ensemble characterization is ideal for ensuring that two quantum dot batches are "identical" as synthesized, it is impossible to assess the suitability of a quantum dot as a single photon source without single emitter characterization. To assess how changes to the surface and synthesis of perovskite quantum dots impact their performance as a single photon source we characterize optical performance in three broad categories- photoluminescence intensity, photoluminescence spectrum and single photon purity. Beyond these basic characterization categories, advanced characterization like photon correlation Fourier spectroscopy[9] and Hong-Ou-Mandel interferometry[8] can collect additional valuable information on the highest performing quantum dots such as coherence time and photon indistinguishability.

1.5.1 Photoluminescence Intensity

Photoluminescence intensity encompasses all factors related to emission intensity and consistency. This includes metrics such as quantum yield, count rate, photodegradation and blinking. The ideal single photon source has a high quantum yield, fast radiative lifetime (ie high count rate) and does not blink or photodegrade. Blinking, also known as photoluminescence intermittency, is the terminology used to describe the fluctuations in quantum yield and lifetime which are commonly observed in single emitters. In quantum dots blinking occurs because the non-radiative rate of a single quantum dot is variable in time.[28] This variable non-radiative rate is strongly correlated with surface quality; quantum dots with high quality surfaces show less blinking than those with low quality surfaces.[28]

Analyzing and interpreting blinking is a complex process. At the simplest level blinking traces can be segmented into two states which are referred to as ON and OFF.[29] The ON state occurs when the radiative rate is much larger than the non-radiative rate and the OFF state occurs when the non-radiative rate is much larger than the radiative rate. Experimentally these two states are delineated by the dark counts of the detector ($I_{dark}+ 3\sigma_{dark}$).[29] However, ON/OFF segmentation is far from the ideal method to analyze blinking. ON/OFF segmentation is vulnerable to binning artefacts, fails to describe systems with more than two intensity levels, and completely ignores the valuable information contained in lifetime-intensity correlations.[30]

For a more detailed analysis of blinking Watkins and Yang developed Change Point Analysis (CPA) which is an unbiased method used to categorize and reconstruct blinking traces on a photon-by-photon emission basis.[31] First developed for time-tagged time-resolved blinking data, CPA has since been extended to detectors with a Gaussian noise profile such as cameras.[32] CPA consists of four main steps. First the algorithm detects points where the emission intensity changes significantly, producing a list of N change points.[31,32] These change points represent the boundary between two segments with different emission intensities. So, a blinking trace with N change points can have a maximum of N intensity levels. In the second step CPA uses agglomerative hierarchical clustering to group the most similar N intensity levels together.[31,32] This step produces N possible clusterings of the blinking trace with the total number of intensity levels ranging from N to 1. In step three CPA uses an expectation-maximization optimization algorithm to optimize the descriptors of each identified intensity level in the N clustered fits.[31,32] For practical run-time considerations the optimization step and further analysis are typically limited such that the maximum number of intensity levels is 20.[33] Finally, CPA uses a Bayesian information criterion (BIC) to assess the goodness of fit for each of the N clustered and optimized fits.[31,32] The fit with the smallest BIC score is returned and contains information about the total number of intensity levels and their associated lifetimes and expected durations. In addition to providing an unbiased analysis of blinking, CPA also enables the exploration of lifetime-intensity correlations which provide valuable information about the non-radiative mechanisms responsible for blinking.[34]

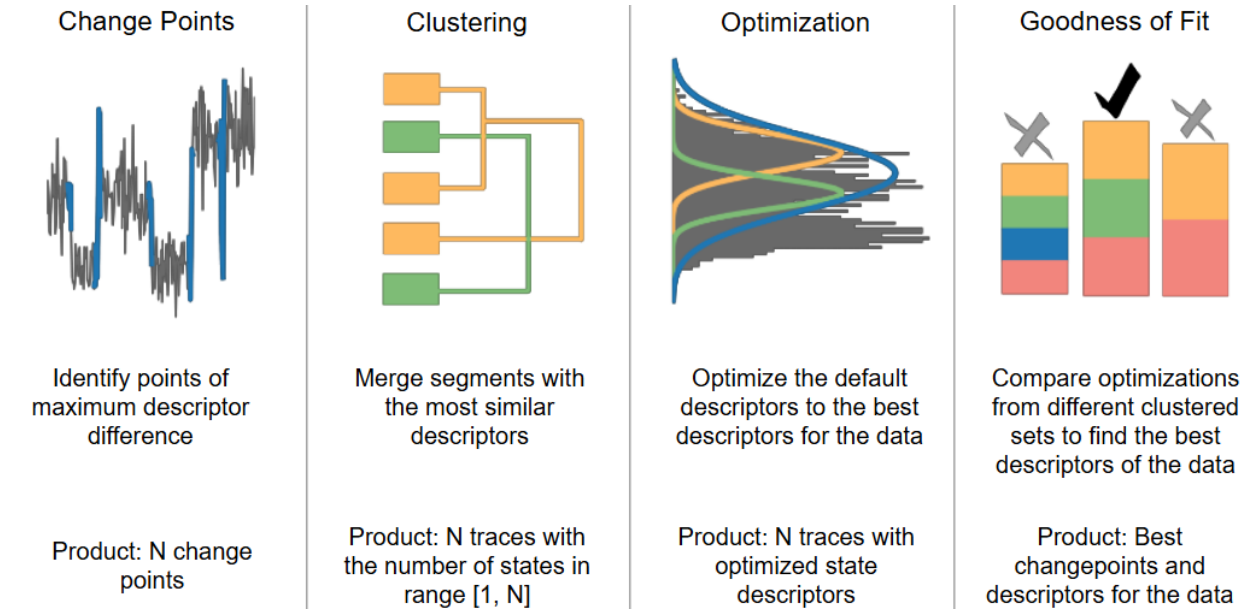

Figure 1.3: Components of Change Point Analysis. CPA consists of four steps. (1) Change point identification which selects points where there are statistically significant intensity changes. (2) Clustering which merges the most similar segments together to create traces with 1 to N possible intensity states. (3) Optimization which finds the best set of descriptors for each intensity state. (4) Goodness of fit which compares the traces with different number of intensity states to find the number of intensity states which best describes the data

Fluoresce lifetime intensity diagrams (FLIDs) are constructed by correlating the intensity and lifetime of all CPA identified segments. There are three common lifetime-intensity correlations, each of which corresponds to a different non-radiative mechanism. The most distinctive correlation is a lifetime which is independent of intensity (ie the lifetime does not change with decreasing intensity). This pattern is characteristic of hot-carrier trapping where carriers are trapped before relaxing to the band-edge and as such the trapping has no impact on band-edge radiative recombination rates.[34,35] The other two common patterns have lifetimes which decrease as the intensity decrease and correspond to trapping after the carriers have relaxed to the band-edge. A pattern which shows a linear lifetime-intensity correlation indicates band-edge carrier (BC) trapping where carriers recombine non-radiatively from shallow traps.[34,35] Characteristically BC blinking exhibits the following relationship: $I_{max}/t_{max} = I_{min}/t_{min}$.[35] A pattern which shows a non-linear lifetime-intensity correlation indicates the presence of auger non-radiative recombination indicating trion formation via long-lived traps.[34,35] Characteristically auger blinking has $2I_{max}/t_{max} = I_{min}/t_{min}$.[35] FLIDs provide an invaluable characterization technique for understanding the root causes of blinking in each quantum dot.

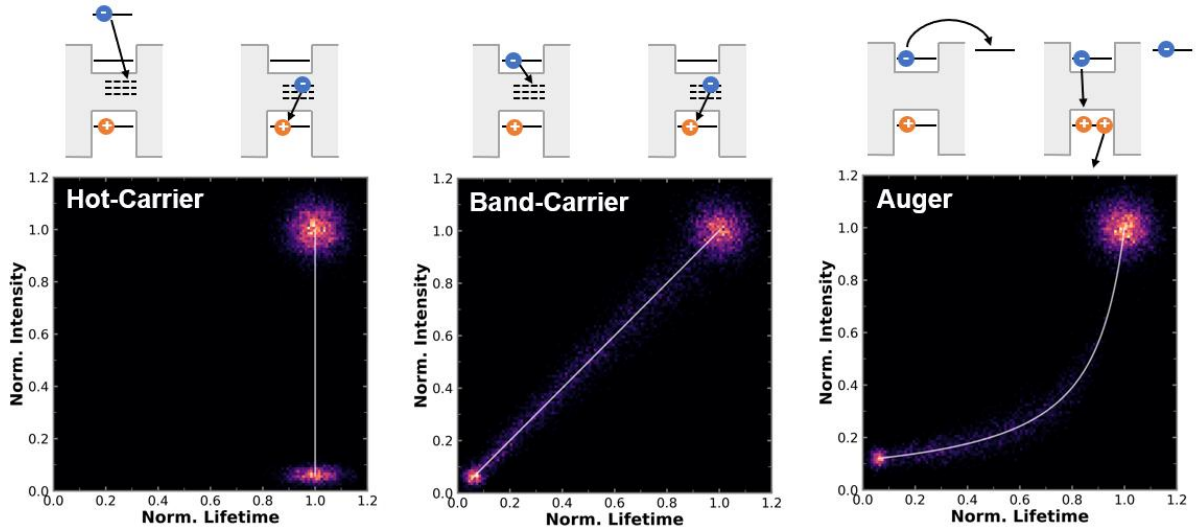

Figure 1.4: Non-radiative Recombination Mechanisms Behind Blinking and their FLID Patterns. In hot carrier (HC) trapping a charge carrier is trapped before it relaxes to the band-edge and results in a lifetime that is independent of intensity. Band-edge carrier (BC) trapping occurs *via* short-lived traps and results in a linear FLID pattern. Auger-Meitner recombination occurs when a carrier occupies a long-lived trap, and a secondary excitation of the quantum dot occurs. This results in a non-linear FLID pattern.

1.5.2 Photoluminescence Spectrum

The second category used to quantify the performance of a single quantum dot is the photoluminescence spectrum. This category involves metrics such as emission energy, linewidth and spectral stability. Quantifying performance at room temperature is relatively simple, as the linewidth is the most important factor and the only spectral stability factor to consider is photodegradation which is often captured during blinking measurements.

Quantifying spectral performance at 4K is slightly more complicated, primarily because quantum dots have instantaneous changes in emission energy and linewidth, called spectral diffusion, which are analogous to blinking. Spectral diffusion happens at all temperatures but is only visible at low temperatures where exciton-phonon coupling is reduced and the linewidth is significantly narrower. Spectral diffusion can occur for three reasons – radiative recombination from a trion or biexciton state or fluctuations in the local electric field (quantum stark effect). As such it is important to quantify the average instantaneous spectrum and the long-time integrated spectrum to assess the suitability of a quantum dot for single photon emission applications. While a quantum dot may have a narrow instantaneous linewidth, significant spectral diffusion broadens the integrated linewidth in time and prevents photon indistinguishability. Like blinking, spectral diffusion is strongly correlated to surface passivation and as the passivation improves, spectral diffusion is reduced.

1.5.3 Single Photon Purity

The final performance category for single quantum dots is single photon purity – which is measured *via* the second order correlation function, also known as a $g^2(\tau)$. This measurement utilizes a Hanbury Brown Twiss interferometer (a 50:50 beamsplitter and two avalanche photo diodes) to measure how many photons are emitted per laser pulse. A $g^2(\tau)$measures the difference between the arrival times

of photons at detectors A and B. If we measure a single photon source, detectors A and B should not have photons arriving at the same time (ie $g^2(\tau = 0) = 0$). However, there should be strong peaks at times which correspond to multiples of the laser repetition rate ($g^2(\tau = nR) = 1$). This pattern is known as anti-bunching. While a $g^2(\tau = 0) = 0$ is the ideal single photon source, practically any emitter with a $g^2(\tau = 0) < 0.5$ is considered a single emitter.

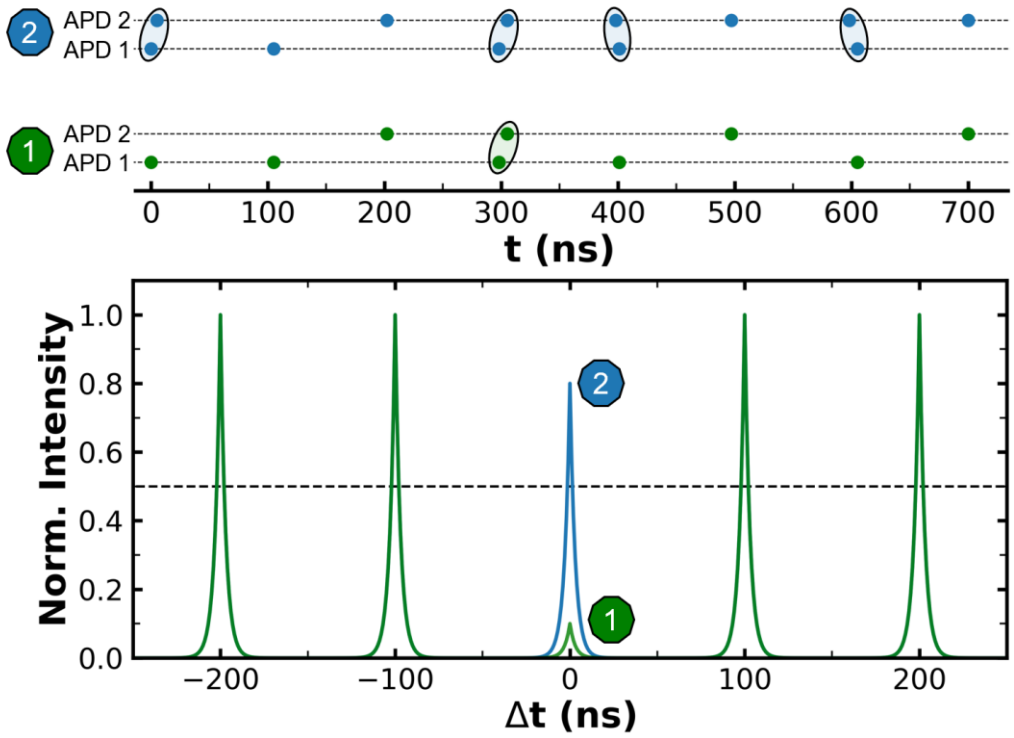

Figure 1.5: Measuring Single Photon Purity. (top) Arrival time of photons from quantum dots 1 (green) and 2 (blue) at two APDs. (bottom) g2(t) traces for quantum dots 1 (green) and 2 (blue). Quantum dot 1 shows anti-bunching behavior because most of the time a photon is only detected on APD 1 or APD 2 resulting in a less intense peak at t = 0. Quantum dot 2 does not show anti-bunching behavior since photons are detected at the same time on APDs 1 and 2 resulting in a more intense peak at t = 0.

1.6 References

(1) Protesescu, L.; Yakunin, S.; Bodnarchuk, M. I.; Krieg, F.; Caputo, R.; Hendon, C. H.; Yang, R. X.; Walsh, A.; Kovalenko, M. V. Nanocrystals of Cesium Lead Halide Perovskites (CsPbX3, X = Cl, Br, and I): Novel Optoelectronic Materials Showing Bright Emission with Wide Color Gamut. *Nano Lett* **2015**, *15* (6), 3692–3696. https://doi.org/10.1021/nl5048779.

(2) Akkerman, Q. A.; Rainò, G.; Kovalenko, M. V.; Manna, L. Genesis, Challenges and Opportunities for Colloidal Lead Halide Perovskite Nanocrystals. *Nature Materials 2018 17:5* **2018**, *17* (5), 394–405. https://doi.org/10.1038/s41563-018-0018-4.

(3) Han, T. H.; Jang, K. Y.; Dong, Y.; Friend, R. H.; Sargent, E. H.; Lee, T. W. A Roadmap for the Commercialization of Perovskite Light Emitters. *Nature Reviews Materials 2022 7:10* **2022**, *7* (10), 757–777. https://doi.org/10.1038/s41578-022-00459-4.

(4) Kortlever, R.; Shen, J.; Schouten, K. J. P.; Calle-Vallejo, F.; Koper, M. T. M.; Huang, J.; Buonsanti, R.; Nitopi, S. Industry Outlook of Perovskite Quantum Dots for Display Applications. *Nature Nanotechnology 2022 17:8* **2022**, *17* (8), 813–816. https://doi.org/10.1038/s41565-022-01163-8.

(5) Kim, Y. H.; Kim, S.; Kakekhani, A.; Park, J.; Park, J.; Lee, Y. H.; Xu, H.; Nagane, S.; Wexler, R. B.; Kim, D. H.; Jo, S. H.; Martínez-Sarti, L.; Tan, P.; Sadhanala, A.; Park, G. S.; Kim, Y. W.; Hu, B.; Bolink, H. J.; Yoo, S.; Friend, R. H.; Rappe, A. M.; Lee, T. W. Comprehensive Defect Suppression in Perovskite Nanocrystals for High-Efficiency Light-Emitting Diodes. *Nature Photonics 2021 15:2* **2021**, *15* (2), 148–155. https://doi.org/10.1038/s41566-020-00732-4.

(6) Akkerman, Q. A.; Gandini, M.; Di Stasio, F.; Rastogi, P.; Palazon, F.; Bertoni, G.; Ball, J. M.; Prato, M.; Petrozza, A.; Manna, L. Strongly Emissive Perovskite Nanocrystal Inks for High-Voltage Solar Cells. *Nat Energy* **2017**, *2* (2), 1–7. https://doi.org/10.1038/nenergy.2016.194.

(7) Lu, L.; Sun, M.; Wu, T.; Lu, Q.; Chen, B.; Huang, B. All-Inorganic Perovskite Nanocrystals: Next-Generation Scintillation Materials for High-Resolution X-Ray Imaging. *Nanoscale Adv* **2022**, *4* (3), 680–696. https://doi.org/10.1039/D1NA00815C.
(8) Kaplan, A. E. K.; Krajewska, C. J.; Proppe, A. H.; Sun, W.; Sverko, T.; Berkinsky, D. B.; Utzat, H.; Bawendi, M. G. Hong–Ou–Mandel Interference in Colloidal CsPbBr3 Perovskite Nanocrystals. *Nature Photonics 2023 17:9* **2023**, *17* (9), 775–780. https://doi.org/10.1038/s41566-023-01225-w.
(9) Utzat, H.; Sun, W.; Kaplan, A. E. K.; Krieg, F.; Ginterseder, M.; Spokoyny, B.; Klein, N. D.; Shulenberger, K. E.; Perkinson, C. F.; Kovalenko, M. V.; Bawendi, M. G. Coherent Single-Photon Emission from Colloidal Lead Halide Perovskite Quantum Dots. *Science (1979)* **2019**, *363* (6431). https://doi.org/10.1126/SCIENCE.AAU7392.
(10) Kuhlmann, A. V.; Houel, J.; Ludwig, A.; Greuter, L.; Reuter, D.; Wieck, A. D.; Poggio, M.; Warburton, R. J. Charge Noise and Spin Noise in a Semiconductor Quantum Device. *Nat Phys* **2013**, *9* (9), 570–575. https://doi.org/10.1038/NPHYS2688.
(11) Akkerman, Q. A.; Nguyen, T. P. T.; Boehme, S. C.; Montanarella, F.; Dirin, D. N.; Wechsler, P.; Beiglböck, F.; Rainò, G.; Erni, R.; Katan, C.; Even, J.; Kovalenko, M. V. Controlling the Nucleation and Growth Kinetics of Lead Halide Perovskite Quantum Dots. *Science (1979)* **2022**. https://doi.org/10.1126/SCIENCE.ABQ3616.
(12) Montanarella, F.; Akkerman, Q. A.; Bonatz, D.; Van Der Sluijs, M. M.; Van Der Bok, J. C.; Prins, P. T.; Aebli, M.; Mews, A.; Vanmaekelbergh, D.; Kovalenko, M. V. Growth and Self-Assembly of CsPbBr3Nanocrystals in the TOPO/PbBr2Synthesis as Seen with X-Ray Scattering. *Nano Lett* **2022**, *8*, 28. https://doi.org/10.1021/ACS.NANOLETT.2C04532.
(13) Almeida, G.; Ashton, O. J.; Goldoni, L.; Maggioni, D.; Petralanda, U.; Mishra, N.; Akkerman, Q. A.; Infante, I.; Snaith, H. J.; Manna, L. The Phosphine Oxide Route toward Lead Halide Perovskite Nanocrystals. **2018**. https://doi.org/10.1021/jacs.8b08978.
(14) Almeida, G.; Goldoni, L.; Akkerman, Q.; Dang, Z.; Khan, A. H.; Marras, S.; Moreels, I.; Manna, L. Role of Acid-Base Equilibria in the Size, Shape, and Phase Control of Cesium Lead Bromide Nanocrystals. *ACS Nano* **2018**, *12* (2), 1704–1711. https://doi.org/10.1021/ACSNANO.7B08357.
(15) Morad, V.; Stelmakh, A.; Svyrydenko, M.; Feld, L. G.; Boehme, S. C.; Aebli, M.; Affolter, J.; Kaul, C. J.; Schrenker, N. J.; Bals, S.; Sahin, Y.; Dirin, D. N.; Cherniukh, I.; Raino, G.; Baumketner, A.; Kovalenko, M. V. Designer Phospholipid Capping Ligands for Soft Metal Halide Nanocrystals. *Nature 2023 626:7999* **2023**, *626* (7999), 542–548. https://doi.org/10.1038/s41586-023-06932-6.
(16) Ye, J.; Li, Z.; Kubicki, D. J.; Zhang, Y.; Dai, L.; Otero-Martínez, C.; Reus, M. A.; Arul, R.; Dudipala, K. R.; Andaji-Garmaroudi, Z.; Huang, Y. T.; Li, Z.; Chen, Z.; Müller-Buschbaum, P.; Yip, H. L.; Stranks, S. D.; Grey, C. P.; Baumberg, J. J.; Greenham, N. C.; Polavarapu, L.; Rao, A.; Hoye, R. L. Z. Elucidating the Role of Antisolvents on the Surface Chemistry and Optoelectronic Properties of CsPbBrxI3-x Perovskite Nanocrystals. *J Am Chem Soc* **2022**, *144* (27), 12102–12115. https://doi.org/10.1021/JACS.2C02631.
(17) Zhang, B.; Goldoni, L.; Zito, J.; Dang, Z.; Almeida, G.; Zaccaria, F.; De Wit, J.; Infante, I.; De Trizio, L.; Manna, L. Alkyl Phosphonic Acids Deliver CsPbBr3 Nanocrystals with High Photoluminescence Quantum Yield and Truncated Octahedron Shape. *Chemistry of Materials* **2019**, *31* (21), 9140–9147. https://doi.org/10.1021/ACS.CHEMMATER.9B03529.
(18) Cho, E.; Kim, M.; Ouyang, L.; Kim, H.; Bonifas, G.; Coppel, Y.; Nayral, C.; Delpech, F.; Jeong, S. Unraveling the Facet-Dependent Surface Chemistry at Molecular Scale: Photoassisted Oxidation of InP Nanocrystals. *J Am Chem Soc* **2024**. https://doi.org/10.1021/JACS.4C10231.
(19) Panda, M. K.; Acharjee, D.; Mahato, A. B.; Ghosh, S. Facet Dependent Photoluminescence Blinking from Perovskite Nanocrystals. *Small* **2024**, *20* (33), 2311559. https://doi.org/10.1002/SMLL.202311559.
(20) Titus, T.; Vishnu, E. K.; Garai, A.; Dutta, S. K.; Sandeep, K.; Shelke, A.; Ajithkumar, T. G.; Shaji, A.; Pradhan, N.; Thomas, K. G. Biexciton Emission in CsPbBr3 Nanocrystals: Polar Facet Matters. *Nano Lett* **2024**, *23*, 49. https://doi.org/10.1021/ACS.NANOLETT.4C01186.
(21) Krieg, F.; Ochsenbein, S. T.; Yakunin, S.; Ten Brinck, S.; Aellen, P.; Süess, A.; Clerc, B.; Guggisberg, D.; Nazarenko, O.; Shynkarenko, Y.; Kumar, S.; Shih, C. J.; Infante, I.; Kovalenko, M. V. Colloidal CsPbX3 (X = Cl, Br, I) Nanocrystals 2.0: Zwitterionic Capping Ligands for Improved Durability and Stability. *ACS Energy Lett* **2018**, *3* (3), 641–646. https://doi.org/10.1021/ACSENERGYLETT.8B00035.
(22) Krieg, F.; Ong, Q. K.; Burian, M.; Rainò, G.; Naumenko, D.; Amenitsch, H.; Süess, A.; Grotevent, M. J.; Krumeich, F.; Bodnarchuk, M. I.; Shorubalko, I.; Stellacci, F.; Kovalenko, M. V. Stable Ultraconcentrated and Ultradilute Colloids of CsPbX3 (X = Cl, Br) Nanocrystals Using Natural Lecithin as a Capping Ligand. *J Am Chem Soc* **2019**, *141* (50), 19839–19849. https://doi.org/10.1021/JACS.9B09969.
(23) Ahmed, G. H.; Yin, J.; Bakr, O. M.; Mohammed, O. F. Successes and Challenges of Core/Shell Lead Halide Perovskite Nanocrystals. *ACS Energy Lett* **2021**, *6* (4), 1340–1357. https://doi.org/10.1021/ACSENERGYLETT.1C00076.
(24) Yin, J.; Yang, H.; Gutiérrez-Arzaluz, L.; Zhou, Y.; Brédas, J. L.; Bakr, O. M.; Mohammed, O. F. Luminescence and Stability Enhancement of Inorganic Perovskite Nanocrystals via Selective Surface Ligand Binding. *ACS Nano* **2021**, *15* (11), 17998–18005. https://doi.org/10.1021/ACSNANO.1C06480.
(25) Bodnarchuk, M. I.; Boehme, S. C.; Ten Brinck, S.; Bernasconi, C.; Shynkarenko, Y.; Krieg, F.; Widmer, R.; Aeschlimann, B.; Günther, D.; Kovalenko, M. V.; Infante, I. Rationalizing and Controlling the Surface Structure and Electronic Passivation of Cesium Lead Halide Nanocrystals. *ACS Energy Lett* **2019**, *4* (1), 63–74. https://doi.org/10.1021/ACSENERGYLETT.8B01669.
(26) Mangnus, M. J. J.; Wit, J. W. de; Vonk, S. J. W.; Geuchies, J. J.; Albrecht, W.; Bals, S.; Houtepen, A. J.; Rabouw, F. T. High-Throughput Characterization of Single-Quantum-Dot Emission Spectra and Spectral Diffusion by Multiparticle Spectroscopy. *ACS Photonics* **2023**. https://doi.org/10.1021/ACSPHOTONICS.3C00420.
(27) Gallagher, S.; Kline, J.; Jahanbakhshi, F.; Sadighian, J. C.; Lyons, I.; Shen, G.; Hammel, B. F.; Yazdi, S.; Dukovic, G.; Rappe, A. M.; Ginger, D. S. Ligand Equilibrium Influences Photoluminescence Blinking in CsPbBr3: A Change Point Analysis of Widefield Imaging Data. *ACS Nano* **2024**, *18* (29), 19208–19219. https://doi.org/10.1021/ACSNANO.4C04968.
(28) Frantsuzov, P. A.; Volkán-Kacsó, S.; Jankó, B. Universality of the Fluorescence Intermittency in Nanoscale Systems: Experiment and Theory. *Nano Lett* **2013**, *13* (2), 402–408. https://doi.org/10.1021/NL3035674.
(29) Kuno, M.; Fromm, D. P.; Hamann, H. F.; Gallagher, A.; Nesbitt, D. J. "On"/"off" Fluorescence Intermittency of Single Semiconductor Quantum Dots. *J Chem Phys* **2001**, *115* (2), 1028. https://doi.org/10.1063/1.1377883.
(30) Crouch, C. H.; Sauter, O.; Wu, X.; Purcell, R.; Querner, C.; Drndic, M.; Pelton, M. Facts and Artifacts in the Blinking Statistics of Semiconductor Nanocrystals. *Nano Lett* **2010**, *10* (5), 1692–1698. https://doi.org/10.1021/NL100030E.
(31) Watkins, L. P.; Yang, H. Detection of Intensity Change Points in Time-Resolved Single-Molecule Measurements. *Journal of Physical Chemistry B* **2005**, *109* (1), 617–628. https://doi.org/10.1021/JP0467548.

(32) Li, H.; Yang, H. Statistical Learning of Discrete States in Time Series. *Journal of Physical Chemistry B* **2019**, *123* (3), 689–701. https://doi.org/10.1021/ACS.JPCB.8B10561.
(33) Palstra, I. M.; Koenderink, A. F. A Python Toolbox for Unbiased Statistical Analysis of Fluorescence Intermittency of Multilevel Emitters. *Journal of Physical Chemistry C* **2021**, *125* (22), 12050–12060. https://doi.org/10.1021/ACS.JPCC.1C01670.
(34) Galland, C.; Ghosh, Y.; Steinbrück, A.; Sykora, M.; Hollingsworth, J. A.; Klimov, V. I.; Htoon, H. Two Types of Luminescence Blinking Revealed by Spectroelectrochemistry of Single Quantum Dots. *Nature 2011 479:7372* **2011**, *479* (7372), 203–207. https://doi.org/10.1038/nature10569.
(35) Yuan, G.; Gómez, D. E.; Kirkwood, N.; Boldt, K.; Mulvaney, P. Two Mechanisms Determine Quantum Dot Blinking. *ACS Nano* **2018**, *12* (4), 3397–3405. https://doi.org/10.1021/ACSNANO.7B09052.

Chapter 2: Ligand Equilibrium Influences Photoluminescence Blinking in $CsPbBr_3$: A Change Point Analysis of Widefield Imaging Data

Jessica Kline, Shaun Gallagher, Farzaneh Jahanbakhshi, James C. Sadighian, Ian Lyons, Gillian Shen, Benjamin F. Hammel, Sadegh Yazdi, Gordana Dukovic, Andrew M. Rappe, and David S. Ginger

This chapter is adapted from: ACS Nano 2024, 18, 19208−19219.
https://doi.org/10.1021/acsnano.4c04968.

Table of Contents

2.1 Overview

Photoluminescence intermittency remains one of the biggest challenges to realizing perovskite quantum dots (QDs) as scalable single photon emitters. We compare $CsPbBr_3$ QDs capped with different ligands, lecithin, and a combination of oleic acid and oleylamine, to elucidate the role of surface chemistry on photoluminescence intermittency. We employ widefield photoluminescence microscopy, sampling the blinking behavior of hundreds of QDs. Using change point analysis, we achieve the robust classification of blinking trajectories, and we analyze representative distributions from large numbers of QDs ($N_{lecithin}$ = 1308, $N_{oleic\ acid/oleylamine}$ =1317). We find that lecithin suppresses blinking in $CsPbBr_3$ QDs compared to oleic acid/oleylamine. Under common experimental conditions, lecithin-capped QDs are 7.5 times more likely to be non-blinking and spend 2.5 times longer in their most emissive state, despite both QDs having nearly identical solution photoluminescence quantum yields. We measure photoluminescence as a function of dilution and show that the differences between lecithin and oleic acid/oleylamine capping emerge at low concentrations during preparation for single particle experiments. From experiment and first principles calculations, we attribute the differences in lecithin and oleic acid/oleylamine performance to differences in their ligand binding equilibria. Consistent with our experimental data, density functional theory calculations suggest a stronger binding affinity of lecithin to the QD surface compared to oleic acid/oleylamine, implying a reduced likelihood of ligand desorption during dilution. These results suggest that using more tightly binding ligands is a necessity for surface passivation and consequently, blinking reduction in perovskite QDs used for single particle and quantum light experiments.

2.2 Introduction

Inorganic cesium lead bromide ($CsPbBr_3$) perovskite quantum dots (QDs) are promising solution-processable materials for a wide range of optoelectronic applications.[1] These materials exhibit high (>90%) photoluminescence quantum yields (PLQY),[2] narrow ensemble photoluminescence linewidths,[3] and emission spectra that can be tuned throughout the visible region.[4] These properties have motivated increased efforts to use perovskite QDs as the active layer in devices such as light-emitting diodes (QLEDs),[5] photovoltaics,[6] and even X-ray detectors.[7] More recently, their high degree of quantum coherence has positioned $CsPbBr_3$ QDs as leading candidates for next-generation quantum light sources - scalable, coherent single photon emitters[8–11]

Successful single photon emitters must demonstrate a high degree of single photon purity, have long coherence times, and be deterministically positioned within nanophotonic cavities.[12] Undesirable characteristics for single emitter candidates include photobleaching, particle heterogeneity, spectral diffusion, and photoluminescence intermittency.[12] Prior reports for $CsPbBr_3$ QDs have shown high single photon purity,[13,14] quantum interference between sequential photons,[15] and progress towards deterministic cavity positioning.[16–18] However, as even the highest quality perovskite QDs currently exhibit photoluminescence intermittency and spectral diffusion, events which have been linked in other quantum dot systems;[12,19] these challenges must be overcome to further improve these systems and reduce their photoluminescence linewidth.[8,20,21]

Quantum-confined materials possess high surface-area-to-volume ratios, meaning their properties are heavily influenced by their surfaces as has been extensively explored for II-VI quantum dots.[22–27] Improving $CsPbBr_3$ single photon emitters requires a more fundamental understanding and optimization of their surface chemistry.[12,28] $CsPbBr_3$ QDs are often described as defect tolerant and can achieve narrow

linewidths and high PLQYs without the use of a core-shell heterostructure (as in II-VI or III-VI QDs). However as defect formation is still a thermodynamically favorable process, $CsPbBr_3$ QDs require an organic ligand shell for both colloidal stability and surface defect passivation.[29,30] Due to the highly ionic bonding character of $CsPbBr_3$ QDs, many popular ligand systems contain both positive and negative charges, either in the form of zwitterions or monodentate ligand pairs.[31,32] The identity of this ligand layer plays a major role in modulating the properties of $CsPbBr_3$ QDs, including PLQY,[33] linewidth,[34] device performance,[35–39] and colloidal stability.[31,32]

Sustained synthetic efforts have identified several promising ligand species for $CsPbBr_3$ QDs. These include monodentate ligand pairs, like oleic acid/oleylamine[40], quaternary amines, like didodecyldimethylammonium bromide[41,42] and multi-dentate ligands, such as sulfobetaine,[43] lecithin,[44] diquaternary amines,[34] and phosphonic acids.[45,46] Despite ligands resulting in measurably different ensemble properties, including long-term colloidal stability,[44] and surface-defect induced electronic traps[37] there has been a lack of emphasis on understanding how these ligands affect the properties of single QDs. While some multi-dentate ligands display improved ensemble linewidths and near unity PLQY,[43,44] results from device integration are mixed,[38] underscoring the need for application-specific investigations, particularly at the single-particle level.

One way to probe the effects of surface chemistry on the optical properties of individual QDs is through monitoring their photoluminescence intermittency, or blinking.[47,48] Like other single photon emitters,[12] $CsPbBr_3$ QDs exhibit time-dependent variations in photoluminescence intensity at the single emitter level.[49] This variation in photoluminescence intensity arises from fluctuations in the non-radiative decay rates.[49] Prior studies of blinking in perovskite QDs have focused on understanding and passivating defects – through temperature-dependent measurements[50], and in-situ halide treatments.[51] However, relatively few studies have examined how varying the surface ligand chemistry of $CsPbBr_3$ QDs affects their blinking behavior.

Here we study the blinking dynamics of $CsPbBr_3$ QDs prepared via two different synthetic routes that result in dots passivated with two different ligands, a typical oleic acid/oleylamine based hot injection resulting in oleic acid/oleylamine-capped dots, and a recently reported room-temperature slow growth synthesis, leading to lecithin-capped dots via ligand exchange.[52] We utilize widefield photoluminescence microscopy and implement an automated particle selection and a change point analysis algorithm adapted to the noise profile of scientific cameras. This approach allows for significantly improved throughput and more robust sampling of the QD distributions. We find that, while both syntheses produce QDs with comparable PLQYs as synthesized, the lecithin-capped dots show dramatically reduced blinking when prepared and studied at the single particle level. We show that this difference primarily arises from the difference in ligand capping, and, despite similar ensemble characteristics, lecithin passivation leads to a dramatic decrease in blinking, seen through an improved ON percent distribution, a larger ON/OFF ratio, and a larger non-blinking fraction. We reconcile the apparent discrepancy between the ensemble photoluminescence properties and those of single dots by showing that the oleic acid/oleylamine dots suffer from significant degradation of their photoluminescence properties upon dilution to appropriate concentrations for single particle experiments. We present experimental evidence and theoretical analysis using density functional theory (DFT) calculations that rationalize these differences in terms of the ligand binding affinity, with lecithin showing significantly stronger binding to the QD surface compared to oleic acid/oleylamine.

2.3 Results and Discussion

We synthesized $CsPbBr_3$ QDs using one of two different methods from the literature to produce QDs with either oleic acid/oleylamine[40] or lecithin[52] as surface ligands (Figure 2.1a). Figures 2.1c and d show the UV-Vis absorption and photoluminescence spectra for representative synthetic batches of oleic acid/oleylamine-capped, and lecithin-capped dots, respectively. We find that the two ligand compositions impart similar ensemble properties to the QDs. The band-edge absorbance onset is nearly identical for both sets of QDs. However, lecithin-capped QDs show distinctly sharper excitonic features due to their spheroidal shape. The lecithin dots exhibit an emission at 506 nm with a FWHM of 19 nm, while the photoluminescence of oleic acid/oleylamine-capped QDs is slightly broader, as expected from the hot-injection synthesis, with an emission maximum at 507 nm and a 24 nm FWHM (Figures 2.1c and d). The lecithin-capped QDs batches tend to have slightly higher PLQY (95 ± 2% compared to 90 ± 5% when averaged across five synthetic batches) but shorter lifetimes (4.43 ± 0.04 ns vs 4.95 ± 0.02 ns) than oleic acid/oleylamine-capped QDs (Figure 2.1b-d). The shorter lifetime is qualitatively consistent with predictions for a spherical crystal habit, which was predicted to have faster recombination due to difference in dielectric confinement and asymmetry of the photon's electric field between spherical and cubic QDs at comparable sizes.[53] Interestingly, the spheroidal lecithin-capped QDs also show a low-energy tail in the photoluminescence lineshape, consistent with prior reports.[52,54] As the PLQYs and lifetimes of lecithin- and oleic acid/oleylamine- capped QDs are comparable at the ensemble level we can consider these QDs similarly passivated by both ligands. Additional discussion of the initial ligand coverage of the QDs can be found in Appendix A. From TEM the oleic acid/oleylamine-capped QDs are determined to be 9.3 ± 2.6 nm, comparable in size to our 9.7 ± 1.5 nm lecithin-capped QDs (Figure A1). Figure A2 shows HAADF-STEM images with the possible crystal facets associated with oleic acid/oleylamine- and lecithin- capped QDs.

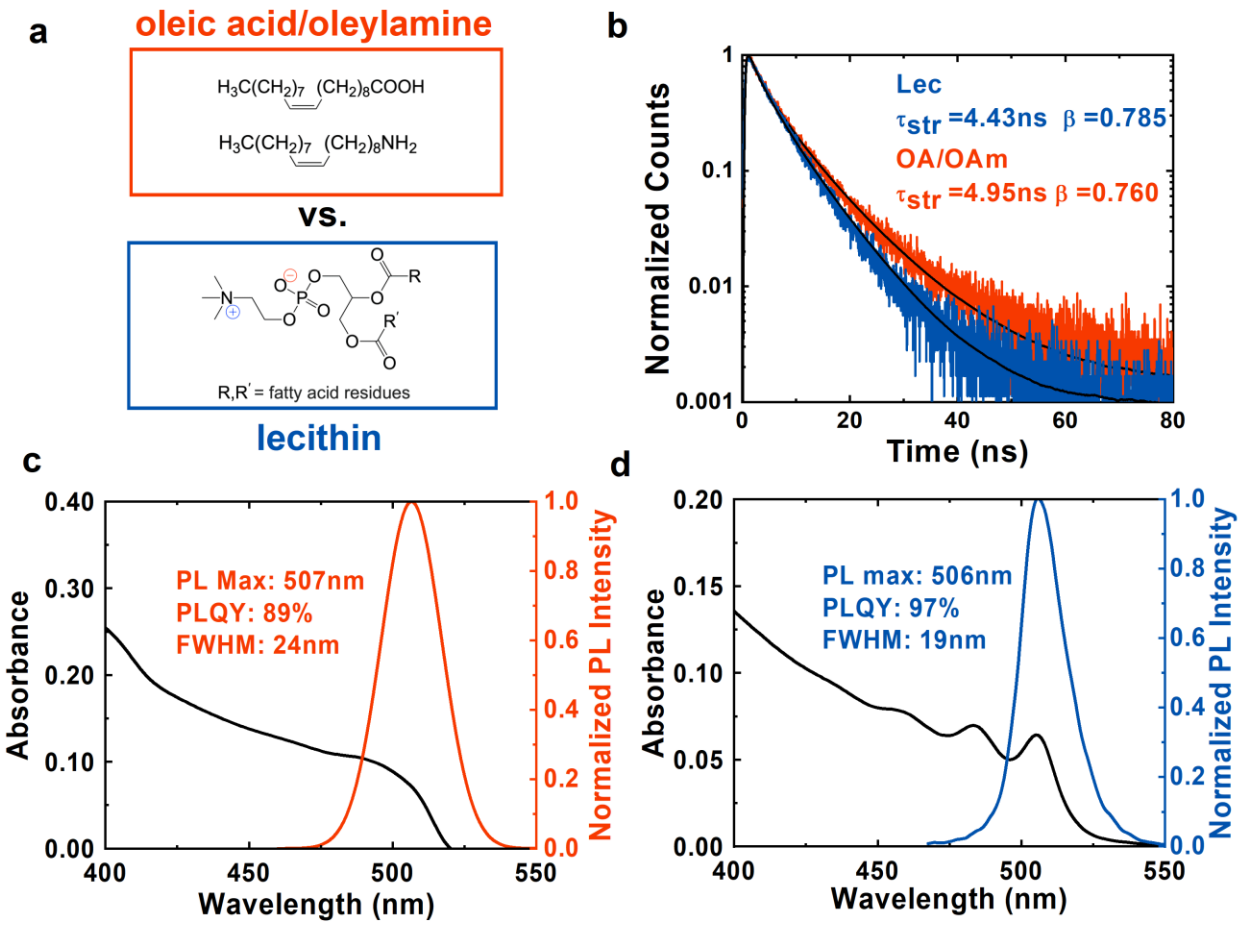

Figure 2.1: Ensemble characterization of lecithin and oleylamine/oleic acid capped QDs a) Chemical structures of zwitterionic lecithin (blue) and the monodentate ligand pair oleic acid (OA) and oleylamine (OAm) (red). **b)** Ensemble lifetimes of oleic acid/oleylamine-capped and lecithin-capped $CsPbBr_3$ QDs fit to a stretch exponential function (Equation A1) **c)** Ensemble solution characterization of oleic acid/oleylamine-capped $CsPbBr_3$ QDs **d)** Ensemble solution characterization lecithin-capped $CsPbBr_3$ QDs.

Studies of QD blinking statistics are commonly limited by two factors: the quantity of observed QDs and the analysis method.[55,56] Using confocal microscopy, blinking traces must be collected in series; limiting typical sample distributions to tens of QDs.[57] Instead, we collect blinking traces in parallel using widefield photoluminescence microscopy, allowing rapid collection of thousands of blinking traces.[58] Perovskite QDs also display complex blinking statistics, including multi-level dynamics, beyond simple two-level ON/OFF dynamics.[59] A data set of this size and complexity requires an automated, robust analysis method to extract accurate statistics. We satisfy this requirement through change point analysis (CPA) adapted to the noise profile of scientific cameras.[60–62] This combination of widefield imaging and CPA provides more representative sampling than previously possible, enabling a more accurate description of intermittency in these systems.

Figure 2.2 provides an overview of our analysis method on a representative image sequence of lecithin-capped $CsPbBr_3$ QDs. After the collection of a widefield image sequence, our analysis method works to extract the time series describing each QD's behavior and completes an unbiased classification of the photoluminescence trajectory. Figure 2.2a shows the mean intensity image of a widefield image

sequence. Single QDs (shown circled in red and labeled with a white number) are identified by an automated particle picking algorithm, designed to select small bright spots from a dark background.[63] Figure 2.2b shows the time series behavior of representative QDs (2, 6, and 11) extracted from the same widefield image sequence as Figure 2.2a. We generate these time series by intensity averaging the central pixels of selected QDs at each image in the sequence. Figures 2.2c and d show the photoluminescence trajectories identified for QD 2 (2-level) and QD 6 (3-level) respectively. We use change point analysis[60,61], which applies Bayesian statistics to find the photoluminescence trajectory which best describes a time series and to assign states to the photoluminescence vs. time trajectories. The methods section contains additional details about the analysis. Figure A3 shows representative trajectories from the oleic acid/oleylamine-capped quantum dots.

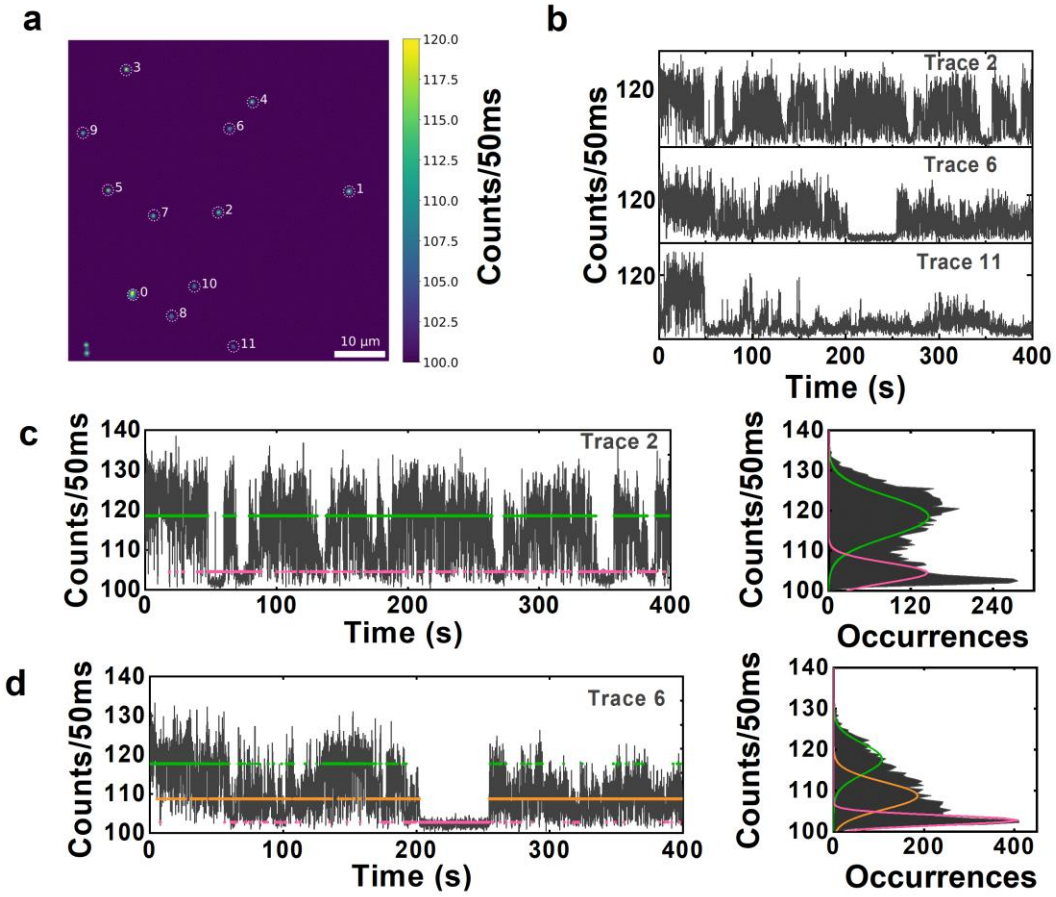

Figure 2.2: Workflow of widefield photoluminescence microscopy measurements. a) Automated particle selection results; particle selections are plotted on the mean intensity image in the sequence. For clarity, we show results from a small region of the overall image. Red circles labeled with a white number indicate quantum dot locations. **b)** Photoluminescence time series extracted from the selected regions in 2a corresponding to identified QDs 2, 6 and 11. **c)** CPA fitting of the time series from QD 2 (a). CPA finds that this time series is best described by a photoluminescence trajectory containing two average intensity levels (pink and green). **d)** CPA fitting of the time series from QD 6 (a). CPA finds that this time series is best described by a photoluminescence trajectory containing three average intensity levels (pink, orange and green).

To classify the blinking dynamics of lecithin-capped QD samples systematically, we analyzed the dynamics of five separate synthetic batches of comparable quality (Table A1 and Figure A4) to control for

batch-to-batch variation, which can often serve as a confounding variable.[64] Figures A5 and A6 explore the statistics for these five synthetic batches in more detail. The blinking statistics of lecithin-capped QDs we report in the main text of this paper are aggregated from the blinking behavior of all five batches.

We focus on four key metrics to compare blinking statistics: the non-blinking fraction, the ON percentage, the number of CPA levels in each trajectory, and the weighted ON/OFF ratio. We define the non-blinking fraction as all the QDs which are in their highest intensity level for greater than 95% of the observation time, consistent with previously reported widefield blinking studies.[48] The ON percentage quantifies how long we observed each QD in its highest intensity level state during the observation window. The weighted ON/OFF ratio quantifies, given an infinite observation time frame, how much more likely a QD is to be in its most emissive intensity level. Further details explaining how we calculate these statistics from our CPA results are in Appendix A. Here, we compare the blinking statistics across five different synthetic batches of lecithin-capped QDs (1308 QDs in total), to an oleic acid/oleylamine synthetic batch (1317 QDs in total). Additional comparisons between other synthetic batches of lecithin-capped and oleic acid/oleylamine-capped QDs are shown in Figure A7.

Surprisingly, despite similar ensemble properties, at the single particle level, we observe disparate blinking behaviors from the two QD compositions. Figure 2.3b shows a similar distribution of identified CPA levels between the two compositions. Nevertheless, at the single particle level lecithin-capped QDs significantly outperform those capped by oleic acid/oleylamine. Lecithin-capped QDs exhibit a larger non-blinking fraction (0.15 vs 0.02, Figure 2.3a), higher average ON percentage (68% vs 30%, Figure 2.3c), and a larger weighted ON/OFF ratio (3.1 vs 0.73, Figure 2.3d); all metrics are consistent with dramatic reductions in their blinking. Additional metrics comparing blinking in lecithin-capped and oleic acid/oleylamine-capped $CsPbBr_3$ QDs are shown in Figure A8. At face value, this result seems surprising – after all, the ensemble is the sum of the individual single particles, yet the single particle data differ dramatically.

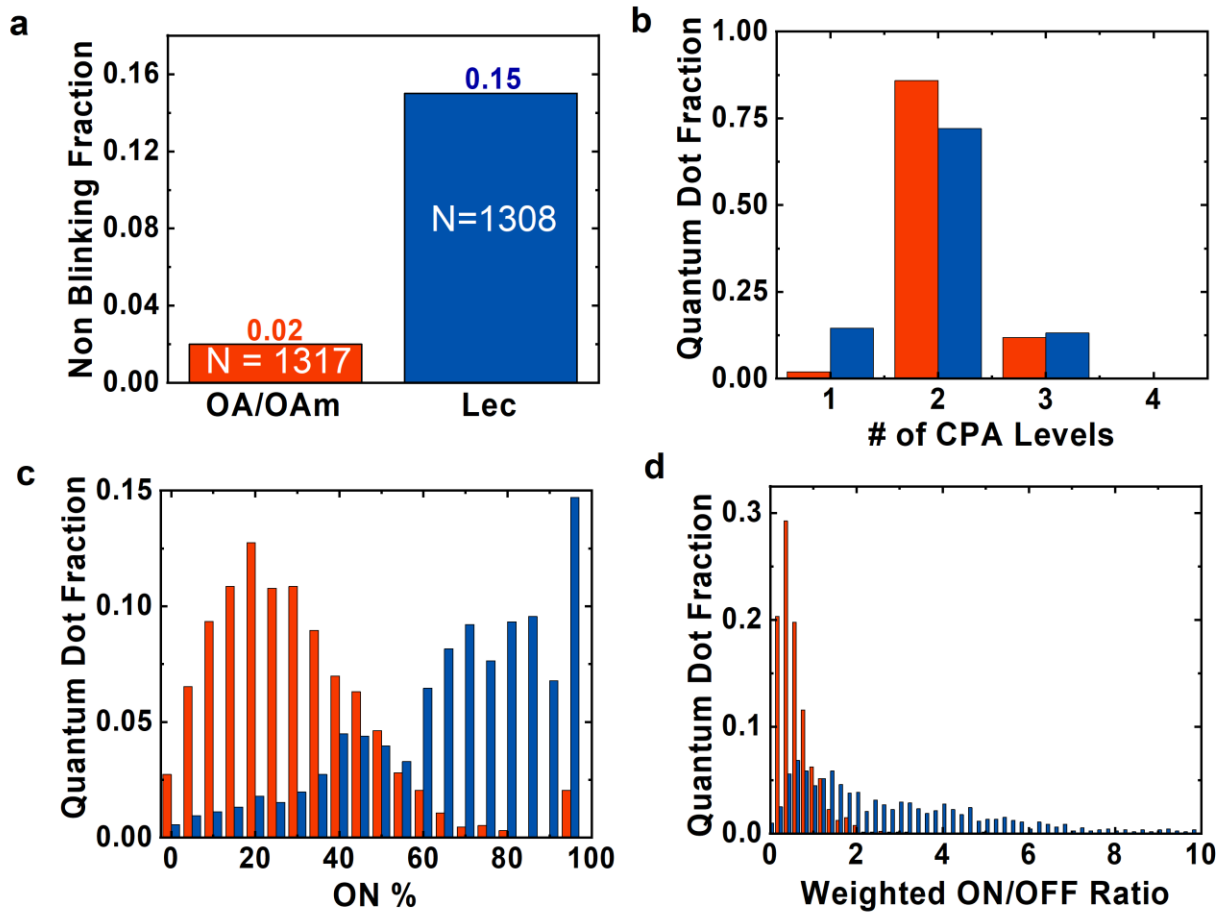

Figure 2.3: Comparison of blinking statistics between oleic acid/oleylamine-capped (OA/OAm, red) and lecithin-capped (Lec, blue) CsPbBr3. a) The non-blinking fraction (>95% ON). **b)** The distribution of the number of intensity levels fit by CPA across all studied QDs. **c)** Distribution of the ON percentages for all QDs. **d)** The weighted ON/OFF ratio distribution.

To better understand these contrasting blinking distributions, we turn to concentration dependent photoluminescence and time-resolved photoluminescence (TRPL) studies. First, we use TRPL for a comparative estimate of surface quality based on lifetime duration. At the QD concentration used to acquire our ensemble PLQY data the oleic acid/oleylamine-capped QDs have an average lifetime of 4.95 ± 0.02 ns and a stretching exponent of $\beta = 0.779 \pm 0.001$ (Figure 2.4a). After diluting the QD sample to the concentration used to prepare single particle samples, we find that the average lifetime has decreased to 2.08 ± 0.03 ns with a stretching exponent of $\beta = 0.455 \pm 0.002$ (Figure 2.4a). The observed decrease in average lifetime and stretching exponent indicates that the surface passivation and sample homogeneity have worsened during the dilution process, and that the OA/OAm QDs show a broader distribution of photoluminescence lifetimes.[65] In contrast, Figure 2.4b shows the average lifetime for lecithin-capped QDs remains essentially constant during the dilution process (4.43 ± 0.04 ns vs 4.50 ± 0.08 ns). Additional concentration dependent lifetimes for oleic acid/oleylamine-capped and lecithin-capped QDs are shown in Figures A9 and A10 and the concentration dependent beta-factors are shown in Figure A11.

We next turn to concentration-dependent photoluminescence studies for a more quantitative understanding of the changes in surface passivation inferred from the TRPL data. If the PLQY of a material remains constant with dilution, the integrated photoluminescence intensity should scale linearly with

concentration. A sub-linear trend would indicate a loss of PLQY with dilution. This fact allows integrated photoluminescence intensity to serve as a proxy for PLQY at concentrations too dilute to be directly measured. Figure 2.4c plots the photoluminescence intensity versus concentration for both the lecithin-capped and oleic acid/oleylamine-capped QDs. For the lecithin-capped dots, we observe a linear relationship between the photoluminescence intensity and concentration over three orders of magnitude in concentration, spanning from typical measurement concentrations for solution PLQY to a concentration range below that used in our single QD microscopy experiments. In contrast, Figure 2.4c shows that the integrated photoluminescence intensity for the oleic acid/oleylamine-capped QDs is linear at higher concentrations, but falls off rapidly as the concentration decreases. This additional decrease in intensity is consistent with the change in the non-radiative recombination dynamics we deduce from the TRPL shown in Figure 2.4a. Approximately midway between the PLQY concentration (indicated with a green square) and the single QD microscopy concentration (indicated with a green circle), oleic acid/oleylamine-capped QDs see a significant decrease in integrated photoluminescence intensity, which we interpret as a decrease in PLQY due to ligand desorption. This interpretation is supported by Figure A12 which shows the PLQY as a function of dilution for more concentrated solutions. Even across the range of concentrations measurable by an integrating sphere the PLQY of oleic acid/oleylamine-capped QDs is decreasing. PL linearity plots for additional sizes and morphologies of lecithin- and oleic acid/oleylamine- capped QDs are shown in Figures A13 and A14, indicating that these observed concentration results are generalizable across different QD sizes and morphologies.

Previous studies on a range of QDs have attributed photoluminescence decreases during washing to an equilibrium between the ligand bound to the QD surface and free-ligand in solution which shifts to favor free-ligand during dilution or antisolvent washing.[41] As the concentration of unbound ligand decreases during dilution, the equilibrium shifts, and monodentate ligands like oleic acid and oleylamine are likely to detach from perovskite QDs in two ways – as a neutral ligand pair (OAm-OA) or as ligand-ion pairs (OA^--Cs^+ and OAm^+-Br^-) which leave behind additional vacancies.[31] As the ligands desorb from the surface, the number of surface traps increases which can explain both the sub-linear photoluminescence trend and increased blinking observed in oleic acid/oleylamine-capped QDs. These single particle results are consistent with prior reports of decreased PLQY in halide perovskite QDs at low concentrations.[66]

To test whether ligand desorption might cause the observed non-linear decrease in quantum dot emission with decreasing concentration, we investigate the effect of the adding back additional ligand to dilute solutions of oleic acid/oleylamine-capped QDs. Figure 2.4d plots the photoluminescence intensity of a dilute solution oleic acid/oleylamine-capped QDs as a function of excess ligand addition. The solution's photoluminescence intensity increases after adding small amounts of oleylamine or lecithin, resulting in a maximum 120% increase in photoluminescence intensity. The photoluminescence change associated with ligand addition shows three clear phases. From 0-0.2 mmols of ligand added the photoluminescence increases as the additional ligand passivates vacancies. Between 0.2 and 0.4 additional mmols of ligand the photoluminescence remains constant as the quantum dots are fully passivated. Above 0.4 mmols of additional ligand the photoluminescence intensity decreases as excess ligand etches the surface of the quantum dots. Figure A15 shows evidence of QD etching with excess ligand addition. The photoluminescence recovery associated with the addition of other ligands is shown in Figure A16.

Taken together the results above suggest that the increased blinking behavior in the oleic acid/oleylamine-capped QDs stems from ligand loss with dilution. We speculate that the lack of full

photoluminescence recovery (which is expected to be approximately 220% according to the trend line) after excess ligand addition might indicate that ligand loss in oleic acid/oleylamine-capped $CsPbBr_3$ contributes to the irreversible degradation of a fraction of these QDs. These results are consistent with widefield photoluminescence images of lecithin-capped and oleic acid/oleylamine-capped samples prepared at the same concentration indicating that a smaller fraction of oleic acid/oleylamine capped QDs remain emissive after dilution (Figure A17).

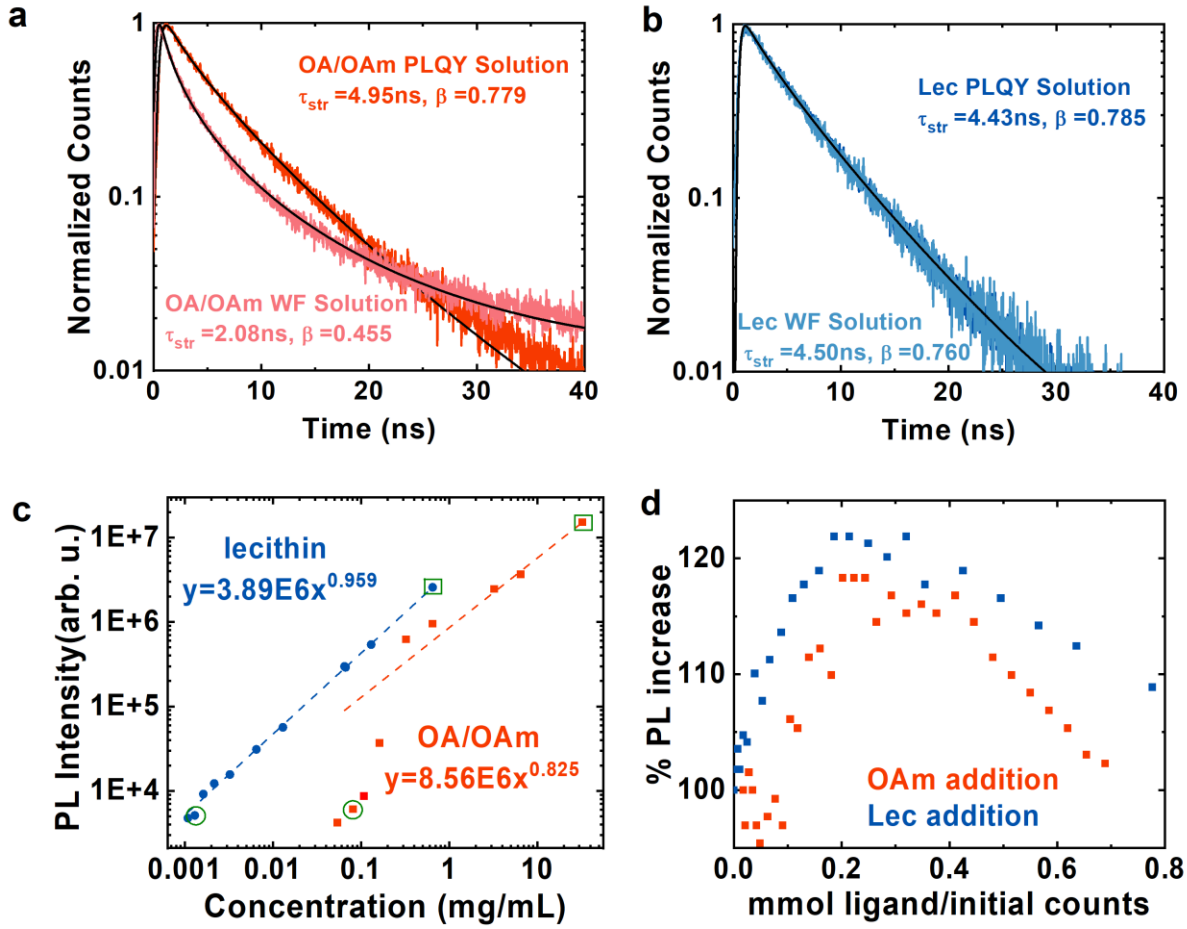

Figure 2.4: Rationalizing reduced blinking in lecithin-capped QDs. **a)** Concentration dependent TRPL for oleic acid/oleylamine-$CsPbBr_3$ at the PLQY concentration (green box in (c)) and widefield (WF) concentration (green circle in (c)). **b)** Concentration dependent TRPL for lecithin-capped $CsPbBr_3$ at the PLQY concentration (green box in (c)) and widefield concentration (green circle in (c)). **c)** Concentration dependent photoluminescence intensity for oleic acid/oleylamine (OA/OAm, red) and lecithin (blue) capped QDs. Intensity vs. concentration values are fit to a power law (a power law exponent of 1 indicates a linear relationship). The experimental concentrations for PLQY and widefield photoluminescence blinking measurements on both compositions are indicated with green box and a green circle, respectively. **d)** Photoluminescence increase resulting from the addition of oleylamine (OAm) and lecithin (Lec) to a widefield concentration solution (green circle in (c)) of oleic acid/oleylamine-capped $CsPbBr_3$ QDs.

To rationalize the differences in blinking behavior between oleic acid/oleylamine- and lecithin-capped QDs, we study the quantum dot electronic structure and compute the binding energies of the capping ligands to the surface of the QDs. To begin, we calculated the density of states for the pristine and the defective (containing v•Br or v'Cs) slabs of $CsPbBr_3$, shown in Figure A18. We performed DFT-PBE calculations considering spin orbit coupling effects, which are known to strongly influence the position of

band edges in lead halide perovskites.[67] We calculated the band gaps of the pristine slab as well as $v^{\bullet}_{Br}$ and v'_{Cs} containing slabs of $CsPbBr_3$ to be 1.4 eV, 1.17 eV and 1.05 eV, respectively. Additionally, we calculate the band gap of $CsPbBr_3$ at the PBE0+SOC level using a dense k-point grid and find the band gap to be 2.40 eV in good agreement with our experimentally observed band gap. Figures A18b and A18c depict near gap states due to the presence of surface vacancies ($v^{\bullet}_{Br}$ and v'_{Cs}) that are known potential recombination centers,[68] and the band gap closure that stems from them compared to the pristine slab (Figure A18a). We posit that the origin of the difference in blinking behavior between lecithin- and oleic acid/oleylamine-capped QDs lies in the ability of the ligands to passivate these defects. To this end, we investigated the potential difference in surface binding energy between lecithin and oleic acid/oleylamine using first principles studies.

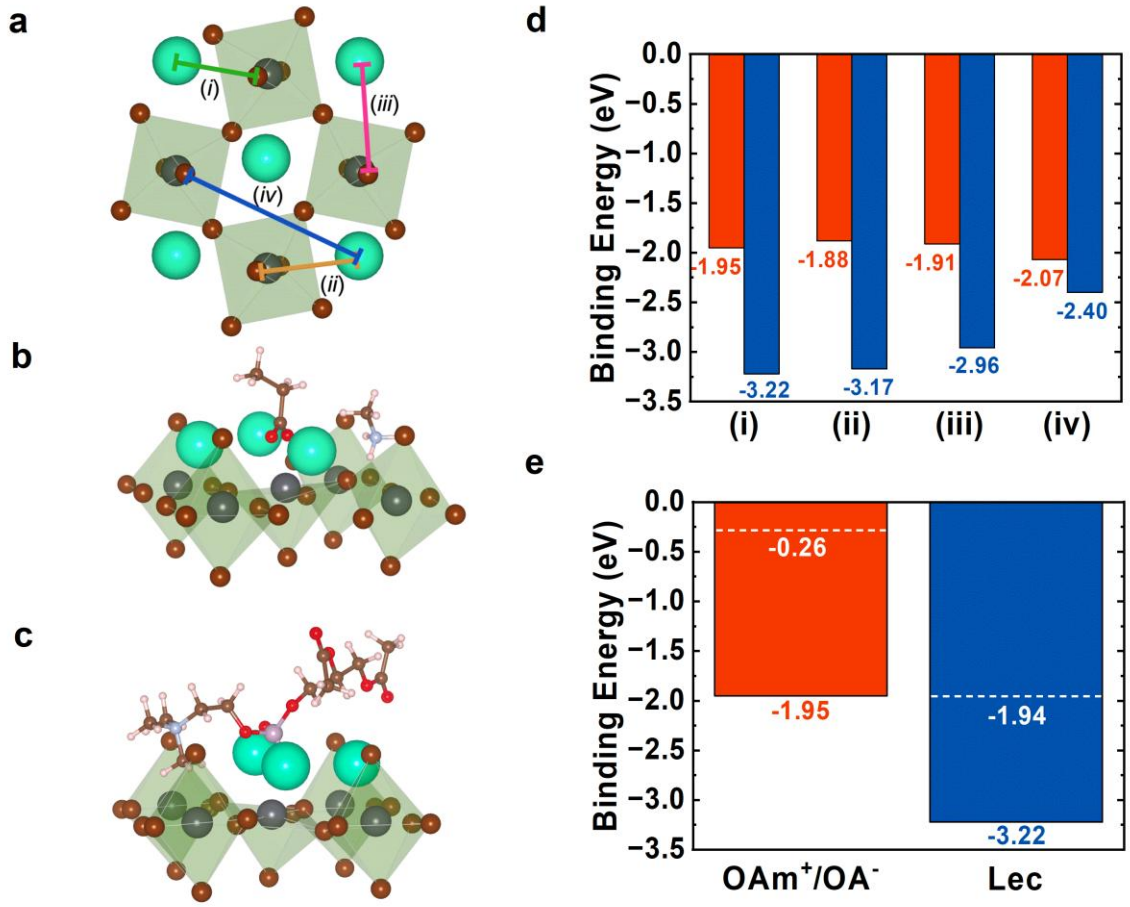

Figure 2.5: Calculated binding energies for oleic acid/oleylamine and lecithin a) Top view of the PBE-relaxed lattice of orthorhombic $CsPbBr_3$ (8.19 Å, 8.54 Å, 11.99 Å) and different types of vacancy pairs studied here marked as *i, ii, iii* and *iv* **b)** PBE+D3-relaxed $CsPbBr_3$ slab with a type *i* vacancy pair passivated by oleic acid/oleylamine **c)** PBE+D3-relaxed $CsPbBr_3$ slab with a type *i* vacancy pair passivated by lecithin **d)** Calculated binding energies in eV for $CsPbBr_3$ slabs containing v'_{Cs} and $v^{\bullet}_{Br}$ passivated by oleic acid/oleylamine (red) and lecithin (blue), at PBE+D3 level of theory. **e)** Vacancy pair type *i* binding energy for both lecithin and oleic acid/oleylamine with binding energy in the presence of solvent represented by white dashed lines.

We conducted a comparative study on the passivation of v'_{Cs}-$v^{\bullet}_{Br}$ vacancy pairs by oleic acid/oleylamine and lecithin ligands. Figure 2.5a shows the orthorhombic phase of $CsPbBr_3$ and different types of the adjacent (types *i, ii* and *iii*) and non-adjacent (type *iv*) vacancy pairs used in our calculations.

Figures 2.5b and c depict the monodentate ligand pair and the bidentate ligand binding the QD surface and passivating an adjacent surface vacancy pair. As we do not expect the long alkyl tails of the ligands to participate in surface binding, we use simplified forms of the ligands (methylamine, propionic acid and truncated lecithin, Figure A19 for computational purposes. Given the dynamic equilibrium between the charged and neutral ligands in the solution, we studied surface defect passivation for both cases. Between charged and neutral ligands, we found that OAm^+/OA^- passivating an adjacent vacancy pair is the most stable configuration and that the neutral ligand pair could only passivate a non-adjacent vacancy pair and exhibits a lower binding affinity (-1.07 eV) than that of the charged ligands (-1.95 eV). Additionally, our calculations revealed that the neutral ligand pair binding the defective surface in the presence of solvent is relatively thermodynamically unfavorable (Table A2). As such, we can consider the passivation of the studied QDs to consist of only charged ligand pairs bound to defective sites as the process of ligands binding to the pristine surface results in the creation of additional vacancy pairs.[69] Figure 2.5d shows the binding energies calculated at the DFT level for lecithin and OAm^+/OA^- (-3.22 eV and -1.95 eV, respectively), when passivating the vacancy pairs. Figure 2.5d and Table A3 summarize the binding energies calculated for the different vacancy pair types and show that for both adjacent and non-adjacent vacancies, lecithin binds the QD surface more strongly than OAm^+/OA^-. However, for non-adjacent vacancies, the relative binding energy of OAm^+/OA^- increases while the lecithin binding energy decreases. For both ligands we rationalize this difference by considering the larger distance between the non-adjacent vacancies (3.7-5.0 Å vs 8.5 Å). For OAm^+/OA^-, the larger distance between the two vacancies results in a weaker intermolecular interaction and a subsequent higher affinity for the QD surface. Lecithin, as a bidentate ligand, demonstrates a preference for passivating adjacent vacancy pairs. Our theoretical findings suggest that lecithin binds more strongly to the QD surface, which aligns qualitatively with experiments. However, the magnitudes of calculated binding energies do not reproduce the observed ligand equilibrium shifting to unbound ligands over the experimental concentrations. Such observed difference led us to consider the impact of solvents that appear critical in representing the experimental conditions.

Since experiments indicate that the dilution effects on ligand binding equilibria should be significant, we further refined the binding energies by including solvation effects (Figure A20). As shown in Figure 2.5e, the net change in the binding energy due to solvation effects is notable for both ligands in the representative case of a type *i* vacancy pair. The calculated binding energy of -0.26 eV for OAm^+/OA^- suggests a high likelihood of ligand desorption which we speculate to be the root cause of the observed difference in the blinking behavior between oleic acid/oleylamine- and lecithin-capped $CsPbBr_3$ QDs. However, the binding energy of lecithin remains significantly large (more negative) upon solvation and can explain the observed reduction in blinking. Notably, the binding energy for OAm^+/OA^- calculated *via* DFT (-0.26 eV) is in good agreement with the analogous binding energy estimated from Figure 2.4c (-0.34 eV). We ascribe the remaining discrepancies between the calculated and experimental binding energies to the absence of entropy and finite-temperature effects in our calculations, the inherent challenges in accurately modelling solvation effects, and the limitations in the assumptions behind the experimental analysis (see Appendix A). Appendix A contains a detailed explanation of solvation effects calculations, equilibrium constants and binding energies summarized in Table A4.

2.4 Conclusion

We use widefield photoluminescence microscopy and CPA to analyze the blinking statistics of 2,600 QDs to compare the effect of bidentate and monodentate ligands on photoluminescence intermittency

in $CsPbBr_3$. We show that, despite similar ensemble properties, using lecithin as a capping ligand results in QDs with a non-blinking fraction 7.5 times larger than that of the oleic acid/oleylamine ligand pair. This difference in performance is explained through a ligand binding equilibrium where oleic acid and oleylamine desorb during serial dilutions, degrading the surface. This ligand binding model is supported by two key sets of findings. First, concentration dependent photoluminescence measurements, which expose a non-linear relationship between oleic acid/oleylamine photoluminescence intensity and concentration. Second, theoretical investigation and binding energy calculations at the DFT level highlight striking differences in solvated-binding energy between lecithin and OAm^+/OA^-. This blinking suppression highlights the promise of these lecithin capped $CsPbBr_3$ QDs as scalable single photon emitters.

We also demonstrate the promising capabilities of widefield photoluminescence microscopy paired with CPA. Together, these two techniques facilitate rapid, representative sampling of QD blinking statistics, allowing more accurate determinations of QD behavior and its connections to surface chemistry. This method can compare blinking through the number of intensity levels, the non-blinking fraction, the percent of time spent in the most intense state, the expected dwell time in an ON state, the expected dwell time in an OFF state and the weighted ON/OFF ratio. The variety of statistics available from this analysis method, combined with the larger sample size available *via* widefield microscopy allow us to determine representative blinking statistics of a sample more accurately, enabling deeper and more accurate investigations of the role QD surface chemistry plays in blinking.

While we address the difference in blinking caused by using oleic acid/oleylamine and lecithin as ligands, it is also possible that the spheroidal shape of these QDs influences their blinking as well. Though we have demonstrated, through several control experiments, the significant impact ligand binding has on photoluminescence blinking, it is still possible that the spheroidal shape of these QDs contributes to their better stability. Given the interest in these materials for such a wide range of applications and their impressive non-blinking characteristics, a more detailed understanding of how the spherical crystal habit affects trap density and the ligand-binding equilibrium could prove valuable. Future work is needed to explore this relationship. The differences in blinking behavior observed here also lead naturally to the exploration of other ligands used to passivate $CsPbBr_3$, including alternative zwitterions,[69] dications,[34] and tightly binding monodentate ligands.[29]

High throughput of widefield imaging, combined with the robust nature of CPA, permits detailed analysis of larger sample sizes of QDs. As we have demonstrated, the choice of surface ligand is vital to ensure that the QDs maintain their properties at the low concentrations required for both single particle characterization and nanophotonic cavity integration. The experimental techniques discussed here enable systematic investigations into the root causes of photoluminescence intermittency in QDs.

2.5 Acknowledgements

This work, and the roles of S.G., J.K. J.C.S., I.L., G.S., F.J., A.M.R., B.F.H, S.Y, G.D and D.S.G. were primarily supported by the National Science Foundation under the STC IMOD Grant (No. DMR-2019444). The authors acknowledge the use of facilities and instruments at the Photonics Research Center (PRC) at the Department of Chemistry, University of Washington, as well as that at the Research Training Testbed (RTT), part of the Washington Clean Energy Testbeds system. Part of this work was carried out at the Molecular Analysis Facility, a National Nanotechnology Coordinated Infrastructure site at the University of Washington which is supported in part by the National Science Foundation (NNCI-1542101), the Molecular Engineering & Sciences Institute, and the Clean Energy Institute. Computational

support was provided by the National Energy Research Scientific Computing Center (NERSC), a US Department of Energy, Office of Science User Facility, located at Lawrence Berkeley National Laboratory, operated under contract no. DE-AC02-05CH11231. TEM was carried out at the Facility for Electron Microscopy of Materials at the University of Colorado Boulder (CU FEMM, RRID: SCR_019306). B.F.H. acknowledges support from the National Science Foundation through the Graduate Research Fellowship Program (NSF-GRFP) under Grant No. DGE 2040434.

S.G. and J.K. would like to acknowledge Margherita Taddei (graduate student, University of Washington) for scientific discussions related to photoluminescence lifetime measurements, Muammer Yaman (graduate student, University of Washington) for his particle identification code and Seth Dale (graduate student, Colorado School of Mines) for his insights into improving the runtime of our change point analysis code. We also thank Hannah Even for her contribution during her stay in the Rappe group as part of the Research Experience for Undergraduates program supported by IMOD.

2.6 References

(1) Dey, A.; Ye, J.; De, A.; Debroye, E.; Ha, S. K.; Bladt, E.; Kshirsagar, A. S.; Wang, Z.; Yin, J.; Wang, Y.; Quan, L. N.; Yan, F.; Gao, M.; Li, X.; Shamsi, J.; Debnath, T.; Cao, M.; Scheel, M. A.; Kumar, S.; Steele, J. A.; Gerhard, M.; Chouhan, L.; Xu, K.; Wu, X. G.; Li, Y.; Zhang, Y.; Dutta, A.; Han, C.; Vincon, I.; Rogach, A. L.; Nag, A.; Samanta, A.; Korgel, B. A.; Shih, C. J.; Gamelin, D. R.; Son, D. H.; Zeng, H.; Zhong, H.; Sun, H.; Demir, H. V.; Scheblykin, I. G.; Mora-Seró, I.; Stolarczyk, J. K.; Zhang, J. Z.; Feldmann, J.; Hofkens, J.; Luther, J. M.; Pérez-Prieto, J.; Li, L.; Manna, L.; Bodnarchuk, M. I.; Kovalenko, M. V.; Roeffaers, M. B. J.; Pradhan, N.; Mohammed, O. F.; Bakr, O. M.; Yang, P.; Müller-Buschbaum, P.; Kamat, P. V.; Bao, Q.; Zhang, Q.; Krahne, R.; Galian, R. E.; Stranks, S. D.; Bals, S.; Biju, V.; Tisdale, W. A.; Yan, Y.; Hoye, R. L. Z.; Polavarapu, L. State of the Art and Prospects for Halide Perovskite Nanocrystals. *ACS Nano* **2021**, *15*, 10775–10981. https://doi.org/10.1021/acsnano.0c08903.

(2) Xian-gang Wu; Honglei Ji; Xiaolin Yan; and Haizheng Zhong. Industry Outlook of Perovskite Quantum Dots for Display Applications. *Nat Nanotechnol* **2022**, *17* (8), 811–813. https://doi.org/10.1038/s41565-022-01147-8.

(3) Han, T. H.; Jang, K. Y.; Dong, Y.; Friend, R. H.; Sargent, E. H.; Lee, T. W. A Roadmap for the Commercialization of Perovskite Light Emitters. *Nat Rev Mater* **2022**, *7* (10), 757–777. https://doi.org/10.1038/s41578-022-00459-4.

(4) Akkerman, Q. A.; Rainò, G.; Kovalenko, M. V.; Manna, L. Genesis, Challenges and Opportunities for Colloidal Lead Halide Perovskite Nanocrystals. *Nat Mater* **2018**, *17*, 394–405. https://doi.org/10.1038/s41563-018-0018-4.

(5) Kim, Y. H.; Kim, S.; Kakekhani, A.; Park, J.; Park, J.; Lee, Y. H.; Xu, H.; Nagane, S.; Wexler, R. B.; Kim, D. H.; Jo, S. H.; Martínez-Sarti, L.; Tan, P.; Sadhanala, A.; Park, G. S.; Kim, Y. W.; Hu, B.; Bolink, H. J.; Yoo, S.; Friend, R. H.; Rappe, A. M.; Lee, T. W. Comprehensive Defect Suppression in Perovskite Nanocrystals for High-Efficiency Light-Emitting Diodes. *Nat Photonics* **2021**, *15*, 148–155. https://doi.org/10.1038/s41566-020-00732-4.

(6) Akkerman, Q. A.; Gandini, M.; Di Stasio, F.; Rastogi, P.; Palazon, F.; Bertoni, G.; Ball, J. M.; Prato, M.; Petrozza, A.; Manna, L. Strongly Emissive Perovskite Nanocrystal Inks for High-Voltage Solar Cells. *Nat Energy* **2017**, *2* (2). https://doi.org/10.1038/nenergy.2016.194.

(7) Lu, L.; Sun, M.; Wu, T.; Lu, Q.; Chen, B.; Huang, B. All-Inorganic Perovskite Nanocrystals: Next-Generation Scintillation Materials for High-Resolution X-Ray Imaging. *Nanoscale Adv* **2022**, *4* (3), 680–696. https://doi.org/10.1039/d1na00815c.

(8) Utzat, H.; Sun, W.; Kaplan, A. E. K.; Krieg, F.; Ginterseder, M.; Spokoyny, B.; Klein, N. D.; Shulenberger, K. E.; Perkinson, C. F.; Kovalenko, M. V.; Bawendi, M. G. Coherent Single Photon Emission from Colloidal Lead Halide Perovskite Quantum Dots. *Science (1979)* **2018**, *7392*, 1068–1072. https://doi.org/10.1126/science.aau7392.

(9) Ricci, F.; Marougail, V.; Varnavski, O.; Wu, Y.; Padgaonkar, S.; Irgen-Gioro, S.; Weiss, E. A.; Goodson, T. Enhanced Exciton Quantum Coherence in Single CsPbBr 3 Perovskite Quantum Dots Using Femtosecond Two-Photon Near-Field Scanning Optical Microscopy . *ACS Nano* **2021**. https://doi.org/10.1021/acsnano.1c01615.

(10) Kagan, C. R.; Bassett, L. C.; Murray, C. B.; Thompson, S. M. Colloidal Quantum Dots as Platforms for Quantum Information Science. *Chem Rev* **2021**, *121* (5), 3186–3233. https://doi.org/10.1021/acs.chemrev.0c00831.

(11) Rainò, G.; Becker, M. A.; Bodnarchuk, M. I.; Mahrt, R. F.; Kovalenko, M. V.; Stöferle, T. Superfluorescence from Lead Halide Perovskite Quantum Dot Superlattices. *Nature* **2018**, *563* (7733), 671–675. https://doi.org/10.1038/s41586-018-0683-0.

(12) Nguyen, H. A.; Dixon, G.; Dou, F. Y.; Gallagher, S.; Gibbs, S.; Ladd, D. M.; Marino, E.; Ondry, J. C.; Shanahan, J. P.; Vasileiadou, E. S.; Barlow, S.; Gamelin, D. R.; Ginger, D. S.; Jonas, D. M.; Kanatzidis, M. G.; Marder, S. R.; Morton, D.; Murray, C. B.; Owen, J. S.; Talapin, D. V.; Toney, M. F.; Cossairt, B. M. Design Rules for Obtaining Narrow Luminescence from Semiconductors Made in Solution. *Chem Rev* **2023**, *123* (12), 7890–7952. https://doi.org/10.1021/acs.chemrev.3c00097.

(13) Zhu, C.; Marczak, M.; Feld, L.; Boehme, S. C.; Bernasconi, C.; Moskalenko, A.; Cherniukh, I.; Dirin, D.; Bodnarchuk, M. I.; Kovalenko, M. V; Raino, G. Room-Temperature, Highly Pure Single-Photon Sources from All- Inorganic Lead Halide Perovskite Quantum Dots. *Nano Lett* **2022**, *22*, 3751–3760. https://doi.org/10.1021/acs.nanolett.2c00756.

(14) Boehme, S. C.; Bodnarchuk, M. I.; Burian, M.; Bertolotti, F.; Cherniukh, I.; Bernasconi, C.; Zhu, C.; Erni, R.; Amenitsch, H.; Naumenko, D.; Andrusiv, H.; Semkiv, N.; John, R. A.; Baldwin, A.; Galkowski, K.; Masciocchi, N.; Stranks, S. D.; Rainò, G.; Guagliardi, A.; Kovalenko, M. V. Strongly Confined CsPbBr $_3$ Quantum Dots as Quantum Emitters and Building Blocks for Rhombic Superlattices. *ACS Nano* **2023**. https://doi.org/10.1021/acsnano.2c07677.

(15) Kaplan, A. E. K.; Krajewska, C. J.; Proppe, A. H.; Sun, W.; Sverko, T.; Berkinsky, D. B.; Utzat, H.; Bawendi, M. G. Hong–Ou–Mandel Interference in Colloidal CsPbBr3 Perovskite Nanocrystals. *Nat Photonics* **2023**, *17*, 775–780. https://doi.org/10.1038/s41566-023-01225-w.

(16) Chen, Y.; Ryou, A.; Friedfeld, M. R.; Fryett, T.; Whitehead, J.; Cossairt, B. M.; Majumdar, A. Deterministic Positioning of Colloidal Quantum Dots on Silicon Nitride Nanobeam Cavities. *Nano Lett* **2018**, *18* (10), 6404–6410. https://doi.org/10.1021/acs.nanolett.8b02764.

(17) Cohen, T. A.; Sharp, D.; Kluherz, K. T.; Chen, Y.; Munley, C.; Anderson, R. T.; Swanson, C. J.; De Yoreo, J. J.; Luscombe, C. K.; Majumdar, A.; Gamelin, D. R.; Mackenzie, J. D. Direct Patterning of Perovskite Nanocrystals on Nanophotonic Cavities with Electrohydrodynamic Inkjet Printing. *Nano Lett* **2022**, *22*, 5681–5688. https://doi.org/10.1021/acs.nanolett.2c00473.

(18) Nguyen, H. A.; Sharp, D.; Fröch, J. E.; Cai, Y. Y.; Wu, S.; Monahan, M.; Munley, C.; Manna, A.; Majumdar, A.; Kagan, C. R.; Cossairt, B. M. Deterministic Quantum Light Arrays from Giant Silica-Shelled Quantum Dots. *ACS Appl Mater Interfaces* **2023**, *15* (3), 4294–4302. https://doi.org/10.1021/acsami.2c18475.

(19) Neuhauser, R. G.; Shimizu, K. T.; Woo, W. K.; Empedocles, S. A.; Bawendi, M. G. Correlation between Fluorescence Intermittency and Spectral Diffusion in Single Semiconductor Quantum Dots. *Phys Rev Lett* **2000**, *85* (15), 3301–3304. https://doi.org/10.1103/PhysRevLett.85.3301.

(20) Rainoì, G.; Nedelcu, G.; Protesescu, L.; Bodnarchuk, M. I.; Kovalenko, M. V.; Mahrt, R. F.; Stöferle, T. Single Cesium Lead Halide Perovskite Nanocrystals at Low Temperature: Fast Single-Photon Emission, Reduced Blinking, and Exciton Fine Structure. *ACS Nano* **2016**, *10* (2), 2485–2490. https://doi.org/10.1021/acsnano.5b07328.

(21) Rainò, G.; Yazdani, N.; Boehme, S. C.; Kober-Czerny, M.; Zhu, C.; Krieg, F.; Rossell, M. D.; Erni, R.; Wood, V.; Infante, I.; Kovalenko, M. V. Ultra-Narrow Room-Temperature Emission from Single CsPbBr3 Perovskite Quantum Dots. *Nat Commun* **2022**, *13* (1). https://doi.org/10.1038/s41467-022-30016-0.

(22) Munro, A. M.; Plante, I. J. La; Ng, M. S.; Ginger, D. S. Quantitative Study of the Effects of Surface Ligand Concentration on CdSe Nanocrystal Photoluminescence. *Journal of Physical Chemistry C* **2007**, *111* (17), 6220–6227. https://doi.org/10.1021/jp068733e.

(23) Munro, A. M.; Ginger, D. S. Photoluminescence Quenching of Single CdSe Nanocrystals by Ligand Adsorption. *Nano Lett* **2008**, *8* (8), 2585–2590. https://doi.org/10.1021/nl801132t.

(24) Chen, Y.; Vela, J.; Htoon, H.; Casson, J. L.; Werder, D. J.; Bussian, D. A.; Klimov, V. I.; Hollingsworth, J. A. "Giant" Multishell CdSe Nanocrystal Quantum Dots with Suppressed Blinking. *J Am Chem Soc* **2008**, *130* (15), 5026–5027. https://doi.org/10.1021/ja711379k.

(25) Pal, B. N.; Ghosh, Y.; Brovelli, S.; Laocharoensuk, R.; Klimov, V. I.; Hollingsworth, J. A.; Htoon, H. "Giant" CdSe/CdS Core/Shell Nanocrystal Quantum Dots as Efficient Electroluminescent Materials: Strong Influence of Shell Thickness on Light-Emitting Diode Performance. *Nano Lett* **2012**, *12* (1), 331–336. https://doi.org/10.1021/nl203620f.

(26) Ghosh, Y.; Mangum, B. D.; Casson, J. L.; Williams, D. J.; Htoon, H.; Hollingsworth, J. A. New Insights into the Complexities of Shell Growth and the Strong Influence of Particle Volume in Nonblinking "Giant" Core/Shell Nanocrystal Quantum Dots. *J Am Chem Soc* **2012**, *134* (23), 9634–9643. https://doi.org/10.1021/ja212032q.

(27) Peterson, M. D.; Cass, L. C.; Harris, R. D.; Edme, K.; Sung, K.; Weiss, E. A. The Role of Ligands in Determining the Exciton Relaxation Dynamics in Semiconductor Quantum Dots. *Annu Rev Phys Chem* **2014**, *65*, 317–339. https://doi.org/10.1146/annurev-physchem-040513-103649.

(28) Sadighian, J. C.; Wong, C. Y. Just Scratching the Surface:In Situand Surface-Specific Characterization of Perovskite Nanocrystal Growth. *Journal of Physical Chemistry C* **2021**, *125* (38), 20772–20782. https://doi.org/10.1021/acs.jpcc.1c06582.

(29) Fiuza-Maneiro, N.; Sun, K.; López-Fernández, I.; Gómez-Graña, S.; Müller-Buschbaum, P.; Polavarapu, L. Ligand Chemistry of Inorganic Lead Halide Perovskite Nanocrystals. *ACS Energy Lett* **2023**, 1152–1191. https://doi.org/10.1021/acsenergylett.2c02363.

(30) Kang, J.; Wang, L. W. High Defect Tolerance in Lead Halide Perovskite CsPbBr3. *Journal of Physical Chemistry Letters* **2017**, *8* (2), 489–493. https://doi.org/10.1021/acs.jpclett.6b02800.

(31) De Trizio, L.; Infante, I.; Manna, L. Surface Chemistry of Lead Halide Perovskite Colloidal Nanocrystals. *Acc Chem Res* **2023**, *51*, 1815–1825. https://doi.org/10.1021/acs.accounts.3c00174.

(32) Almeida, G.; Goldoni, L.; Akkerman, Q.; Dang, Z.; Khan, A. H.; Marras, S.; Moreels, I.; Manna, L. Role of Acid-Base Equilibria in the Size, Shape, and Phase Control of Cesium Lead Bromide Nanocrystals. *ACS Nano* **2018**, *12* (2), 1704–1711. https://doi.org/10.1021/acsnano.7b08357.

(33) Zhang, Y.; Siegler, T. D.; Thomas, C. J.; Abney, M. K.; Shah, T.; De Gorostiza, A.; Greene, R. M.; Korgel, B. A. A "Tips and Tricks" Practical Guide to the Synthesis of Metal Halide Perovskite Nanocrystals. *Chemistry of Materials* **2020**, *32* (13), 5410–5423. https://doi.org/10.1021/acs.chemmater.0c01735.

(34) Ginterseder, M.; Sun, W.; Shcherbakov-Wu, W.; McIsaac, A. R.; Berkinsky, D. B.; Kaplan, A. E. K.; Wang, L.; Krajewska, C.; Šverko, T.; Perkinson, C. F.; Utzat, H.; Tisdale, W. A.; Van Voorhis, T.; Bawendi, M. G. Lead Halide Perovskite Nanocrystals with Low Inhomogeneous Broadening and High Coherent Fraction through Dicationic Ligand Engineering. *Nano Lett* **2023**. https://doi.org/10.1021/acs.nanolett.2c03354.

(35) Ye, J.; Li, Z.; Kubicki, D. J.; Zhang, Y.; Dai, L.; Otero-mart, C.; Reus, M. A.; Arul, R.; Dudipala, K. R.; Andaji-garmaroudi, Z.; Huang, Y.; Li, Z.; Chen, Z.; Mu, P.; Yip, H.; Stranks, S. D.; Grey, C. P.; Baumberg, J. J.; Greenham, N. C.; Polavarapu, L.; Rao, A.; Hoye, R. L. Z. Elucidating the Role of Antisolvents on the Surface Chemistry and Optoelectronic Properties of CsPbBrxI3-x. *J Am Chem Soc* **2022**, *144* (27), 12102–12115. https://doi.org/10.1021/jacs.2c02631.

(36) Mir, W. J.; Alamoudi, A.; Yin, J.; Yorov, K. E.; Maity, P.; Naphade, R.; Shao, B.; Wang, J.; Lintangpradipto, M. N.; Nematulloev, S.; Emwas, A. H.; Genovese, A.; Mohammed, O. F.; Bakr, O. M. Lecithin Capping Ligands Enable Ultrastable Perovskite-Phase CsPbI3Quantum Dots for Rec. 2020 Bright-Red Light-Emitting Diodes. *J Am Chem Soc* **2022**, *144* (29), 13302–13310. https://doi.org/10.1021/jacs.2c04637.

(37) Li, J.; Xu, L.; Wang, T.; Song, J.; Chen, J.; Xue, J.; Dong, Y.; Cai, B.; Shan, Q.; Han, B.; Zeng, H. 50-Fold EQE Improvement up to 6.27% of Solution-Processed All-Inorganic Perovskite CsPbBr3 QLEDs via Surface Ligand Density Control. *Advanced Materials* **2017**, *29* (5). https://doi.org/10.1002/adma.201603885.

(38) Manoli, A.; Papagiorgis, P.; Sergides, M.; Bernasconi, C.; Athanasiou, M.; Pozov, S.; Choulis, S. A.; Bodnarchuk, M. I.; Kovalenko, M. V.; Othonos, A.; Itskos, G. Surface Functionalization of CsPbBr3 Nanocrystals for Photonic Applications. *ACS Appl Nano Mater* **2021**, *4* (5), 5084–5097. https://doi.org/10.1021/acsanm.1c00558.

(39) Hassan, Y.; Park, J. H.; Crawford, M. L.; Sadhanala, A.; Lee, J.; Sadighian, J. C.; Mosconi, E.; Shivanna, R.; Radicchi, E.; Jeong, M.; Yang, C.; Choi, H.; Park, S. H.; Song, M. H.; De Angelis, F.; Wong, C. Y.; Friend, R. H.; Lee, B. R.; Snaith, H. J. Ligand-Engineered Bandgap Stability in Mixed-Halide Perovskite LEDs. *Nature* **2021**, *591* (7848), 72–77. https://doi.org/10.1038/s41586-021-03217-8.

(40) Protesescu, L.; Yakunin, S.; Bodnarchuk, M. I.; Krieg, F.; Caputo, R.; Hendon, C. H.; Yang, R. X.; Walsh, A.; Kovalenko, M. V. Nanocrystals of Cesium Lead Halide Perovskites (CsPbX3, X = Cl, Br, and I): Novel Optoelectronic Materials Showing Bright Emission with Wide Color Gamut. *Nano Lett* **2015**, *15* (6), 3692–3696. https://doi.org/10.1021/nl5048779.

(41) Bodnarchuk, M. I.; Boehme, S. C.; Ten Brinck, S.; Bernasconi, C.; Shynkarenko, Y.; Krieg, F.; Widmer, R.; Aeschlimann, B.; Günther, D.; Kovalenko, M. V.; Infante, I. Rationalizing and Controlling the Surface Structure and Electronic Passivation of Cesium Lead Halide Nanocrystals. *ACS Energy Lett* **2019**, *4* (1), 63–74. https://doi.org/10.1021/acsenergylett.8b01669.

(42) Boehme, S. C.; Bodnarchuk, M. I.; Burian, M.; Bertolotti, F.; Cherniukh, I.; Bernasconi, C.; Zhu, C.; Erni, R.; Amenitsch, H.; Naumenko, D.; Andrusiv, H.; Semkiv, N.; John, R. A.; Baldwin, A.; Galkowski, K.; Masciocchi, N.; Stranks, S. D.; Rainò, G.; Guagliardi, A.; Kovalenko, M. V. Strongly Confined CsPbBr3 Quantum Dots as Quantum Emitters and Building Blocks for Rhombic Superlattices. *ACS Nano* **2023**, *17* (3), 2089–2100. https://doi.org/10.1021/acsnano.2c07677.

(43) Krieg, F.; Ochsenbein, S. T.; Yakunin, S.; Ten Brinck, S.; Aellen, P.; Süess, A.; Clerc, B.; Guggisberg, D.; Nazarenko, O.; Shynkarenko, Y.; Kumar, S.; Shih, C. J.; Infante, I.; Kovalenko, M. V. Colloidal CsPbX3 (X = Cl, Br, I) Nanocrystals 2.0: Zwitterionic Capping Ligands for Improved Durability and Stability. *ACS Energy Lett* **2018**, *3* (3), 641–646. https://doi.org/10.1021/acsenergylett.8b00035.

(44) Krieg, F.; Ong, Q. K.; Burian, M.; Rainò, G.; Naumenko, D.; Amenitsch, H.; Süess, A.; Grotevent, M. J.; Krumeich, F.; Bodnarchuk, M. I.; Shorubalko, I.; Stellacci, F.; Kovalenko, M. V. Stable Ultraconcentrated and Ultradilute Colloids of CsPbX3 (X = Cl, Br) Nanocrystals Using Natural Lecithin as a Capping Ligand. *J Am Chem Soc* **2019**, *141* (50), 19839–19849. https://doi.org/10.1021/jacs.9b09969.

(45) Zhang, B.; Goldoni, L.; Zito, J.; Dang, Z.; Almeida, G.; Zaccaria, F.; De Wit, J.; Infante, I.; De Trizio, L.; Manna, L. Alkyl Phosphonic Acids Deliver CsPbBr3 Nanocrystals with High Photoluminescence Quantum Yield and Truncated Octahedron Shape. *Chemistry of Materials* **2019**, *31* (21), 9140–9147. https://doi.org/10.1021/acs.chemmater.9b03529.

(46) Zhang, B.; Goldoni, L.; Lambruschini, C.; Moni, L.; Imran, M.; Pianetti, A.; Pinchetti, V.; Brovelli, S.; De Trizio, L.; Manna, L. Stable and Size Tunable CsPbBr3Nanocrystals Synthesized with Oleylphosphonic Acid. *Nano Lett* **2020**, *20* (12), 8847–8853. https://doi.org/10.1021/acs.nanolett.0c03833.

(47) Efros, A. L.; Nesbitt, D. J. Origin and Control of Blinking in Quantum Dots. *Nat Nanotechnol* **2016**, *11* (8), 661–671. https://doi.org/10.1038/nnano.2016.140.

(48) Mahler, B.; Spinicelli, P.; Buil, S.; Quelin, X.; Hermier, J. P.; Dubertret, B. Towards Non-Blinking Colloidal Quantum Dots. *Nat Mater* **2008**, *7* (8), 659–664. https://doi.org/10.1038/nmat2222.

(49) Frantsuzov, P. A.; Volkán-Kacsó, S.; Jankó, B. Universality of the Fluorescence Intermittency in Nanoscale Systems: Experiment and Theory. *Nano Lett* **2013**, *13* (2), 402–408. https://doi.org/10.1021/nl3035674.

(50) Gerhard, M.; Louis, B.; Camacho, R.; Merdasa, A.; Li, J.; Kiligaridis, A.; Dobrovolsky, A.; Hofkens, J.; Scheblykin, I. G. Microscopic Insight into Non-Radiative Decay in Perovskite Semiconductors from Temperature-Dependent Luminescence Blinking. *Nat Commun* **2019**, *10* (1). https://doi.org/10.1038/s41467-019-09640-w.

(51) Biju, V.; Chouhan, L.; Ito, S.; Thomas, E. M.; Takano, Y.; Ghimire, S.; Miyasaka, H. Real-Time Blinking Suppression of Perovskite Quantum Dots by Halide Vacancy Filling. *ACS Nano* **2021**, *15* (2), 2831–2838. https://doi.org/10.1021/acsnano.0c08802.

(52) Akkerman, Q. A.; Nguyen, T. P. T.; Boehme, S. C.; Montanarella, F.; Dirin, D. N.; Wechsler, P.; Beiglböck, F.; Rainò, G.; Erni, R.; Katan, C.; Even, J.; Kovalenko, M. V. Controlling the Nucleation and Growth Kinetics of Lead Halide Perovskite Quantum Dots. *Science (1979)* **2022**, *377* (6613), 1406–1412. https://doi.org/10.1126/science.abq3616.

(53) Becker, M. A.; Vaxenburg, R.; Nedelcu, G.; Sercel, P. C.; Shabaev, A.; Mehl, M. J.; Michopoulos, J. G.; Lambrakos, S. G.; Bernstein, N.; Lyons, J. L.; Stöferle, T.; Mahrt, R. F.; Kovalenko, M. V.; Norris, D. J.; Rainò, G.; Efros, A. L. Bright Triplet Excitons in Caesium Lead Halide Perovskites. *Nature* **2018**, *553* (7687), 189–193. https://doi.org/10.1038/nature25147.

(54) Barfüßer, A.; Rieger, S.; Dey, A.; Tosun, A.; Akkerman, Q. A.; Debnath, T.; Feldmann, J. Confined Excitons in Spherical-Like Halide Perovskite Quantum Dots. *Nano Lett* **2022**, *22*, 8810–8817. https://doi.org/10.1021/acs.nanolett.2c02223.

(55) Sun, Y.; Zhao, J. Unconventional Blinking Characteristics of Single Quantum Dots Revealed by Timing Analyses. *Journal of Physical Chemistry C* **2021**, *125* (2), 1171–1179. https://doi.org/10.1021/acs.jpcc.0c09721.

(56) Crouch, C. H.; Sauter, O.; Wu, X.; Purcell, R.; Querner, C.; Drndic, M.; Pelton, M. Facts and Artifacts in the Blinking Statistics of Semiconductor Nanocrystals. *Nano Lett* **2010**, *10* (5), 1692–1698. https://doi.org/10.1021/nl100030e.

(57) Fernée, M. J.; Tamarat, P.; Lounis, B. Spectroscopy of Single Nanocrystals. *Chem Soc Rev* **2014**, *43* (4), 1311–1337. https://doi.org/10.1039/c3cs60209e.

(58) Cordones, A. A.; Leone, S. R. Mechanisms for Charge Trapping in Single Semiconductor Nanocrystals Probed by Fluorescence Blinking. *Chem Soc Rev* **2013**, *42* (8), 3209–3221. https://doi.org/10.1039/c2cs35452g.

(59) Palstra, I. M.; de Buy Wenniger, I. M.; Patra, B. K.; Garnett, E. C.; Koenderink, A. F. Intermittency of CsPbBr3Perovskite Quantum Dots Analyzed by an Unbiased Statistical Analysis (). *Journal of Physical Chemistry C* **2021**, *125* (22), 12061–12072. https://doi.org/10.1021/acs.jpcc.1c01671.

(60) Watkins, L. P.; Yang, H. Detection of Intensity Change Points in Time-Resolved Single-Molecule Measurements. *Journal of Physical Chemistry B* **2005**, *109* (1), 617–628. https://doi.org/10.1021/jp0467548.

(61) Li, H.; Yang, H. Statistical Learning of Discrete States in Time Series. *Journal of Physical Chemistry B* **2019**, *123* (3), 689–701. https://doi.org/10.1021/acs.jpcb.8b10561.

(62) Pálmai, M.; Beckwith, J. S.; Emerson, N. T.; Zhao, T.; Kim, E. B.; Yin, S.; Parajuli, P.; Tomczak, K.; Wang, K.; Sapkota, B.; Tien, M.; Jiang, N.; Klie, R. F.; Yang, H.; Snee, P. T. Parabolic Potential Surfaces Localize Charge Carriers in Nonblinking Long-Lifetime "Giant" Colloidal Quantum Dots. *Nano Lett* **2022**, *22*, 9470–9476. https://doi.org/10.1021/acs.nanolett.2c03563.

(63) Yaman, M. Y.; Kalinin, S. V.; Guye, K. N.; Ginger, D. S.; Ziatdinov, M. Learning and Predicting Photonic Responses of Plasmonic Nanoparticle Assemblies via Dual Variational Autoencoders. *Small* **2023**, *19* (25). https://doi.org/10.1002/smll.202205893.

(64) Cui, J.; Beyler, A. P.; Marshall, L. F.; Chen, O.; Harris, D. K.; Wanger, D. D.; Brokmann, X.; Bawendi, M. G. Direct Probe of Spectral Inhomogeneity Reveals Synthetic Tunability of Single-Nanocrystal Spectral Linewidths. *Nat Chem* **2013**, *5* (7), 602–606. https://doi.org/10.1038/nchem.1654.

(65) Taddei, M.; Smith, J. A.; Gallant, B. M.; Zhou, S.; Westbrook, R. J. E.; Shi, Y.; Wang, J.; Drysdale, J. N.; McCarthy, D. P.; Barlow, S.; Marder, S. R.; Snaith, H. J.; Ginger, D. S. Ethylenediamine Addition Improves Performance and Suppresses Phase Instabilities in Mixed-Halide Perovskites. *ACS Energy Lett* **2022**, *7* (12), 4265–4273. https://doi.org/10.1021/acsenergylett.2c01998.

(66) Nenon, D. P.; Pressler, K.; Kang, J.; Koscher, B. A.; Olshansky, J. H.; Osowiecki, W. T.; Koc, M. A.; Wang, L. W.; Alivisatos, A. P. Design Principles for Trap-Free CsPbX 3 Nanocrystals: Enumerating and Eliminating Surface Halide Vacancies with Softer Lewis Bases. *J Am Chem Soc* **2018**, *140* (50), 17760–17772. https://doi.org/10.1021/jacs.8b11035.

(67) Even, J.; Pedesseau, L.; Jancu, J. M.; Katan, C. Importance of Spin-Orbit Coupling in Hybrid Organic/Inorganic Perovskites for Photovoltaic Applications. *Journal of Physical Chemistry Letters* **2013**, *4* (17), 2999–3005. https://doi.org/10.1021/jz401532q.

(68) Li, W.; Sun, Y. Y.; Li, L.; Zhou, Z.; Tang, J.; Prezhdo, O. V. Control of Charge Recombination in Perovskites by Oxidation State of Halide Vacancy. *J Am Chem Soc* **2018**, *140* (46), 15753–15763. https://doi.org/10.1021/jacs.8b08448.

(69) Morad, V.; Stelmakh, A.; Svyrydenko, M.; Feld, L. G.; Boehme, S. C.; Aebli, M.; Affolter, J.; Kaul, C. J.; Schrenker, N. J.; Bals, S.; Sahin, Y.; Dirin, D. N.; Cherniukh, I.; Raino, G.; Baumketner, A.; Kovalenko, M. V. Designer Phospholipid Capping Ligands for Soft Metal Halide Nanocrystals. *Nature* **2023**, *625*, 542–548. https://doi.org/10.1038/s41586-023-06932-6.

(70) Giannozzi, P.; Baroni, S.; Bonini, N.; Calandra, M.; Car, R.; Cavazzoni, C.; Ceresoli, D.; Chiarotti, G. L.; Cococcioni, M.; Dabo, I.; Dal Corso, A.; De Gironcoli, S.; Fabris, S.; Fratesi, G.; Gebauer, R.; Gerstmann, U.; Gougoussis, C.; Kokalj, A.; Lazzeri, M.; Martin-Samos, L.; Marzari, N.; Mauri, F.; Mazzarello, R.; Paolini, S.; Pasquarello, A.; Paulatto, L.; Sbraccia, C.; Scandolo, S.; Sclauzero, G.; Seitsonen, A. P.; Smogunov, A.; Umari, P.; Wentzcovitch, R. M. QUANTUM ESPRESSO: A Modular and Open-Source Software Project for Quantum Simulations of Materials. *Journal of Physics Condensed Matter* **2009**, *21* (39). https://doi.org/10.1088/0953-8984/21/39/395502.

(71) Perdew, J. P.; Burke, K.; Ernzerhof, M. Generalized Gradient Approximation Made Simple. *Phys. Rev. Lett.* **1996**, *77* (18), 3865–3868. https://doi.org/10.1103/PhysRevLett.77.3865.

(72) Grimme, S. Semiempirical GGA-Type Density Functional Constructed with a Long-Range Dispersion Correction. *J Comput Chem* **2006**, *27* (15), 1787–1799. https://doi.org/10.1002/jcc.20495.

Chapter 3: Emissive Traps Lead to Asymmetric Photoluminescence Line Shape in Spheroidal $CsPbBr_3$ Quantum Dots

Jessica Kline, Shaun Gallagher, Benjamin F. Hammel, Reshma Mathew, Dylan M. Ladd, Robert J. E. Westbrook, Jalen N. Pryor, Michael F. Toney, Matthew Pelton, Sadegh Yazdi, Gordana Dukovic and David S. Ginger

This chapter is adapted from: Nano Lett. 2025, 25, 13, 5063–5070
https://doi.org/10.1021/acsnano.4c04968.

Table of Contents

3.1 Overview

The morphology of quantum dots plays an important role in governing their photophysics. Here, we explore the photoluminescence of spheroidal $CsPbBr_3$ quantum dots synthesized *via* the room-temperature trioctlyphosphine oxide/$PbBr_2$ method. Despite photoluminescence quantum yields nearing 100%, these spheroidal quantum dots exhibit an elongated red photoluminescence tail not observed in typical cubic quantum dots synthesized *via* hot injection. We explore the origins of this elongated red tail through structural and optical characterization including small-angle x-ray scattering, transmission electron microscopy and time-resolved, steady-state, and single quantum dot photoluminescence. From these measurements we conclude that the red tail originates from emissive traps. We show that treating spheroidal quantum dots with phenethyl ammonium bromide decreases the line shape asymmetry and increases passivation – consistent with emissive traps due to polar facets.

3.2 Introduction

Lead halide perovskite quantum dots (QDs) are a promising material for a variety of next-generation optoelectronics.[1] Lead halide perovskite QDs exhibit tunable emission,[2] narrow linewidths[3] and near unity photoluminescence quantum yields (PLQYs)[4] making them attractive for both quantum and classical optoelectronics. The narrow linewidths of perovskite QDs are particularly exciting as narrow linewidths are a prerequisite for any emission-based application– improving color purity and single-photon indistinguishability.[5] However, several factors can result in linewidth broadening and line shape asymmetry– including the chemical environment, size and morphology polydispersity, phonon interactions, fine structure, and spectral diffusion.[5,6] The absolute minimization of QD linewidths requires understanding how these different factors impact the overall line shape.

At the single QD limit, the passivating ligand has a strong effect on the linewidth[7–10] while in ensembles, the size dispersity has a pronounced effect on the linewidth.[6] The most effective way to control size dispersity and ligand passivation is through a high-quality synthesis that produces a narrow size distribution and includes effective surface ligand passivation.[11,12] One very promising synthesis for perovskite QDs that meets these criteria is the room temperature trioctylphosphine oxide (TOPO)/$PbBr_2$ method[13] which both improves QD monodispersity[14] and uses facile ligand exchanges for optimal passivation.[15,16] Additionally, this synthesis produces high PLQY[13,16,17] QDs with faster radiative lifetimes[17] making them attractive candidates for emission-based applications. However, as previously noted,[13,17,18] $CsPbBr_3$ QDs from this synthesis have an asymmetric photoluminescence line shape. Herein, we explore the cause of this elongated red photoluminescence tail using structural characterization and steady-state and time-resolved photoluminescence measurements. We find that emissive traps cause the observed photoluminescence asymmetry and propose that these traps are due to the spheroidal morphology of QDs synthesized *via* the TOPO/$PbBr_2$ method. Finally, we demonstrate a ligand-based framework for passivating these emissive traps and increasing the line shape symmetry.

3.3 Results and Discussion

We begin by synthesizing and characterizing lecithin-capped $CsPbBr_3$ QDs with spheroidal[13] and cubic[19] morphologies. We synthesize four spheroidal QD samples of varying sizes which are referred to as S4, S5, S7 and S12. Our cubic QD sample is referred to as C9. Figure B1 and Tables B1 and B2 contain more details on the synthesis conditions for the spheroidal QDs. Figure B2 shows the morphologies of all QDs as observed with scanning transmission electron microscopy (STEM).

Figure 3.1a compares typical solution photoluminescence spectra from S7 (orange line) and C9 (grey line) samples which are similar in size (7.1 ± 0.6 nm diameter vs 9.3 ± 1.6 nm edge length from TEM). Figure 3.1a also shows Gaussian fits (dashed lines) to each spectrum and the corresponding skew values (Equation B3). The emission from C9 samples is well-described by a Gaussian, with a slight asymmetry indicated by average skew values of -0.03 ± 0.07. In contrast, we find that the S7 sample deviates more from a Gaussian line shape, exhibiting a larger tail on the low energy (red) edge of the spectrum and skew values over ten times larger (-0.50 ± 0.05) than C9. The elongated red photoluminescence tail we see in S7 QDs is also present in S4, S5 and S12 samples. Figure 3.1b is representative of the skew values we observed for all synthesized spheroidal and cubic QD samples. Interestingly, we observe size-dependent line shape asymmetry with the smaller spheroidal QDs having larger skew values. Similarly, when we quantify the sample morphologies using ImageJ's circularity metric[20] (Figure B2), smaller QDs have a more spheroidal shape. This suggests that larger ensemble photoluminescence skew values are correlated to a more spheroidal morphology. Figures 3.1c-f show the ensemble optical characterization for representative synthetic batches of the spheroidal QDs. Figure B3 shows the ensemble optical characterization of a representative batch of the C9 QDs.

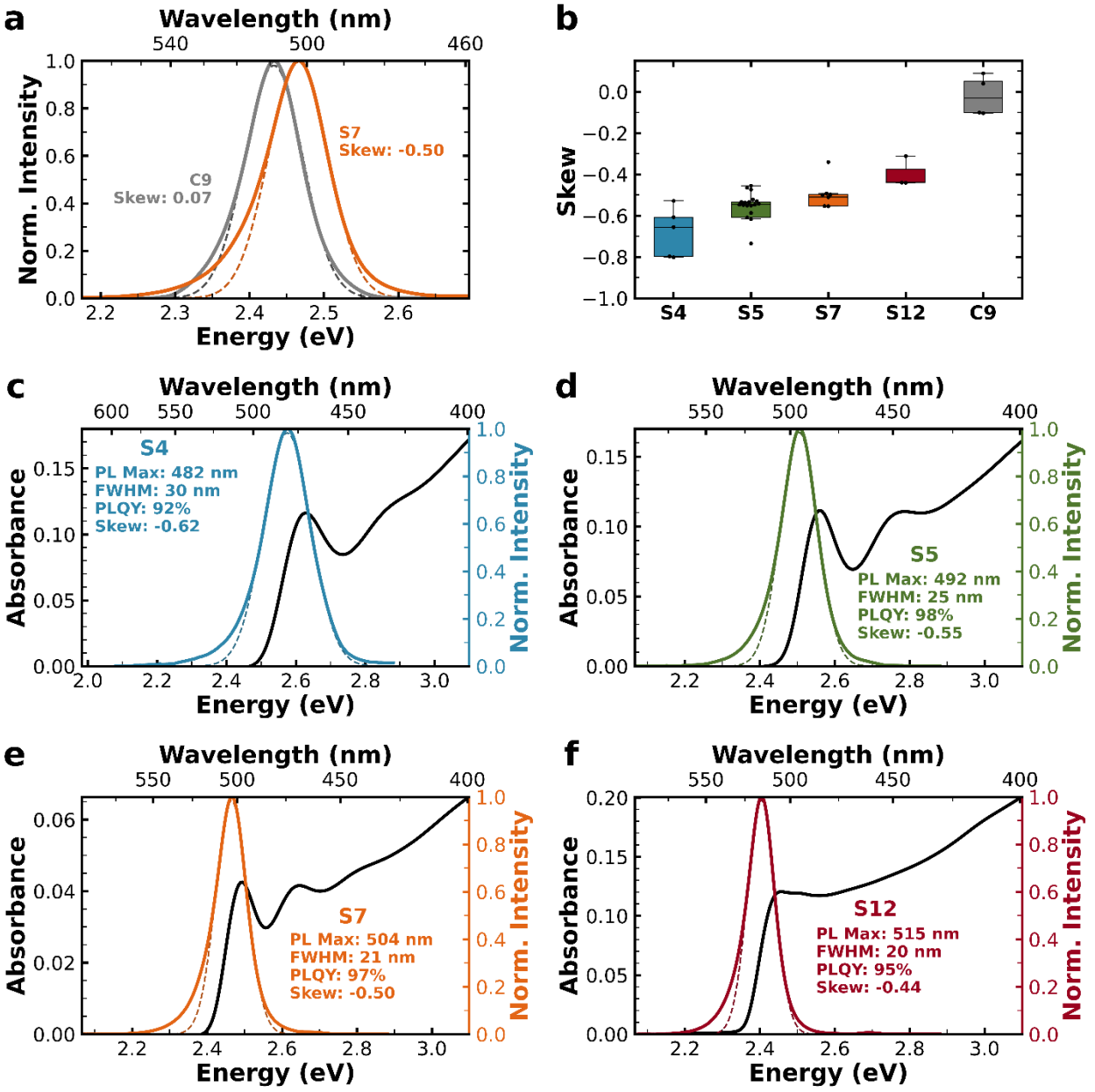

Figure 3.1: Ensemble Characterization. a) Representative photoluminescence spectra of S7 (orange line) and C9 (grey line) QDs and the Gaussian fits to the spectra. The S7 QDs are best fit by a Gaussian with a mean of 2.47 eV and standard deviation of 40 meV. The C9 QDs are best fit by a Gaussian with a mean of 2.43 eV and a standard deviation of 39 meV. S7 QDs exhibit an elongated red photoluminescence tail in contrast to the symmetric photoluminescence from C9 QDs. **b)** Distribution of skew values for S4, S5, S7, and S12 QDs compared to the skew values of C9 QDs. Each distribution comes from at least three synthetic batches for each type of QD which are shown as black dots. Colored boxes extend from the first quartile to the third quartile, with the mean indicated by a solid line. Whiskers extend to 1.5x the interquartile range. **c)** Ensemble solution characterization for S4 QDs. **d)** Ensemble solution spectra for S5 QDs. **e)** Ensemble solution spectra for S7 QDs **f)** Ensemble solution characterization for S12 QDs. Dashed lines show Gaussian fits to the photoluminescence spectra. Absorbance has units proportional to OD·s. Photoluminescence spectra were acquired from dilute room temperature solutions excited at 405 nm. Photoluminescence has units proportional to photons·s^{3}eV^{-1}. We corrected all emission spectra for instrument response as described in the supporting information.

Understanding the origin of the observed line shape asymmetry is important to producing spheroidal QDs with the narrowest possible linewidths. One possible cause of an asymmetric line shape could be an asymmetric QD size distribution.[19,21] Therefore, we measured the size distributions via small angle x-ray scattering (SAXS) and transmission electron microscopy (TEM) to look for evidence of size dispersity. Figure 3.2a shows the size distributions measured *via* SAXS, and Figure B4 compares the size distributions acquired by SAXS and TEM on the same samples. Figure B5 shows the fits to the SAXS scattering patterns for all spheroidal QDs and Table B3 contains the fit parameters.

We find that the SAXS data is well fit by a bimodal Schulz distribution which describes the primary QD population and a secondary background population between 2 and 4 nm in diameter. This secondary population is indistinguishable from the background in TEM due to low contrast, however Figure B6 confirms the presence of this secondary population using STEM. We find that all considered possible identities for this secondary population are optically inactive and cannot cause the observed photoluminescence asymmetry (see supporting information for more detail).

We find that the QD size distributions acquired from both methods are in good agreement, with mean diameters that are less than 9% different. Most importantly, the two sizing methods agree on the width and shape of the size distribution for all samples. While the spheroidal QD populations are slightly skewed (0.22 to 0.30 according to SAXS), these size skew values are not extreme enough to reproduce the experimental photoluminescence skew values. Figure B7 and Table 3.1 compare the estimated inhomogeneous broadening contributions to the photoluminescence based on the size-distributions. For all samples the inhomogeneous line shape is blue skewed and we estimate that the size distribution skew would have to be two to three times larger to reproduce the observed line shape purely by size. These results suggest that the asymmetric photoluminescence does not primarily result from size dispersion in the ensemble.

Table 3.1: Comparison of QD size distributions and the estimated inhomogeneous contributions to the photoluminescence line shape and the measured experimental photoluminescence line shape

	Size Distribution	**Size Distribution Skew**	**Estimated Photoluminescence Skew**	**Experimental Photoluminescence Skew**
S4	4.6 ± 0.7 nm	0.28	0.44	-0.62
S5	5.1 ± 0.6 nm	0.22	0.34	-0.55
S7	7.5 ± 0.9 nm	0.22	0.43	-0.50
S12	12.4 ± 1.9 nm	0.30	0.65	-0.44
C9	9.3 ± 1.6 nm	0.20	0.58	-0.07

To further explore the potential effect of size dispersity on the ensemble skew, we also measure single QD photoluminescence spectra. Figure 3.2b shows representative single QD photoluminescence spectra from several individual particles. The spectra of the single spheroidal QDs display an elongated red tail (skew values of -0.65 ± 0.15), while the spectra of C9 QDs are more symmetric (skew values of -0.02 ± 0.08). Figure 3.2c shows the distribution of skew values from all single QD photoluminescence spectra and Figure 3.2d compares the skew values from the single QD photoluminescence spectra to their maximum emission energy. We find that the average skew of a single QD spectrum is within 0.05 of the ensemble skew for all samples and that within samples skew does not trend with size, confirming that the ensemble skew is primarily due to the photophysical properties of the individual QD and not size dispersion.

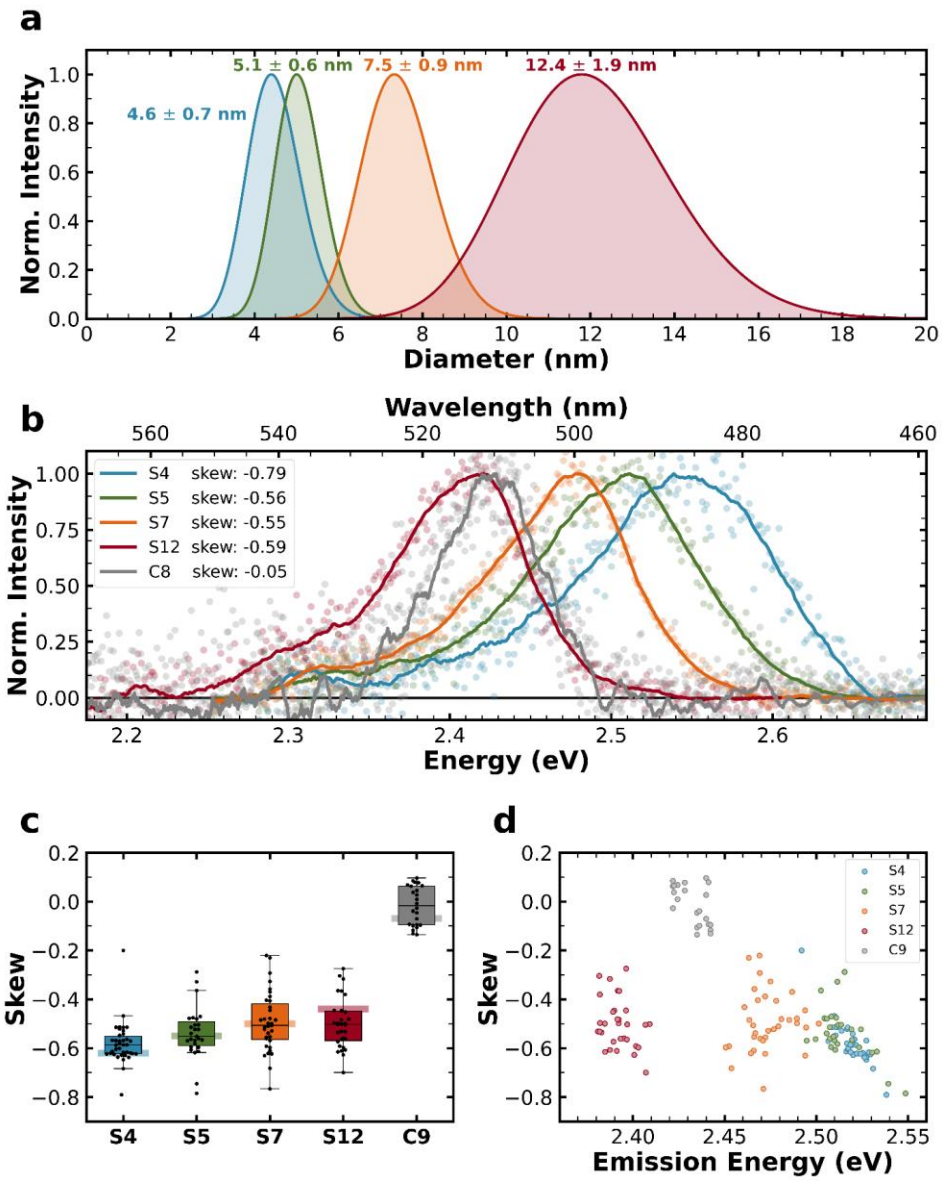

Figure 3.2: Photoluminescence asymmetry is not an ensemble effect. a) SAXS size distributions for spheroidal QDs. Size distributions are best described by a bimodal Schulz distribution which represents the larger QD population along with a population of smaller particles at 2-4 nm. The secondary population is not shown here (see Table B3 and Figure B6 for details on this population). The average QD diameter and standard deviation are written above the distributions. **b)** Single QD photoluminescence spectra for spheroidal and cubic QDs. Dots represent the raw data and solid lines the smoothed data. Spheroidal QDs exhibit elongated red tails and have skew values between -0.80 and -0.50. C9 QD spectra are more symmetric with skew values between +0.08 and -0.10. QDs were drop-cast onto glass coverslips with no polymer matrix, and photoluminescence was measured at room temperature under nitrogen using 420 nm excitation. Emission maxima and line widths match well with ensemble characterization (see Table B4 for more details). Correlated blinking and photoluminescence spectra are shown in Figure B8. Spectra baselines are zeroed at the mean value of the high-energy baseline. **c)** Skew values of single QD spectra. N = 23 for all QDs. Spheroidal QDs have large negative skew values (-0.70 to -0.50) while the cubic QDs maintain skew values near zero (-0.10 to 0.10). Black dots represent individual spectra and the pale line represents the ensemble skew for the synthetic batch used in this measurement. The average skew of the single QD spectra is in good agreement (± 0.05) with the ensemble skew value for all samples. **d)** Skew values of single QD spectra compared to their maximum emission energy. Within a synthetic batch the photoluminescence skew of individual QDs is uncorrelated to their relative sizes.

After eliminating photoluminescence asymmetry arising from the size distribution as the primary cause of the elongated red tail, we consider other potential causes. First, we consider whether a strong biexciton contribution to the ensemble photoluminescence causes the elongated red tail. Such an effect could lead to a red tail as biexciton emission is a lower energy process than excitonic emission. [22–24] In that case, we expect the photoluminescence asymmetry to increase with higher excitation powers. To look for evidence of biexciton emission, we acquired photoluminescence spectra with varying excitation powers. Figure B9 shows the photoluminescence of the S7 QDs measured at powers from 0.95 mW/cm^2 to 170 mW/cm^2. The photoluminescence intensity varies linearly with excitation power over four orders of magnitude with no observable change in line shape. We thus rule out biexciton emission as the cause of the observed photoluminescence asymmetry under our experimental conditions.

Next, we consider that the change in QD morphology results in different exciton fine structure, introducing a second emissive state.[25–27] In that case, we expect to see differences in the absorption fine structure of spheroidal and cubic QDs. We use photoluminescence excitation spectroscopy to monitor and compare band-edge fine structure. Figure B10 compares photoluminescence excitation spectra from S7, S12 and C9 samples. The photoluminescence excitation spectra show no difference in band-edge fine structure between these cubic and spheroidal QDs. We thus rule out exciton fine structure as the cause of the observed photoluminescence asymmetry in spheroidal QDs.

Having ruled out a secondary excitonic contribution to the photoluminescence, we now consider band-edge disorder related causes, including emissive traps[22,23,28] and exciton-phonon coupling.[29] In a disordered system, the band edge can vary spatially or temporally, resulting in potential minima, which form a band-tail of shallow states associated with phonon modes and traps.[28,30]

If band-edge disorder is the cause of the elongated photoluminescence tail, we expect to see signs of disorder in the absorbance spectrum. Specifically, the onset of the absorption band-edge contains information about the density of band-tail states. We quantify the slope of the absorption onset in our QD samples using an Urbach tail fit. Shallower slopes indicate increased disorder and a higher density of band-tail states. As the absorbance spectrum of a QD sample contains contributions from excitonic and continuum components, the Urbach tail cannot be determined simply by fitting the measured absorbance onset. Thus, we use an Elliott model function to separate excitonic and continuum contributions.[31] Figure B11 shows Elliott model fits to the QD absorbance spectra in Figure 3.3a, and Table B5 contains the fit parameters. Figure 3.3a shows the measured absorbance (solid lines) and the continuum absorbance contributions (dashed lines) for both spheroidal and cubic QDs. We characterized the Urbach tails by fitting the onset of the continuum contribution to Equation 1.[31]

$$A_{continuum}(E) = A_0 \sqrt{\frac{k_B T}{2 m_{urbach}}} \exp\left[\frac{m_{urbach}}{k_B T}\left(E - E_g\right) - \frac{1}{2}\right] \quad (1)$$

A_0 is a prefactor with units of nm·s·eV$^{-3/2}$, k_B is the Boltzmann constant, T is the temperature, m_{urbach} describes the slope of the exponential onset and E_g is the optical bandgap. Figure B12 shows the fits of Equation 1 to the continuum absorbance contributions. Within the spheroidal QD samples, the onset slope exhibits a clear trend, with smaller QDs having a shallower onset. The S4 sample has the shallowest onset ($m_{urbach} = 0.899 \pm 0.005$), and the S12 sample has the steepest onset ($m_{urbach} = 0.942 \pm 0.003$) indicating that band-edge disorder scales with size. This is an expected trend, as the strongest contributing factor to band-edge disorder in perovskites is exciton-phonon coupling[29] which increases in strength as QD size

decreases.[32] However, the C9 QDs do not fit the size-based trend seen in the spheroidal QDs; despite the mid-range size, the C9 sample has a steeper onset ($m_{urbach} = 0.994 \pm 0.004$) than either the S7 or S12 QDs. The deviation of the C9 sample from the trend in spheroidal QDs indicates that spheroidal QDs have significantly more band-edge disorder than cubic QDs. We consider two likely causes for the increased band-edge disorder in spheroidal QDs: increased exciton-phonon coupling strength and increased trap density.

We turn to emission-energy-dependent photoluminescence lifetimes to distinguish between band-tail states resulting from exciton-phonon coupling and trap density. If the elongated red tail is caused by increased exciton-phonon coupling strength, we expect to see a lifetime independent of emission energy. [29] However, if the elongated red tail is caused by radiative recombination at trap states, the lifetime should increase as the emission energy decreases and the traps become deeper. [22,23,33] Figure 3.3b shows emission-energy-dependent lifetimes for the spheroidal QDs acquired *via* streak camera (see supporting information section on streak camera measurements for details). We fit lifetimes using a stretched exponential (Equation B4) to capture the distribution of recombination dynamics present in a heterogenous ensemble.[34] Figure B13 shows the photoluminescence lifetime data and fits for selected emission energies. In the spheroidal QD samples, the lifetime increases as the emission energy decreases, which suggests a red-edge emission that arises from emissive traps. In contrast, the C9 QDs have an emission energy independent lifetime. We acknowledge that our observed lifetimes do not show the sigmodal trend expected for emissive traps in semiconductors. However, our observed linear trend can be explained by the combination of a mobility edge near the band-edge and very shallow traps. And having ruled out other possible causes of a linear trend in lifetime (Appendix B- *Interpreting Emission Energy Dependent Lifetimes*, Table B6 and Figure B14) we are left with a lifetime trend that is more consistent with a red tail caused by emissive traps than by exciton phonon coupling.

To directly probe for emissive traps, we collected excitation-energy-dependent photoluminescence spectra. We compare spectra collected with above-gap excitation, which creates a population of excitons that primarily recombine at the band-edge, and sub-gap excitation, which creates an initial population of excitons in the band-tail states, to distinguish between trap-mediated emission and band-edge emission. If the spectrum acquired with sub-gap excitation is identical to its above-gap counterpart, then the initial population of band-tail excitons up-convert and recombine at the band-edge.[35,36] If the spectrum acquired with sub-gap excitation is red-shifted and broader than its above-gap counterpart, then radiative recombination occurs in the band-tail states. [37] Figure 3.3c shows selected photoluminescence spectra of the QD samples acquired using above-gap and sub-gap excitation. Table B7 and Figure B16 compare the emission maxima and line widths from above-gap and sub-gap excitation, and Figure B15 shows additional excitation energy-dependent spectra from the QD samples. The spectra from C9 QDs with sub-gap and above-gap excitation are identical – indicating there is no emission from trap states in cubic QDs. In contrast, the spectra from spheroidal QDs with sub-gap excitation are red-shifted and broader than their above-gap counterparts – indicating that spheroidal QDs have emissive traps. The observed overlap between spectra with above-gap and sub-gap excitation suggests that the emissive traps in these QDs are extremely shallow - consistent with the magnitude of the changes in lifetime time with emission energy observed in Figure 3.3b.

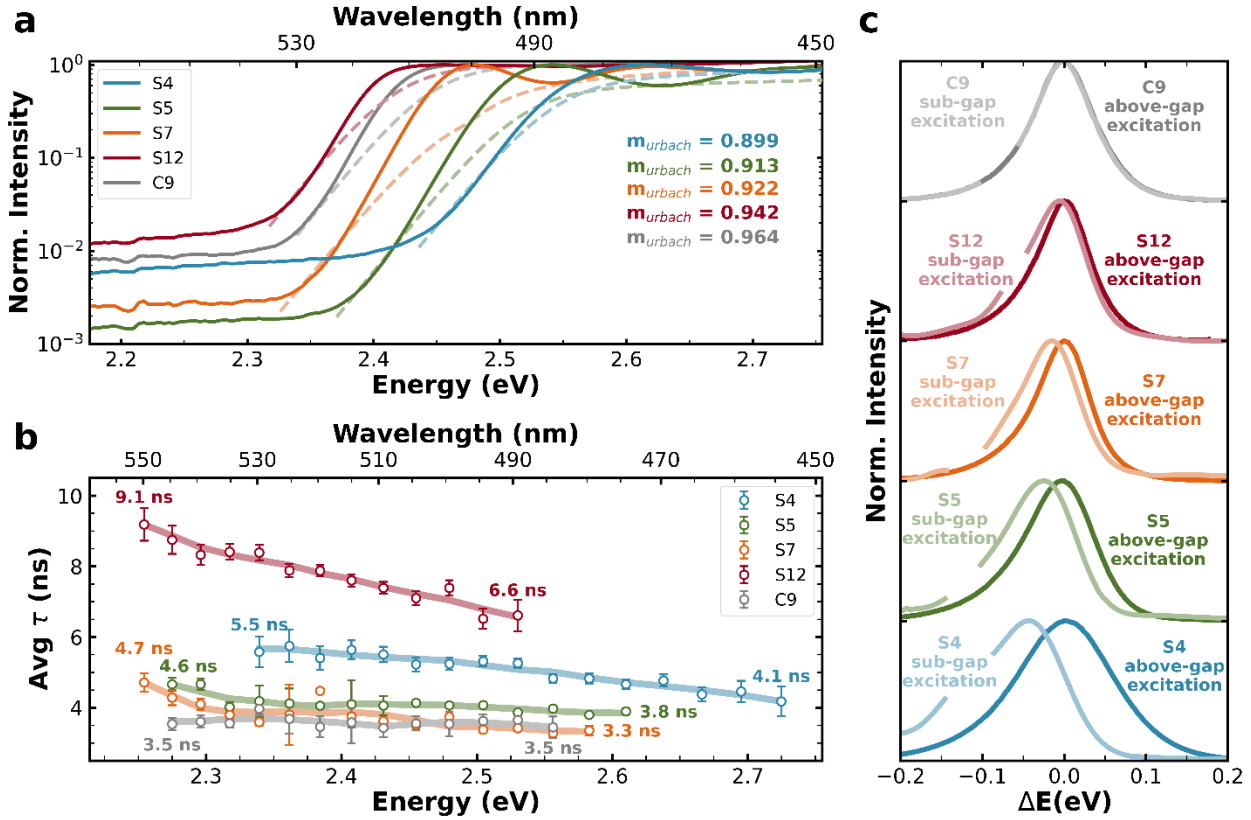

Figure 3.3: Evidence for Traps. a) Absorbance spectra for spheroidal and cubic QDs. The contributions of the continuum absorbance are shown with a dashed line. The slope of the continuum onset (m_{urbach}) becomes shallower with decreasing QD size for spheroidal QDs and is the steepest in cubic QDs. **b)** Emission energy dependent photoluminescence lifetimes for spheroidal QDs. Lines represent the general trends in lifetime for each sample. Error bars represent the uncertainty in the average lifetime as propagated from the standard error of the fitting parameters. For spheroidal QDs the lifetimes increase as the emission energy decreases indicating emission from traps on the low energy side. However, for the cubic QDs the lifetime remains constant as emission energy changes. **c)** Overlayed photoluminescence spectra acquired with above-gap or sub-gap excitation for spheroidal and cubic QDs. Sub-gap excitation photoluminescence in spheroidal QDs arises from emissive traps. Spectra labeled above-gap excitation were acquired by exciting at 400 nm. Spectra labeled sub-gap excitation were acquired by exciting at 510 nm, 520 nm, 530 nm, 540 nm, and 530 nm, respectively, for S4, S5, S7, S12, and C9 QDs. Scatter from the sub-gap excitation was removed from the spectrum for clarity. Figure B17 shows the spectral stability of the S12 quantum dots over 4 hours of continuous excitation.

If traps cause the observed photoluminescence asymmetry, passivating these traps should reduce the asymmetry. To explore the effects of different passivation on the photoluminescence asymmetry of spheroidal quantum dots we synthesized spheroidal $CsPbBr_3$ quantum dots with four other ligands. We chose to test di-dodecylammonium bromide (DDAB), the di-quaternaryammonium (dicationic) ligand reported by Ginterseder et al,[9] N,N-dimethyloctadecylammoniopropanesulfonate (ASC18),[38] and dodecyloctlyphosphoethanolamine (peaC8C12)[16] as some of the most commonly used ligands for $CsPbBr_3$ quantum dots. Figure 3.4a shows the chemical structure of our selected ligands and Figure 3.4b compares the photoluminescence skew values of spheroidal $CsPbBr_3$ quantum dots with the selected ligands to the photoluminescence skew of the C9 quantum dots. Interestingly, none of these ligands improve the photoluminescence skew – with skew values ranging between -0.4 and -1.1 depending on the ligand and emission energy. The only tested ligand which reduces the measured photoluminescence skew is

combination of lecithin and phenethylammonium bromide (PEABr) – with skew values ranging between -0.2 and -0.3. Figure B18 shows further optical characterization of lecithin/PEABr-capped quantum dots – which have higher PLQYs, steeper Urbach tails, and more homogenous lifetimes. Figure B19 shows TEM characterization of lecithin/PEABr-capped quantum dots which reveal that the addition of PEABr causes surface etching which results in quantum dots with a more cubic morphology. These results suggest that the asymmetric photoluminescence is associated with the polar facets of the spheroidal quantum dots and that PEABr improves the photoluminescence symmetry by providing additional passivation to polar facets[39] and/or selectively etching polar facets.

While adding PEABr to lecithin-capped spheroidal quantum dots results in a more symmetric photoluminescence line shape, PEABr is not an ideal ligand for long-term QD passivation. Figure B20 shows that PEABr addition results in the formation of quasi-two-dimensional perovskite byproducts, and Figure B21 shows that PEABr decreases storage stability. However, the reduction of the elongated red tail after PEABr addition indicates the promise of similar ligands and the importance of facet-specific investigations of ligand binding in perovskite QDs.

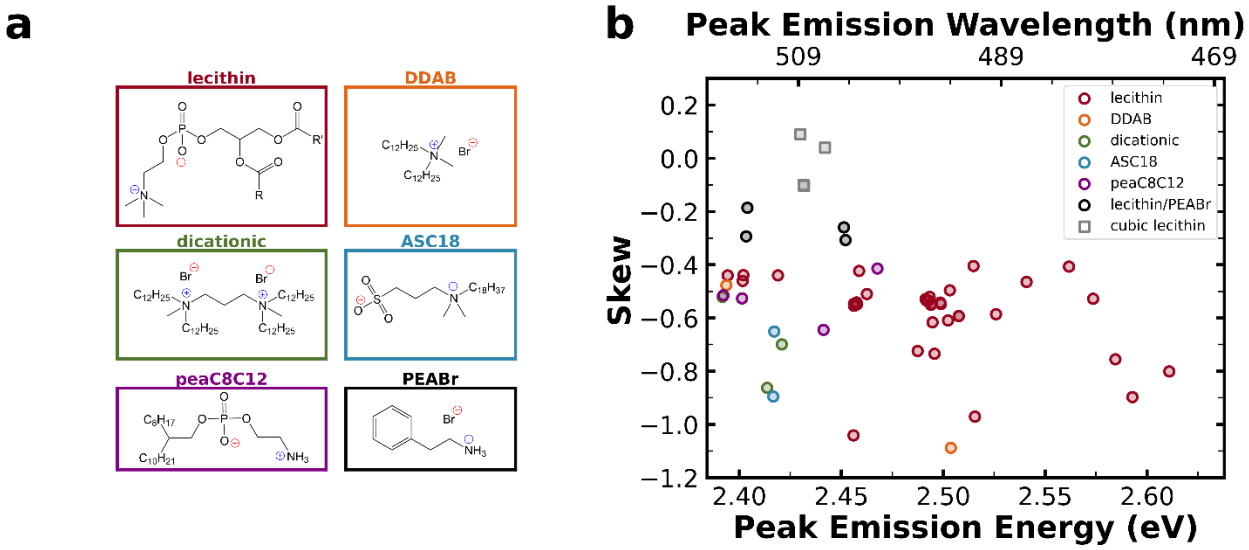

Figure 3.4: Ligand Dependent Photoluminescence Skew. a) chemical structures of selected ligands used for $CsPbBr_3$ passivation. **b)** photoluminescence skew of $CsPbBr_3$ quantum dots with different shapes, sizes and ligands. When used on spheroidal quantum dot, none of the ligands commonly used for $CsPbBr_3$ passivation (lecithin, DDAB, dicationic, ASC18 and peaC8C12) produce photoluminescence skew values smaller than -0.40. The only ligand combination which reduces the photoluminescence skew of spheroidal quantum dots is lecithin and PEABr.

3.4 Conclusion

Through a variety of steady-state and time-resolved spectroscopies, we study the asymmetric red photoluminescence tail of spheroidal $CsPbBr_3$ QDs. Single QD photoluminescence spectra, SAXS, and TEM confirm that an asymmetric size distribution does not cause the observed asymmetric photoluminescence tail. Based on emission energy dependent lifetimes, Urbach tail fittings, and photoluminescence spectra with sub-gap excitation, we conclude that emissive traps are responsible for the observed photoluminescence asymmetry. Furthermore, ligand dependent photoluminescence skew studies reveal that many common ligands do not passivate these emissive traps. Of the studied ligands only a combination of lecithin and PEABr results in a more symmetric line shape – suggesting that the polar facets

present in spheroidal quantum dots play an important role in the observed line shape. These findings indicate the promise of other highly polarizable ligands, such as N,N-diphenacyl oleylammonium, aromatic phosphoethanolamine derivatives and 1-(*p*-tolyl)ethylamine, for passivating spheroidal QDs. They also highlight the drastic impact of morphology and faceting on the fundamental optical properties of perovskite QDs.

3.5 Acknowledgements

This work, and the roles of J.K., S.G., B.F.H, R.M., D.M.L., J.N.P., M.F.T., M.P., S.Y., G.D. and D.S.G were primarily supported by the U.S. National Science Foundation under the STC IMOD Cooperative Agreement (No. DMR-2019444). B.F.H. and D.M.L. acknowledge support from the U.S. National Science Foundation through the Graduate Research Fellowship Program (NSF-GRFP) under Grant No. DGE 2040434. R.J.E.W. carried out streak camera measurements and was supported by the Office of Naval Research (ONR N000-14-20-1-2191) and the Momental Foundation via the Mistletoe Fellowship. The authors acknowledge the use of facilities and instruments at the Photonics Research Center (PRC) at the Department of Chemistry, University of Washington, as well as that at the Research Training Testbed (RTT), part of the Washington Clean Energy Testbeds system. Part of this work was carried out at the Molecular Analysis Facility, a National Nanotechnology Coordinated Infrastructure site at the University of Washington which is supported in part by the U.S. National Science Foundation (NNCI-1542101), the Molecular Engineering & Sciences Institute, and the Clean Energy Institute. TEM was supported in part by the Colorado Higher Education Competitiveness Research Authority and carried out at the Facility for Electron Microscopy of Materials at the University of Colorado Boulder (CU FEMM, RRID: SCR_019306).

J.K. acknowledges David M. Jonas (professor, University of Colorado Boulder) for discussion regarding potential causes of an elongated red photoluminescence tail in quantum dots.

D.M.L. acknowledges use of the SasView application for fitting SAXS data. SasView was originally developed under NSF award DMR-0520547 and contains code developed with funding from the European Union's Horizon 2020 research and innovation program under the SINE2020 project, grant agreement No 654000.

B.F.H. acknowledges Olivia F. Bird (graduate student, University of Colorado Boulder) and Sophia M. Click (postdoctoral researcher, University of Colorado Boulder) for discussions related to TEM image segmentation and size analysis using Trainable Weka Segmentation in ImageJ.

The authors declare no competing financial interests.

3.6 References

(1) Dey, A.; Ye, J.; De, A.; Debroye, E.; Ha, S. K.; Bladt, E.; Kshirsagar, A. S.; Wang, Z.; Yin, J.; Wang, Y.; Quan, L. N.; Yan, F.; Gao, M.; Li, X.; Shamsi, J.; Debnath, T.; Cao, M.; Scheel, M. A.; Kumar, S.; Steele, J. A.; Gerhard, M.; Chouhan, L.; Xu, K.; Wu, X. G.; Li, Y.; Zhang, Y.; Dutta, A.; Han, C.; Vincon, I.; Rogach, A. L.; Nag, A.; Samanta, A.; Korgel, B. A.; Shih, C. J.; Gamelin, D. R.; Son, D. H.; Zeng, H.; Zhong, H.; Sun, H.; Demir, H. V.; Scheblykin, I. G.; Mora-Seró, I.; Stolarczyk, J. K.; Zhang, J. Z.; Feldmann, J.; Hofkens, J.; Luther, J. M.; Pérez-Prieto, J.; Li, L.; Manna, L.; Bodnarchuk, M. I.; Kovalenko, M. V.; Roeffaers, M. B. J.; Pradhan, N.; Mohammed, O. F.; Bakr, O. M.; Yang, P.; Müller-Buschbaum, P.; Kamat, P. V.; Bao, Q.; Zhang, Q.; Krahne, R.; Galian, R. E.; Stranks, S. D.; Bals, S.; Biju, V.; Tisdale, W. A.; Yan, Y.; Hoye, R. L. Z.; Polavarapu, L. State of the Art and Prospects for Halide Perovskite Nanocrystals. *ACS Nano* 2021, *15* (7), 10775–10981. https://doi.org/10.1021/ACSNANO.0C08903.

(2) Akkerman, Q. A.; Rainò, G.; Kovalenko, M. V.; Manna, L. Genesis, Challenges and Opportunities for Colloidal Lead Halide Perovskite Nanocrystals. *Nature Materials 2018 17:5* 2018, *17* (5), 394–405. https://doi.org/10.1038/s41563-018-0018-4.

(3) Han, T. H.; Jang, K. Y.; Dong, Y.; Friend, R. H.; Sargent, E. H.; Lee, T. W. A Roadmap for the Commercialization of Perovskite Light Emitters. *Nature Reviews Materials 2022 7:10* 2022, *7* (10), 757–777. https://doi.org/10.1038/s41578-022-00459-4.

(4) Kortlever, R.; Shen, J.; Schouten, K. J. P.; Calle-Vallejo, F.; Koper, M. T. M.; Huang, J.; Buonsanti, R.; Nitopi, S. Industry Outlook of Perovskite Quantum Dots for Display Applications. *Nature Nanotechnology 2022 17:8* 2022, *17* (8), 813–816. https://doi.org/10.1038/s41565-022-01163-8.

(5) Nguyen, H. A.; Dixon, G.; Dou, F. Y.; Gallagher, S.; Gibbs, S.; Ladd, D. M.; Marino, E.; Ondry, J. C.; Shanahan, J. P.; Vasileiadou, E. S.; Barlow, S.; Gamelin, D. R.; Ginger, D. S.; Jonas, D. M.; Kanatzidis, M. G.; Marder, S. R.; Morton, D.; Murray, C. B.; Owen, J. S.; Talapin, D. V.; Toney, M. F.; Cossairt, B. M. Design Rules for Obtaining Narrow Luminescence from Semiconductors Made in Solution. *Chem Rev* 2023, *123* (12), 7890–7952. https://doi.org/10.1021/ACS.CHEMREV.3C00097.

(6) Berkinsky, D. B.; Proppe, A. H.; Utzat, H.; Krajewska, C. J.; Sun, W.; Šverko, T.; Yoo, J. J.; Chung, H.; Won, Y. H.; Kim, T.; Jang, E.; Bawendi, M. G. Narrow Intrinsic Line Widths and Electron-Phonon Coupling of InP Colloidal Quantum Dots. *ACS Nano* 2023, *17* (4), 3598–3609. https://doi.org/10.1021/ACSNANO.2C10237.

(7) Yazdani, N.; Volk, S.; Yarema, O.; Yarema, M.; Wood, V. Size, Ligand, and Defect-Dependent Electron-Phonon Coupling in Chalcogenide and Perovskite Nanocrystals and Its Impact on Luminescence Line Widths. *ACS Photonics* 2020, *7* (5), 1088–1095. https://doi.org/10.1021/ACSPHOTONICS.0C00034.

(8) Manoli, A.; Papagiorgis, P.; Sergides, M.; Bernasconi, C.; Athanasiou, M.; Pozov, S.; Choulis, S. A.; Bodnarchuk, M. I.; Kovalenko, M. V.; Othonos, A.; Itskos, G. Surface Functionalization of CsPbBr3Nanocrystals for Photonic Applications. *ACS Appl Nano Mater* 2021, *4* (5), 5084–5097. https://doi.org/10.1021/ACSANM.1C00558.

(9) Ginterseder, M.; Sun, W.; Shcherbakov-Wu, W.; McIsaac, A. R.; Berkinsky, D. B.; Kaplan, A. E. K.; Wang, L.; Krajewska, C.; Šverko, T.; Perkinson, C. F.; Utzat, H.; Tisdale, W. A.; Van Voorhis, T.; Bawendi, M. G. Lead Halide Perovskite Nanocrystals with Low Inhomogeneous Broadening and High Coherent Fraction through Dicationic Ligand Engineering. *Nano Lett* 2023, *23* (4), 1128–1134. https://doi.org/10.1021/ACS.NANOLETT.2C03354.

(10) Rainò, G.; Yazdani, N.; Boehme, S. C.; Kober-Czerny, M.; Zhu, C.; Krieg, F.; Rossell, M. D.; Erni, R.; Wood, V.; Infante, I.; Kovalenko, M. V. Ultra-Narrow Room-Temperature Emission from Single CsPbBr3 Perovskite Quantum Dots. *Nature Communications 2022 13:1* 2022, *13* (1), 1–8. https://doi.org/10.1038/s41467-022-30016-0.

(11) Sun, C.; Jiang, Y.; Zhang, L.; Wei, K.; Yuan, M. Toward the Controlled Synthesis of Lead Halide Perovskite Nanocrystals. *ACS Nano* 2023, *17* (18), 17600–17609. https://doi.org/10.1021/ACSNANO.3C05609.

(12) Ye, J.; Gaur, D.; Mi, C.; Chen, Z.; Fernández, I. L.; Zhao, H.; Dong, Y.; Polavarapu, L.; Hoye, R. L. Z. Strongly-Confined Colloidal Lead-Halide Perovskite Quantum Dots: From Synthesis to Applications. *Chem Soc Rev* 2024. https://doi.org/10.1039/D4CS00077C.

(13) Akkerman, Q. A.; Nguyen, T. P. T.; Boehme, S. C.; Montanarella, F.; Dirin, D. N.; Wechsler, P.; Beiglböck, F.; Rainò, G.; Erni, R.; Katan, C.; Even, J.; Kovalenko, M. V. Controlling the Nucleation and Growth Kinetics of Lead Halide Perovskite Quantum Dots. *Science (1979)* 2022. https://doi.org/10.1126/SCIENCE.ABQ3616.

(14) Montanarella, F.; Akkerman, Q. A.; Bonatz, D.; Van Der Sluijs, M. M.; Van Der Bok, J. C.; Prins, P. T.; Aebli, M.; Mews, A.; Vanmaekelbergh, D.; Kovalenko, M. V. Growth and Self-Assembly of CsPbBr3Nanocrystals in the TOPO/PbBr2Synthesis as Seen with X-Ray Scattering. *Nano Lett* 2022, *8*, 28. https://doi.org/10.1021/ACS.NANOLETT.2C04532.

(15) Bodnarchuk, M. I.; Feld, L. G.; Zhu, C.; Boehme, S. C.; Bertolotti, F.; Avaro, J.; Aebli, M.; Mir, S. H.; Masciocchi, N.; Erni, R.; Chakraborty, S.; Guagliardi, A.; Rainò, G.; Kovalenko, M. V. Colloidal Aziridinium Lead Bromide Quantum Dots. *ACS Nano* 2024, *18*, 28. https://doi.org/10.1021/ACSNANO.3C11579.

(16) Morad, V.; Stelmakh, A.; Svyrydenko, M.; Feld, L. G.; Boehme, S. C.; Aebli, M.; Affolter, J.; Kaul, C. J.; Schrenker, N. J.; Bals, S.; Sahin, Y.; Dirin, D. N.; Cherniukh, I.; Raino, G.; Baumketner, A.; Kovalenko, M. V. Designer Phospholipid Capping Ligands for Soft Metal Halide Nanocrystals. *Nature 2023 626:7999* 2023, *626* (7999), 542–548. https://doi.org/10.1038/s41586-023-06932-6.

(17) Gallagher, S.; Kline, J.; Jahanbakhshi, F.; Sadighian, J. C.; Lyons, I.; Shen, G.; Hammel, B. F.; Yazdi, S.; Dukovic, G.; Rappe, A. M.; Ginger, D. S. Ligand Equilibrium Influences Photoluminescence Blinking in CsPbBr3: A Change Point Analysis of Widefield Imaging Data. *ACS Nano* 2024, *18* (29), 19208–19219. https://doi.org/10.1021/ACSNANO.4C04968.

(18) Barfüßer, A.; Rieger, S.; Dey, A.; Tosun, A.; Akkerman, Q. A.; Debnath, T.; Feldmann, J. Confined Excitons in Spherical-Like Halide Perovskite Quantum Dots. *Nano Lett* 2022, *22* (22), 8810–8817. https://doi.org/10.1021/ACS.NANOLETT.2C02223.

(19) Krieg, F.; Ong, Q. K.; Burian, M.; Rainò, G.; Naumenko, D.; Amenitsch, H.; Süess, A.; Grotevent, M. J.; Krumeich, F.; Bodnarchuk, M. I.; Shorubalko, I.; Stellacci, F.; Kovalenko, M. V. Stable Ultraconcentrated and Ultradilute Colloids of CsPbX3 (X = Cl, Br) Nanocrystals Using Natural Lecithin as a Capping Ligand. *J Am Chem Soc* 2019, *141* (50), 19839–19849. https://doi.org/10.1021/JACS.9B09969.

(20) Nguyen, H. A.; Hammel, B. F.; Sharp, D.; Kline, J.; Schwartz, G.; Harvey, S.; Nishiwaki, E.; Sandeno, S. F.; Ginger, D. S.; Majumdar, A.; Yazdi, S.; Dukovic, G.; Cossairt, B. M. Colossal Core/Shell CdSe/CdS Quantum Dot Emitters. *ACS Nano* 2024, *18* (31), 20726–20739. https://doi.org/10.1021/ACSNANO.4C06961.

(21) Zhitomirsky, D.; Kramer, I. J.; Labelle, A. J.; Fischer, A.; Debnath, R.; Pan, J.; Bakr, O. M.; Sargent, E. H. Colloidal Quantum Dot Photovoltaics: The Effect of Polydispersity. *Nano Lett* 2012, *12* (2), 1007–1012. https://doi.org/10.1021/NL2041589.

(22) Li, J.; Gan, L.; Fang, Z.; He, H.; Ye, Z. Bright Tail States in Blue-Emitting Ultrasmall Perovskite Quantum Dots. *Journal of Physical Chemistry Letters* 2017, *8* (24), 6002–6008. https://doi.org/10.1021/ACS.JPCLETT.7B02786.

(23) He, H.; Yu, Q.; Li, H.; Li, J.; Si, J.; Jin, Y.; Wang, N.; Wang, J.; He, J.; Wang, X.; Zhang, Y.; Ye, Z. Exciton Localization in Solution-Processed Organolead Trihalide Perovskites. *Nature Communications 2016 7:1* 2016, *7* (1), 1–7. https://doi.org/10.1038/ncomms10896.

(24) Schmidt, T.; Lischka, K.; Zulehner, W. Excitation-Power Dependence of the near-Band-Edge Photoluminescence of Semiconductors. *Phys Rev B* 1991, *8*, 15–1992.

(25) Caram, J. R.; Bertram, S. N.; Utzat, H.; Hess, W. R.; Carr, J. A.; Bischof, T. S.; Beyler, A. P.; Wilson, M. W. B.; Bawendi, M. G. PbS Nanocrystal Emission Is Governed by Multiple Emissive States. *Nano Lett* 2016, *16* (10), 6070–6077. https://doi.org/10.1021/ACS.NANOLETT.6B02147.

(26) Ryu, J.; Park, S. D.; Baranov, D.; Rreza, I.; Owen, J. S.; Jonas, D. M. Relations between Absorption, Emission, and Excited State Chemical Potentials from Nanocrystal 2D Spectra. *Sci Adv* 2021, *7* (22), 4741–4769. https://doi.org/10.1126/SCIADV.ABF4741.

(27) Hu, Z.; Kim, Y.; Krishnamurthy, S.; Avdeev, I. D.; Nestoklon, M. O.; Singh, A.; Malko, A. V.; Goupalov, S. V.; Hollingsworth, J. A.; Htoon, H. Intrinsic Exciton Photophysics of PbS Quantum Dots Revealed by Lowerature Single Nanocrystal Spectroscopy. *Nano Lett* 2019, *19* (12), 8519–8525. https://doi.org/10.1021/ACS.NANOLETT.9B02937.

(28) Wright, A. D.; Milot, R. L.; Eperon, G. E.; Snaith, H. J.; Johnston, M. B.; Herz, L. M.; Wright, A. D.; Milot, R. L.; Eperon, G. E.; Snaith, H. J.; Johnston, M. B.; Herz, L. M. Band-Tail Recombination in Hybrid Lead Iodide Perovskite. *Adv Funct Mater* 2017, *27* (29), 1700860. https://doi.org/10.1002/ADFM.201700860.

(29) Masada, S.; Yamada, T.; Tahara, H.; Hirori, H.; Saruyama, M.; Kawawaki, T.; Sato, R.; Teranishi, T.; Kanemitsu, Y. Effect of A-Site Cation on Photoluminescence Spectra of Single Lead Bromide Perovskite Nanocrystals. *Nano Lett* 2020, *20* (5), 4022–4028. https://doi.org/10.1021/ACS.NANOLETT.0C01417.

(30) Li, M.; Huang, P.; Zhong, H. Current Understanding of Band-Edge Properties of Halide Perovskites: Urbach Tail, Rashba Splitting, and Exciton Binding Energy. *Journal of Physical Chemistry Letters* 2023, *14* (6), 1592–1603. https://doi.org/10.1021/ACS.JPCLETT.2C03525.

(31) Pejova, B. Optical Absorption of Semiconductor Quantum Dot Solids. *Semicond Sci Technol* 2014, *29* (4), 045007. https://doi.org/10.1088/0268-1242/29/4/045007.

(32) Zhu, C.; Feld, L. G.; Svyrydenko, M.; Cherniukh, I.; Dirin, D. N.; Bodnarchuk, M. I.; Wood, V.; Yazdani, N.; Boehme, S. C.; Kovalenko, M. V; Rainò, G.; Zhu, C.; Feld, L. G.; Svyrydenko, M.; Cherniukh, I.; Dirin, D. N.; Bodnarchuk, M. I.; Boehme, S. C.; Kovalenko, M. V; Rainò, G. Quantifying the Size-Dependent Exciton-Phonon Coupling Strength in Single Lead-Halide Perovskite Quantum Dots. *Adv Opt Mater* 2024, 2301534. https://doi.org/10.1002/ADOM.202301534.

(33) Gourdon, C.; Lavallard, P. Exciton Transfer between Localized States in CdS1–XSex Alloys. *physica status solidi (b)* 1989, *153* (2), 641–652. https://doi.org/10.1002/PSSB.2221530222.

(34) Taddei, M.; Smith, J. A.; Gallant, B. M.; Zhou, S.; Westbrook, R. J. E.; Shi, Y.; Wang, J.; Drysdale, J. N.; McCarthy, D. P.; Barlow, S.; Marder, S. R.; Snaith, H. J.; Ginger, D. S. Ethylenediamine Addition Improves Performance and Suppresses Phase Instabilities in Mixed-Halide Perovskites. *ACS Energy Lett* 2022, *7* (12), 4265–4273. https://doi.org/10.1021/ACSENERGYLETT.2C01998.

(35) Zhang, W.; Ye, Y.; Liu, C.; Wang, J.; Ruan, J.; Zhao, X.; Han, J.; Zhang, W.; Ye, Y.; Liu, C.; Wang, J.; Ruan, J.; Zhao, X.; Han, J. Two-Step Anti-Stokes Photoluminescence of CsPbX3 Nanocrystals. *Adv Opt Mater* 2021, *9* (6), 2001885. https://doi.org/10.1002/ADOM.202001885.

(36) Zhang, Z.; Ghonge, S.; Ding, Y.; Zhang, S.; Berciu, M.; Schaller, R. D.; Jankó, B.; Kuno, M. Resonant Multiple-Phonon Absorption Causes Efficient Anti-Stokes Photoluminescence in CsPbBr3 Nanocrystals. *ACS Nano* 2024, *18* (8), 6438–6444. https://doi.org/10.1021/ACSNANO.3C11908.

(37) Rakovich, Y. P.; Donegan, J. F. Anti-Stokes Photoluminescence in Semiconductor Nanocrystal Quantum Dots. In *Semiconductor Nanocrystal Quantum Dots: Synthesis, Assembly, Spectroscopy and Applications*; Rogach, A. L., Ed.; SpringerWienNewYork, 2008; pp 257–275.

(38) Krieg, F.; Ochsenbein, S. T.; Yakunin, S.; Ten Brinck, S.; Aellen, P.; Süess, A.; Clerc, B.; Guggisberg, D.; Nazarenko, O.; Shynkarenko, Y.; Kumar, S.; Shih, C. J.; Infante, I.; Kovalenko, M. V. Colloidal CsPbX3 (X = Cl, Br, I) Nanocrystals 2.0: Zwitterionic Capping Ligands for Improved Durability and Stability. *ACS Energy Lett* 2018, *3* (3), 641–646. https://doi.org/10.1021/ACSENERGYLETT.8B00035.

(39) Ma, C.; Kang, M. C.; Lee, S. H.; Zhang, Y.; Kang, D. H.; Yang, W.; Zhao, P.; Kim, S. W.; Kwon, S. J.; Yang, C. W.; Yang, Y.; Park, N. G. Facet-Dependent Passivation for Efficient Perovskite Solar Cells. *J Am Chem Soc* 2023, *145* (44), 24349–24357. https://doi.org/10.1021/JACS.3C09327.

Chapter 4: Trion Formation Hampers Single Quantum Dot Performance in Silane-Coated $FAPbBr_3$ Quantum Dots

Jessica Kline, Shaoni Kar, Benjamin F. Hammel, Yunping Huang, Zixu Huang, Seth R. Marder, Sadegh Yazdi, Gordana Dukovic, Henry Snaith, David S. Ginger

Table of Contents

4.1 Overview

We explore silane-coated formamidinium lead bromide ($FAPbBr_3$) quantum dots as single photon emitters and compare them to $FAPbBr_3$ quantum dots passivated with a phosphoethylammonium derivative ($PEAC_8C_{12}$), which represents current state-of-the-art in zwitterionic molecular surface ligand passivation. We compare properties including single-photon purity ($g^{(2)}(\tau)$), linewidth, blinking, and photostability. We find that at room temperature, these silane-coated dots perform comparably to the $PEAC_8C_{12}$ passivation in terms of single-photon performance metrics, while exhibiting improvements in photostability. However, we find that at 4K, silane-coated $FAPbBr_3$ quantum dots perform worse than the $PEAC_8C_{12}$-passivated samples, exhibiting faster blue-shifting and photobleaching under illumination. Analysis of fluorescence lifetime intensity distributions from the photon-counting data indicates increased efficiency of fast non-radiative processes in the silane-coated quantum dots at 4K. We propose a trion-related degradation pathway at low temperatures that is consistent with the observed kinetics and estimate that at 4K with 6.1 $\mu J/cm^2$, 472 nm excitation the silane-coated quantum dots build up double the trion population of their $PEAC_8C_{12}$-passivated counterparts.

4.2 Introduction

Lead halide perovskite quantum dots are a promising material for a variety of optoelectronic applications, owing to their large absorption cross sections, high photoluminescence quantum yields,[1] narrow linewidths[2] and tunable emission.[3] These properties make them especially interesting for implementation in light emitting diodes (LEDs),[4] photovoltaics[5] and photodetectors.[6] Additionally perovskite quantum dots have recently emerged as a promising colloidal single photon source, given their strong anti-bunching behavior at all temperatures[7] and radiative lifetimes which approach the transform limit at low temperatures.[8] Indeed, Kaplan et al. have successfully demonstrated Hong-Ou-Mandel interference using colloidal perovskite quantum dots – proving this material can indeed serve as a source of indistinguishable single photons.[9] These advances are particularly exciting given emerging capabilities to pattern single colloidal emitters on demand, providing a pathway for chip-scale nanophotonic integration.[10] Despite these advantages, perovskite quantum dots still exhibit sub-optimal behaviors, including photoluminescence intermittency and spectral wandering (commonly known as blinking and spectral diffusion) that can impact long term photon indistinguishability. However, these are problems that are common to all types of quantum dots, indeed to most sources of single photons.[11]

In colloidal quantum dots, blinking and spectral diffusion depend on the quantum dot surface, and variations in the local environment.[11] As such, the first step to reducing blinking and spectral diffusion is to improve passivation of the quantum dot surface, which has the dual effect of filling traps and screening the quantum dot from the local environment. Colloidal quantum dot passivation generally falls into two standard motifs – the use of ligands that bind to the quantum dot surface or overgrown layers of a wider bandgap material (shells). For II-VI and III-V quantum dots, core-shell heterostructures have proven more successful in suppressing blinking and spectral diffusion than ligand passivation.[12] In fact, with the right shell researchers have been able to produce entirely non-blinking CdSe quantum dots.[13–15] This method has recently been extended to grow "colossal" shells[16] resulting in non-blinking quantum dots which are sufficiently large for deterministic positioning.[10] The success of this approach provides an excellent blueprint for creating a deterministically positionable single photon source, if a suitable shelling material can be identified.

Unfortunately, viable candidates for perovskite quantum dot core-shell heterostructures remain limited. As such perovskite quantum dot passivation has focused on ligand development, and many of the recent improvements in perovskite quantum dots as a single photon source have focused on optimizing the ligand chemistry.[17–21] Currently, state-of-the-art ligands for high performing single perovskite quantum dots are zwitterions derived from sulfobetaine and phosphoethlyammonium.[8,9,17] However, there is a significant amount of on-going work aimed at finding a good shelling material for perovskite quantum dots. Currently, oxide-based shells such as titania, alumina and silica are some of the most promising candidates.[22] Oxide-based shells provide significant improvements in the lifetimes of perovskite quantum dot thin films and increase the stability of thin films in the presence of heat, UV light, oxygen and water.[23–27] As such oxide-shelled perovskite quantum dots have received significant interest for LEDs.[26,28,29] These characteristics also suggest that oxide-based shells may work well for perovskite quantum dot single photon sources, as photostability at high fluences remains a challenge for this application as well.[30,31]

Here, we explore passivation of formamidinium lead bromide ($FAPbBr_3$) quantum dots with the diaminosilane N-(2-Aminoethyl)-3-aminopropyltriethoxysilane (AEAPTES), focusing on the performance of these quantum dots for single photon emission applications. To this end, we benchmark their performance against $FAPbBr_3$ quantum dots passivated with the current top-performing[17,32] ligand ($PEAC_8C_{12}$) both at room temperature and 4K. We find that silane-coated $FAPbBr_3$ quantum dots have excellent performance at room temperature but show reduced photostability at 4K when compared to the $PEAC_8C_{12}$-passivated dots.

4.3 Results and Discussion

We synthesized our $PEAC_8C_{12}$-passivated $FAPbBr_3$ quantum dots via the trioctylphosphine oxide/$PbBr_2$ method.[17,33] We first grew the dots using weakly bound ligands and exchanged them with the strongly binding $PEAC_8C_{12}$ post-synthesis using established protocols.[17] We synthesized the AEAPTES-modified $FAPbBr_3$ quantum dots via hot-injection[34] using oleylammonium and oleate as ligands and then ligand exchanged to AEAPTES as described in the method section. We chose AEAPTES for its ability to provide two functions: first, surface passivation *via* the head groups (amine and ammonium) and second, the possibility of cross linking by triethoxysilane hydrolysis. It is possible that AEAPTES may also react with FA^+ during the ligand exchange to form an imidazole-silane cation[35] which is functionally similar to mono-protonated AEAPTES (amine, ammonium and triethoxysilane). This first silane coating is essential for growing thicker silica shells using orthosilicates.[36] However, for these experiments, we did not overgrow the silane coating to accumulate significant thickness but compare the AEAPTES-exchanged quantum dots directly against $PEAC_8C_{12}$-exchanged dots. Figure C1 shows the chemical structures of $PEAC_8C_{12}$ and AEAPTES and Figure C2 shows that, under our synthesis, storage and sample preparation conditions, some AEAPTES undergoes triethoxysilane hydrolysis to form a partially cross-linked tail.

We carefully matched the quantum dot sizes (after ligand exchange/treatment) for this study to obtain similar absorption and emission spectra and minimize size-dependent effects. Figure 4.1 shows the solution characterization of the two near-identical batches of post-ligand exchange quantum dots. Both batches have photoluminescence quantum yields (PLQYs) near unity (Figures 4.1a and 4.1b), emission maxima of approximately 2.41 eV (Figures 4.1a and 4.1b) and photoluminescence lifetimes of approximately 4 ns (Figure 4.1c). Figure 4.1d shows the HAADF-STEM-measured size distributions for both samples and Figure C3 shows representative HAADF-STEM images. We find that the silane-coated quantum dots are ~1.1 nm larger than their $PEAC_8C_{12}$-passivated counterparts. However, given that the two

samples have matched optical bandgaps, we ascribe this size difference to an orthosilicate monolayer (a ~ 0.5 nm) formed by hydrolysis of AEAPTES. Figure C4 shows that the silane-coated quantum dots also have a slightly larger ligand sphere (1.5 nm) than their $PEAC_8C_{12}$-passivated counterparts (1 nm). We also find that silane-coated quantum dots have a slightly broader size distribution – which is consistent with our observed difference in ensemble photoluminescence linewidth (121 vs 134 meV, Figures 4.1a and 4.1b).

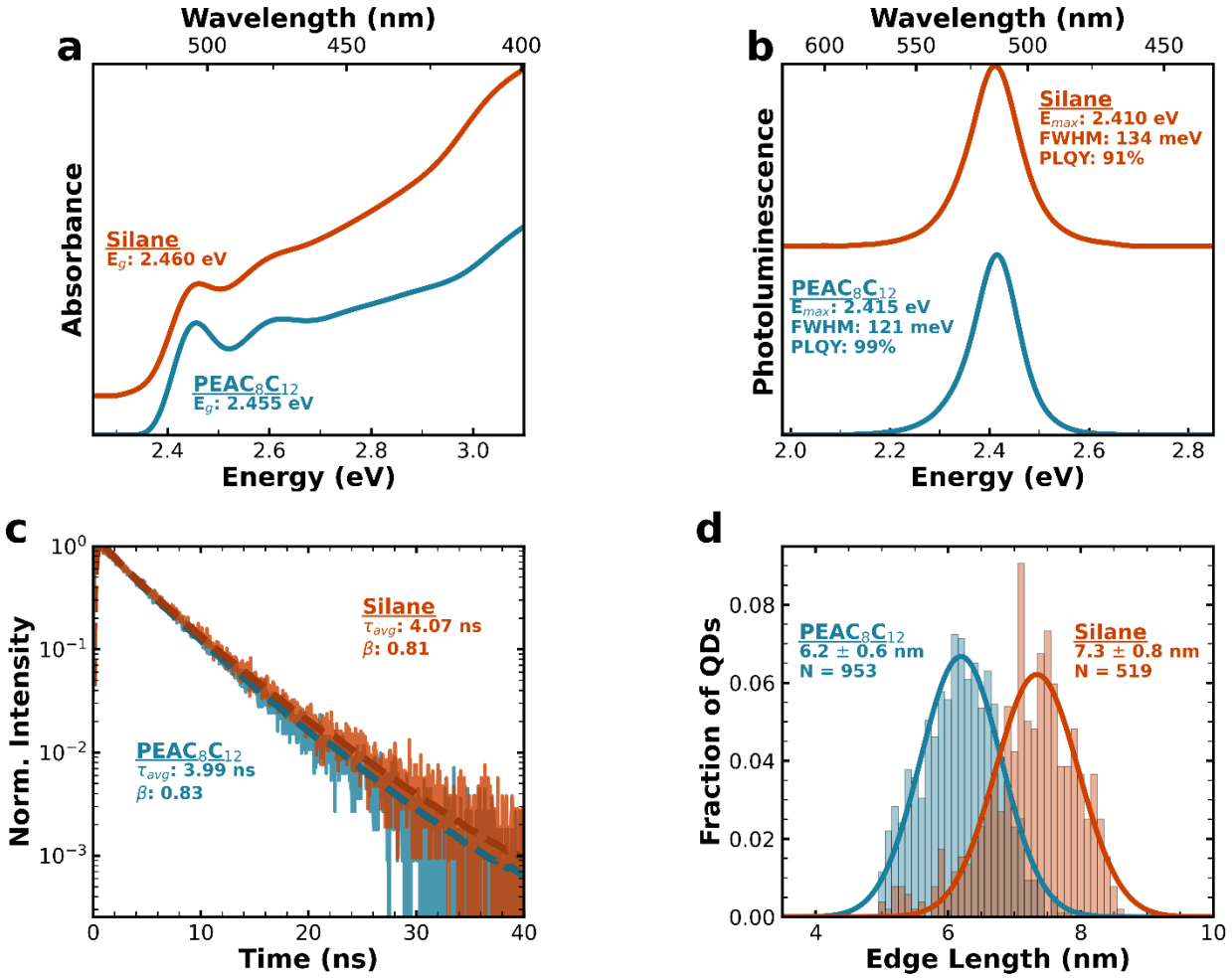

Figure 4.1. Ensemble characterization of quantum dot samples. **a)** absorbance spectra of $PEAC_8C_{12}$-passivated (blue) and silane-coated (orange) $FAPbBr_3$ quantum dots. Spectra are offset for clarity. $PEAC_8C_{12}$-passivated quantum dots have a first absorbance peak at 2.455 eV and silane-coated quantum dots have a first absorbance peak at 2.460 eV. **b)** photoluminescence spectra of $PEAC_8C_{12}$-passivated (blue) and silane-coated (orange) $FAPbBr_3$ quantum dots. Spectra are offset for clarity. $PEAC_8C_{12}$-passivated quantum dots have a photoluminescence peak is at 2.413 eV, a full width at half maximum of 121 meV and a PLQY of 99%. Silane-coated quantum dots have a photoluminescence peak is at 2.410 eV, has a full width at half maximum of 134 meV and a PLQY of 91%. **c)** photoluminescence lifetimes for our $PEAC_8C_{12}$-passivated (blue) and silane-coated (orange) $FAPbBr_3$ quantum dots. We fit the lifetimes to a stretched exponential (dashed lines, Equation C3) to best describe lifetime of a heterogeneous sample.[37] **d)** TEM-measured size distribution for our $PEAC_8C_{12}$-passivated (blue) and silane-coated (orange) $FAPbBr_3$ quantum dots. We fit the size distributions to a Gaussian (solid lines) to extract the average size. Figure C3 shows the HAADF-STEM images we used to extract the size distribution. Since the two samples have identical first absorption peaks and emission maxima, we ascribe the size difference between the two samples to the AEAPTES-passivation step.

We begin characterizing the behavior of our two samples as single quantum dots *via* widefield microscopy. Widefield microscopy is well-suited for characterizing the blinking behavior of a statistically

significant number (N >> 100) of quantum dots in low-power regimes and can reveal disparate blinking behavior between comparable ensemble samples.[21] Figure C5 shows the blinking behavior we observed for our $PEAC_8C_{12}$-passivated and silane-coated quantum dots using widefield microscopy. We find that, at room temperature under low excitation power (405 nm, 9 mW/cm^2), both our $PEAC_8C_{12}$-passivated and silane-coated quantum dots perform well relative to current literature on room-temperature perovskite quantum dot blinking. Consistent with other reports,[17] we find that $PEAC_8C_{12}$-passivated quantum dots have an average ON% of 96% and a non-blinking fraction of 81%. We observed slightly improved performance from silane-coated quantum dots which have an average ON% of 95% and a non-blinking fraction of 90%. Even this minor improvement in performance is notable since $PEAC_8C_{12}$ is currently reported to be one of the best-performing surface passivation strategies for single-photon emitting perovskite quantum dots.[17,32]

Having observed encouraging blinking performance from both the $PEAC_8C_{12}$-passivated and silane-coated quantum dots under low excitation powers, we continue our room temperature single quantum dot characterization in a higher excitation power regime (472 nm, 6.1 $\mu J/cm^2$) using pulsed confocal illumination at a repetition rate of 15.6 MHz. For comparison, this combination of pulse energy, duration, and frequency represents a time-averaged power of 95 W/cm^2 and a peak power of 3.1 MW/cm^2 which is orders of magnitude higher than typical test conditions for down-conversion phosphors.[38,39] Figures C6 and C7 show the full characterization of representative single quantum dots for $PEAC_8C_{12}$ passivation and silane coating respectively. We consider three main metrics to assess how well quantum dots perform as single photon emitters – linewidth, second order photon autocorrelation functions ($g^{(2)}(\tau)$) and weighted ON%. The ideal single photon emitters should have a narrow (transform-limited) linewidth, a low $g^{(2)}(\tau = 0)$ and a high ON%. Figure 4.2a shows the distribution of linewidths measured from our samples at room temperature. Single $PEAC_8C_{12}$-passivated quantum dots have a linewidth of 72 ± 2 meV (median ± interquartile deviation) and silane-coated quantum dots have a linewidth of 70 ± 3 meV. While the siliane-coated dots have a broader ensemble linewidths, the comparable single quantum dot linewidths indicate that much of the ensemble linewidth difference is due to differences in the size distribution (Figure 4.1d) – which is further supported by the difference in the distribution of the individual dot emission maxima (Figure C8).

Next, we compare the second order autocorrelation functions, $g^{(2)}(\tau)$, for silane-coated and $PEAC_8C_{12}$-passivated quantum dots. Figure 4.2b shows the distribution of measured values for $g^{(2)}(\tau = 0)$ which measures the single-photon purity of each quantum dot and confirms that we have measured a single quantum dot. We limit our sample size to quantum dots with a $g^{(2)}(\tau = 0)$ under 0.5, as that is the statistical limit for a photon source to be considered a single emitter. However, an excellent single-photon emitter should generally have a $g^{(2)}(\tau = 0)$ of less than 0.1.[7,31,40] By this metric, $PEAC_8C_{12}$-passivated and silane-coated quantum dots perform similarly at room temperature, with $PEAC_8C_{12}$-passivated quantum dots showing a slightly higher percentage of quantum dots with a $g^{(2)}(\tau = 0)$ under 0.1 (42 ± 10% vs 36 ± 10%), though the difference is close to the statistical uncertainty after measuring N = 53 and N = 65 quantum dots.

Finally, we compare the blinking behavior of our single quantum dots. Figure 4.2c shows the distribution of intensity-weighted ON percentages calculated from Change Point Analysis (CPA)-classified[41,42] blinking traces for both quantum dot samples. The intensity weighted ON percentage is defined in Equation C7, but in brief we deviate from traditional ON/OFF[17,43] and ON/OFF/GREY[44,45] analysis and treat all mid-intensity CPA-identified states as a linear combination of the ON (maximum

intensity) and OFF ($I_{dark} + 3\sigma_{dark}$) states. This choice reduces the complex multi-level blinking dynamics of perovskite quantum dots ($n_{levels} > 10$)[46] to a simple system without completely ignoring the dynamics of the GREY states. We find that under our measurement conditions both silane-coated and $PEAC_8C_{12}$-passivated quantum dots perform similarly with average weighed ON percentages of 49 ± 13% and 46 ± 12% respectively.

Our choice to use an intensity-weighted ON percentage means that both blinking events and photobleaching can affect this figure of merit. Unfortunately, we see evidence of photobleaching during our measurement (Figures C6 and C7) which is unsurprising as perovskite quantum dots are known to photobleach at high excitation densities.[30,31] To distinguish photobleaching from blinking, we use large (10 s) time bins[47] and record the highest intensity observed in each window. We fit our maximum intensity traces to a linear decay where the slope is the average photobleaching rate. Figure C8 shows the distribution of the total intensity losses for both samples and Figure 4.2d shows, on average, how the maximum intensity changes in time for both samples. We find that, on average, $PEAC_8C_{12}$-passivated quantum dots lose 40% of their maximum intensity (approximately 6.7 kcps) during the 600 second measurement, under these rather intense excitation conditions. In contrast, silane-coated quantum dots are much more photostable and only lose 5-10% of their maximum intensity (approximately 1.8 kcps) over the same duration. These results indicate that at room temperature, silane coating results in significantly more photostable quantum dots than $PEAC_8C_{12}$ passivation. Since the silane coating is relatively thin, we speculate that in addition to providing a physical barrier, triethoxysilane polymerization and physical confinement may also serve to suppress photoinduced ligand desorption, thus contributing to increased stability.

Overall, using the state-of-the-art $PEAC_8C_{12}$ ligand as a benchmark, we find that silane-coated $FAPbBr_3$ quantum dots perform well as colloidal single photon emitters at room temperature. They have a comparable linewidth and weighted ON% to the $PEAC_8C_{12}$-passivated quantum dots. And while silane-coated quantum dots have a slightly worse $g^{(2)}(\tau = 0)$ distribution than $PEAC_8C_{12}$-passivated quantum dots, they are four times more photostable. The performance of our silane-coated quantum dots is even more impressive when we consider the size of our quantum dots (~ 6 nm edge length) and our excitation density (6.1 μJ/cm^2). These conditions should significantly increase the sensitivity of the observed single quantum dot performance to surface and environmental effects, as these effects are amplified in small quantum dots, causing small changes in passivation to result in large changes in performance.[48] And at the same time high excitation densities increase the impact of any detrimental higher order processes.[49,50] Given these conditions, it is all the more impressive that our silane-coated quantum dots keep up with, and even outperform, our $PEAC_8C_{12}$-passivated quantum dots; indicating that silane-coated perovskite quantum dots are in fact a promising direction to explore for room temperature single photon emitters.

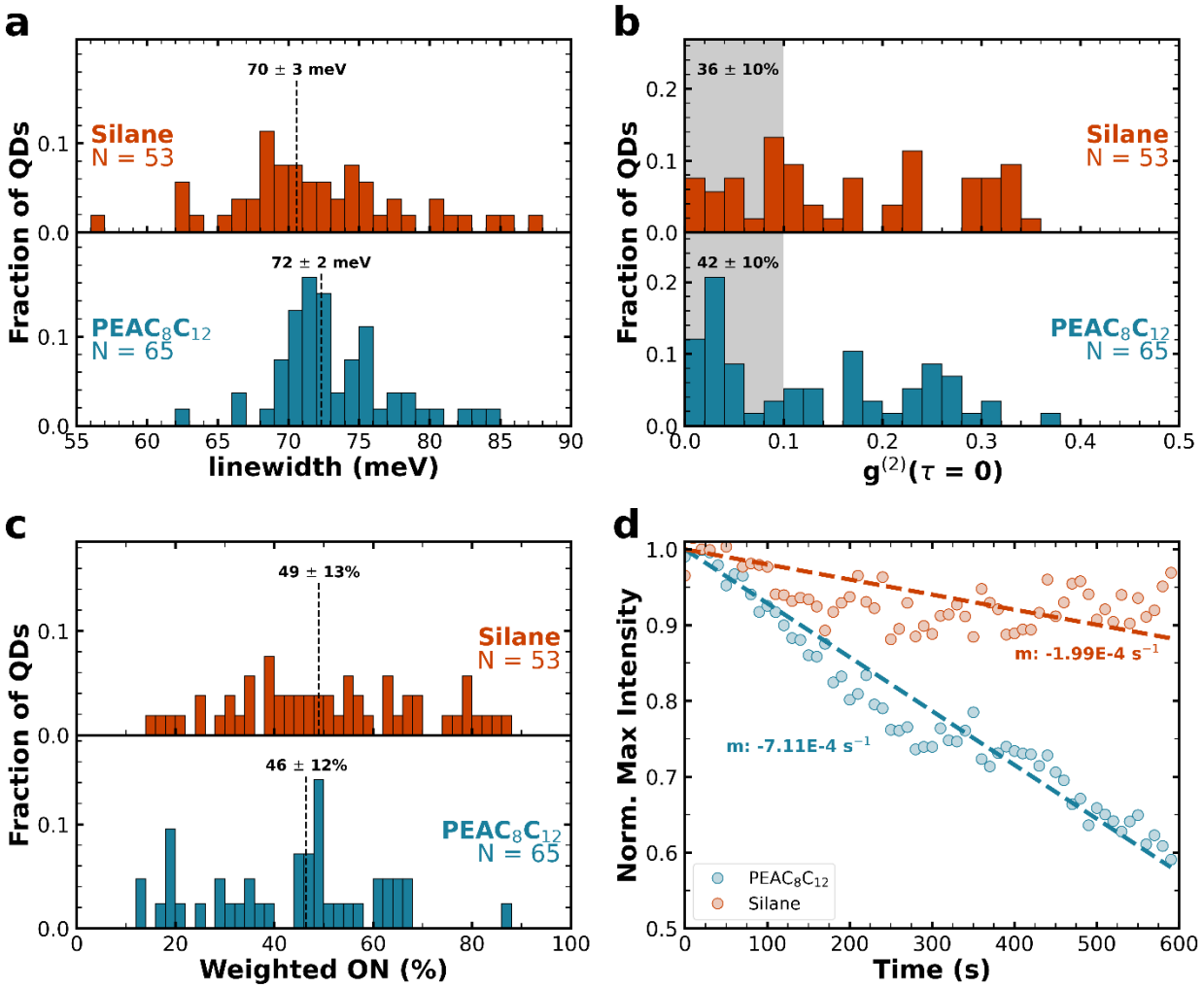

Figure 4.2. Single quantum dot characterization at room temperature a) Distribution of single quantum dot photoluminescence linewidths. Dashed lines and corresponding numbers represent the median ± interquartile deviation b**)** Distribution of $g^{(2)}(t=0)$ for single quantum dots. $g^{(2)}(t=0)$ values under 0.1 are considered excellent (grey box) and make up 42 ± 10% and 36 ± 10% of the measured quantum dots for $PEAC_8C_{12}$ passivation and silane coating respectively. **c)** Distribution of weighted ON%s for single quantum dots. Dashed lines and corresponding numbers represent the median ± interquartile deviation. **d)** Quantum dot photobleaching seen through a decreasing maximum intensity in time. Scattered points are the average of all ($N_{PEAC8C12} = 65$, $N_{silane} = 53$) single quantum dot photobleaching traces. Dashed lines are linear fits to the data of the form $y = mx + 1$.

Having explored the potential of our two samples as single photon sources at room temperature we continue our characterization at 4K. Figures C9 and C10 show the full 4K characterization of representative single quantum dots with $PEAC_8C_{12}$ passivation and silane coating, respectively. Our three main metrics to assess how well these quantum dots perform as single photon emitters remain the same as for the room temperature measurements. Additionally, at low temperatures spectral diffusion slows down, and linewidths narrow allowing us to assess the impact of spectral diffusion by measuring linewidths at both short (1s) and long (600 s) integration times. Figure 4.3a compares the average linewidth at a short integrations time (1 s) to the linewidth at a long integration time (600 s). While the $PEAC_8C_{12}$-passivated and silane-coated samples have similar linewidths at short times (20 ± 4 meV and 25 ± 5 meV respectively, Figure C11) silane-coated quantum dots have a much larger linewidth at long integration times (31 ± 8 meV

and 44 ± 15 meV respectively, Figure C11). Surprisingly, this difference in short- and long-time linewidths does not appear to arise primarily from the random spectral fluctuations associated with spectral diffusion. Instead, as shown in Figure C12, the changing linewidth is strongly correlated to a continuous spectral blueshift. Figure 4.3b shows the average blue shift in time for both samples. While $PEAC_8C_{12}$-passivated quantum dots show a small spectral blue shift (averaging 8 meV over 20 minutes), silane-coated quantum dots blue shift nearly three times as far (averaging 23 meV over 20 minutes). Spectral blue-shifts are a common sign of photodegradation[51] – which is further confirmed by the observation of photobleaching during the blinking measurements (Figure C12).

Next, we compare the second order correlation functions $g^{(2)}(\tau)$ for silane-coated and $PEAC_8C_{12}$-passivated quantum dots. Figure 4.3c shows the distribution of measured values for $g^{(2)}(\tau = 0)$. Again, $PEAC_8C_{12}$-passivated quantum dots perform better than their silane-coated counterparts. 61 ± 10% of the $PEAC_8C_{12}$-passivated quantum dots have a $g^{(2)}(\tau = 0)$ under 0.1, compared to 49 ± 11% of the silane-coated quantum dots. The difference in the distribution of the $g^{(2)}(\tau = 0)$ values indicates that silane-coated quantum dots likely have either a larger chance of biexciton formation, or a higher biexciton quantum yield.

Finally, we compare the photoluminescence lifetimes and blinking behavior of our quantum dots. Figure 4.3d shows the distribution of intensity weighted ON percentages calculated from CPA classified blinking traces for both quantum dot samples. Once again, $PEAC_8C_{12}$-passivated quantum dots outperform their silane-coated counterparts. $PEAC_8C_{12}$-passivated quantum dots have an ON% of 66 ± 11%, while silane-coated quantum dots have an ON% of 55 ± 11%. We also compare the distribution of single quantum dot photoluminescence lifetimes, which are shown in Figure C13. We fit the lifetimes using a stretched exponential because the lifetime of a single quantum dot can vary during blinking events[52,53] – resulting in a measured lifetime analogous to a lifetime from a heterogenous sample.[37] Consistent with the observed higher ON%, $PEAC_8C_{12}$-passivated quantum dots also have longer lifetimes (383 ± 101 ps) than their silane-coated counterparts (276 ± 61 ps).

Overall, our characterization at 4K paints a different picture of silane-coated quantum dots as single photon emitters than the room temperature measurements. Silane-coated $FAPbBr_3$ quantum dots exhibit a persistent spectral blue shift, stronger photobleaching, a lower weighted ON% and shorter photoluminescence lifetimes than $PEAC_8C_{12}$-passivated quantum dots. These measurements indicate that at 4K $PEAC_8C_{12}$ provides better passivation for $FAPbBr_3$ quantum dots than the current generation of silane coating. This difference is especially puzzling given the favorable room temperature performance of these silane-coated perovskite quantum dots. Next, we explore the reasons for this change in performance at low temperature.

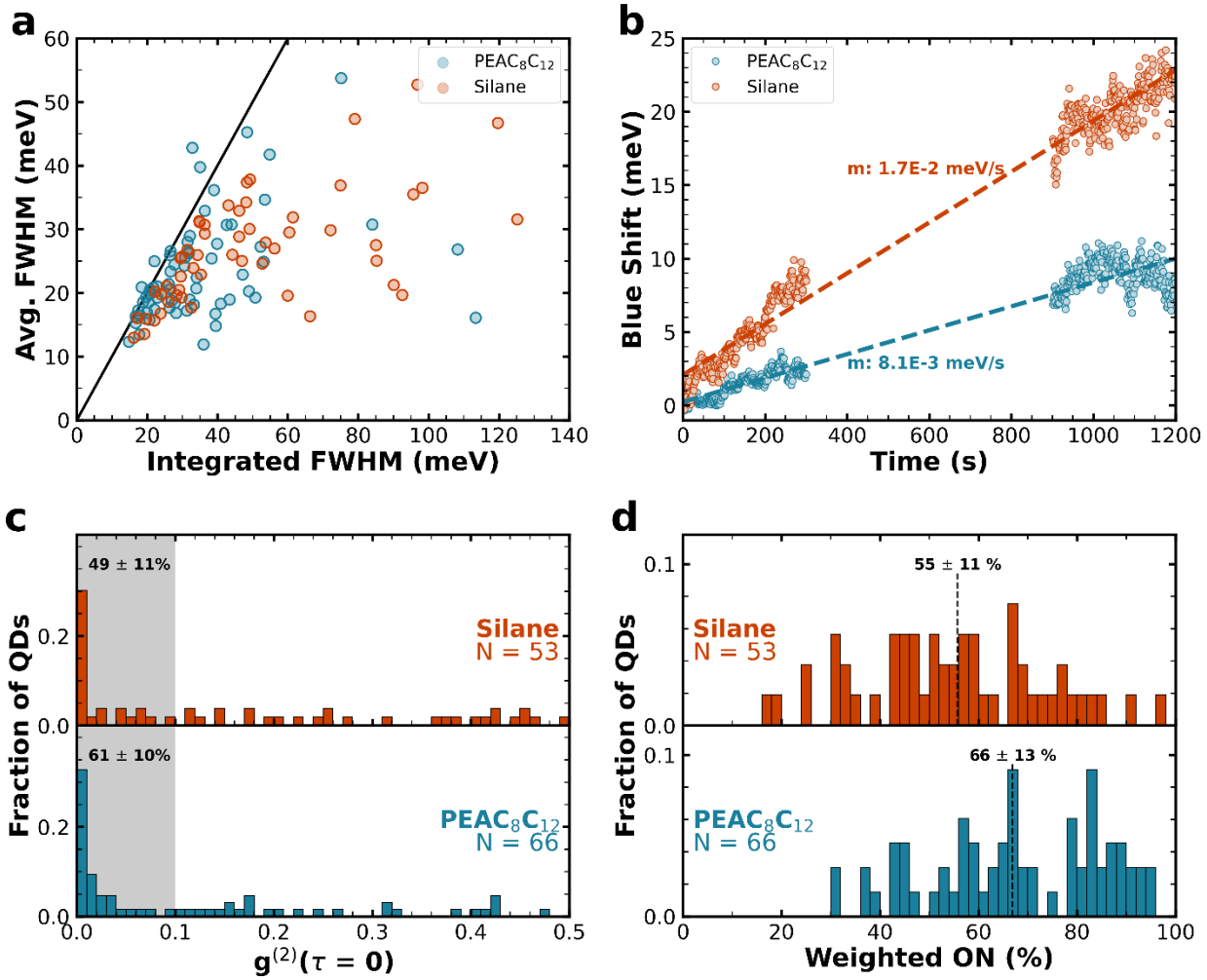

Figure 4.3. Single quantum dot characterization at 4K a) Average linewidth at short integration times (1s) compared to the linewidth at long integration times (600 s) for single quantum dots. y=x is represented by the solid black line. **b)** Photodegradation seen through a spectral blue shift in time. Dashed lines are linear fits to the data of the form y = mx + b. The gap from 300 to 900 seconds corresponds to the measurement time for quantum dot blinking, lifetime and $g^2(\tau)$. **c)** Distribution of $g^{(2)}(\tau = 0)$ for single quantum dots. $g^{(2)}(\tau = 0)$ values under 0.1 are considered excellent (grey box) and make up 61 ± 10% and 49 ± 11% of the measured quantum dots for $PEAC_8C_{12}$ passivation and silane coating respectively. **d)** Distribution of weighted ON%s for single quantum dots. Dashed lines and corresponding numbers represent the median ± interquartile deviation.

We find the first hint towards the cause of the decreased performance by exploring the underlying non-radiative decay mechanisms responsible for blinking at room temperature and 4K. Different non-radiative decay mechanisms have unique lifetime-intensity correlations, which can be easily identified by fluorescence lifetime intensity distributions (FLIDs). There are three non-radiative pathways which are most commonly considered responsible for quantum dot blinking – band-carrier (BC) trapping, Auger-Meitner recombination and hot-carrier (HC) trapping.[53,54] BC trapping is associated with the multiple recombination center model of quantum dot blinking, where the quantum dot remains neutral and blinking occurs because of short-lived traps.[53–55] In this model, blinking occurs as the non-radiative recombination rate changes while the radiative recombination rate remains constant resulting in a linear lifetime-intensity correlation.[53,54] Auger-Meitner mediated blinking is associated with quantum dot charging and trion formation, which could occur either by photoionization or long-lived traps.[53,54] In this scenario both the

radiative and non-radiative recombination rates vary as the quantum dot blinks resulting in a non-linear correlation between the lifetime and intensity.[52–54] HC trapping is also associated with neutral quantum dots, but in this model carriers are trapped before relaxing to the band-edge resulting in a lifetime which is independent of intensity.[54] Importantly, these pathways are not mutually exclusive and a single quantum dot can show a combination of HC trapping, BC trapping and Auger-Meitner recombination.[52]

Representative FLIDs for $PEAC_8C_{12}$-passivated and silane-coated quantum dots at room temperature are shown in Figures 4.4a and 4.4b respectively. These FLIDs are constructed by summing the lifetime and intensity normalized single quantum dot FLIDs for each sample. We do not see the signature of HC trapping in any of our FLIDs at room temperature (unsurprising given that our excitation is only 200 meV above the bandgap) and as such discard HC trapping as a possible blinking mechanism in our samples under these measurement conditions. However, our FLIDs do show signs of both BC trapping and Auger-Meitner recombination. At room temperature, both samples show a predominantly linear relationship between lifetime and intensity indicating that BC trapping is the dominant non-radiative recombination channel. For a more detailed analysis we use Equation C8, which assumes that the overall FLID pattern is a linear sum of the two underlying patterns,[56] to resolve the relative percentage of non-radiative decay which can be attributed to BC trapping and Auger-Meitner recombination. The solid white line shows the fit of the representative FLIDs to Equation C8, and dashed lines represent the 100% BC and 100% Auger-Meitner mediated extremes. At room temperature blinking in $PEAC_8C_{12}$-passivated quantum dots is primarily mediated by BC trapping (99%), with less than 1% of blinking attributed to Auger-Meitner recombination. Blinking in silane-coated quantum dots is also primarily mediated by BC trapping (93%), but we find that Auger-Meitner recombination plays a more significant role at 7%. Figure C8 shows the distributions of BC trapping and Auger-Meitner mediated blinking for individual quantum dots at room temperature. These FLID patterns indicate that at room temperature non-radiative recombination predominately occurs *via* short-lived traps. However, silane-coated quantum dots likely have a slightly higher probability of trion and/or biexciton formation consistent with their observed tendency for larger $g^{(2)}(\tau = 0)$ values (Figure 4.2b).

Figures 4.4c and 4.4d show the representative FLIDs for $PEAC_8C_{12}$-passivated and silane-coated quantum dots acquired at 4K. At 4K, neither of our samples show a predominantly linear relationship between lifetime and intensity. Instead, both samples show a strong non-linear correlation indicating that Auger-Meitner recombination plays a more significant role in non-radiative recombination at 4K. To resolve the relative percentage of non-radiative decay which can be attributed to BC trapping and Auger-Meitner recombination we fit our FLIDs to Equation C8. At 4K we find that blinking in $PEAC_8C_{12}$-passivated quantum dots is primarily mediated by Auger-Meitner recombination (58%), although BC trapping still plays a significant role (42%). We find that blinking in silane-coated quantum dots is significantly more likely to be mediated by Auger-Meitner recombination (80%) with BC trapping playing a smaller role (20%). Figure C13 shows the distributions of BC trapping and Auger-Meitner mediated blinking for individual quantum dots at 4K.

The general trend of increased Auger-Meitner recombination contributions indicates that at 4K perovskite quantum dots tend to have long-lived traps while at room temperature the traps are mostly short-lived. And while the non-radiative decay mechanisms for silane-coated and $PEAC_8C_{12}$-passivated quantum dots are very similar at room temperature, at 4K Auger-Meitner recombination is significantly more likely in silane-coated quantum dots than in $PEAC_8C_{12}$-passivated quantum dots. This suggests that silane-coated quantum dots have an additional source of traps which play a significant role at 4K. As Auger-Meitner recombination is most likely to be associated with trion and biexciton formation – we further explore trion and biexciton formation in these samples to understand their differences in 4K performance.

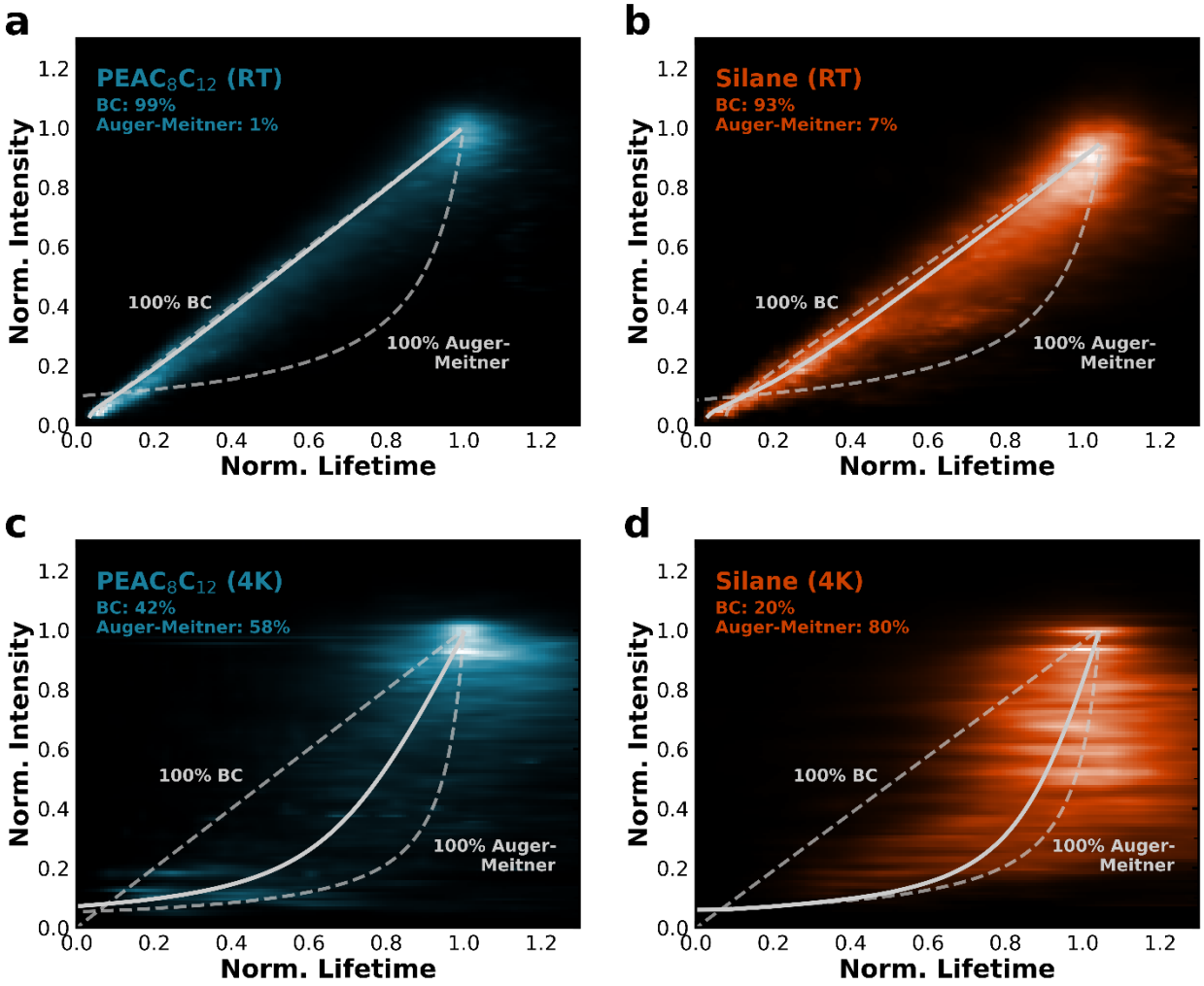

Figure 4.4. Comparing non-radiative decay mechanisms at room temperature and 4K with Fluorescence Lifetime Intensity Distributions. FLID plots summed from all ($N_{PEAC8C12}$ = 65, N_{silane} = 53) single quantum dot to represent the average single quantum dot at room temperature for **a)** $PEAC_8C_{12}$-passivated and **b)** silane-coated. FLID plots aggregated from single quantum dots ($N_{PEAC8C12}$ = 66, N_{silane} = 53) to represent the average single quantum dot at 4K for **c)** $PEAC_8C_{12}$-passivated and **d)** silane-coated. The solid line represents the best fit of the data as a combination of BC trapping and Auger-Meitner recombination, while the dashed lines represent the two extremes. While the non-radiative decay mechanisms for silane-coated and $PEAC_8C_{12}$-passivated quantum dots are very similar at room temperature, at 4K Auger-Meitner recombination is significantly more likely in silane-coated quantum dots than in $PEAC_8C_{12}$-passivated quantum dots. This suggests that silane-coated quantum dots have an additional source of traps which play a significant role at 4K.

First, we look for signs of trion and biexciton formation in the fluence dependent PLQY. Figure 4.5a describes a simple possible physical model for the formation of trions and biexcitons in quantum dots. In this model we consider three states: the exciton (X), the trion ($X^{\pm}$) and the biexciton (XX). The formation rate of the exciton is linear with respect to the excitation density, while the trion and biexciton formation rates have a second-order dependence on the excitation density. Each state has an associated radiative ($k_{r,n}$) and non-radiative ($k_{nr,n}$) recombination rate and the biexciton has an additional trapping rate (k_t) associated with the long-term trapping of a charge carrier which populates the trion.

Figure 4.5b shows the fluence dependent PLQY of quantum dot thin films made from both samples. We calculate the expected number of excitons formed per pulse (<N>) by estimating the absorption cross section from the fluence dependent intensity of the thin film (Equation C11 and Figure C14).[57,58] The highest <N> value corresponds to our single quantum dot characterization fluence (6.1 μJ/cm^2). Qualitatively, the PLQY of the silane-coated quantum dots has a steeper roll off than the PLQY of the $PEAC_8C_{12}$-passivated quantum dots which is consistent with increased higher-order non-radiative recombination. To check that the observed fluence dependence is consistent with the trion interpretation from the FLID distributions, we next fit the fluence dependent PLQY using Equations 4.1a-4.1e which are derived from the physical model depicted in Figure 4.5a:

$$QY(\langle N\rangle) = \frac{N_X(\langle N\rangle)k_{r,X} + N_{X\pm}(\langle N\rangle)k_{r,X\pm} + N_{XX}(\langle N\rangle)k_{r,XX}}{N_X(\langle N\rangle)(k_{r,X}+k_{nr,X}) + N_{X\pm}(\langle N\rangle)(k_{r,X\pm}+k_{nr,X\pm}) + N_{XX}(\langle N\rangle)(k_{r,XX}+k_{nr,XX}+k_t)} \quad (4.1a)$$

$$\frac{\partial N_X}{\partial t} = -N_X(k_{r,X} + k_{nr,X}) + N_{XX}(k_{r,XX} + k_{nr,XX}), \qquad N_X(0) = n \quad (4.1b)$$

$$\frac{\partial N_{X\pm}}{\partial t} = N_{XX}(k_t) - N_{X\pm}(k_{r,X\pm} + k_{nr,X\pm}), \qquad N_{X\pm}(0) = 0 \quad (4.1c)$$

$$\frac{\partial N_{XX}}{\partial t} = -N_{XX}(k_{r,XX} + k_{nr,XX} + k_t), \qquad N_{XX}(0) = n^2 \quad (4.1d)$$

$$\langle N\rangle = n + 0.5n^2 \quad (4.1e)$$

Equation 4.1a describes the expected behavior of the PLQY with changing excitation density; and depends on the fluence dependent state populations $N_n(\langle N\rangle)$ and the various radiative and non-radiative recombination rates. Equations 4.1b-4.1d are a system of differential equations and initial conditions which describe how the population of each state changes in time. Equation 4.1e describes the expected branching ratio between exciton and biexciton generation for a given excitation density based on Poisson statistics. The system of equations in Equations 4.1b-4.1d describe an initial value problem which can be solved for the fluence dependent state populations. To find physically reasonable recombination rates we constrain our radiative and non-radiative rates based on the lifetime and quantum yield of the samples at our lowest fluence (0.45 nJ/cm^2, Figure C15) and the expected statistical scaling of recombination rates in higher order states.[59] These constraints, along with model limitations and alternative PLQY models are discussed in more detail in the Supplementary Information under the heading "Fluence Dependent PLQY" and in Figure C16.

Table 4.1 shows the recombination rates found by fitting the data in Figure 4.5b using Equations 4.1a-4.1e. Additionally, as shown in Table C1 and Figure C15, the recombination rates found from fitting the fluence dependent PLQY data are consistent with the experimental dynamics of the exciton and trion states from our single quantum dot data and our experimental fluence dependent lifetimes. The fitting reveals two primary differences in the recombination dynamics of the $PEAC_8C_{12}$-passivated and silane-coated quantum dots. First, silane-coated quantum dots have larger biexciton and trion non-radiative rate constants leading to lower state quantum yields, consistent with the low temperature FLIDs (Figures 4.1c and 4.1d) where silane-coated quantum dots are more likely to recombine *via* Auger-Meitner recombination. And second, silane-coated quantum dots have a larger trapping rate constant (k_t), suggesting that silane-coated quantum dots also have a larger population of trions due to a more efficient trapping process.

Table 4.1. Recombination rates and quantum yields for exciton (X), trion (X±) and biexciton (XX) states extracted from fluence dependent PLQY measurements.

	Exciton (X)			**Trion ($X^{\pm}$)**			**Biexciton (XX)**				
	$k_{r,X}$ (ns^{-1})	$k_{nr,X}$ (ns^{-1})	QY_X	$k_{r,X\pm}$ (ns^{-1})	$k_{nr,X\pm}$ (ns^{-1})	$QY_{X\pm}$	$k_{r,XX}$ (ns^{-1})	$k_{nr,XX}$ (ns^{-1})	QY_{XX}	k_t (ns^{-1})	$P_{t,XX}$
PEA C_8C_{12}	1.9 ± 0.2	0.06 ± 0.01	0.97	2.8 ± 0.3	0.12 ± 0.02	0.96	6.5 ± 0.7	0.46 ± 0.05	0.68	2.7 ± 0.3	0.28
Silane	1.9 ± 0.2	0.11 ± 0.01	0.95	2.9 ± 0.4	0.81 ± 0.07	0.78	6.7 ± 0.8	3.0 ± 0.4	0.39	7.6 ± 0.8	0.44

Having shown that silane-coated quantum dots have a steeper PLQY roll-off primarily due to increased Auger-Meitner recombination, we look to further assess the relative probability of forming a trion in both of our samples. To do this we look for the signature of trion emission in our single quantum dot photoluminescence spectra. At 4K single quantum dots are expected to have five spectral contributions – the zero-phonon line (ZPL), trion emission, biexciton emission and two longitudinal optical (LO) phonons. The other spectral contributors are expected to be red-shifted from the ZPL, although emission energy and intensity are size-dependent. The emission contributions of the LO phonons are size-independent and occur at -4.9 and -19.5 meV,[60,61] while the trion and biexciton emission contributions are size-dependent.[50,60,62] For $FAPbBr_3$ quantum dots with an edge-length between 5.5 and 6.5 nm, the trion and biexciton emission peaks are expected to be between -30 and -20 meV and -50 and -40 meV respectively.[60]

Since our samples exhibit significant spectral variations in time, we chose to correct our spectra according to Gumbsheimer et al.[63] in order to better resolve the emission structure. After correcting our spectra, we integrate across the collection time and look for the signatures of trion and biexciton emission. Figure 4.5c shows representative corrected and integrated single quantum dot photoluminescence spectrum for both samples.

Qualitatively, the spectra for silane-coated and $PEAC_8C_{12}$-passivated quantum dots show one major difference: silane-coated quantum dots have a pronounced shoulder around -20 meV. This is exactly the range of emission which should correspond to trion emission in approximately 6 nm $FAPbBr_3$ quantum dots.[60] This peak is likely broadened due to overlap with the LO phonon mode at -19.6 meV, leading to a broader flat shoulder instead of a distinct peak. Both samples have minimal emission in the range of biexciton emission (-50 to -40 meV) which is consistent with our measured in $g^{(2)}(\tau = 0)$ values (Figure 4.3b). The dashed lines in Figure 4.5c show fits to the spectra using a five Gaussian model which considers emissive contributions from the zero phonon line, the two LO phonons and trion and biexciton emission. Figure C17 shows the details of this fitting for the representative spectra shown in Figure 4.5c and Figure C18 shows the distribution of emission by state extracted from this fitting for all of our quantum dots. On average we find that the $PEAC_8C_{12}$-passivated quantum dots have emission split 80/16/4 between the exciton, trion and biexciton respectively, while silane-coated quantum dots have emission split 72/22/6 between the exciton, trion and biexciton.

Using the results of these fittings we can estimate the relative population of each state by correcting for quantum yields, trapping and fluence-dependent emission intensity trends according to Equation 4.2a:

$$I_n = N_n I_{ex}^{\beta_n} QY_n \quad (4.2a)$$

$$N_{eff,n} = (1 - P_{t,n}) N_n \quad (4.2b)$$

Where I_n is the measured emission intensity of a given state, N_n is the population of a given state, I_{ex} is the excitation intensity, β_n describes the fluence-dependent emission intensity trend of a given state and QY_n is the quantum yield of a given state. For states which have an additional trapping pathway (biexciton) we further calculate the population that is not trapped ($N_{eff,n}$) based on the probability of trapping ($P_{t,n}$) using Equation 4.2b. Using the experimental state quantum yields and trapping probabilities calculated from our fluence dependent PLQY model (Table 4.1) and literature fluence-dependent emission intensity trends[50,60] we calculate the probability of occupying each state, which is shown in Table 4.2. We find that, under our measurement conditions, the trion state of silane-coated quantum dots is twice as likely to be occupied as its $PEAC_8C_{12}$-passivated counterpart.

Table 4.2. Relative population of exciton, trion and biexciton states determined from single quantum dot photoluminescence spectra

	$PEAC_8C_{12}$	**Silane**
Exciton	0.92 ± 0.08	0.82 ± 0.03
Trion	0.08 ± 0.04	0.16 ± 0.02
Biexciton	0.01 ± 0.01	0.02 ± 0.01

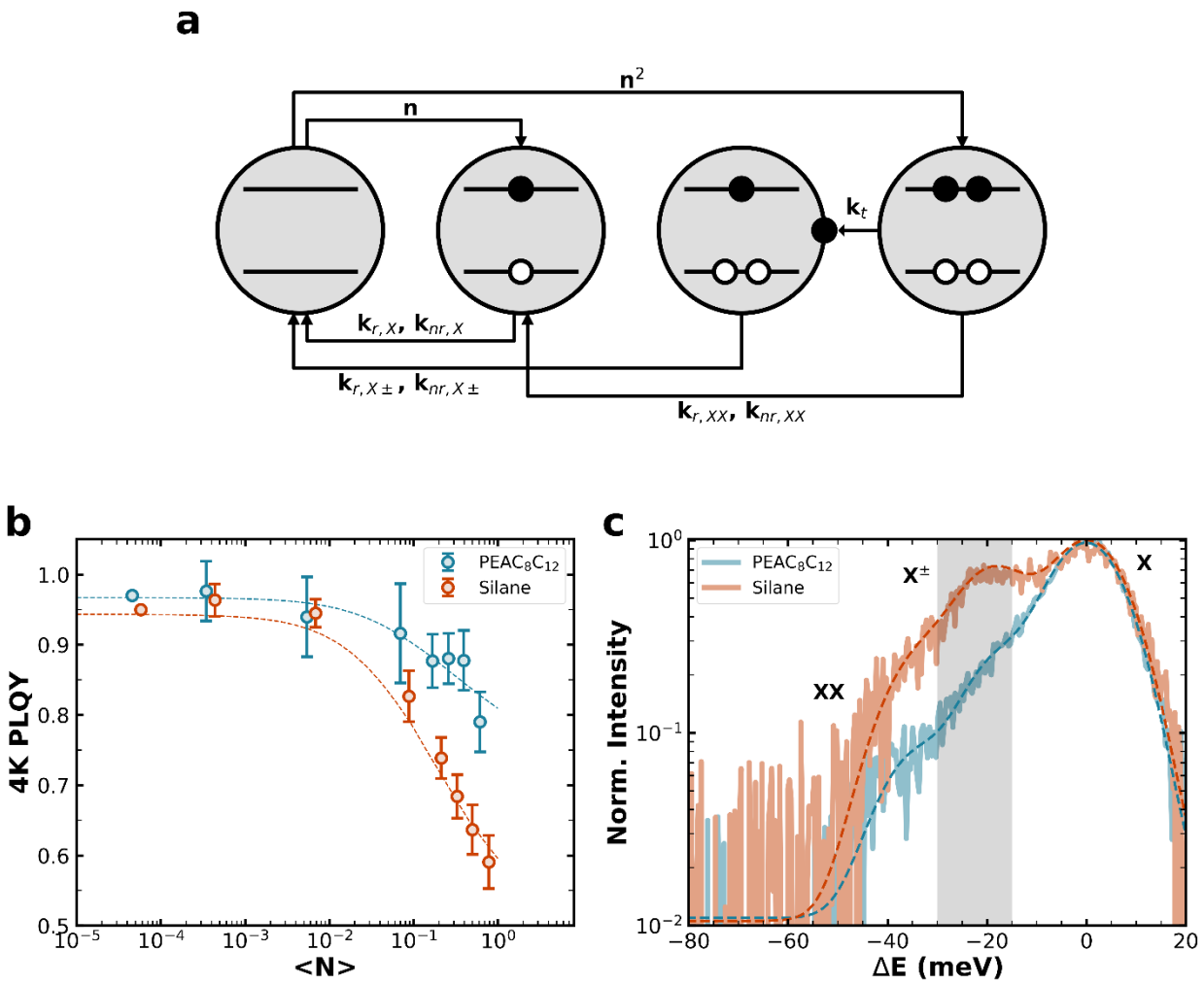

Figure 4.5. Evidence for increased trion formation in silane-coated quantum dots at 4K. a) Photophysical model for the formation and recombination of excitons, trions and biexcitons in quantum dots **b)** Fluence dependent PLQY measurements for quantum dot thin films. Dashed lines are the fit to Equation 4.1, see Table 4.1 for fit parameters. Silane-coated quantum dots see an early roll off due to higher order non-radiative recombination. **c)** Representative long integration time single quantum dot photoluminescence spectra aggregated from spectral diffusion corrected short integration time spectra (solid lines). Dashed lines are the fit to Equation C10. Silane-coated quantum dots show more emission from the trion ($X^{\pm}$) states.

Together, the observed fluence dependent PLQY trends, single quantum dot photoluminescence spectra and FLIDs paint a self-consistent picture where silane-coated quantum dots perform worse at 4K due to trion formation. We find that the trion state in silane-coated quantum dots has a lower quantum yield and higher population at high fluence than the trion state in its $PEAC_8C_{12}$-passivated counterpart. This combination of factors means that silane-coated quantum dots have significantly more Auger-Meitner non-radiative recombination under intense fluence at low T and increases the amount of time the quantum dot spends charged.

We hypothesize what could be two likely causes of long-lived traps and surface charging at 4K with our silane-coated quantum dots: head group variations and tail group variations. AEAPTES, our silane

passivation, is a diamine– meaning that it has two amines which could act as head groups. To displace the as-synthesized oleylammonium passivation, it is likely that one of AEAPTES' amines becomes an ammonium during the ligand exchange providing strong passivation for A-site vacancies in the perovskite lattice. However, X-site vacancies can only be passivated by the remaining amine or residual oleate. Both oleates and amines are considered weak passivants and their usage for X-site passivation in these quantum dots may result in an additional source of traps with a higher occupation probability at 4K. In contrast $PEAC_8C_{12}$ is a zwitterionic ligand and as such can passivate both A- and X-site vacancies well. The effectiveness of using solely cationic or dicationic ligands for single quantum dot applications is still being debated, with both good[18,64] and bad[32] performances reported, but we consider this difference in head groups to be a potential source of the worse performance of our silane-coated quantum dots at 4K.

We propose that a second potential cause of long-lived traps and surface charging at 4K for our silane-coated quantum dots could be the silane tail. Silane layers, and their associated silanols and siloxanes are often considered a poor optoelectronic material due to deep carrier traps [65–67] and have proved largely ineffective in organic LEDs. Additionally, the blinking dynamics of silica-shelled CdSe/CdS quantum dots show evidence for the formation of a large number of trion, biexciton and other higher-order charged states at room temperature thanks to traps at the CdS-silica interface.[59,68] While AEAPTES does not directly create a perovskite-silane interface[69,70] for a similar trapping mechanism to silica-shelled CdSe/CdS quantum dots, the silane tail is plausibly within tunneling distance of the quantum dot surface which would allow for trapping within the silane tail, consistent with the larger trapping rate constant for silane-coated quantum dots.

4.4 Conclusion

Here we have explored the performance of silane-coated $FAPbBr_3$ quantum dots as single photon emitters. We find that at room temperature silane coating performs as well as passivation from the literature-best ligand $PEAC_8C_{12}$. Both passivation methods have narrow linewidths (~71 meV), low $g^{(2)}(\tau = 0)$ values (> 36% below 0.1) and a comparable ON% (50%). We also find that at room temperature silane-coated quantum dots are more photostable than their $PEAC_8C_{12}$-passivated counterparts. However, at 4K we find that silane-coated quantum dots perform worse than their $PEAC_8C_{12}$-passivated counter parts with broader linewidths, higher $g^{(2)}(\tau = 0)$ values and a lower ON%.

From FLIDs acquired at 4K we observe that silane-coated quantum dots tend toward Auger-Meitner dominated non-radiative recombination. This result suggests that silane-coated quantum dots form more trions and other higher order excitonic states such as biexcitons under high fluences at low temperature. This result is further supported by single particle spectra and fluence dependent PLQY measurements which indicate that the silane-coated quantum dots are two times more likely to form trions than the $PEAC_8C_{12}$-passivated quantum dots. We suggest that this increased trion formation, and the subsequent prevalence of surface charging, is the cause of the photodegradation we observe at 4K.

Although, our silane coating performs worse than $PEAC_8C_{12}$ passivation at 4K – its excellent performance at room temperature indicates that passivation using similar motifs are worth further exploration. One consideration is an aminoalkyl triethoxysilane with a longer alkyl chain which could prevent surface charges from tunneling to the silane tail or changing the amine/ammonium head group to a zwitterionic head group to provide better X-site passivation. Alternatively, we may be able to keep the

benefits of passivation using a cross-linked ligand and remove the 4K trapping mechanism by choosing a ligand with a different cross-linking moiety, such as a thiol, which is less likely to have a large trap density.

4.5 Acknowledgements

This work, and the roles of J.K., B.F.H, Y.H., S.R.M., S.Y., G.D. and D.S.G, were primarily supported by the National Science Foundation under the STC IMOD Grant (No. DMR-2019444). B.F.H. acknowledges support from the National Science Foundation through the Graduate Research Fellowship Program (NSF-GRFP) under Grant No. DGE 2040434. S.K., H.S. and B.W. acknowledge funding from the European Union's Horizon 2020 research and innovation program under the Marie Skłodowska-Curie grant agreement No. 956270 for supporting synthesis and ligand exchange of the silane-coated quantum dots. Z.H. acknowledges funding from the Washington Research Foundation for supporting ATR-IR characterization of the quantum dots.

The authors acknowledge the use of facilities and instruments at the Photonics Research Center (PRC) at the Department of Chemistry, University of Washington, as well as that at the Research Training Testbed (RTT), part of the Washington Clean Energy Testbeds system. HAADF-STEM imaging was carried out at the Facility for Electron Microscopy of Materials at the University of Colorado Boulder (CU FEMM, RRID: SCR_019306).

J.K. would like to acknowledge Akash Dasgupta (University of Washington) for discussions regarding modeling fluence dependent PLQY in quantum dots.

4.6 References

(1) Kortlever, R.; Shen, J.; Schouten, K. J. P.; Calle-Vallejo, F.; Koper, M. T. M.; Huang, J.; Buonsanti, R.; Nitopi, S. Industry Outlook of Perovskite Quantum Dots for Display Applications. *Nature Nanotechnology 2022 17:8* **2022**, *17* (8), 813–816. https://doi.org/10.1038/s41565-022-01163-8.

(2) Han, T. H.; Jang, K. Y.; Dong, Y.; Friend, R. H.; Sargent, E. H.; Lee, T. W. A Roadmap for the Commercialization of Perovskite Light Emitters. *Nature Reviews Materials 2022 7:10* **2022**, *7* (10), 757–777. https://doi.org/10.1038/s41578-022-00459-4.

(3) Akkerman, Q. A.; Rainò, G.; Kovalenko, M. V.; Manna, L. Genesis, Challenges and Opportunities for Colloidal Lead Halide Perovskite Nanocrystals. *Nature Materials 2018 17:5* **2018**, *17* (5), 394–405. https://doi.org/10.1038/s41563-018-0018-4.

(4) Kim, Y. H.; Kim, S.; Kakekhani, A.; Park, J.; Park, J.; Lee, Y. H.; Xu, H.; Nagane, S.; Wexler, R. B.; Kim, D. H.; Jo, S. H.; Martínez-Sarti, L.; Tan, P.; Sadhanala, A.; Park, G. S.; Kim, Y. W.; Hu, B.; Bolink, H. J.; Yoo, S.; Friend, R. H.; Rappe, A. M.; Lee, T. W. Comprehensive Defect Suppression in Perovskite Nanocrystals for High-Efficiency Light-Emitting Diodes. *Nature Photonics 2021 15:2* **2021**, *15* (2), 148–155. https://doi.org/10.1038/s41566-020-00732-4.

(5) Akkerman, Q. A.; Gandini, M.; Di Stasio, F.; Rastogi, P.; Palazon, F.; Bertoni, G.; Ball, J. M.; Prato, M.; Petrozza, A.; Manna, L. Strongly Emissive Perovskite Nanocrystal Inks for High-Voltage Solar Cells. *Nat Energy* **2017**, *2* (2), 1–7. https://doi.org/10.1038/nenergy.2016.194.

(6) Lu, L.; Sun, M.; Wu, T.; Lu, Q.; Chen, B.; Huang, B. All-Inorganic Perovskite Nanocrystals: Next-Generation Scintillation Materials for High-Resolution X-Ray Imaging. *Nanoscale Adv* **2022**, *4* (3), 680–696. https://doi.org/10.1039/D1NA00815C.

(7) Feld, L. G.; Boehme, S. C.; Sabisch, S.; Frenkel, N.; Yazdani, N.; Morad, V.; Zhu, C.; Svyrydenko, M.; Tao, R.; Bodnarchuk, M.; Lubin, G.; Kazes, M.; Wood, V.; Oron, D.; Rainò, G.; Kovalenko, M. V. Phonon-Driven Wavefunction Localization Promotes Room-Temperature, Pure Single-Photon Emission in Large Organic-Inorganic Lead-Halide Quantum Dots. https://doi.org/10.48550/arXiv.2404.15920.

(8) Utzat, H.; Sun, W.; Kaplan, A. E. K.; Krieg, F.; Ginterseder, M.; Spokoyny, B.; Klein, N. D.; Shulenberger, K. E.; Perkinson, C. F.; Kovalenko, M. V.; Bawendi, M. G. Coherent Single-Photon Emission from Colloidal Lead Halide Perovskite Quantum Dots. *Science (1979)* **2019**, *363* (6431). https://doi.org/10.1126/SCIENCE.AAU7392.

(9) Kaplan, A. E. K.; Krajewska, C. J.; Proppe, A. H.; Sun, W.; Sverko, T.; Berkinsky, D. B.; Utzat, H.; Bawendi, M. G. Hong–Ou–Mandel Interference in Colloidal CsPbBr3 Perovskite Nanocrystals. *Nature Photonics 2023 17:9* **2023**, *17* (9), 775–780. https://doi.org/10.1038/s41566-023-01225-w.

(10) Guymon, G. G.; Nguyen, H. A.; Sharp, D.; Nguyen, T.; Lei, H.; Ginger, D. S.; Fu, K.-M. C.; Majumdar, A.; Cossairt, B. M.; MacKenzie, J. D. Deterministic Printing of Single Quantum Dots. *Advanced Materials* **2025**, e13707. https://doi.org/10.1002/ADMA.202513707.

(11) Frantsuzov, P. A.; Volkán-Kacsó, S.; Jankó, B. Universality of the Fluorescence Intermittency in Nanoscale Systems: Experiment and Theory. *Nano Lett* **2013**, *13* (2), 402–408. https://doi.org/10.1021/NL3035674.

(12) Nirmal, M.; Dabbousi, B. O.; Bawendi, M. G.; Macklin, J. J.; Trautman, J. K.; Harris, T. D.; Brus, L. E. Fluorescence Intermittency in Single Cadmium Selenide Nanocrystals. *Nature* **1996**, *383* (6603), 802–804. https://doi.org/10.1038/383802A0.

(13) Galland, C.; Ghosh, Y.; Steinbrück, A.; Hollingsworth, J. A.; Htoon, H.; Klimov, V. I. Lifetime Blinking in Nonblinking Nanocrystal Quantum Dots. *Nat Commun* **2012**, *3* (1), 1–7. https://doi.org/10.1038/NCOMMS1916.

(14) García-Santamaría, F.; Chen, Y.; Vela, J.; Schaller, R. D.; Hollingsworth, J. A.; Klimov, V. I. Suppressed Auger Recombination in "Giant" Nanocrystals Boosts Optical Gain Performance. *Nano Lett* **2009**, *9* (10), 3482–3488. https://doi.org/10.1021/NL901681D.

(15) Chen, Y.; Vela, J.; Htoon, H.; Casson, J. L.; Werder, D. J.; Bussian, D. A.; Klimov, V. I.; Hollingsworth, J. A. "Giant" Multishell CdSe Nanocrystal Quantum Dots with Suppressed Blinking. *J Am Chem Soc* **2008**, *130* (15), 5026–5027. https://doi.org/10.1021/JA711379K.

(16) Nguyen, H. A.; Hammel, B. F.; Sharp, D.; Kline, J.; Schwartz, G.; Harvey, S.; Nishiwaki, E.; Sandeno, S. F.; Ginger, D. S.; Majumdar, A.; Yazdi, S.; Dukovic, G.; Cossairt, B. M. Colossal Core/Shell CdSe/CdS Quantum Dot Emitters. *ACS Nano* **2024**, *18* (31), 20726–20739. https://doi.org/10.1021/ACSNANO.4C06961.

(17) Morad, V.; Stelmakh, A.; Svyrydenko, M.; Feld, L. G.; Boehme, S. C.; Aebli, M.; Affolter, J.; Kaul, C. J.; Schrenker, N. J.; Bals, S.; Sahin, Y.; Dirin, D. N.; Cherniukh, I.; Raino, G.; Baumketner, A.; Kovalenko, M. V. Designer Phospholipid Capping Ligands for Soft Metal Halide Nanocrystals. *Nature 2023 626:7999* **2023**, *626* (7999), 542–548. https://doi.org/10.1038/s41586-023-06932-6.

(18) Ginterseder, M.; Sun, W.; Shcherbakov-Wu, W.; McIsaac, A. R.; Berkinsky, D. B.; Kaplan, A. E. K.; Wang, L.; Krajewska, C.; Šverko, T.; Perkinson, C. F.; Utzat, H.; Tisdale, W. A.; Van Voorhis, T.; Bawendi, M. G. Lead Halide Perovskite Nanocrystals with Low Inhomogeneous Broadening and High Coherent Fraction through Dicationic Ligand Engineering. *Nano Lett* **2023**, *23* (4), 1128–1134. https://doi.org/10.1021/ACS.NANOLETT.2C03354.

(19) Krieg, F.; Ong, Q. K.; Burian, M.; Rainò, G.; Naumenko, D.; Amenitsch, H.; Süess, A.; Grotevent, M. J.; Krumeich, F.; Bodnarchuk, M. I.; Shorubalko, I.; Stellacci, F.; Kovalenko, M. V. Stable Ultraconcentrated and Ultradilute Colloids of CsPbX3 (X = Cl, Br) Nanocrystals Using Natural Lecithin as a Capping Ligand. *J Am Chem Soc* **2019**, *141* (50), 19839–19849. https://doi.org/10.1021/JACS.9B09969.

(20) Krieg, F.; Ochsenbein, S. T.; Yakunin, S.; Ten Brinck, S.; Aellen, P.; Süess, A.; Clerc, B.; Guggisberg, D.; Nazarenko, O.; Shynkarenko, Y.; Kumar, S.; Shih, C. J.; Infante, I.; Kovalenko, M. V. Colloidal CsPbX3 (X = Cl, Br, I) Nanocrystals 2.0: Zwitterionic Capping Ligands for Improved Durability and Stability. *ACS Energy Lett* **2018**, *3* (3), 641–646. https://doi.org/10.1021/ACSENERGYLETT.8B00035.

(21) Gallagher, S.; Kline, J.; Jahanbakhshi, F.; Sadighian, J. C.; Lyons, I.; Shen, G.; Hammel, B. F.; Yazdi, S.; Dukovic, G.; Rappe, A. M.; Ginger, D. S. Ligand Equilibrium Influences Photoluminescence Blinking in CsPbBr3: A Change Point Analysis of Widefield Imaging Data. *ACS Nano* **2024**, *18* (29), 19208–19219. https://doi.org/10.1021/ACSNANO.4C04968.

(22) Ahmed, G. H.; Yin, J.; Bakr, O. M.; Mohammed, O. F. Successes and Challenges of Core/Shell Lead Halide Perovskite Nanocrystals. *ACS Energy Lett* **2021**, *6* (4), 1340–1357. https://doi.org/10.1021/ACSENERGYLETT.1C00076.

(23) Li, Z. J.; Hofman, E.; Li, J.; Davis, A. H.; Tung, C. H.; Wu, L. Z.; Zheng, W. Photoelectrochemically Active and Environmentally Stable Cspbbr3/Tio2 Core/Shell Nanocrystals. *Adv Funct Mater* **2018**, *28* (1), 1704288. https://doi.org/10.1002/ADFM.201704288.

(24) Zhang, F.; Shi, Z.; Li, S.; Ma, Z.; Li, Y.; Wang, L.; Wu, D.; Tian, Y.; Du, G.; Li, X.; Shan, C. Synergetic Effect of the Surfactant and Silica Coating on the Enhanced Emission and Stability of Perovskite Quantum Dots for Anticounterfeiting. *ACS Appl Mater Interfaces* **2019**, *11* (31), 28013–28022. https://doi.org/10.1021/ACSAMI.9B07518.

(25) Guggisberg, D.; Yakunin, S.; Neff, C.; Aebli, M.; Günther, D.; Kovalenko, M. V.; Dirin, D. N. Colloidal CsPbX3 Nanocrystals with Thin Metal Oxide Gel Coatings. *Chemistry of Materials* **2023**, *35* (7), 2827–2834. https://doi.org/10.1021/ACS.CHEMMATER.2C03562.

(26) Wang, S.; Chen, D.; Xu, K.; Hu, J.; Liang, S.; He, K.; Zhu, H.; Hong, M. Boosting Stability and Inkjet Printability of Pure-Red CsPb(Br/I)3 Quantum Dots through Dual-Shell Encapsulation for Micro-LED Displays. *ACS Energy Lett* **2024**, *9* (6), 2517–2526. https://doi.org/10.1021/ACSENERGYLETT.4C00803.

(27) Cai, Y.; Yang, Y.; Dong, H.; Xuan, T.; Tang, X.; Xie, R. J. Pure Red CsPbBr 0.96 I 2.04 /SiO 2 Core/Shell Nanocrystals with Simultaneous High Efficiency and Stability for Mini-LEDs. *J Mater Chem C Mater* **2023**, *11* (28), 9486–9494. https://doi.org/10.1039/D3TC01362F.

(28) Cai, Y.; Yang, Y.; Dong, H.; Xuan, T.; Tang, X.; Xie, R. J. Pure Red CsPbBr0.96I2.04/SiO2 Core/Shell Nanocrystals with Simultaneous High Efficiency and Stability for Mini-LEDs. *J Mater Chem C Mater* **2023**, *11* (28), 9486–9494. https://doi.org/10.1039/D3TC01362F.

(29) Sun, C.; Zhang, Y.; Ruan, C.; Yin, C.; Wang, X.; Wang, Y.; Yu C Sun, W. W.; Zhang, Y.; Ruan, C.; Wang, Y.; Yu, W. W.; Yin, C.; Wang, X. Efficient and Stable White LEDs with Silica-Coated Inorganic Perovskite Quantum Dots. *Advanced Materials* **2016**, *28* (45), 10088–10094. https://doi.org/10.1002/ADMA.201603081.

(30) Mi, C.; Gee, G. C.; Lander, C. W.; Shin, D.; Atteberry, M. L.; Akhmedov, N. G.; Hidayatova, L.; DiCenso, J. D.; Yip, W. T.; Chen, B.; Shao, Y.; Dong, Y. Towards Non-Blinking and Photostable Perovskite Quantum Dots. *Nature Communications 2024 16:1* **2025**, *16* (1), 1–13. https://doi.org/10.1038/s41467-024-55619-7.

(31) Wang, B.; Lim, J. W. M.; Loh, S. M.; Mayengbam, R.; Ye, S.; Feng, M.; He, H.; Liang, X.; Cai, R.; Zhang, Q.; Kwek, L. C.; Demir, H. V.; Mhaisalkar, S. G.; Blundell, S. A.; Chien Sum, T. Weakly Confined Organic-Inorganic Halide Perovskite Quantum Dots as High-Purity Room-Temperature Single Photon Sources. *ACS Nano* **2024**, *18* (16), 10807–10817. https://doi.org/10.1021/ACSNANO.3C12311.

(32) Bodnarchuk, M. I.; Feld, L. G.; Zhu, C.; Boehme, S. C.; Bertolotti, F.; Avaro, J.; Aebli, M.; Mir, S. H.; Masciocchi, N.; Erni, R.; Chakraborty, S.; Guagliardi, A.; Rainò, G.; Kovalenko, M. V. Colloidal Aziridinium Lead Bromide Quantum Dots. *ACS Nano* **2024**, *18*, 28. https://doi.org/10.1021/ACSNANO.3C11579.

(33) Akkerman, Q. A.; Nguyen, T. P. T.; Boehme, S. C.; Montanarella, F.; Dirin, D. N.; Wechsler, P.; Beiglböck, F.; Rainò, G.; Erni, R.; Katan, C.; Even, J.; Kovalenko, M. V. Controlling the Nucleation and Growth Kinetics of Lead Halide Perovskite Quantum Dots. *Science (1979)* **2022**. https://doi.org/10.1126/SCIENCE.ABQ3616.

(34) Protesescu, L.; Yakunin, S.; Bodnarchuk, M. I.; Krieg, F.; Caputo, R.; Hendon, C. H.; Yang, R. X.; Walsh, A.; Kovalenko, M. V. Nanocrystals of Cesium Lead Halide Perovskites (CsPbX3, X = Cl, Br, and I): Novel Optoelectronic Materials Showing Bright Emission with Wide Color Gamut. *Nano Lett* **2015**, *15* (6), 3692–3696. https://doi.org/10.1021/nl5048779.

(35) Huang, Z.; Akrami, F.; Zhang, J.; Barlow, S.; Marder, S. R.; Ginger, D. S. Surface Passivation for Halide Optoelectronics: Comparing Optimization and Reactivity of Amino-Silanes with Formamidinium. *J Am Chem Soc* **2025**, *147* (46), 42918–42925. https://doi.org/10.1021/JACS.5C15574.

(36) Meng, C.; Yang, D.; Wu, Y.; Zhang, X.; Zeng, H.; Li, X. Synthesis of Single CsPbBr3@SiO2 Core–Shell Particles via Surface Activation. *J Mater Chem C Mater* **2020**, *8* (48), 17403–17409. https://doi.org/10.1039/D0TC03932B.

(37) Taddei, M.; Jariwala, S.; Westbrook, R. J. E.; Gallagher, S.; Weaver, A. C.; Pothoof, J.; Ziffer, M. E.; Snaith, H. J.; Ginger, D. S. Interpreting Halide Perovskite Semiconductor Photoluminescence Kinetics. *ACS Energy Lett* **2024**, *9* (6), 2508–2516. https://doi.org/10.1021/ACSENERGYLETT.4C00614.

(38) Yoon, H. C.; Kang, H.; Lee, S.; Oh, J. H.; Yang, H.; Do, Y. R. Study of Perovskite QD Down-Converted LEDs and Six-Color White LEDs for Future Displays with Excellent Color Performance. *ACS Appl Mater Interfaces* **2016**, *8* (28), 18189–18200. https://doi.org/10.1021/ACSAMI.6B05468.

(39) Zhang, Q.; Wang, B.; Zheng, W.; Kong, L.; Wan, Q.; Zhang, C.; Li, Z.; Cao, X.; Liu, M.; Li, L. Ceramic-like Stable CsPbBr3 Nanocrystals Encapsulated in Silica Derived from Molecular Sieve Templates. *Nature Communications 2020 11:1* **2020**, *11* (1), 1–9. https://doi.org/10.1038/s41467-019-13881-0.

(40) Zhu, C.; Marczak, M.; Feld, L.; Boehme, S. C.; Bernasconi, C.; Moskalenko, A.; Cherniukh, I.; Dirin, D.; Bodnarchuk, M. I.; Kovalenko, M. V.; Rainò, G. Room-Temperature, Highly Pure Single-Photon Sources from All-Inorganic Lead Halide Perovskite Quantum Dots. *Nano Lett* **2022**, *17*, 14. https://doi.org/10.1021/ACS.NANOLETT.2C00756.

(41) Palstra, I. M.; Koenderink, A. F. A Python Toolbox for Unbiased Statistical Analysis of Fluorescence Intermittency of Multilevel Emitters. *Journal of Physical Chemistry C* **2021**, *125* (22), 12050–12060. https://doi.org/10.1021/ACS.JPCC.1C01670.

(42) Watkins, L. P.; Yang, H. Detection of Intensity Change Points in Time-Resolved Single-Molecule Measurements. *Journal of Physical Chemistry B* **2005**, *109* (1), 617–628. https://doi.org/10.1021/JP0467548.

(43) Kuno, M.; Fromm, D. P.; Hamann, H. F.; Gallagher, A.; Nesbitt, D. J. "On"/"off" Fluorescence Intermittency of Single Semiconductor Quantum Dots. *J Chem Phys* **2001**, *115* (2), 1028. https://doi.org/10.1063/1.1377883.

(44) Gao, F.; Bajwa, P.; Nguyen, A.; Heyes, C. D. Shell-Dependent Photoluminescence Studies Provide Mechanistic Insights into the Off-Grey-On Transitions of Blinking Quantum Dots. *ACS Nano* **2017**, *11* (3), 2905–2916. https://doi.org/10.1021/ACSNANO.6B08040.

(45) Ye, M.; Searson, P. C. Blinking in Quantum Dots: The Origin of the Grey State and Power Law Statistics. *Phys Rev B Condens Matter Mater Phys* **2011**, *84* (12), 125317. https://doi.org/10.1103/PhysRevB.84.125317.

(46) Palstra, I. M.; de Buy Wenniger, I. M.; Patra, B. K.; Garnett, E. C.; Koenderink, A. F. Intermittency of CsPbBr3Perovskite Quantum Dots Analyzed by an Unbiased Statistical Analysis. *Journal of Physical Chemistry C* **2021**, *125* (22), 12061–12072. https://doi.org/10.1021/ACS.JPCC.1C01671.

(47) Crouch, C. H.; Sauter, O.; Wu, X.; Purcell, R.; Querner, C.; Drndic, M.; Pelton, M. Facts and Artifacts in the Blinking Statistics of Semiconductor Nanocrystals. *Nano Lett* **2010**, *10* (5), 1692–1698. https://doi.org/10.1021/NL100030E.

(48) Efros, A. L.; Nesbitt, D. J. Origin and Control of Blinking in Quantum Dots. *Nature Nanotechnology 2016 11:8* **2016**, *11* (8), 661–671. https://doi.org/10.1038/nnano.2016.140.

(49) Bruhn, B.; Qejvanaj, F.; Sychugov, I.; Linnros, J. Blinking Statistics and Excitation-Dependent Luminescence Yield in Si and CdSe Nanocrystals. *Journal of Physical Chemistry C* **2014**, *118* (4), 2202–2208. https://doi.org/10.1021/JP4100685.

(50) Zhu, C.; Nguyen, T.; Boehme, S. C.; Moskalenko, A.; Dirin, D. N.; Bodnarchuk, M. I.; Katan, C.; Even, J.; Rainò, G.; Kovalenko, M. V. Many-Body Correlations and Exciton Complexes in CsPbBr3 Quantum Dots. *Advanced Materials* **2023**, *35* (9), 2208354. https://doi.org/10.1002/ADMA.202208354.

(51) Yuan, G.; Ritchie, C.; Ritter, M.; Murphy, S.; Gómez, D. E.; Mulvaney, P. The Degradation and Blinking of Single CsPbI3 Perovskite Quantum Dots. *The Journal of Physical Chemistry C* **2017**, *122* (25), 13407–13415. https://doi.org/10.1021/ACS.JPCC.7B11168.

(52) Trinh, C. T.; Minh, D. N.; Ahn, K. J.; Kang, Y.; Lee, K. G. Verification of Type-A and Type-B-HC Blinking Mechanisms of Organic–Inorganic Formamidinium Lead Halide Perovskite Quantum Dots by FLID Measurements. *Scientific Reports 2020 10:1* **2020**, *10* (1), 1–8. https://doi.org/10.1038/s41598-020-58926-3.

(53) Yuan, G.; Gómez, D. E.; Kirkwood, N.; Boldt, K.; Mulvaney, P. Two Mechanisms Determine Quantum Dot Blinking. *ACS Nano* **2018**, *12* (4), 3397–3405. https://doi.org/10.1021/ACSNANO.7B09052.

(54) Galland, C.; Ghosh, Y.; Steinbrück, A.; Sykora, M.; Hollingsworth, J. A.; Klimov, V. I.; Htoon, H. Two Types of Luminescence Blinking Revealed by Spectroelectrochemistry of Single Quantum Dots. *Nature 2011 479:7372* **2011**, *479* (7372), 203–207. https://doi.org/10.1038/nature10569.

(55) Cordones, A. A.; Leone, S. R. Mechanisms for Charge Trapping in Single Semiconductor Nanocrystals Probed by Fluorescence Blinking. *Chem Soc Rev* **2013**, *42* (8), 3209–3221. https://doi.org/10.1039/C2CS35452G.

(56) Han, X.; Zhang, G.; Li, B.; Yang, C.; Guo, W.; Bai, X.; Huang, P.; Chen, R.; Qin, C.; Hu, J.; Ma, Y.; Zhong, H.; Xiao, L.; Jia Han, S. X.; Zhang, G.; Li, B.; Yang, C.; Guo, W.; Bai, X.; Chen, R.; Qin, C.; Hu, J.; Ma, Y.; Xiao, L.; Jia, S.; Huang, P.; Zhong, H. Blinking Mechanisms and Intrinsic Quantum-Confined Stark Effect in Single Methylammonium Lead Bromide Perovskite Quantum Dots. *Small* **2020**, *16* (51), 2005435. https://doi.org/10.1002/SMLL.202005435.

(57) Trinh, C. T.; Minh, D. N.; Ahn, K. J.; Kang, Y.; Lee, K. G. Organic-Inorganic FAPbBr 3 Perovskite Quantum Dots as a Quantum Light Source: Single-Photon Emission and Blinking Behaviors. *ACS Photonics* **2018**, *5* (12), 4937–4943. https://doi.org/10.1021/ACSPHOTONICS.8B01130.

(58) Eperon, G. E.; Jedlicka, E.; Ginger, D. S. Biexciton Auger Recombination Differs in Hybrid and Inorganic Halide Perovskite Quantum Dots. *Journal of Physical Chemistry Letters* **2018**, *9* (1), 104–109. https://doi.org/10.1021/ACS.JPCLETT.7B02805.

(59) Sampat, S.; Karan, N. S.; Guo, T.; Htoon, H.; Hollingsworth, J. A.; Malko, A. V. Multistate Blinking and Scaling of Recombination Rates in Individual Silica-Coated CdSe/CdS Nanocrystals. *ACS Photonics* **2015**, *2* (10), 1505–1512. https://doi.org/10.1021/ACSPHOTONICS.5B00423.

(60) Cho, K.; Yamada, T.; Tahara, H.; Tadano, T.; Suzuura, H.; Saruyama, M.; Sato, R.; Teranishi, T.; Kanemitsu, Y. Luminescence Fine Structures in Single Lead Halide Perovskite Nanocrystals: Size Dependence of the Exciton-Phonon Coupling. *Nano Lett* **2021**, *21* (17), 7206–7212. https://doi.org/10.1021/ACS.NANOLETT.1C02122.

(61) Zhu, C.; Feld, L. G.; Svyrydenko, M.; Cherniukh, I.; Dirin, D. N.; Bodnarchuk, M. I.; Wood, V.; Yazdani, N.; Boehme, S. C.; Kovalenko, M. V; Rainò, G.; Zhu, C.; Feld, L. G.; Svyrydenko, M.; Cherniukh, I.; Dirin, D. N.; Bodnarchuk, M. I.; Boehme, S. C.; Kovalenko, M. V; Rainò, G. Quantifying the Size-Dependent Exciton-Phonon Coupling Strength in Single Lead-Halide Perovskite Quantum Dots. *Adv Opt Mater* **2024**, 2301534. https://doi.org/10.1002/ADOM.202301534.

(62) Cho, K.; Sato, T.; Yamada, T.; Sato, R.; Saruyama, M.; Teranishi, T.; Suzuura, H.; Kanemitsu, Y. Size Dependence of Trion and Biexciton Binding Energies in Lead Halide Perovskite Nanocrystals. *ACS Nano* **2023**, *18*, 45. https://doi.org/10.1021/ACSNANO.3C11842.

(63) Gumbsheimer, P.; Conradt, F.; Behovits, Y.; Huber, S.; Hinz, C.; Negele, C.; Mecking, S.; Seletskiy, D. V.; Leitenstorfer, A. Enhanced Determination of Emission Fine Structure and Orientation of Individual Quantum Dots Based on Correction Algorithm for Spectral Diffusion. *J Phys D Appl Phys* **2021**, *54* (15), 155106. https://doi.org/10.1088/1361-6463/ABDA83.

(64) Hinkle, A.; Tsao, C.; Duell, A.; Utzat, H. Multi-Dimensional Photon-Correlations Reveal Triexciton Features in Single Perovskite Quantum Dots. **2025**. https://doi.org/10.48550/arXiv.2509.12461.

(65) Griscom, D. L. Self-Trapped Holes in Amorphous Silicon Dioxide. *Phys Rev B* **1989**, *40* (6), 4224. https://doi.org/10.1103/PhysRevB.40.4224.

(66) Kimmel, A.; Sushko, P.; Shluger, A.; Bersuker, G. Positive and Negative Oxygen Vacancies in Amorphous Silica. *ECS Trans* **2009**, *19* (2), 3–17. https://doi.org/10.1149/1.3122083\.

(67) Farnesi Camellone, M.; Reiner, J. C.; Sennhauser, U.; Schlapbach, L. Formation of Electron Traps in Amorphous Silica. *Phys Rev B Condens Matter Mater Phys* **2007**, *76* (12), 125205. https://doi.org/10.1103/PHYSREVB.76.125205.

(68) Biermann, A.; Aubert, T.; Baumeister, P.; Drijvers, E.; Hens, Z.; Maultzsch, J. Interface Formation during Silica Encapsulation of Colloidal CdSe/CdS Quantum Dots Observed by in Situ Raman Spectroscopy. *Journal of Chemical Physics* **2017**, *146* (13). https://doi.org/10.1063/1.4979515/212165.

(69) Pan, Q.; Hu, Y.; Qiu, Y.; Liu, S.; Wang, Y.; Chen, J.; Zhang, Q.; Cao, M. Ligand Engineering for Mitigating Exciton-Phonon Coupling in Mixed Halide Perovskite Nanocrystals. *Journal of Physical Chemistry Letters* **2024**, *15* (12), 3441–3449. https://doi.org/10.1021/ACS.JPCLETT.4C00399.

(70) Xu, K.; Vickers, E. T.; Rao, L.; Lindley, S. A.; Allen, A. C.; Luo, B.; Li, X.; Zhang, J. Z. Synergistic Surface Passivation of CH 3 NH 3 PbBr 3 Perovskite Quantum Dots with Phosphonic Acid and (3-Aminopropyl)Triethoxysilane. *Chemistry - A European Journal* **2019**, *25* (19), 5014–5021. https://doi.org/10.1002/CHEM.201805656.

(71) Protesescu, L.; Yakunin, S.; Bodnarchuk, M. I.; Bertolotti, F.; Masciocchi, N.; Guagliardi, A.; Kovalenko, M. V. Monodisperse Formamidinium Lead Bromide Nanocrystals with Bright and Stable Green Photoluminescence. *J Am Chem Soc* **2016**, *138* (43), 14202–14205. https://doi.org/10.1021/JACS.6B08900.

Appendix A: Supporting Information for Ligand Equilibrium Influences Photoluminescence Blinking in $CsPbBr_3$: A Change Point Analysis of Widefield Imaging Data

Shaun Gallagher, Jessica Kline, Farzaneh Jahanbakhshi, James C. Sadighian, Ian Lyons, Gillian Shen, Benjamin F. Hammel, Sadegh Yazdi, Gordana Dukovic, Andrew M. Rappe, and David S. Ginger

This appendix is adapted from: ACS Nano 2024, 18, 19208−19219.
https://doi.org/10.1021/acsnano.4c04968.

Table of Contents

Methods

Chemicals

Cesium carbonate (Cs_2CO_3, 99.9% metals basis), octadecene (ODE, 90%), oleic acid (OA, ≥ 99%), oleylamine (OAm, 70%), diisooctylphosphinic acid (DOPA, 90%), trioctylphosphine oxide (TOPO, 99%), hexanes (anhydrous 95%), hexanes (≥ 95%), polystyrene (PS, MW 280,000), toluene (anhydrous 99.8%), octane (anhydrous ≥ 99%), acetone (90%), isopropyl alcohol (IPA, 90%) and acetonitrile (ACN, anhydrous 99.8%) were purchased from Millipore Sigma. Lecithin (90%) and lead (II) bromide ($PbBr_2$, 99.998% metals basis) were purchased from Alfa Aesar. ODE and OAm were degassed by freeze-pump-thaw method and stored in a glovebox at 0°C. Cs_2CO_3 was dried in a vacuum oven at 120°C for 8 hours and stored in a glovebox. All other chemicals were used as received.

Synthesis of oleic acid/oleylamine-capped $CsPbBr_3$ QDs

Oleic acid/oleylamine-capped $CsPbBr_3$ were synthesized according to Protesescu et al[1] and washed with ACN according to Zhang et al.[2] After washing, the resulting QDs were dissolved in 2 mL anhydrous hexanes, filtered through a 0.45 μm PTFE filter and stored at 0°C in a glovebox.

Synthesis of Lecithin-Capped $CsPbBr_3$ QDs

The precursor solutions for lecithin-capped $CsPbBr_3$ were prepared according to Akkerman et al.[3] The QDs were synthesized under ambient conditions in 6 mL hexanes with 160 μL of 0.04 M $PbBr_2$-TOPO, 320 μL of 0.2 M TOPO, 80 μL of 0.02 M Cs-DOPA. After 30 minutes of stirring at room temperature 80 μL of 0.13 M lecithin was added to the reaction. The QDs were subsequently washed by adding acetone in a 3:1 v:v ratio and centrifuged at 10,000 rpm for 5 minutes. The supernatant was discarded, and the precipitate was dissolved in 2 mL anhydrous hexanes, filtered through a 0.45 μm PTFE filter and stored at 0°C in a glovebox.

Ensemble Characterization

Absorbance spectra of the QD solutions were performed using a Perkin-Elmer Lambda 950 UV/Vis/NIR Spectrometer with a range of 400-700 nm with an integration time of 0.5 s.

Steady-state photoluminescence spectra were acquired using Perkin-Elmer Fluorescence Spectrometer LS 55. Spectra were collected using an excitation wavelength of 405 nm. The emission bandwidth was kept at 3 nm and dwell time at 0.2 s.

Time resolved photoluminescence measurements at 405 nm excitation were acquired using a commercial PicoQuant FluorTime 100 system with LDH-405 laser diode, a 405 nm picosecond pulsed diode laser. The repetition rate is controlled by an external trigger input from a PicoHarp PDL 800-B laser driver and was set to 5 MHz. A photomultiplier tube (PMT) detector was used in TCSPC mode with an instrumental response function (IRF) of approximately 400 ps. The instrument response function (IRF) was measured via laser scatter from a solution of colloidal silica (LUDOX). Concentration dependent photoluminescence was collected on the same instrument with a laser repetition rate of 50 MHz. TRPL lifetime analysis was performed using a custom Python IRF-reconvolution package. Lifetimes were fit using a stretch exponential decay (Equation A1).[4]

$$I(t) = A \exp\left(-\frac{t}{\tau_k}\right)^{\beta} + C \tag{A1}$$

Where A is the pre-exponential factor, τ_k is the lifetime of the decay, C is the background of the measurement and β is the distribution of decay rates. τ_{str}, the average lifetime of a stretch exponential, is calculated according to Equation A2 where Γ is the gamma function.[4]

$$\tau_{str} = \frac{\tau_k}{\beta}\Gamma\left(\frac{1}{\beta}\right) \quad \text{(A2)}$$

The series of QD solutions prepared for TRPL and concentration dependent TRPL are described in Table A5.

Photoluminescence quantum yield measurements (PLQY) were performed on a commercial integrating sphere system (Hamamatsu Photonics K.K). PLQY values are determined using a white light source (Hamamatsu Mercury Xenon Lamp) and a monochromator for wavelength selection (405 nm) as the excitation source to illuminate the samples in an integrating sphere (Hamamatsu Photonics K.K). The optical density of samples was kept below 0.1 at the excitation wavelength to minimize reabsorption effects. Spectral correction was performed using a calibrated white light source (Ocean Insight HL-3P-INT-CAL) to correct for the responsivity of the detector. PLQY was calculated using the following formula:

$$PLQY = \frac{I_{em,\ sample} - I_{em,\ blank}}{I_{ex,\ blank} - I_{ex,\ sample}} * 100 \quad \text{(A3)}$$

Where $I_{em,sample}$ and $I_{em,blank}$ are the integrated area under the curve in the emission region (450-600 nm) of the sample and the neat hexane blank, respectively. The $I_{ex,sample}$ and $I_{ex,blank}$ are the integrated area under the curve in the excitation region (395-415 nm) of the sample and the neat hexane blank respectively.

Widefield Microscopy Sample Preparation

Low fluorescence glass coverslips (VistaVision #1.5 22x22 mm, VWR) were cleaned through a sequential sonication of 10 minutes in soap solution, de-ionized water (x2), acetone and IPA. Each side of the coverslips were ozone cleaned for 23 minutes before spin coating.

Low concentration QD solutions were prepared in 5 wt% PS in toluene via serial dilutions. For oleic acid/oleylamine-capped QDs 2 µL of stock QD solution were added to 2 mL of PS-toluene (solution $A_{\text{oleic acid/oleylamine}}$). 200 µL of solution $A_{\text{oleic acid/oleylamine}}$ were added to 2 mL of PS-toluene (solution $B_{\text{oleic acid/oleylamine}}$). For lecithin-capped QDs 1 µL of stock QD solution were added to 2 mL of PS-toluene (solution A_{lec}). 100 µL of solution A_{lec} were added to 2 mL of PS-toluene (solution B_{lec}). 100 µL of solution B_{lec} were added to 2 mL of PS-toluene (solution C_{lec}). Single QDs films were prepared via spin coating solution $B_{\text{oleic acid/oleylamine}}$ (60 µL) or solution C_{lec} (60 µL) onto the cleaned coverslips at 2,000 rpm for 40 seconds. The films were stored in a glovebox until measurement.

Widefield Microscopy

Widefield microscopy measurements were performed on a Nikon TE2000 inverted optical microscope using a CFI Super Fluor 40x Oil immersion objective (NA = 1.3), with Olympus F immersion oil. The illumination source was a 415 nm LED (SOLIS-415C, Thor Labs) at a power density of 9 mW/cm^2. The following filters were used for the measurement: ET510/80m (Chroma), FF01-424/SP-25 (Semrock) and ZT442rdc (Chroma) mounted in Chroma Laser TIRF for Nikon TE2000/T filter cube. Videos of the sample photoluminescence in time were collected on a Prime 95B (Photometrics) camera

for 6 minutes and 40 seconds (8000 total images) with an integration time of 50 ms per image. Individual QD blinking traces were extracted from the videos using a custom-built Python package for selecting bright objects from a dark background.[5] Briefly, individual quantum dots were selected using the Laplacian of Gaussian method to automatically identify bright single particles from the mean image. The image coordinates of these identified particles were used to extract the relevant single particle time traces from the image sequence for further analysis. The efficacy of particle identification was assessed by constricting the microscope field of view to rule out false positive selections (Figure A21).

Analysis of Blinking Traces Using Change Point Analysis

We used a version of Change Point Analysis (CPA) adapted for a Gaussian-distributed time series. Our home-built Python CPA package is based on the equations published by Yang et al.[6] A more detailed explanation of our CPA package can be found under the heading "Change Point Analysis to Blinking Statistics"– including a confusion matrix quantifying the performance of our CPA package on synthetically generated blinking data (Figure A22) and a detailed breakdown of how we extract our main blinking statistics from CPA fit traces. Our particle selection and CPA code is publicly available at: https://github.com/GingerLabUW/Widefield-CPA.

Computational Methods

To investigate the passivation of different types of adjacent and non-adjacent vacancies, nonstoichiometric Cs-terminated slabs with a vacuum of ~15 Å were constructed from 2x1, 1x2, and 2x2 replications (corresponding to vacancy-pair types i-ii, iii and iv, respectively) of the PBE-relaxed conventional lattice of orthorhombic $CsPbBr_3$ (8.19 Å, 8.54 Å, 11.99 Å), shown in Figure 2.5a. DFT calculations were performed using the Quantum Espresso suite of codes, [70] whereby energetically minimized atomic structures were obtained using the Perdew–Burke–Ernzerhof (PBE) formulation.[7] Ultrasoft pseudopotentials were used to describe the interaction between the valence electrons and the ionic cores. Kohn–Sham orbitals were expanded in a plane wave basis set with a kinetic-energy cutoff of 60 Ry and a density cutoff of 420 Ry. Van der Waals interactions were considered by applying the empirical D3 dispersion correction scheme of Grimme.[8] Band gaps and partial density of states were calculated with PBE[7] , including spin-orbit coupling (SOC) effect,[9] that is known to strongly influence the position of band edges in lead-containing halide perovskites. Although PBE+SOC is not expected to reproduce the experimental gap of this material, we applied SOC to ensure that the band edges and the trap states near them were captured properly. An explicit solvent model was employed to simulate solvation effects, providing a more realistic representation that, unlike implicit models, includes direct and specific interactions between the solvent and solute. A detailed explanation of these calculations can be found in the supporting information.

Transmission electron microscopy (TEM) and scanning transmission electron microscopy (STEM)

TEM was performed with a FEI Tecnai G2 20 S-Twin operated at 200kV. Aberration-corrected STEM was performed with a Thermo Fisher Scientific Titan Themis operated at 300kV. Samples were prepared by drop-casting solutions of CsPbBr3 QDs onto ultrathin carbon film TEM grids (Ted Pella, Prod # 01824, ultrathin carbon film on lacey carbon support film, 400 mesh, Cu). To minimize air exposure, grid prep was performed in a glovebox with an argon atmosphere. After drop-casting, the grids were dried under vacuum in the glovebox antechamber for roughly 30 min, before being transferred back into the glovebox, sealed in an air-tight container, and transported to the microscopy facility.

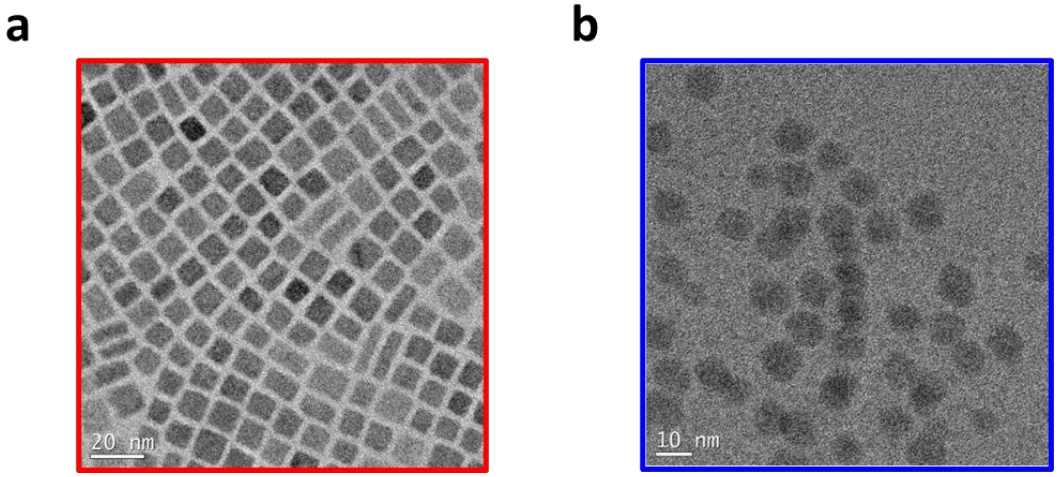

Figure A1: TEM images of **a)** OA/OAm-capped quantum dots showing a cubic crystal habit and **b)** lecithin-capped quantum dots showing a spherical crystal habit

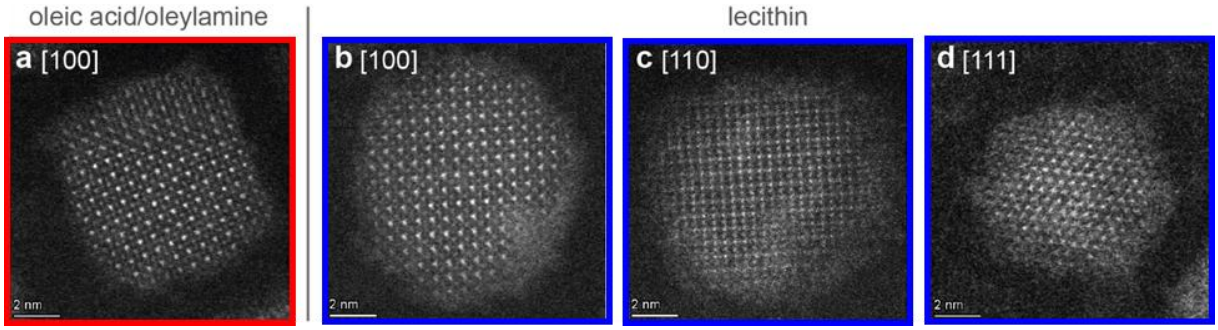

Figure A2: HAADF-STEM images of $CsPbBr_3$ capped with **a)** OA/OAM and **b-d)** lecithin ligands. The cuboidal morphology of the OA/OAM-capped QDs leads to preferential orientation down the [100] direction. At high resolution the rhombicuboctahedral morphology of the "spherical" lecithin-capped QDs allows for orientation down the b) [100], c) [110], and d) [111] directions.

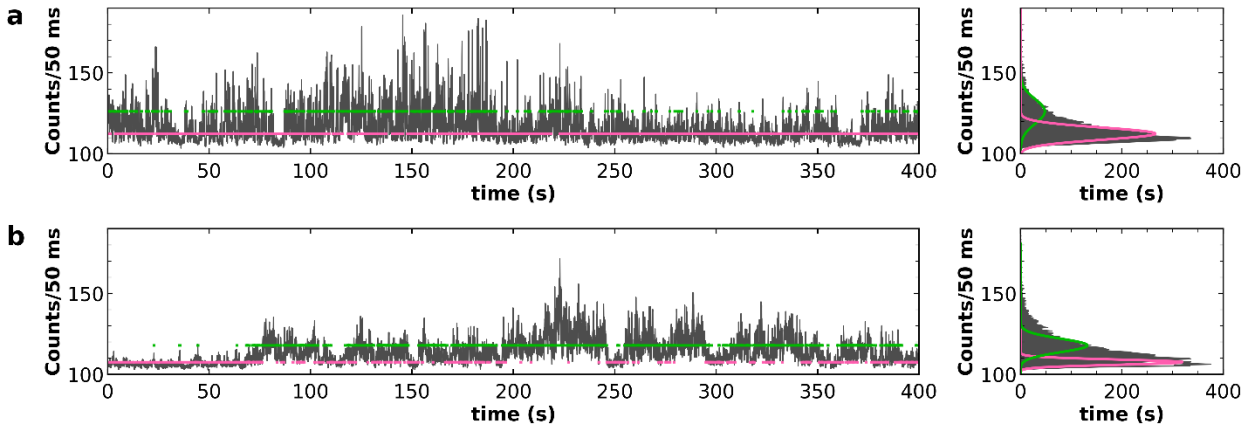

Figure A3: Example blinking traces for OA/OAm-QDs Randomly selected from the sample size showing the CPA identified intensity trajectories. Both traces have been fit to two average intensity-levels (pink and green).

Table A1: Ensemble characteristics of different lecithin synthetic batches. Each of these five batches was used in this study.

	Absorption Band Edge (nm)	PL Maximum (nm)	PL Linewidth (nm)	PLQY (%)
LEC 1	503	505	19	97
LEC 2	505	508	19	97
LEC 3	505	507	17	98
LEC 4	507	509	16	94
LEC 5	507	508	18	93

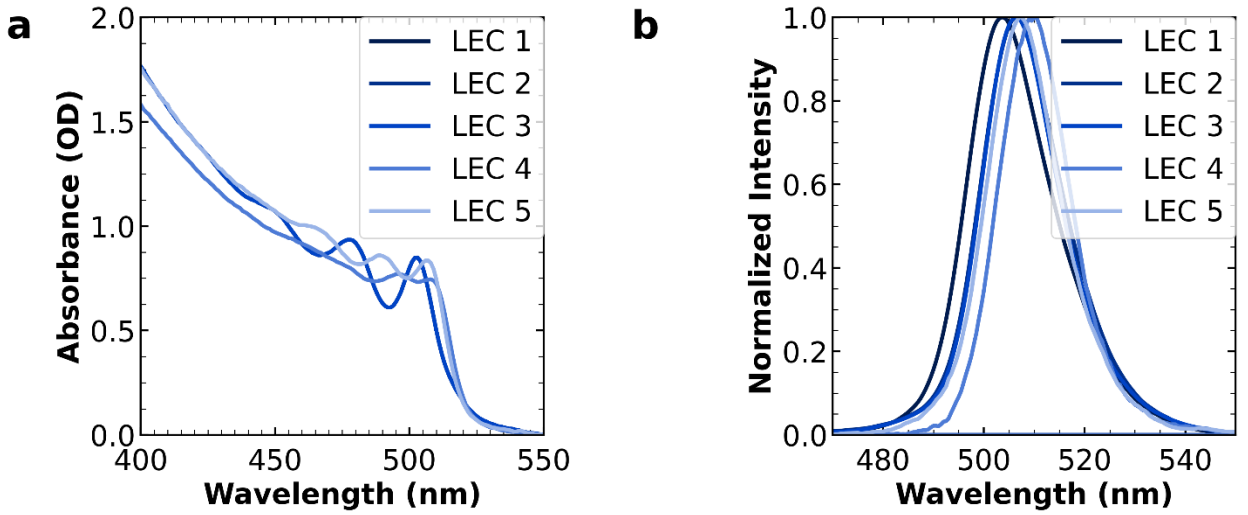

Figure A4: Ensemble characteristics of different lecithin synthetic batches a) absorption spectra of the five lecithin synthetic batches used in this study **b)** PL of five lecithin synthetic batches used in this study

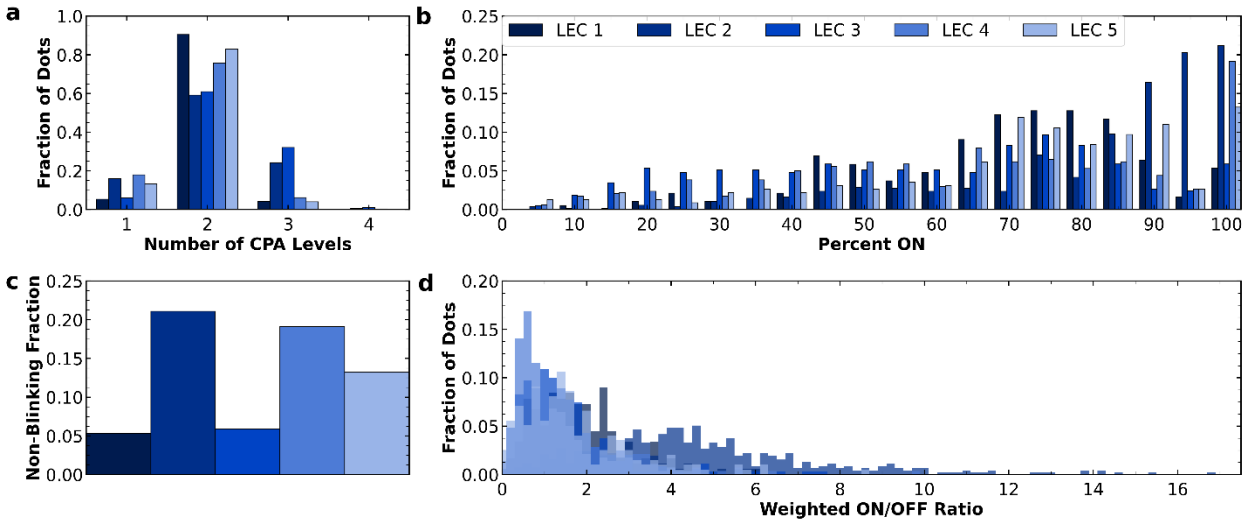

Figure A5: Comparisons of blinking behavior lecithin synthetic batches across our four major blinking metrics. These statistics are comprised of 188, 553, 374, 340 and 227 QDs for batches 1-5 respectively **a)** number of

intensity levels fit to each blinking trace by CPA. The average CPA levels are 2.0 ± 0.3, 2.1 ± 0.6, 2.2 ± 0.6, 1.9 ± 0.5 and 1.9 ± 0.4 for batches 1-5 respectively **b)** percent of the trace duration that each QD spends ON. The average ON percentages are 66 ± 17%, 77 ± 20%, 53 ± 24%, 56 ± 23% and 64 ± 22% for batches 1-5 respectively **c)** non-blinking fraction of QDs in each batch, 0.053, 0.22, 0.059, 0.19 and 0.13 for batches 1-5 respectively and **d)** the weighted ratio of expected time spent ON to expected time spent OFF

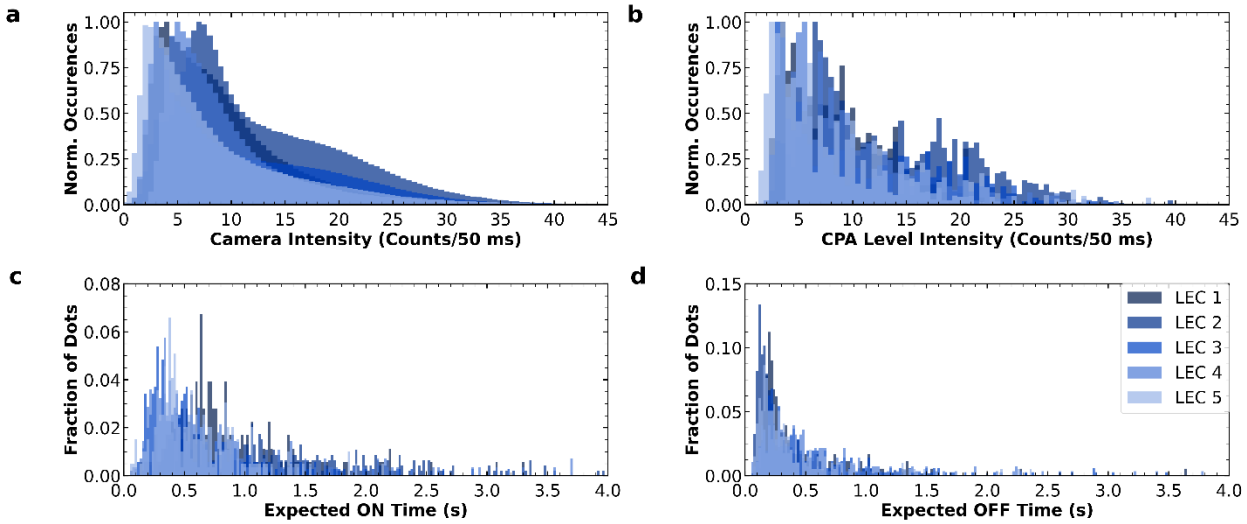

Figure A6: Comparison of blinking behavior between lecithin synthetic batches across four additional metrics **a)** distribution of intensities in the blinking traces according to the camera **b)** distribution of intensities in the blinking traces according to the CPA fits **c)** distribution of the expected ON times from power-law dynamics and **d)** distribution of the expected OFF times from power-law dynamics.

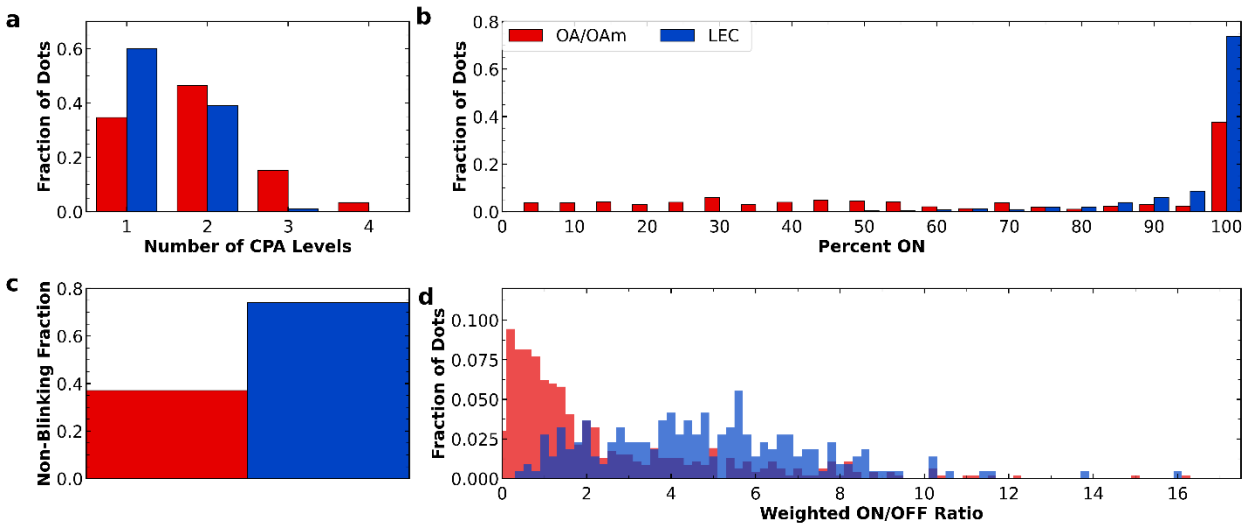

Figure A7: Comparisons of blinking behavior between additional OA/OAm and lecithin synthetic batches across our four major blinking metrics. These data were obtained at an integration time of 200 ms using a 100x NA 0.95 objective. These statistics are comprised of 716 OA/OAm QDs and 543 lecithin QDs. **a)** number of intensity levels fit to each blinking trace by CPA. The average CPA levels are 1.8 ± 0.8 and 1.4 ± 0.5 for OA/OAm and lecithin respectively **b)** percent of the trace duration that each QD spends ON. The average ON percentages are 44 ± 28% and 87 ± 13% for OA/OAm and lecithin respectively **c)** non-blinking fraction of QDs in each batch, 0.38 and 0.73 for OA/OAm and lecithin respectively and **d)** the weighted ratio of time spent ON to time spent OFF

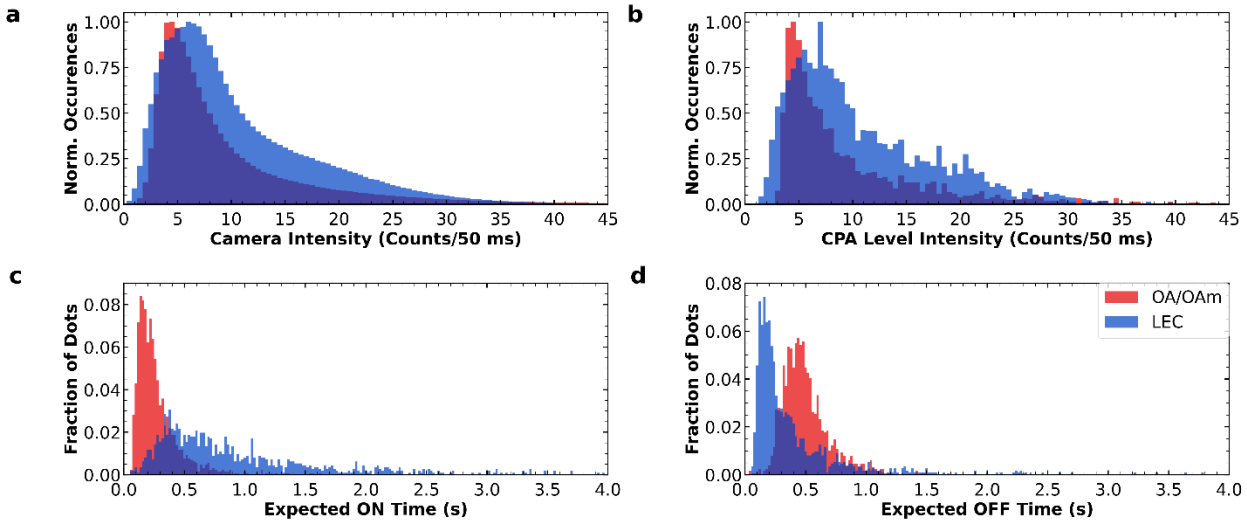

Figure A8: Comparison of blinking behavior between the OA/OAm- and lecithin- capped QDs across four additional metrics **a)** distribution of intensities in the blinking traces according to the camera **b)** distribution of intensities in the blinking traces according to the CPA fits **c)** distribution of the expected ON times from power-law dynamics and **d)** distribution of the expected OFF times from power-law dynamics.

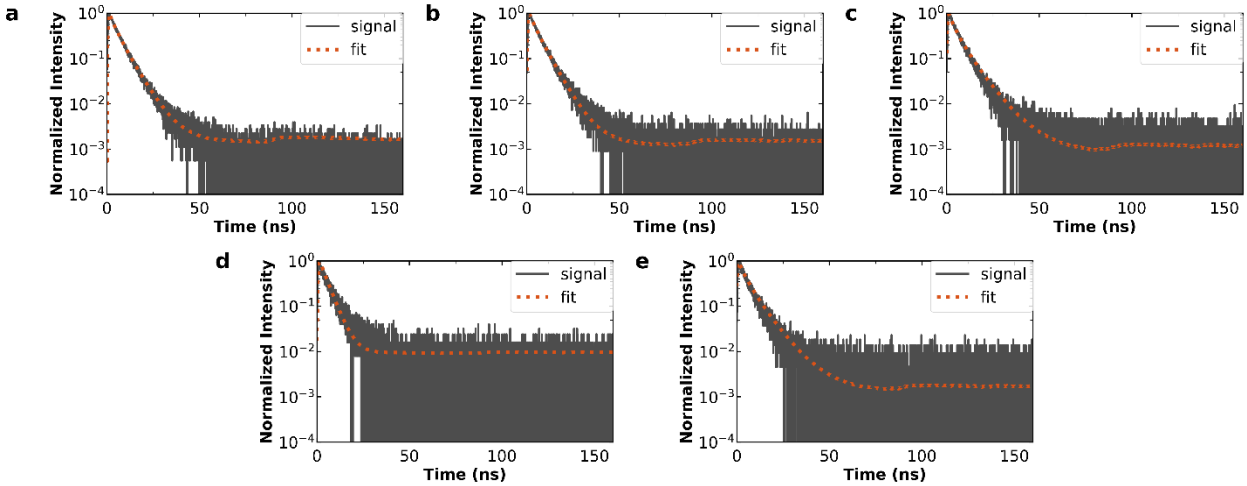

Figure A9: TRPL stretch-exponential fits for lecithin QDs as a function of concentration (see Table A1) **a)** solution 1: τ_{str} = 4.43 ns, β = 0.78, R^2 = 0.994 **b)** solution 2: τ_{str} = 4.71 ns, β = 0.87, R^2 = 0.998 **c)** solution 3: τ_{str} = 4.52 ns, β = 0.74, R^2 = 0.985 **d)** solution 4: τ_{str} = 4.90 ns, β = 0.78, R^2 = 0.960 and **e)** solution 9: τ_{str} = 4.50 ns, β = 0.76, R^2 = 0.982

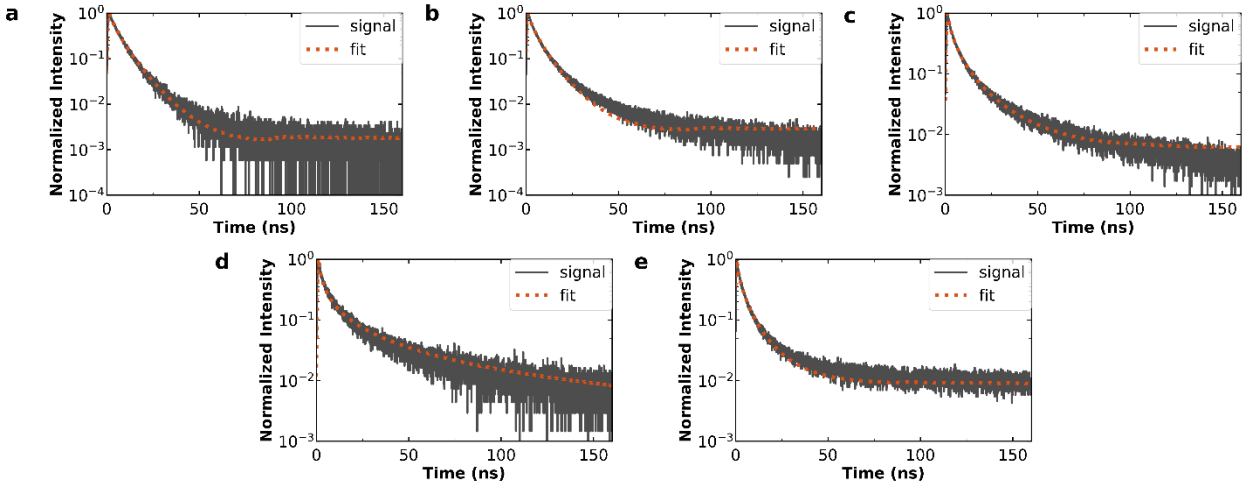

Figure A10: TRPL stretch-exponential fits for OA/OAm QDs as a function of concentration (see Table A1) **a)** solution 1: τ_{str} = 4.95 ns, β = 0.78, R^2 = 0.998 **b)** solution 2: τ_{str} = 4.08 ns, β = 0.67, R^2 = 0.985 **c)** solution 3: τ_{str} = 2.81 ns, β = 0.45, R^2 = 0.993 **d)** solution 4: τ_{str} = 2.51 ns, β = 0.43, R^2 = 0.980 and **e)** solution 9: τ_{str} = 2.08 ns, β = 0.45, R^2 = 0.992

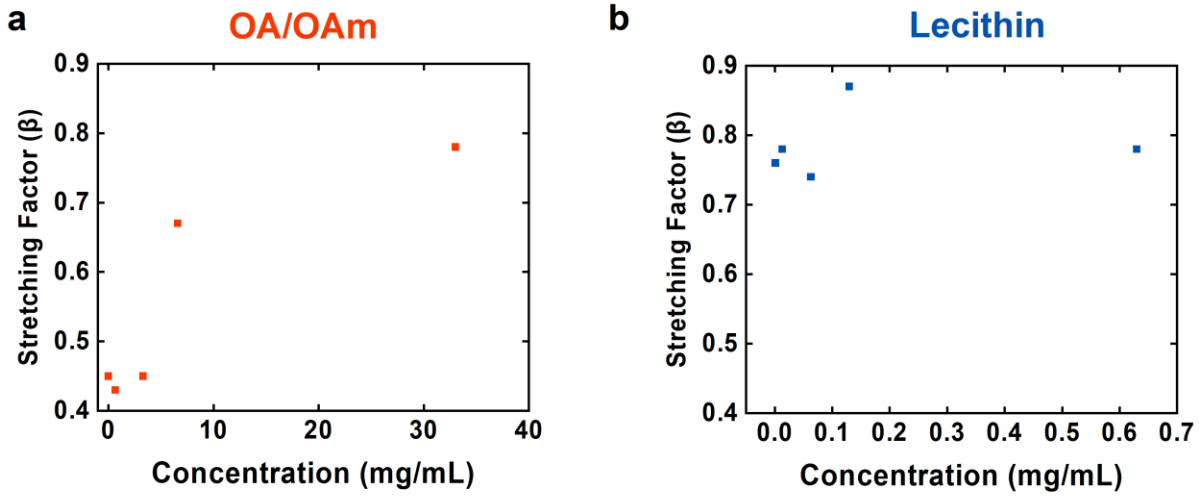

Figure A11: Comparison of stretch exponential beta-factors for concentration dependent lifetime data for **a)** OA/OAm- and **b)** lecithin- capped QDs. Beta-factors are taken from the lifetime fits shown in Figures A8 and A9 respectively.

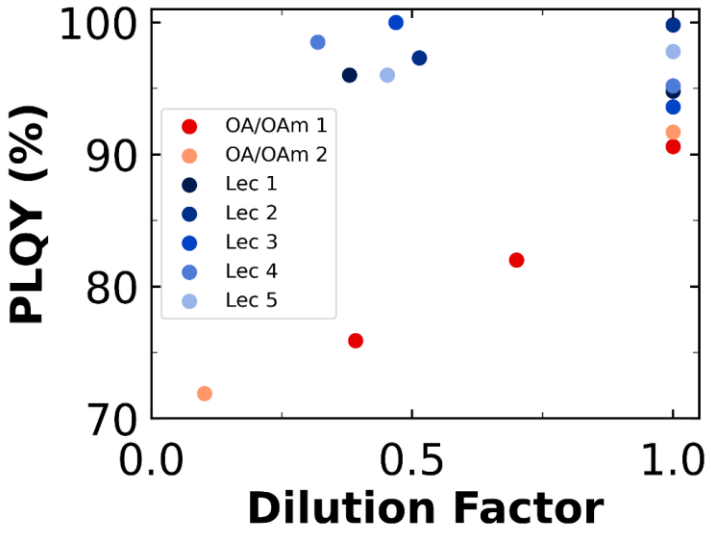

Figure A12: PLQY vs dilution factor for OA/OAm- and lecithin- capped QD solutions at concentrations measurable in an integrating sphere PLQY system.

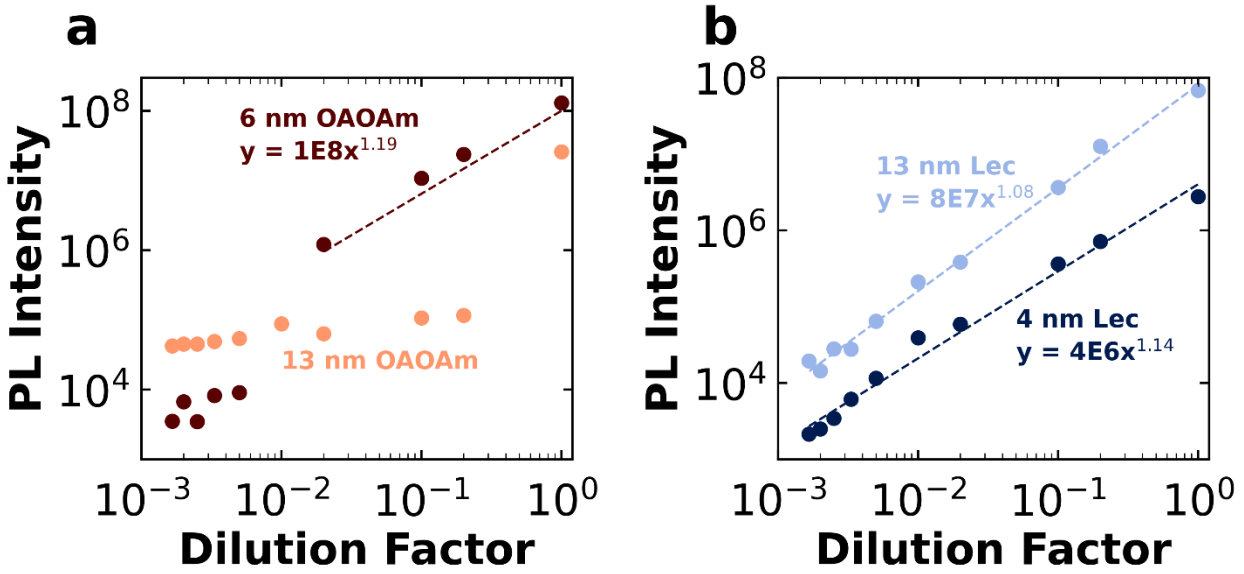

Figure A13: PL linearity for additional QD sizes. a) 6 nm (FWHM = 25 nm, PLQY = 90%) and 13 nm (FWHM = 22 nm, PLQY = 75%) OA/OAm-capped QDs **b)** 4 nm (FWHM = 30 nm, PLQY = 95%) and 13 nm (FWHM = 20 nm, PLQY = 98%) lecithin-capped QDs

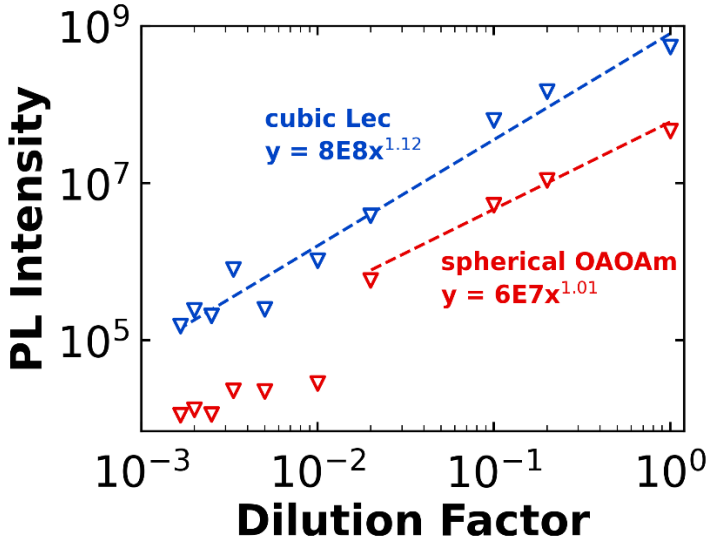

Figure A14: PL linearity for different QD morphologies. Cubic lecithin-capped QDs[10] (FWHM = 20 nm, PLQY = 60%) and spherical OA/OAm-capped QDs (FWHM = 21 nm, PLQY = 80%)

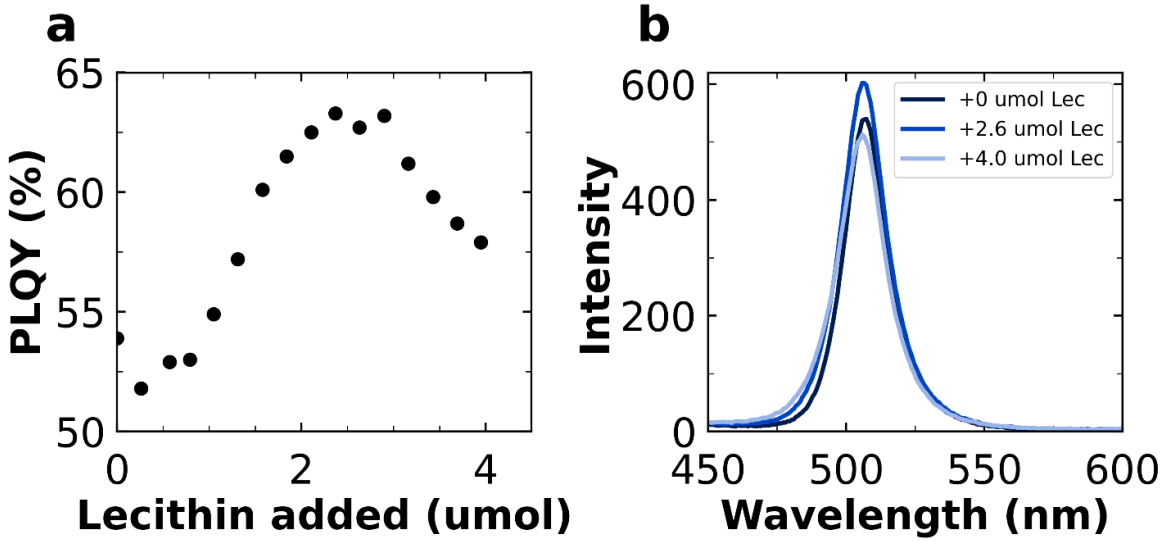

Figure A15: Evidence of etching with excess ligand addition a) PLQY vs. lecithin addition for low surface quality CsPbBr3 QDs (starting PLQY 52%). **b)** Blue shift of PL peak position with surface etching in the presence of excess ligand.

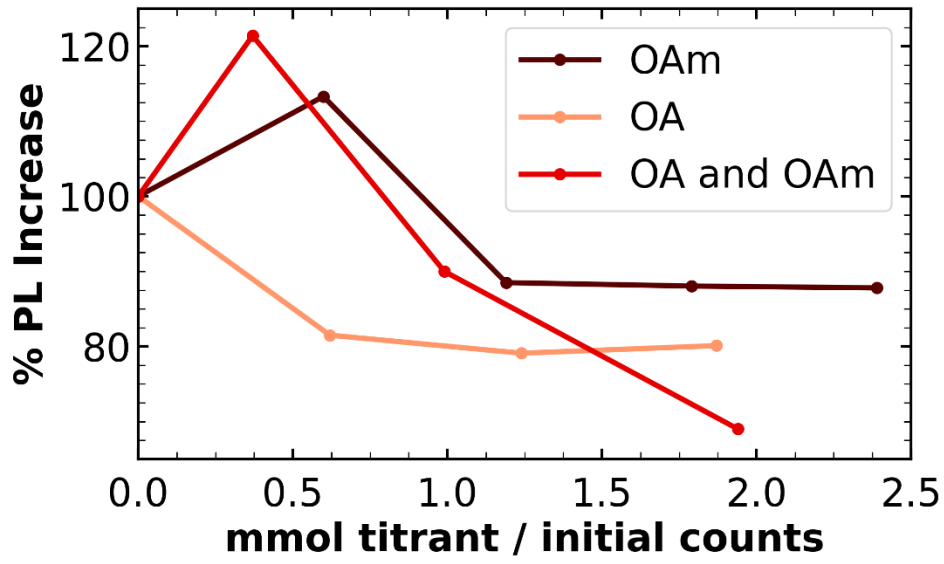

Figure A16: PL increase resulting from the addition of excess ligand to a widefield PL concentration solution of OA/OAm-$CsPbBr_3$ QDs comparing the addition of neat OAm to neat OA and a 1:1 (v:v) mixture of OA and OAm

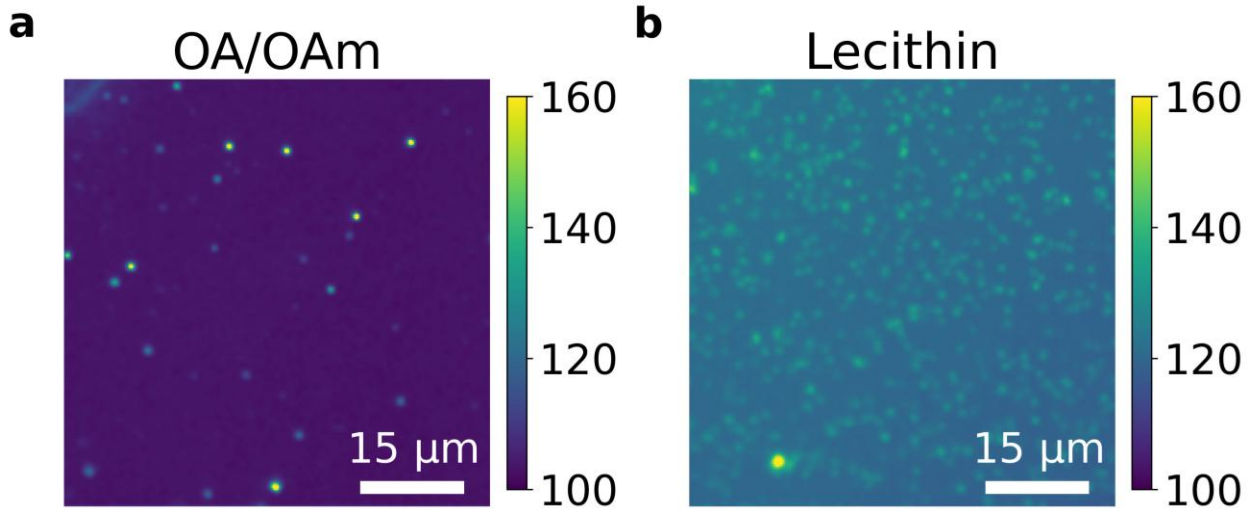

Figure A17: Widefield PL images of **a)** OA/OAm QDs and **b)** lecithin QDs. The sample solutions were prepared identically via serial dilution from stock solutions of the same optical density. The images correspond to samples made from solutions $B_{OA/OAm}$ and B_{lec} respectively.

Computational Details

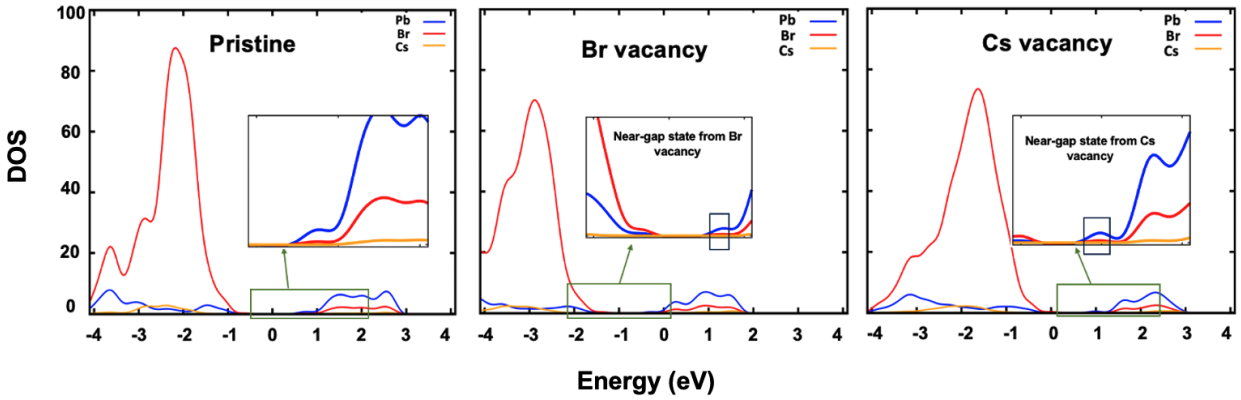

Figure A18: Density of states (DOS) of Cs-terminated slabs of CsPbBr3. Calculations were performed at the PBE level with spin orbit coupling (SOC) effects on top of PBE-relaxed structures of the pristine slab (a) as well as slabs containing $v\bullet_{Br}$ (b) and v'_{Cs} (c). Near gap states due to the presence of v•Br and v'Cs are observed and marked with rectangles in the insets of panels b and c.

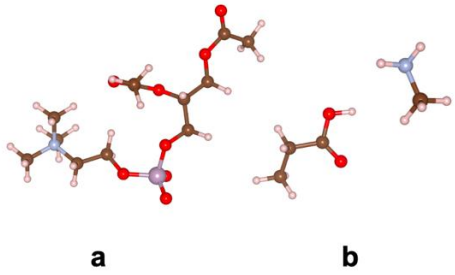

Figure A19: Simplified/truncated forms of the bidentate ligand and monodentate ligand pair used for computational purposes. Truncated lecithin (a), methylamine and propionic acid (b).

Table A2: Calculated binding energies (eV), including solvent effects, corresponding to the single (OAm or OA) and binary monodentate (OAm/OA) ligands passivating the pristine surface. OAm and OA correspond to oleylamine and oleic acid binding the OA/OAm-passivated pristine slab, while OAm* and OA* represent oleylamine and oleic acid binding the OA^-/OAm^+-passivated defective surface.

Passivating ligand(s)	OA/OAm	OAm	OA	OAm*	OA*
Solvated Binding Energy (eV)	-0.42	-0.17	-0.65	-0.25	-0.67

Table A3: Calculated binding energies (eV) corresponding to the binary monodentate (OAm^+/OA^-) and the bidentate ligand (lecithin) passivating different types of surface vacancy pairs (shown in Main Text Figure 2.5d)

Vacancy type	**Type *i***	**Type *ii***	**Type *iii***	**Type *iv***
OAm^+/OA^-	-1.95	-1.88	-1.91	-2.07
Lecithin	-3.22	-3.17	-2.96	-2.40

Reaction Mechanism and Binding Energy (BE) Calculation

$$\begin{aligned} &\text{lecithin} + * \rightarrow * - \text{lecithin} && \text{(a)} \\ &(\text{OAm}^+ - \text{OA}^-) + * \rightarrow (* - \text{OAm}^+ - \text{OA}^-) && \text{(b)} \\ &\text{BE} = E_{(*-\text{lig})} - E_{\text{lig}} - E_* && \text{(c)} \end{aligned} \quad \text{(A4)}$$

To compare energetics of lecithin and (OAm^+-OA^-) binding the QD surface, we considered comparable binding mechanisms (Equations A4a and A4b) whereby comparatively to the zwitterionic ligand, the monodentate ligand pair (OAm^+-OA^-) binds the quantum dot surface (* in Equation A4) as a complex. The corresponding binding energies can therefore be calculated per Equation A4c, where E_* and $E_{(*-\text{lig})}$ are DFT energies of the bare and ligand-passivated slabs and E_{lig} represents the energy of either lecithin or the (OAm^+-OA^-) complex.

Solvation Effects on Ligand Binding the QD Surfaces

In principle, the rate of reactions can be controlled by the solvent's polarity, and therefore its dielectric constant, as well as its acceptor (AN) or donor number (DN). To account for the effect of ACN and acetone which are both polar aprotic solvents and used in the washing process of our synthesized QDs, we employed an explicit solvent model.

$$E_{\text{solvn}}{}^{x*\text{solv}} = E_{(*-\text{ligand})}{}^{x*\text{solv}} - E_{(*-\text{ligand})} - x.E_{\text{solv}} \quad \text{(A5)}$$

$$\text{BE}\,|_{\text{solv}} = \text{BE} + (E_{\text{solvn}})_{(*-\text{lig})} - (E_{\text{solvn}})_{\text{lig}} - (E_{\text{solvn}})_* \quad \text{(A6)}$$

We used periodic solvated slab models including a layer of liquid solvents on top of the slabs that were used for binding energy calculations. We first attained the number of solvent molecules required to sufficiently solvate the ligands as well as bare and passivated slabs, by gradually adding solvent molecules (x) to the system and calculating the solvation energy ($E_{\text{solvn}}{}^{x*\text{solv}}$) per Equation A5. In this equation, $x.E_{\text{solv}}$, represents the energy of x solvent molecules in liquid phase, and $E_{(*-\text{ligand})}$ and $E_{(*-\text{ligand})}{}^{x*\text{solv}}$ are total energies of the passivated slab without solvent and containing x solvent molecules, respectively. As a representative, the onset of the plateau in Figures A13b and A13c shows the minimum number of solvent molecules required to sufficiently solvate the (OAm^+-OA^-)-passivated and lecithin-passivated slabs of $CsPbBr_3$. Accordingly, we used 10 and 20 solvents for the adjacent and non-adjacent (twice as large unit cell) vacancy cases, respectively. Finally, to obtain the net effect of solvation on the binding energy, we calculated the solvation energy for the ligand $(E_{\text{solvn}})_{\text{lig}}$, clean slab $(E_{\text{solvn}})_*$ and the ligand-passivated slab $(E_{\text{solvn}})_{(*-\text{lig})}$, and computed the binding energy in the presence of solvents ($\text{BE}\,|_{\text{solv}}$) by applying the obtained net solvation energy to the BE, per Equation A6.

Binding Energy Calculation of Mono-ligand Passivated Single-vacancy Surfaces

In addition to vacancy pairs, we studied Br^--rich and OAm^+-rich conditions where the single vacancy surface is passivated by a monodentate ligand. We calculated the BE of OAm^+ passivating $CsPbBr_3$ by gradually pulling the ligand off the surface and obtained the corresponding energy *vs*. distance plot (Figure A13a). E_d is the energy required to pull the ligand off the surface by a distance of d (Å), marked on the x-axis, d = 0 (Å) refers to the ligand binding the surface, and d = -1 (Å) corresponds to the ligand filling the vacant site. It can be seen that OAm^+ strongly binds the surface (BE = -4.1 eV) which can primarily be attributed to the size of the ligand and therefore, the capability of the ammonium moiety to access and occupy the vacant site (v'_{Cs}).

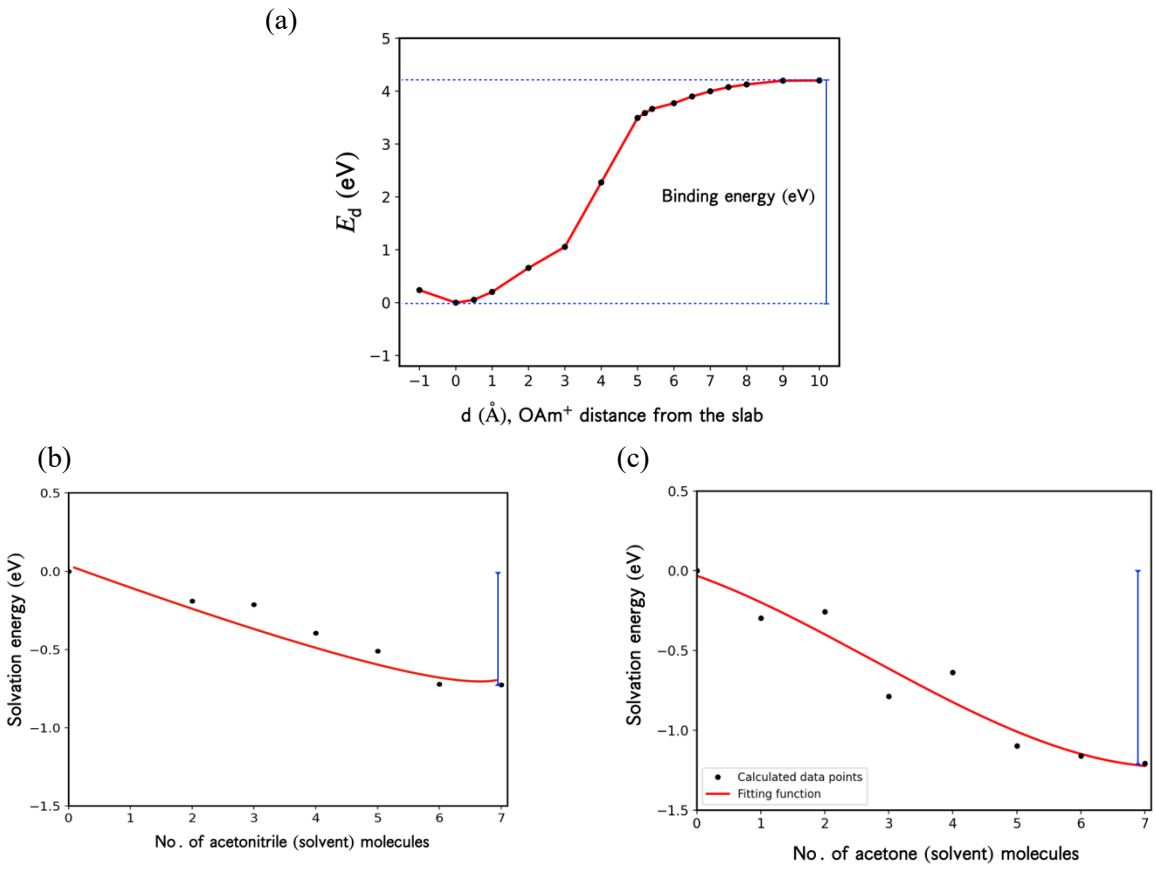

Figure A20: Binding Energy as a function of solvation and distance (a) Binding energy calculation of the OAm^+-passivated slab containing a single Cs vacancy (v'_{Cs}). E_d is the energy required to pull the ligand off the surface by d (Å) (shown on the x-axis), $d = 0$ (Å) refers to the ligand binding the surface, and $d = -1$ (Å) corresponds to the ligand filling the vacant site. (b) Solvation energies versus the number of solvent molecules, calculated per Equation A6, for (OAm^+-OA^-)-passivated and (c) lecithin-passivated slabs of $CsPbBr_3$ are shown. Solid blue lines indicate the solvation energies at the onset of the plateau corresponding to the number of solvent molecules sufficient to solvate the passivated slabs.

Experimental Equilibrium Constants and Binding Energies

To better understand the calculated binding energies in the context of the system – we compute the ligand binding equilibrium constant from both the DFT binding energies (Main Text Figure 2.5d) and the experimental PL dilution results (Main Text Figure 2.4c).

The ligand binding equilibrium constant from DFT was calculated with Equation A7:

$$\Delta G° = -RT\ln(K_{ligand}) \quad \text{(A7)}$$

where $\Delta G°$ is the binding energy in J/mol, R is the gas constant (8.314 J mol^{-1} K^{-1}), T is the temperature and K_{ligand} is the ligand binding equilibrium constant.

The experimental ligand binding equilibrium constant was calculated through a series of steps. First to determine the ligand and nanocrystal solutions we dried 2 mL of a 290 nM solution of the OA/OAm-capped QDs in a centrifuge tube of known weight and measured the total QD and ligand mass to be 3 ± 1 mg. The total mass contribution from the OA/OAm-capped QDs was calculated to be 1 mg so the maximum ligand contribution was 2 mg. The dry mass of 2 mL of a 140 nM solution of lecithin-capped QDs was measured

to be 2 ± 1 mg. The total mass contribution from the lecithin-capped QDs was calculated to be 0.3 mg so the maximum ligand contribution was 1.7 mg.

Assuming 100 binding sites per QD and that the QDs start as completely bound, the initial concentrations at the drop-off point (solution 6, 0.04 nM) were calculated to be [OA/OAm-QD] = 3.6E-11 M, [free OA/OAm] = 1.9E-7 M, [lecithin-QD] = 3.6E-11 M and [free lecithin] = 1.3E-7 M.

Based on Figure 2.4c the OA/OAm the integrated PL intensity at 0.04 nM is ~7 times lower than expected, meaning that at equilibrium only 15% of the QDs are still bound by ligand and emissive. For lecithin the PL intensity is nearly linear and an estimated 99% of the QDs are still bound by ligand and emissive. From these numbers K_{ligand} can be calculated using Equation A8:

$$K_{ligand} = \frac{f_{emissive}[\text{QD-ligand}]}{(1-f_{emssive})[\text{QD-ligand}][\text{free ligand}]} \quad \text{(A8)}$$

Where $f_{emissive}$ is the fraction of quantum dots which are still bound and emissive, [QD-ligand] is the starting concentration of fully bound QDs in solution 6 and [free-ligand] is the starting concentration of free ligand in solution 6.

Table A4: Ligand binding equilibrium constant K_{ligand} for solvated OA/OAm and lecithin QDs computed from DFT and experimental results

		$\mathbf{K_{ligand}}$
DFT	*OA/OAm*	3.7 E4
	lecithin	1.3 E34
Experimental	*OA/OAm*	9.1 ± 0.3 E5
	lecithin	7.4 ± 0.6 E8

Using Equation A8 the experimental binding energy of OA/OAm to $CsPbBr_3$ is -0.34 eV. For lecithin the experimental binding energy is -0.50 eV. The observed discrepancy between our theoretical and experimental binding energies for lecithin can likely be attributed to our decision to use a truncated version of the molecule for computational feasibility. We anticipate that the solvent effects would have been more pronounced, aligning the calculated binding energies more closely with experimental values, had the full molecular structure been incorporated in our analysis.

Table A5: Serial dilutions resulting in QD solutions used for concentration dependent PL. Solutions used for TRPL are indicated with a star.

	Volume of OA/OAm QD Solution	Concentration of OA/OAm QDs (mg/mL)	Volume of lecithin QDs	Concentration of lecithin QDs (mg/mL)	Volume of Hexanes (mL)	Dilution Factor
Solution 1 (Ensemble PLQY Concentration)*	100 µL of stock solution	3.3E1	200 µL of stock solution	6.3E-1	4	1
Solution 2*	20 µL of stock solution	6.6E0	40 µL of stock solution	1.3E-1	4	2E-1
Solution 3*	10 µL of stock solution	3.3E0	20 µL of stock solution	6.3E-2	4	1E-1
Solution 4*	2 µL of stock solution	6.6E-1	4 µL of stock solution	1.3E-2	4	2E-2
Solution 5	1 µL of stock solution	3.3E-1	2 µL of stock solution	6.3E-3	4	1E-2
Solution 6	200 µL of solution 3	1.7E-1	200 µL of solution 3	3.2E-3	4	5E-3
Solution 7	133 µL of solution 3	1.1E-1	133 µL of solution 3	2.1E-3	4	3.3E-3
Solution 8	100 µL of solution 3	8.3E-2	100 µL of solution 3	1.6E-3	4	2.5E-3
Solution 9 (Microscopy Concentration)*	400 µL of solution 4	6.6E-2	400 µL of solution 4	1.3E-3	4	2E-3
Solution 10	333 µL of solution 4	5.5E-2	333 µL of solution 4	1.1E-3	4	1.7E-3

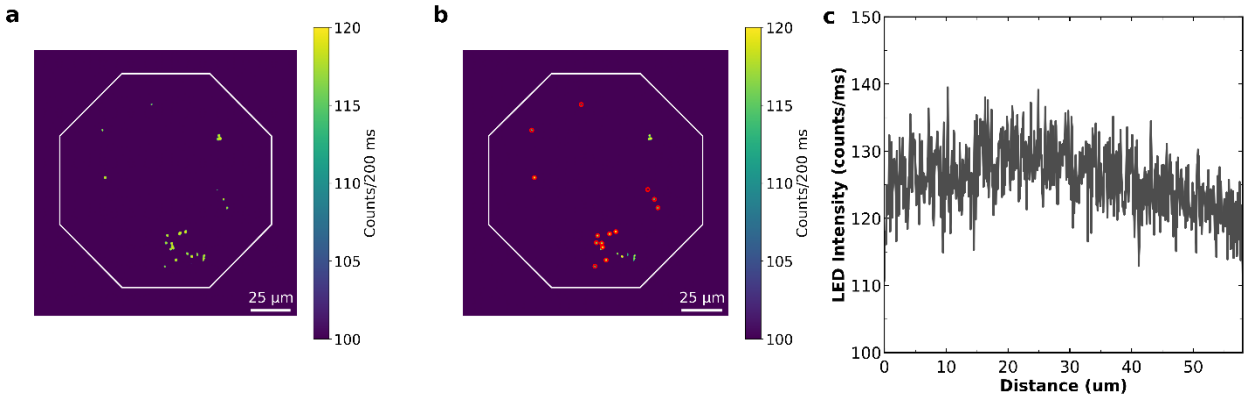

Figure A21: Particle Picking Constraints a) quantum dot sample illuminated with the field-stop (white octagon) partially closed to demonstrate the quality of particle selection. **b)** quantum dot sample illuminated with the field-stop (white octagon) partially closed and selected particles circled in red to demonstrate the quality of particle selection. The particle selection algorithm accounts for particle brightness, size and nearest neighbor distance. **c)** Illumination homogeneity of the LED across the objective flat field of view. Y-axis limits represent ±20% of the mean illumination intensity.

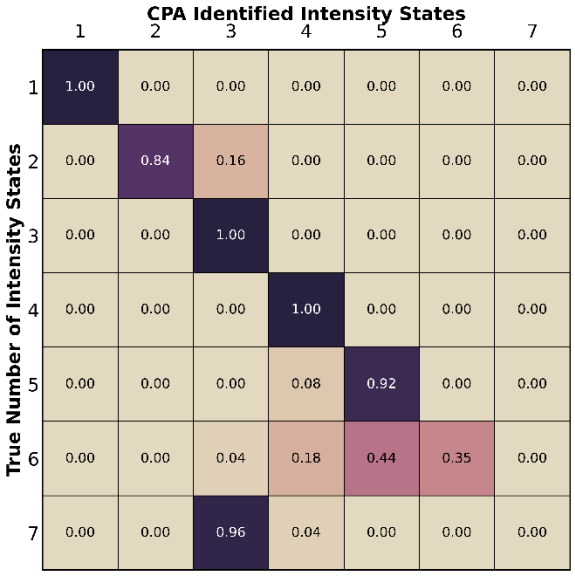

Figure A22: Confusion matrix quantifying the performance of our custom CPA package. Confusion matrix was generated by creating synthetic blinking traces with a power law exponent of α = 1.5, a time step size of 50 ms and *n* states evenly spaced between 100 and 140 counts/50 ms. 100 synthetic traces[11] were generated for each *n* in the range of 1 to 7 (the true number of states). The synthetic traces were analyzed using our CPA package and the number of fit states was extracted (the number of CPA determined states). This test shows that we can reliably resolve up to 5 intensity states in blinking traces at the experimental conditions (time step size = 50 ms and intensity range of 100 to 140 counts/50 ms).

Change Point Analysis to Blinking Statistics

Our analysis package uses CPA to determine the number of intensity levels in each trace and which intensity level each time point belongs to.[12,13] From this information we calculate the dwell time probability distribution for each level and fit to a power law[14] (Equation A9) and a truncated power law[15] (Equation A10). The fit that yields a larger R^2 value is used for further analysis of the intensity level.

$$P(t) = Ct^{-\alpha} \tag{A9}$$

$$P(t) = Ct^{-\alpha}e^{t/T_c} \tag{A10}$$

Where *P(t)* is the dwell time probability distribution, *C* is an exponential pre-factor, *t* is the dwell time, α is the power law exponent and T_c is the cutoff time. From these fits the dwell time expectation value $\langle t \rangle$ can be calculated according to Equations A11 (power law) or A12 (truncated power law).

$$\langle t \rangle = \left(\frac{\alpha+1}{\alpha+2}\right)\left(\frac{t_{max}^{\alpha+2} - t_{min}^{\alpha+2}}{t_{max}^{\alpha+1} - t_{min}^{\alpha+1}}\right) \tag{A11}$$

$$\langle t \rangle = -T_c\left(\frac{\Gamma\left(\alpha+2,\frac{-t_{max}}{T_c}\right) - \Gamma\left(\alpha+2,\frac{-t_{min}}{T_c}\right)}{\Gamma\left(\alpha+1,\frac{-t_{max}}{T_c}\right) - \Gamma\left(\alpha+1,\frac{-t_{min}}{T_c}\right)}\right) \tag{A12}$$

Where t_{max} is the maximum observed dwell time, t_{min} is the minimum observed dwell time and Γ is the upper incomplete gamma function.

For the purposes of the post-CPA analysis an ON-state is defined as the most intense CPA identified level and all other CPA identified intensity levels are defined as OFF-states. From the above information we can calculate our blinking statistics.

$$ON\ \% = \frac{T_{ON}}{T_{total}} * 100 \quad \text{(A13)}$$

$$\tau_{ON} = \langle t \rangle_{ON} \quad \text{(A14)}$$

$$\tau_{OFF} = \sum_n \frac{T_n}{(T_{total} - T_{ON})} \langle t \rangle_n \quad \text{(A15)}$$

$$\tau_{ON/OFF} = \frac{T_{ON}\,\tau_{ON}}{(T_{total} - T_{ON})\tau_{OFF}} \quad \text{(A16)}$$

Where T_{ON} is the total dwell time of the ON-state, T_{total} is the total measurement time, n is the number of OFF states, T_n are the total dwell times of each OFF-state, τ_{ON} is the expected ON event dwell time (Figures A5c and A7c), τ_{OFF} is the weighted expected OFF event dwell time (Figures A5d and A7d) and $\tau_{ON/OFF}$ is the weighted ON/OFF ratio (Figure 2.3d).

References

(1) Protesescu, L.; Yakunin, S.; Bodnarchuk, M. I.; Krieg, F.; Caputo, R.; Hendon, C. H.; Yang, R. X.; Walsh, A.; Kovalenko, M. V. Nanocrystals of Cesium Lead Halide Perovskites (CsPbX3, X = Cl, Br, and I): Novel Optoelectronic Materials Showing Bright Emission with Wide Color Gamut. *Nano Lett* 2015, *15* (6), 3692–3696. https://doi.org/10.1021/nl5048779.

(2) Zhang, Y.; Siegler, T. D.; Thomas, C. J.; Abney, M. K.; Shah, T.; De Gorostiza, A.; Greene, R. M.; Korgel, B. A. A "Tips and Tricks" Practical Guide to the Synthesis of Metal Halide Perovskite Nanocrystals. *Chemistry of Materials* 2020, *32* (13), 5410–5423. https://doi.org/10.1021/ACS.CHEMMATER.0C01735.

(3) Akkerman, Q. A.; Nguyen, T. P. T.; Boehme, S. C.; Montanarella, F.; Dirin, D. N.; Wechsler, P.; Beiglböck, F.; Rainò, G.; Erni, R.; Katan, C.; Even, J.; Kovalenko, M. V. Controlling the Nucleation and Growth Kinetics of Lead Halide Perovskite Quantum Dots. *Science (1979)* 2022. https://doi.org/10.1126/SCIENCE.ABQ3616.

(4) Taddei, M.; Smith, J. A.; Gallant, B. M.; Zhou, S.; Westbrook, R. J. E.; Shi, Y.; Wang, J.; Drysdale, J. N.; McCarthy, D. P.; Barlow, S.; Marder, S. R.; Snaith, H. J.; Ginger, D. S. Ethylenediamine Addition Improves Performance and Suppresses Phase Instabilities in Mixed-Halide Perovskites. *ACS Energy Lett* 2022, *7* (12), 4265–4273. https://doi.org/10.1021/ACSENERGYLETT.2C01998.

(5) Yaman, M. Y.; Kalinin, S. V; Guye, K. N.; Ginger, D. S.; Ziatdinov, M.; Yaman, M. Y.; Guye, K. N.; Ginger, D. S.; Kalinin, S. V; Ziatdinov, M. Learning and Predicting Photonic Responses of Plasmonic Nanoparticle Assemblies via Dual Variational Autoencoders. *Small* 2023, *19* (25), 2205893. https://doi.org/10.1002/SMLL.202205893.

(6) Li, H.; Yang, H. Statistical Learning of Discrete States in Time Series. *Journal of Physical Chemistry B* 2019, *123* (3), 689–701. https://doi.org/10.1021/ACS.JPCB.8B10561.

(7) Perdew, J. P.; Burke, K.; Ernzerhof, M. Generalized Gradient Approximation Made Simple. *Phys Rev Lett* 1996, *77* (18), 3865. https://doi.org/10.1103/PhysRevLett.77.3865.

(8) Grimme, S. Semiempirical GGA-Type Density Functional Constructed with a Long-Range Dispersion Correction. *J Comput Chem* 2006, *27* (15), 1787–1799. https://doi.org/10.1002/JCC.20495.

(9) Even, J.; Pedesseau, L.; Jancu, J. M.; Katan, C. Importance of Spin–Orbit Coupling in Hybrid Organic/Inorganic Perovskites for Photovoltaic Applications. *Journal of Physical Chemistry Letters* 2013, *4* (17), 2999–3005. https://doi.org/10.1021/JZ401532Q.

(10) Krieg, F.; Ong, Q. K.; Burian, M.; Rainò, G.; Naumenko, D.; Amenitsch, H.; Süess, A.; Grotevent, M. J.; Krumeich, F.; Bodnarchuk, M. I.; Shorubalko, I.; Stellacci, F.; Kovalenko, M. V. Stable Ultraconcentrated and Ultradilute Colloids of CsPbX3 (X = Cl, Br) Nanocrystals Using Natural Lecithin as a Capping Ligand. *J Am Chem Soc* 2019, *141* (50), 19839–19849. https://doi.org/10.1021/JACS.9B09969.

(11) Palstra, I. M.; Koenderink, A. F. A Python Toolbox for Unbiased Statistical Analysis of Fluorescence Intermittency of Multilevel Emitters. *Journal of Physical Chemistry C* 2021, *125* (22), 12050–12060. https://doi.org/10.1021/acs.jpcc.1c01670.

(12) Watkins, L. P.; Yang, H. Detection of Intensity Change Points in Time-Resolved Single-Molecule Measurements. *Journal of Physical Chemistry B* 2005, *109* (1), 617–628. https://doi.org/10.1021/jp0467548.

(13) Li, H.; Yang, H. Statistical Learning of Discrete States in Time Series. *Journal of Physical Chemistry B* 2019, *123* (3), 689–701. https://doi.org/10.1021/acs.jpcb.8b10561.

(14) Kuno, M.; Fromm, D. P.; Hamann, H. F.; Gallagher, A.; Nesbitt, D. J. Nonexponential "Blinking" Kinetics of Single CdSe Quantum Dots: A Universal Power Law Behavior. *J Chem Phys* 2000, *112* (7), 3117–3120. https://doi.org/10.1063/1.480896.

(15) Shimizu, K. T.; Neuhauser, R. G.; Leatherdale, C. A.; Empedocles, S. A.; Woo, W. K.; Bawendi, M. G. Blinking Statistics in Single Semiconductor Nanocrystal Quantum Dots. *Phys Rev B Condens Matter Mater Phys* 2001, *63* (20). https://doi.org/10.1103/PhysRevB.63.205316.

Appendix B: Supporting Information for Emissive Traps Lead to Asymmetric Photoluminescence Line Shape in Spheroidal $CsPbBr_3$ Quantum Dots

Jessica Kline, Shaun Gallagher, Benjamin F. Hammel, Reshma Mathew, Dylan M. Ladd, Robert J. E. Westbrook, Jalen N. Pryor, Michael F. Toney, Matthew Pelton, Sadegh Yazdi, Gordana Dukovic and David S. Ginger

Table of Contents

Synthesis

Chemicals

Cesium carbonate (Cs_2CO_3, 99.9% metals basis), diisooctylphosphinic acid (DOPA, 90%), bis(2,4,4-trimethylpentyl)phosphinic acid (BTPA,90%), trioctylphosphine oxide (TOPO, 99%), lead (II) acetate trihydrate (99.999% trace metals basis), octadecene (for synthesis), oleic acid (≥99%), trioctylphosphine (97%, TOP), bromine (≥95%), phenethyl ammonium bromide (PEABr, ≥ 98%), di-dodecyldimethylammonium bromide (DDAB, 98%), N,N- dimethyloctadecylammoniopropanesulfonate (ASC18) , hexanes (≥ 95%), toluene (anhydrous 99.8%), octane (anhydrous ≥ 99%), acetone (90%), isopropanol (IPA, 90%), ethyl acetate (99.5%), 1-butanol (99%) and Ludox TMA (34 wt.%) were purchased from Millipore Sigma. Lecithin (90%) and lead (II) bromide ($PbBr_2$, 99.998% metals basis) were purchased from Alfa Aesar. Di-dodecylpropyldiammonium dibromide (dicationic), and dodecyloctlyphosphoethanolamine (peaC8C12) were synthesized according to previous reports.[1,2] All chemicals were used as received.

Synthesis of Spheroidal Lecithin-Capped $CsPbBr_3$ QDs

The precursor solutions for lecithin-capped $CsPbBr_3$ were prepared according to Akkerman et al with modifications.[3] BTPA (a conformational isomer of DOPA) was substituted for DOPA in an equimolar quantity to the original synthesis. The QDs were synthesized under ambient conditions by combining hexanes with aliquots of 0.04 M $PbBr_2$-TOPO, 0.2 M TOPO and 0.02 M Cs-BTPA.
Table B1 reports the volumes used in the synthesis. After 30 minutes of stirring at room temperature an aliquot of 0.13 M lecithin was added to the reaction. The QDs were subsequently washed by adding acetone in a 3:1 v:v ratio and centrifuged at 10,000 rpm for 5 minutes. The supernatant was discarded, and the precipitate was dissolved in 2 mL anhydrous toluene, filtered through a 0.45 µm PTFE filter and stored in a glovebox.

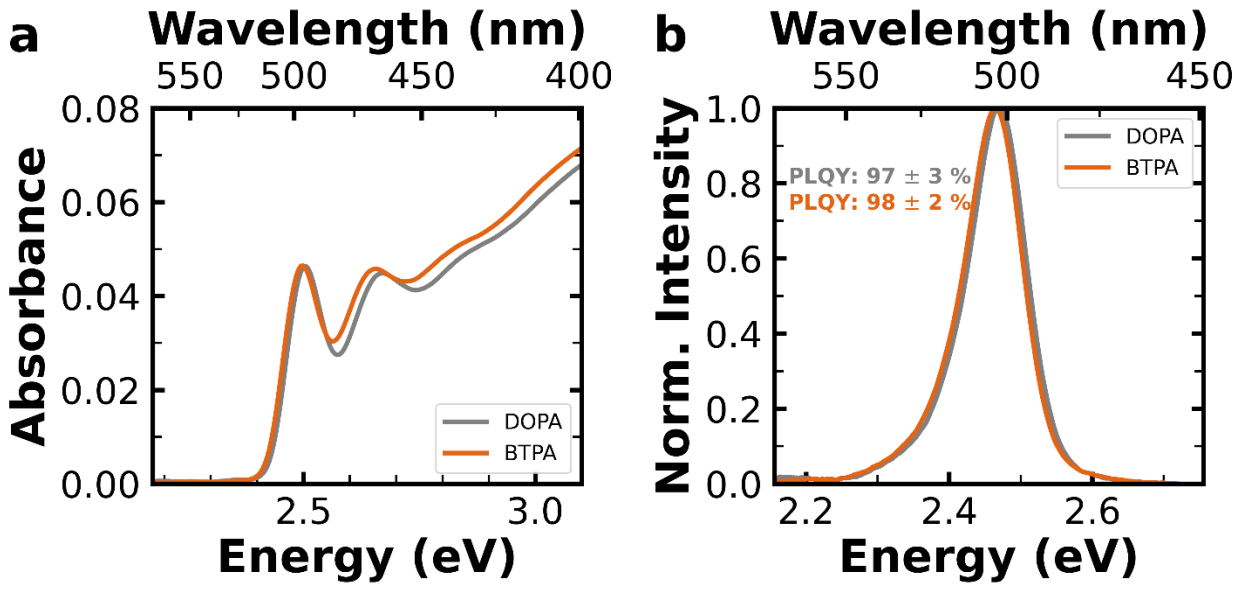

Figure B1: Ensemble characterization of spheroidal $CsPbBr_3$ QDs synthesized using DOPA and BTPA

Table B1: Synthesis conditions for lecithin-capped spheroidal quantum dots

	Hexanes (mL)	$PbBr_2$-TOPO (μL)	TOPO (μL)	Cs-BTPA (μL)	lecithin (μL)
S4	18	240	240	120	120
S5	18	480	480	240	240
S7	12	640	640	320	320
S12	0	960	0	480	480

Extension of Spheroidal Quantum Synthesis to Other Ligands

Spheroidal quantum dots with other ligands were synthesized using the same precursor solutions as the lecithin-capped spheroidal quantum dots. The ligands were dissolved in butanol (dicationic, ASC18), hexanes (peaC8C12) or toluene (DDAB) to form 0.13 M solutions. The ASC18 solution was kept at 50 ℃ prior to use to improve solubility. 160 μL of $PbBr_2$ – TOPO, 320 μL of TOPO, and 80 μL of Cs-BTPA were combined in 6 mL hexanes. After 30 mins of stirring 80 μL of the ligand solution was added to the reaction. The quantum dots were subsequently washed by adding ethyl acetate (C8C12 ASC18) or acetone (DDAB, dicationic) in a 3:1 v:v ratio and centrifuged at 10,000 rpm for 5 minutes. The supernatant was discarded, and the precipitate was dissolved in 2 mL anhydrous toluene, filtered through a 0.45 μm PTFE filter and stored in a glovebox.

Synthesis of Cubic Lecithin-Capped $CsPbBr_3$ QDs

Cubic lecithin-capped quantum dots were prepared according to Kreig et al at 1/3 scale with an injection temperature of 130°C.[4] Quantum dots were washed by adding 2 equivalents of acetone and centrifuging at 10,000 rpm for 10 minutes. Quantum dots were redissolved in 5 mL toluene and washed by adding 2 equivalents of acetone and centrifuging at 10,000 rpm for 1 minute. Quantum dots were redissolved in 2.5 mL toluene and washed by adding 2 equivalents of acetone and centrifuging at 10,000 rpm for 1 minute. Quantum dots were redissolved in 1.2 mL toluene and washed by adding 2 equivalents of acetone and centrifuging at 10,000 rpm for 1 minute. The final product was dissolved in 2 mL anhydrous toluene, filtered through a 0.45 μm PTFE filter and stored in a glovebox.

Lecithin/PEABr-capped Spheroidal QDs

PEABr was dissolved in a 1:1 ratio of IPA:toluene to make a 14 mM solution. Spheroidal quantum dots were washed by adding acetone in a 3:1 v:v ratio and centrifuged at 10,000 rpm for 5 minutes. The quantum dots were resuspended in 2 mL toluene and washed by adding acetone in a 3:1 v:v ratio and centrifuged at 10,000 rpm for 5 minutes. The quantum dots were resuspended in 2 mL toluene filtered through a 0.45 μm PTFE filter. QD solutions were diluted according to Table B2 and the indicated volume of PEABr solution was added. The dilute QD-PEABr solutions were centrifuged at 8,000 rpm for 5 mins and the supernatant was filtered through a 0.45 μm PTFE filter.

Table B2: Synthesis conditions for lecithin/PEABr-capped spheroidal quantum dots

	Toluene (mL)	QD Stock Solution (μL)	PEABr (μL)
S4	3	100	45
S5	3	20	40
S7	3	20	20
S12	3	50	30

Characterization

Ensemble Characterization

Absorbance spectra of the QD solutions were performed using a Perkin-Elmer Lambda 950 UV/Vis/NIR Spectrometer in a range of 400-600 nm with an integration time of 0.5 s. Absorbance spectra were transformed from wavelength to their Einstein B spectrum according to Equation B1.[5]

$$A(E) \propto {}^{A(\lambda)}/_{\nu} \tag{B1}$$

Steady-state photoluminescence spectra were acquired *via* a home-built fluorescence set up. Dilute solutions (OD of 0.0001 at 405 nm) were excited with a 405 nm laser (CrystaLaser) and spectra were collected on an OceanHDX (Ocean Insight). Spectral correction was performed using a calibrated white light source (Ocean Insight HL-3P-INT-CAL) to correct for the responsivity of the detector. Photoluminescence spectra were converted from wavelength to energy and corrected for line shape analysis according to Equation B2.[5]

$$I(E) \propto {}^{I(\lambda)}/_{\nu^3 E^2} \tag{B2}$$

The skew of a photoluminescence spectrum was calculated according to the Fisher-Pearson coefficient of skewness described in Equation B3.[6]

$$skew = \frac{N^{3/2}}{N} \frac{\sum(x-\bar{x})^3}{(\sum(x-\bar{x})^2)^{3/2}} \tag{B3}$$

Photoluminescence quantum yield measurements (PLQY) were performed on a commercial integrating sphere system (Hamamatsu Photonics K.K). PLQY values are determined using a white light source (Hamamatsu Mercury Xenon Lamp) and a monochromator for wavelength selection (405 nm) as the excitation source to illuminate the samples in an integrating sphere (Hamamatsu Photonics K.K). The optical density of samples was kept below 0.1 at the excitation wavelength to minimize reabsorption effects. Spectral correction was performed using a calibrated white light source (Ocean Insight HL-3P-INT-CAL) to correct for the responsivity of the detector.

Time resolved photoluminescence measurements at 470 nm excitation were acquired using a commercial PicoQuant FluorTime 100 system with LDH-470 laser diode, a 470 nm picosecond pulsed diode laser. The repetition rate is controlled by an external trigger input from a PicoHarp PDL 800-B laser driver and was set to 1 MHz. A photomultiplier tube (PMT) detector was used in TCSPC mode with an instrumental response function (IRF) of approximately 400 ps. The instrument response function (IRF) was measured via laser scatter from a solution of Ludox.

Excitation Wavelength Dependent Photoluminescence and PLE

Excitation wavelength dependent photoluminescence spectra and PLE spectra were acquired using Edinburgh FLS1000 spectrometer. The excitation source is a 450 W ozone-free Xenon arc lamp and the detector a Si-PMT with spectral resolution from 200 to 980 nm. The excitation bandwidth was kept at 0.5 nm for all experiments and the emission bandwidth varied between 0.5 nm (all excitation wavelength dependent photoluminescence spectra), and 3 nm (all PLE spectra) based on the experiment. All excitation wavelength dependent spectra were corrected for reabsorption effects. Above-gap excitation spectra were obtained by averaging three spectra collected with an integration time of 2 seconds, and sub-gap excitation spectra were integrated for 10 seconds and averaged over 1,000 spectra.

Streak Camera Measurements

Time-resolved photoluminescence spectra were measured using a streak camera with excitation from an ultrafast tunable laser source. In brief, the fundamental output of a Ti:sapphire amplifier (Coherent, Inc. Libra-HE, 4.0 mJ, 1 kHz, 50 fs) was used to pump an optical parametric amplifier (Coherent, Inc./Light Conversion OPerA Solo) which was used to tune the laser excitation wavelength to 425 nm. Appropriate long-pass and band-pass filters were used after the OPA to ensure a clean laser spectrum, and the beam profile was measured prior to each experiment to quantify the excitation area (Thorlabs BC106N–UV). Excitation power was 770 nJ/cm^2. Luminescence from the sample was collected using a set of f/4 lenses which focused the light into a f/3.9 spectrograph (Princeton Instruments SP-2150, entrance slit width = 200 μm) coupled to a streak camera (Hammamatsu C10910, slow-sweep unit M10913–01). The streak camera was operated in photon-counting mode using maximum gain, and signal levels <5% above the photon counting threshold were maintained using neutral density filters in front of the detector to ensure single photon counting statistics. The time-resolved PL spectra were corrected for the spectral response of the system by measuring the spectrum of a calibrated white light source (Ocean Optics HL-3P-CAL-EXT) on the streak camera operated in focus mode. Appropriate subtraction of a dark spectrum was accounted for when correcting the white light and time-resolved PL spectra. All spectra were additionally corrected for reabsorption effects. The IRF of the streak camera was measured using a solution of Ludox to scatter part of the laser excitation into the detector with the signal attenuated by nonfluorescing neutral density filters.

Lifetime Analysis

TRPL lifetime analysis was performed using a custom Python IRF-reconvolution package. Lifetimes were fit using a stretch exponential decay (Equation B4).[7]

$$I(t) = A \exp\left(-\frac{t}{\tau_k}\right)^{\beta} + C \tag{B4}$$

Where A is the pre-exponential factor, τ_k is the lifetime of the decay, C is the background of the measurement and β is the distribution of decay rates. τ_{str}, the average lifetime of a stretch exponential, is calculated according to Equation B5 where Γ is the gamma function.[7]

$$\tau_{str} = \frac{\tau_k}{\beta}\Gamma\left(\frac{1}{\beta}\right) \tag{B5}$$

Single Quantum Dot Photoluminescence

For single-particle measurements, a serial dilution of $CsPbBr_3$ is prepared in toluene within a glove box. A 10,000x dilution is then utilized, followed by drop-casting onto a glass coverslip. The glass coverslip is mounted on a sample holder which facilitates continuous nitrogen flow. Single-particle fluorescence measurements were performed on a home-built single-particle microscope.[8] The $CsPbBr_3$ on the glass coverslip was illuminated through a 100× oil-immersion objective with ~100 ps pulses at a wavelength of 420 nm from a pulsed laser diode (PicoQuant LDH-D-C-420) with an average power of 3.0 mW. Fluorescence from individual nanocrystals was collected through the same objective and isolated from reflected laser light with a 442 nm dichroic filter and two 430 nm long-pass filters. The emitted light was directed to a grating spectrometer (Princeton Instruments Spectra Pro 500i) with a CCD detector (Princeton Instruments Pixis 400) for measurement of fluorescence spectra. Spectra were smoothed using a 35 point Savitsky Golay.

Transmission Electron Microscopy (TEM) and Scanning Transmission Electron Microscopy (STEM)

TEM was performed with a FEI Tecnai G2 20 S-Twin operated at 200kV. STEM was performed with a Thermo Fisher Scientific Titan Themis operated at 200kV. Samples were prepared as described in Gallagher et al.[9] S12 PEABr/lecithin-capped quantum dots were not centrifuged or filtered prior to drop casting for TEM due to the low solution concentration. Image analysis was performed with ImageJ version 1.54f, specifically with the Fiji distribution.[10] Segmentation of the TEM images was conducted using Trainable Weka Segmentation (v3.3.4).[11] The area of the $CsPbBr_3$ nanocrystals was then measured using the "Analyze Particles" function with restrictions on the size and circularity ranges to avoid measuring noise or aggregated particles. To find particle diameters S4, S5, S7 and S12 particles were treated as perfect circles. To find particle edge lengths the C9 particles were treated as rectangles, with the longest side as the edge length. TEM images were post-processed before calculating circularity as particle picking on the images as acquired resulted in jagged edges which obscured the true shape. Images were post-processed in ImageJ by enhancing the contrast 25%, applying a 7 pixel mean filter, and finally using the binary "fill holes" operation. The circularity was then measured using "Analyze Particles" function with restrictions on the size and circularity ranges to avoid measuring noise or aggregated particles. STEM images required no post-processing prior to circularity analysis.

Small Angle X-ray Scattering (SAXS)

$CsPbBr_3$ quantum dots in toluene were sealed in quartz capillaries under inert atmosphere. SAXS data were taken on a Xenocs XEUSS 3.0 instrument with a Cu Kα source. Scans at four sample-to-detector distances were merged to obtain I(q) over a large q-range. A capillary of solvent was likewise measured; scattered intensity scaled to the sample data and subtracted as background.

Fitting SAXS data was completed in SASview5 (http://www.sasview.org/) using built-in Levenburg-Marquardt (damped least-squares) and DREAM (Markov Chain Monte Carlo) optimization algorithms. Form factor models consisting of a single population of polydisperse spheres were tested but did not produce quality fits ($\chi^2 < 2$) regardless of diameter distribution function (Gaussian, Lognormal, Schulz). Composite models of two polydisperse sphere populations produced quality fits to SAXS data and the refined diameters of the primary nanocrystal population were more consistent with those expected from UV-Vis calibration and extracted from TEM imaging. Secondary populations of smaller particles (2-4 nm in diameter) are hypothesized to be remaining reaction intermediates as suggested in prior works.[12,13] Composite models reported assume that the secondary particle population has the same scattering length density as the primary population of QDs ($SLD_{CsPbBr3} = 3.3 \times 10^{-5}$ Å^{-2}).

Due to the overall consistency and high quality of fits for the Schulz distribution (Equation B6) across the models tested, we elect to analyze these distribution line shapes to allow a skewed distribution of nanocrystal diameters and account for potential inhomogeneous broadening from an asymmetric distribution of nanocrystal diameters that favors large particles. The bimodal Schulz fits are summarized in **Table B3** and plotted in Figure B5.

$$I(d) = N(z+1)^{z+1}\left(d/\bar{d}\right)^2 \frac{\exp\left(-(z+1)d/\bar{d}\right)}{\bar{d}\Gamma(z+1)} \quad \text{(B6a)}$$

$$\text{polydispersity} = 1/\bar{d}\sqrt{z+1} \quad \text{(B6b)}$$

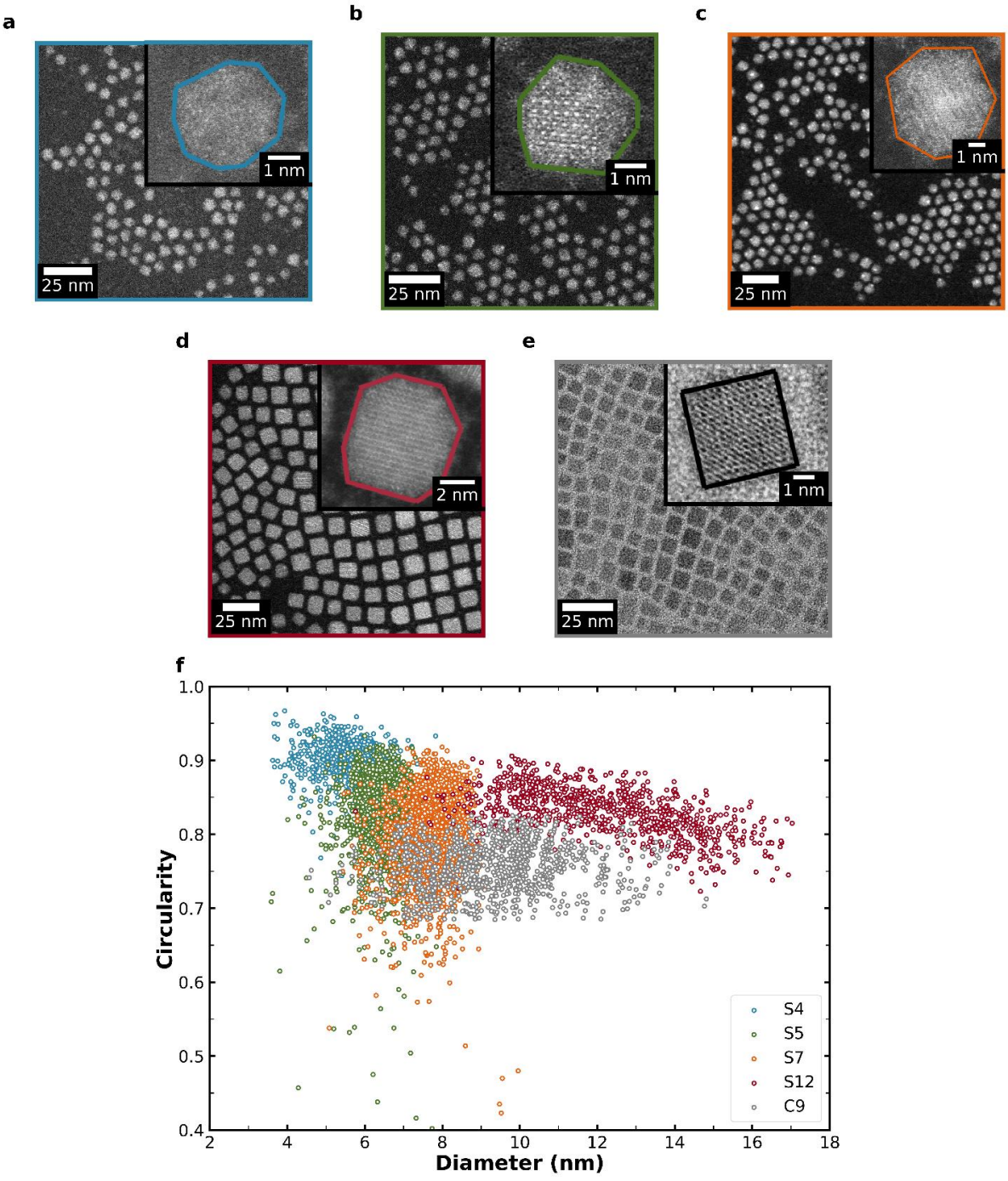

Figure B2: TEM and STEM images and sample morphology. a) STEM image of S4 quantum dots **b)** STEM image of S5 quantum dots **c)** STEM image of S7 quantum dots **d)** STEM image of S12 quantum dots and **e)** TEM image of C9 quantum dots. Inset in each panel is a high-magnification STEM image cropped to show a single representative quantum dot. The overall morphology of the representative quantum dots is highlighted with a colored border. **f)** Quantum dot circularity vs diameter for all samples which shows that smaller spheroidal quantum dots are consistently more circular than larger spheroidal quantum dots. This is particularly apparent in the S12 sample where the 10 nm particles are 13% more circular than the 16 nm particles. This implies that the morphology

of the spheroidal quantum dots is likely becoming more cubic with increased size. This difference in morphology could contribute to the observed trend ensemble photoluminescence skew. Spheroidal quantum dot circularity distributions were obtained from STEM images. Distributions for the C9 sample were obtained from TEM images.

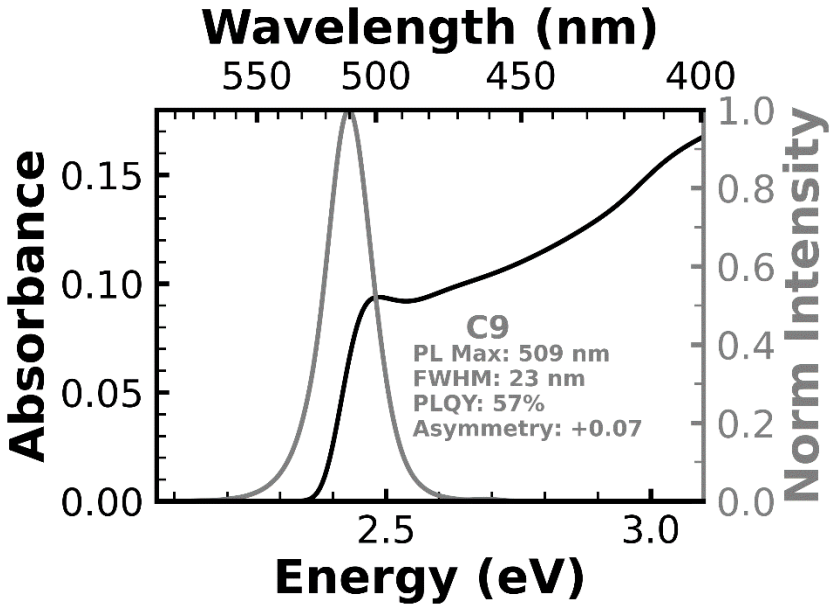

Figure B3: Ensemble characterization for cubic lecithin-capped quantum dots

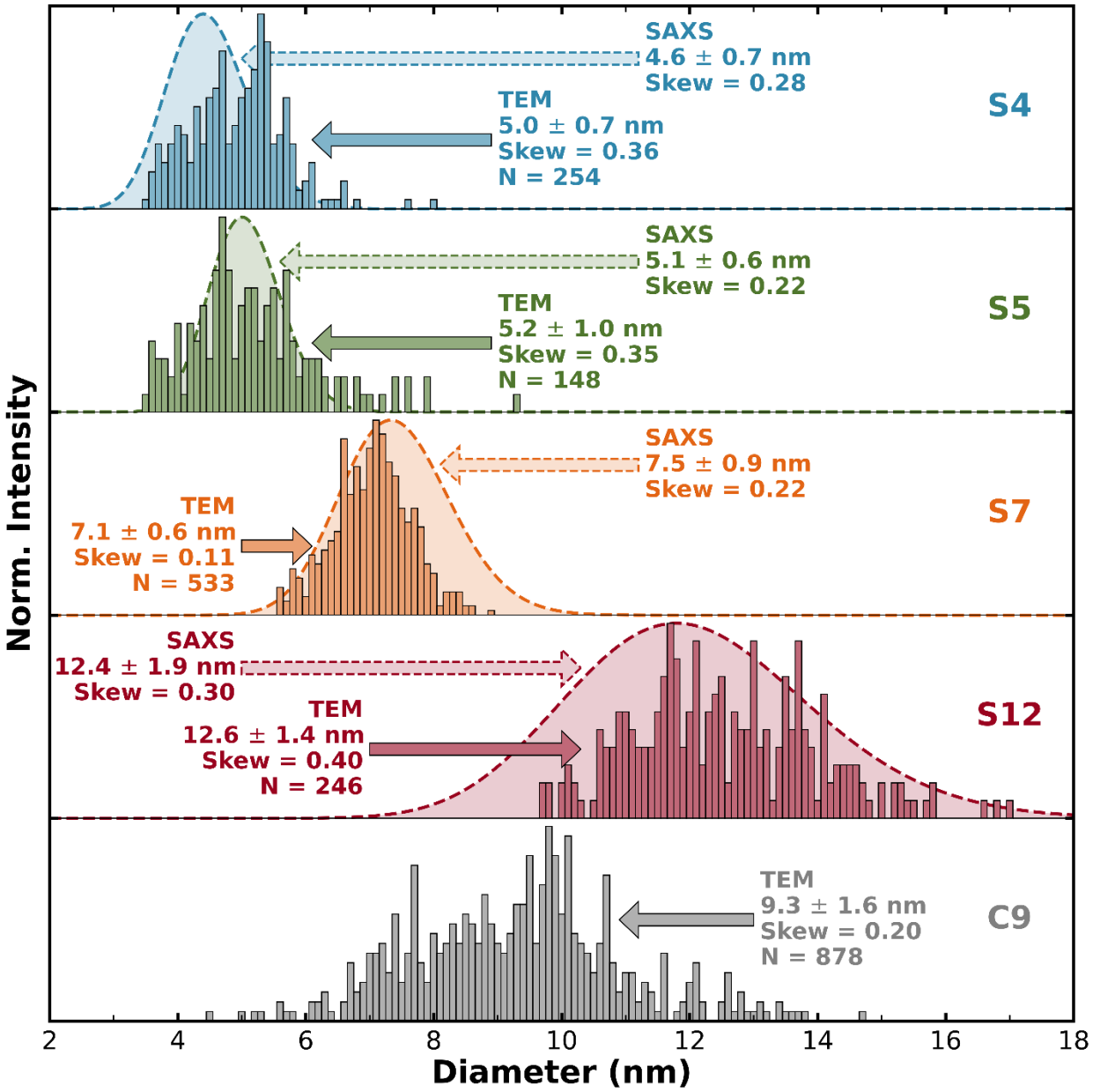

Figure B4: Comparison of TEM and SAXS size distributions. For each sample the TEM (bar graph) and SAXS (light shaded region) size distributions are plotted. We find that the SAXS and TEM size distributions match well for the spheroidal quantum dots. Mean sizes are less than 9% different for all samples. The two methods also agree well on the width and shape of the distributions. Skew values are within 0.13 and standard deviations 0.5 nms.

Table B3: SAXS fitting parameters for bimodal Schulz distributions.

The Schulz distribution is described in Equation B6a. The diameter column reports the mean diameter ($\bar{d}$) and the standard error in the mean diameter as fit. Polydispersity for a Schulz distribution is defined in Equation B6b.

		Primary Population				Secondary Population		
	χ^2	Scale	Diameter (nm)	Polydispersity (%)	Skew	Scale	Diameter (nm)	Polydispersity (%)
S4	1.55	1.4 ± 2.0	4.58 ± 0.08	14 ± 2	0.28	0.8 ± 1.2	2.1 ± 1.0	67 ± 28
S5	1.84	0.9 ± 0.9	5.13 ± 0.04	11 ± 1	0.22	0.7 ± 0.7	3.4 ± 0.2	40 ± 4
S7	1.89	1.1 ± 0.7	7.53 ± 0.01	11.5 ± 0.1	0.22	0.03 ± 0.02	4.09 ± 0.07	NA
S12	1.34	1.1 ± 1.0	12.39 ± 0.02	15.5 ± 0.1	0.30	0.7 ± 0.7	2.55 ± 0.05	42 ± 1

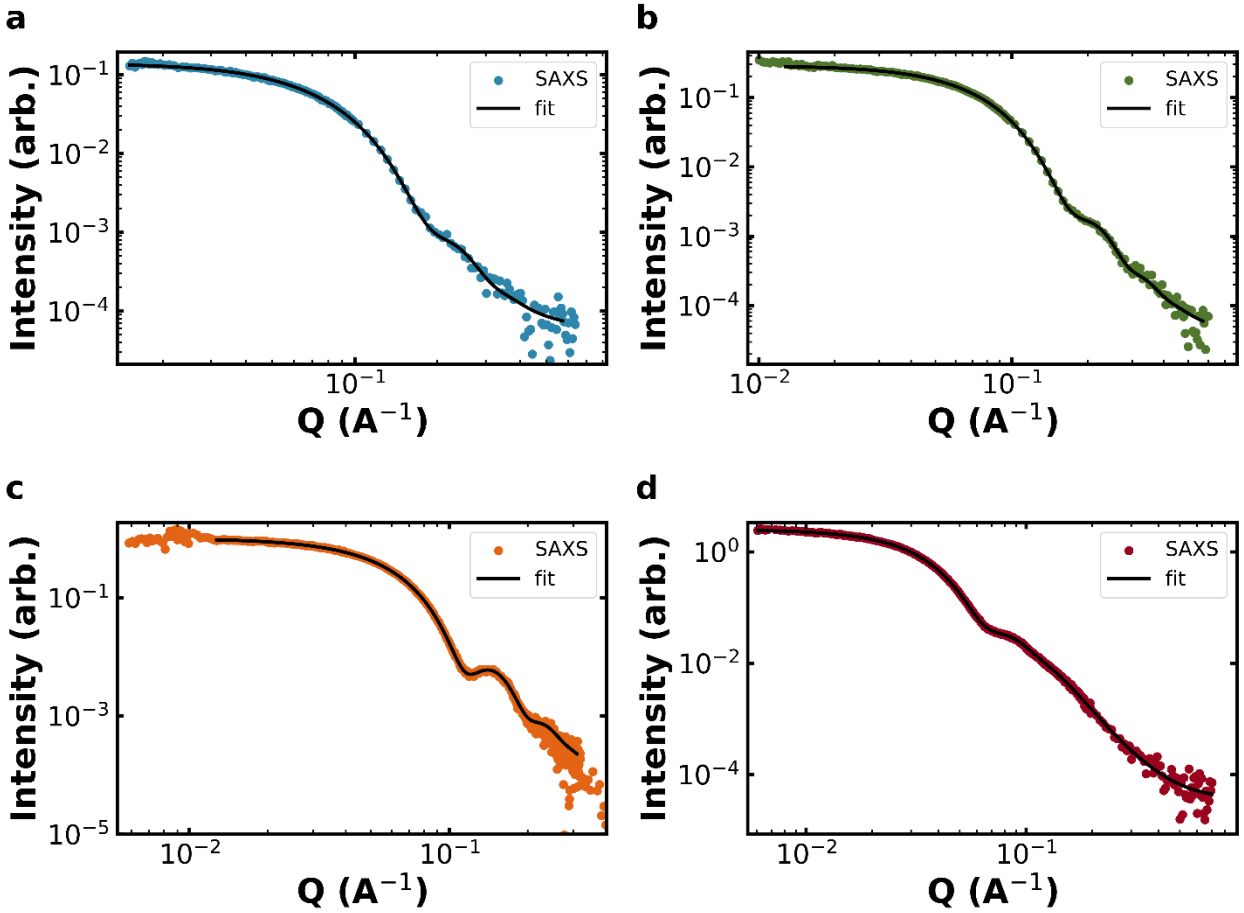

Figure B5: Fits to SAXS scattering data modeled by two distinct populations of spheres, both described using the Schulz distribution for **a)** S4 **b)** S5 **c)** S7 and **d)** S12 samples.

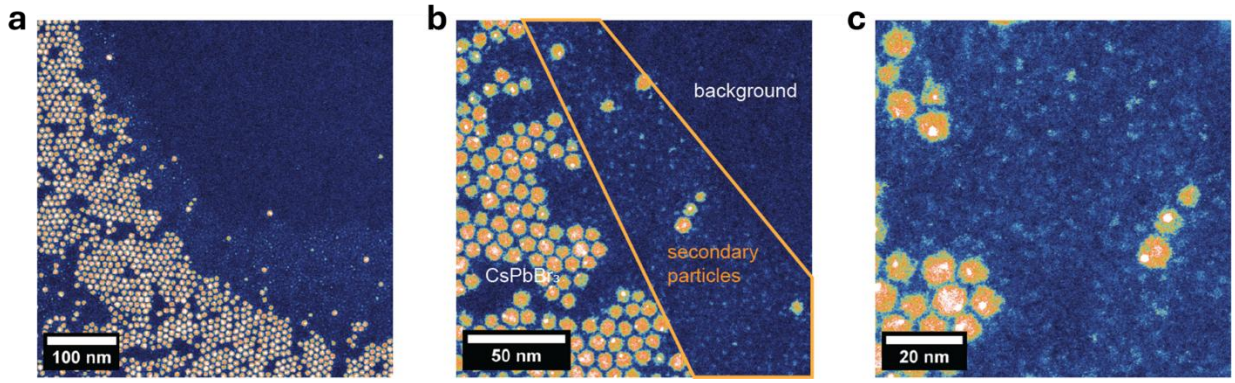

Figure B6: HAADF STEM images of secondary population a) Low-magnification false color STEM image of an S7 sample showing the presence of a secondary population on the edges of a monolayer of $CsPbBr_3$ nanocrystals **b)** medium-magnification false color STEM image of an S7 sample, the secondary population region is highlighted in orange and compared to the background. **c)** high-magnification false color STEM image on an S7 sample showing the secondary population. We consider that this population is most likely unreacted precursors; based on the size and contrast of the secondary species, it is likely they contain some heavy metal. Specifically we consider the potential presence of the amorphous $Cs[PbBr_3]$ agglomerate previously reported by Montanarella et al[13] although both [Cs]BTPA or $[PbBr_2]$TOPO monomers could be possible. As the considered sub-populations are optically inactive over the relevant spectral range (excitation at 405 nm and emission between 470 and 550 nm) they cannot be the cause of the elongated red tail for spheroidal $CsPbBr_3$ quantum dots.

Estimating the Inhomogeneous Linewidth Broadening Contributions

To estimate the inhomogeneous linewidth broadening contributions we first estimated the distribution of bandgaps within each sample using the sizing curve published by Brennan et al[14] (Equation B7).

$$E_g(d) = 2.280 + \frac{0.518}{d^2} + \frac{1.601}{d} \tag{B7}$$

From Equation B7 we calculate the absorption cross section (Equation B8a) and the Einstein B absorption and emission spectra (Equations B8b and B8d respectively).[15]

$$\sigma \propto E d^3 E_g(d) \tag{B8a}$$

$$\sigma \propto E\langle b_{0\to X}\rangle \tag{B8b}$$

$$\langle b_{X\to 0}\rangle \propto \langle b_{0\to X}\rangle \, exp\left(-E/k_B T\right) \tag{B8c}$$

$$\langle b_{X\to 0}\rangle \propto \sigma/E \, exp\left(-E/k_B T\right) \tag{B8d}$$

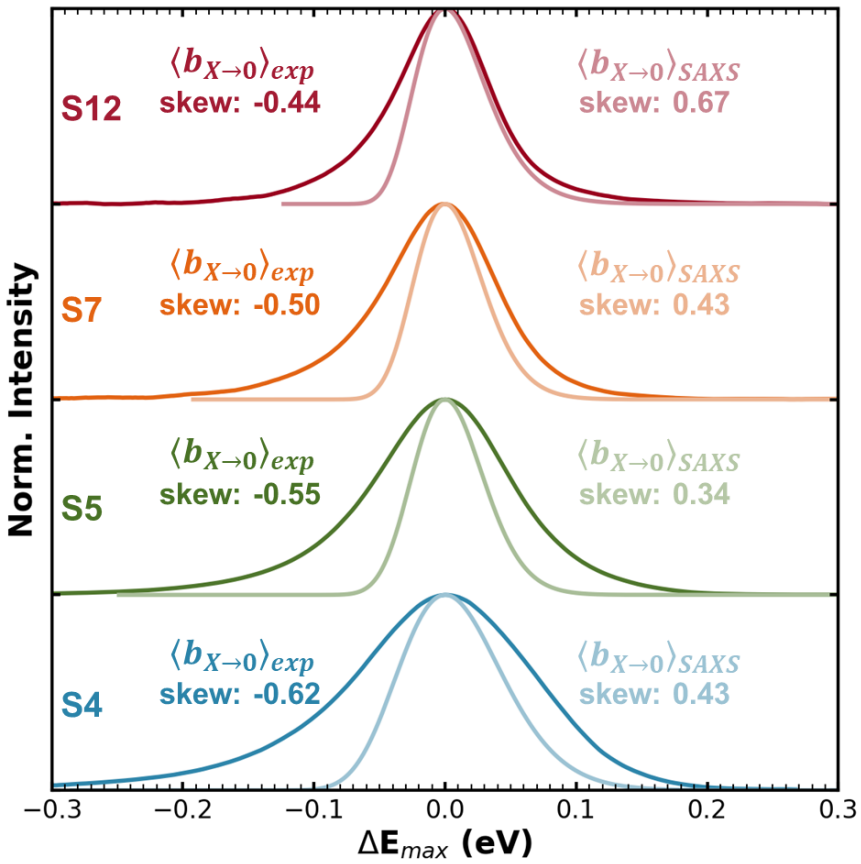

Figure B7: Inhomogeneous Broadening Contributions to the Photoluminescence Line Shape. For all samples the calculated inhomogeneous line shape $\langle b_{X\to 0}\rangle_{SAXS}$ is blue-skewed in direct contrast to the measured line shape $\langle b_{X\to 0}\rangle_{exp}$ which is red-skewed.

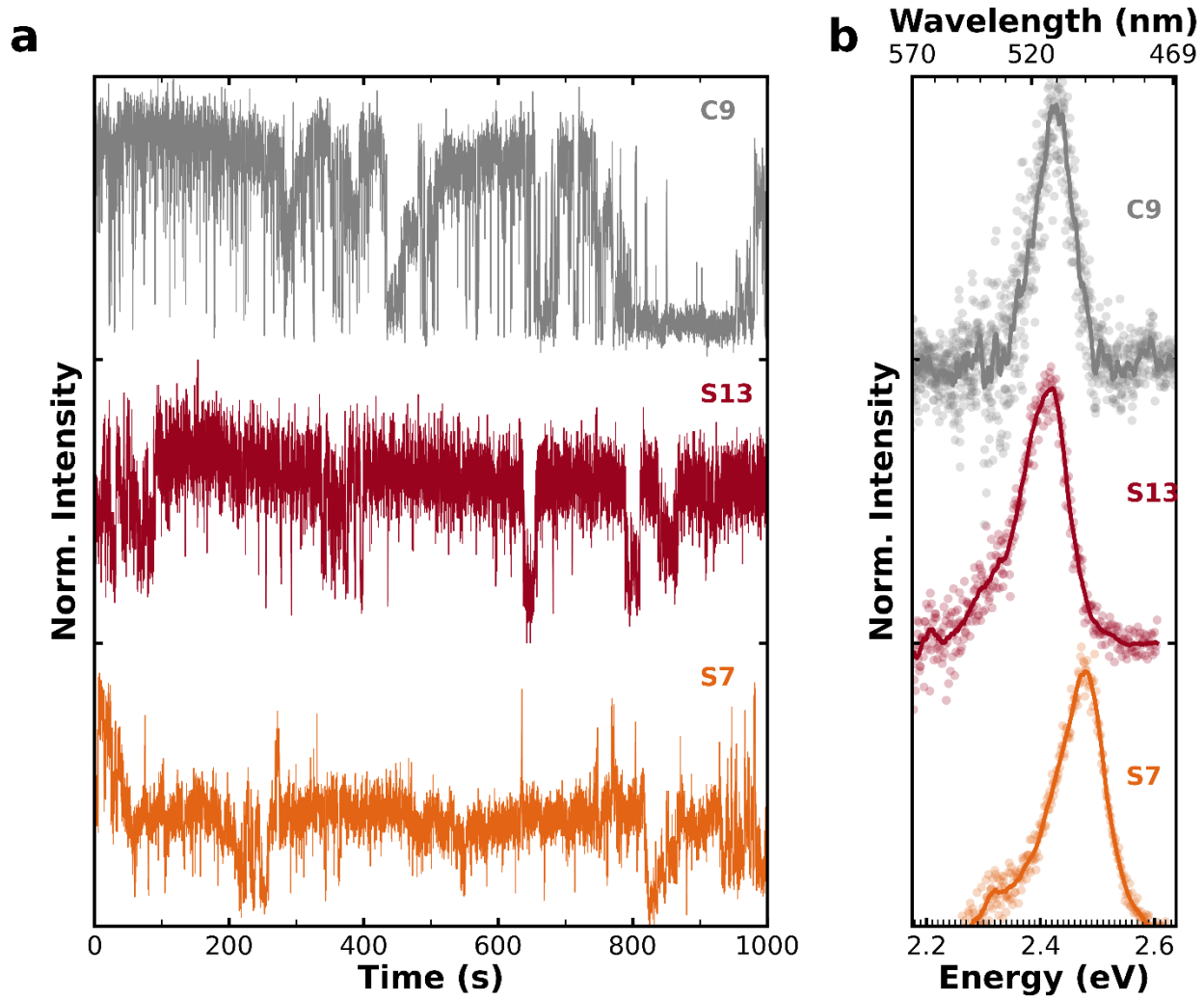

Figure B8: Correlated Blinking Traces and Single Quantum Dot Spectra. a) blinking traces from single quantum dots for S7 (orange), S13 (red) and C9 (grey). **b)** photoluminescence spectra of single quantum dots for S7 (orange), S13 (red) and C9 (grey)

Table B4: Comparison of Single Quantum Dot and Ensemble Spectra

	S4	S5	S7	S12	C9
Ensemble Emission Max (eV)	2.57	2.52	2.46	2.40	2.44
Single QD Emission Max (eV)	2.54	2.50	2.47	2.39	2.42
Ensemble Standard Deviation (meV)	160	130	100	90	110
Single QD Standard Deviation (meV)	110	110	90	90	90

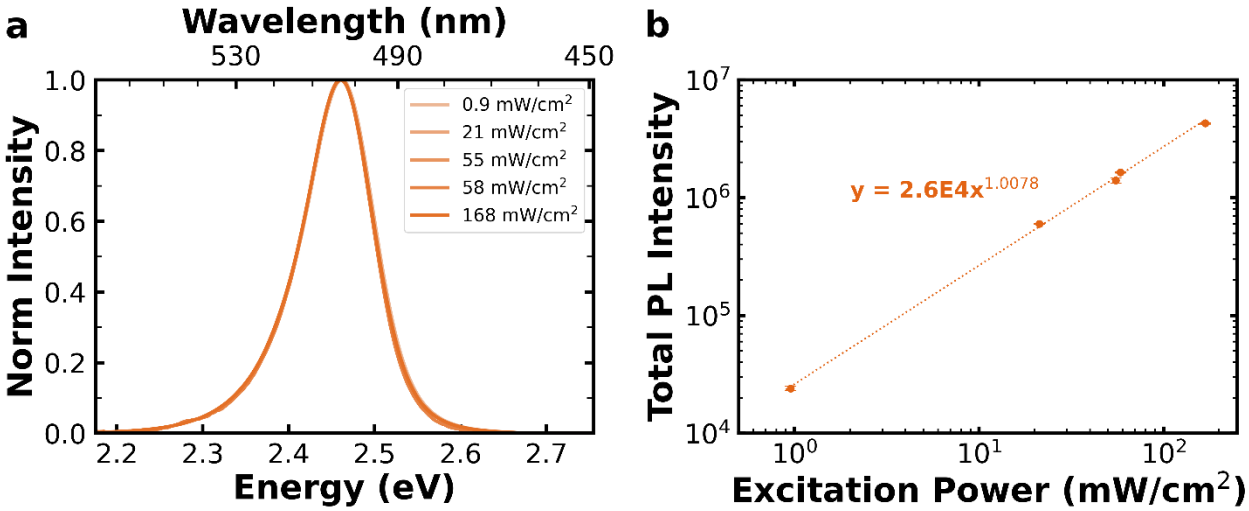

Figure B9: PL Intensity vs Power. a) PL spectra of S7 spheroidal QDs taken under various excitation powers. We observe no change in line shape with increasing excitation power. **b)** Integrated PL intensity compared to excitation power. PL intensity scales linearly with excitation power indicating the biexciton recombination does not significantly impact the line shape.

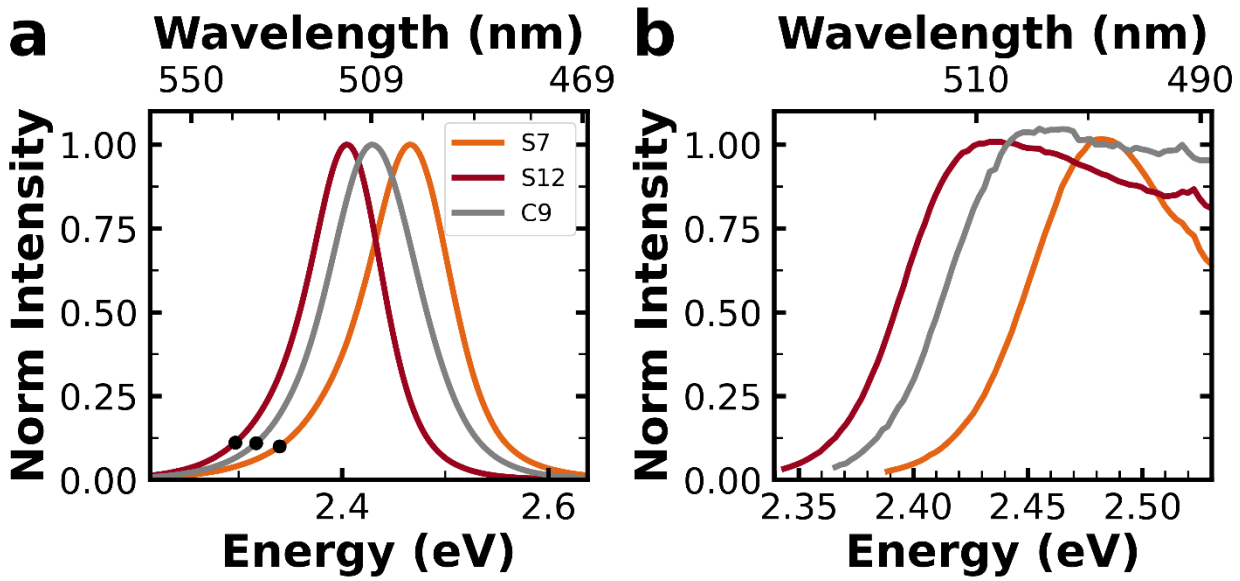

Figure B10: PLE spectra comparing red tail emission for S7 (orange) and S12 (red) quantum dots to C9 (grey) quantum dots for **a)** PL spectra of S7 (orange) and S12 (red) quantum dots to C9 (grey) quantum dots. Black circles mark the monitored wavelength for PLE. **b)** PLE spectra of S7 (orange) and S12 (red) quantum dots to C9 (grey) quantum dots. The PLE spectra for all three quantum dots see one absorptive state at the band edge and no resolvable absorption fine structure. Although cubic perovskite quantum dots are well known to have excitonic fine structure, the room temperature fine structure splitting is estimated to be less than 0.3 meV[16], which is below the resolution limit of our instrument (1 meV). The similar lack of resolvable room temperature absorption fine structure in spheroidal quantum dots indicates fine structure splitting of a similar magnitude in spheroidal and cubic quantum dots.

Elliott Fitting Model for Quantum Dot Absorbance Spectra

The measured absorbance spectra contain excitonic and continuum contributions. As such the measured onset cannot be used to quantitively assess the Urbach tail. Changes in the slope of the measured onset could be attributed to changes in the Urbach tail or to changes in the width of the first excitonic peak. As the width of the first excitonic peak varies with size in quantum dots, the Urbach tail can only be assessed via the continuum contributions. To detangle excitonic and continuum contributions we use the Elliott model function described in Equation B9 with $i = 1$ (cubic and 12 nm quantum dots) or $i = 2$ (4, 5 and 7 nm quantum dots).[17]

$$\alpha(E) = \sum_i \frac{\alpha_i}{\sigma_i\sqrt{2\pi}} \exp\left(-0.5\left(\frac{E-E_i}{\sigma_i}\right)^2\right) + \frac{\alpha_\infty}{1+\exp\left(-(E-E_g)/(k_BT)\right)} \frac{\exp\left(\pi\sqrt{\gamma}\right)}{\sinh\left(\pi\sqrt{\gamma}\right)} \quad \text{(B9)}$$

E_i, α_i and σ_i are the energy, width and absorption coefficient of the *i*th excitonic state, α_∞ is the absorption coefficient of the continuum states and E_g is the band gap of the material. γ is the Sommerfeld factor and is defined in Equation B10 and Ry^* is the binding energy of the 1s exciton.

$$\gamma = \frac{Ry^*}{E-E_g} \quad \text{(B10)}$$

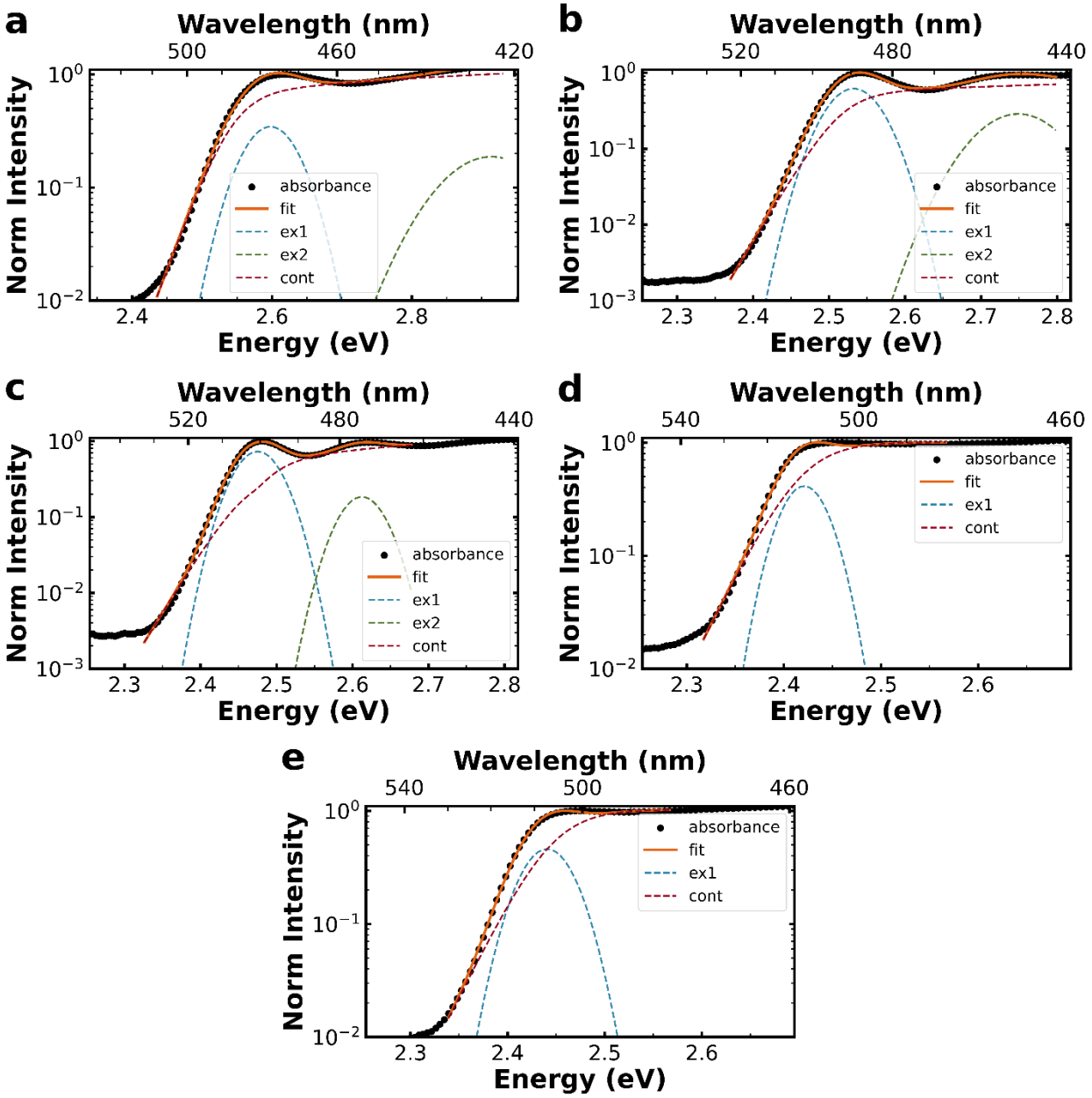

Figure B11: Full Elliott Fits for **a)** S4 absorbance fit to two excitonic peaks and a continuum contribution **b)** S5 absorbance fit to two excitonic peaks and a continuum contribution **c)** S7 absorbance fit to two excitonic peaks and a continuum contribution **d)** S12 absorbance fit to an excitonic peak and a continuum contribution and **e)** C9 absorbance fit to an excitonic peak and a continuum contribution

Table B5: Elliott Fitting Parameters

	E_g (eV)	α_1	E_1 (eV)	σ_1 (meV)	α_2	E_2 (eV)	σ_2 (meV)	α_∞	Ry^* (eV)
S4	2.54	0.0388	2.60	38.9	0.00528	2.89	48.6	0.326	14.5E-3
S5	2.51	0.0489	2.53	32.0	0.0195	2.74	42.1	0.270	21.1E-3
S7	2.47	0.0497	2.48	27.4	0.0125	2.61	28.7	0.220	3.74E-3
S12	2.41	0.0258	2.42	23.7	n/a	n/a	n/a	0.473	1.70
C9	2.44	0.0315	2.44	26.6	n/a	n/a	n/a	0.485	1.35

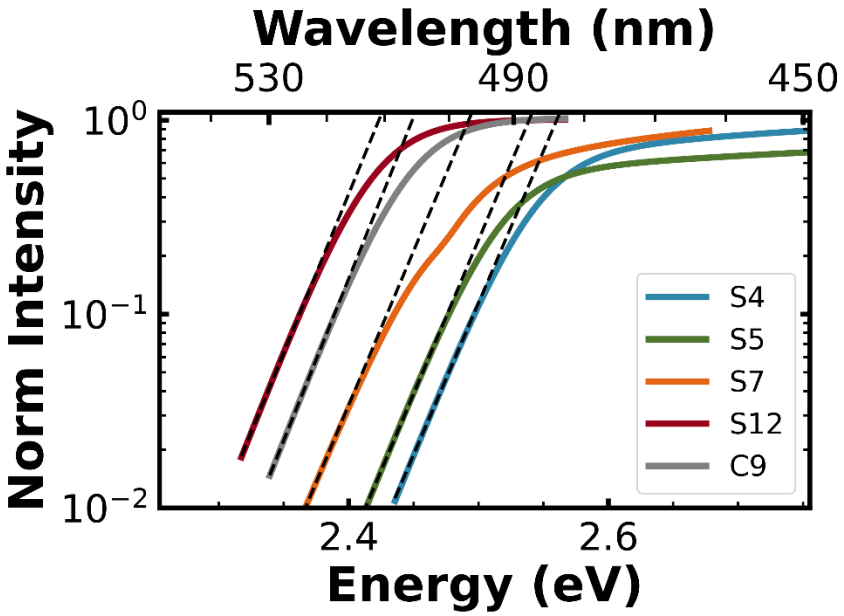

Figure B12: Urbach tail fits to continuum absorbance contributions for S4, S5, S7, S12 and C9 quantum dots quantum dots. Solid line are the continuum absorbance contributions for the different quantum dots. Dashed black line are the fits using equation 3.1 in the main text.

Interpreting Emission Energy Dependent Lifetimes

In Figure 3.3b we show emission energy dependent lifetimes which trend linearly with emission energy, which is contrary to the expected sigmoidal lifetime trend for excitons localized in band-tail states.[18,19] Before further understanding the linear trend, we must rule out other effects which could result in a linear lifetime trend – namely energy transfer between quantum dots. Forster's resonance energy transfer (FRET) could explain an elongated red photoluminescence tail and emission wavelength dependent lifetimes. Using the molar absorption coefficient from Maes et al[20] and equations 20 and 23 from Forster[21] we can calculate the Forster critical radius (R_0), Forster critical concentration (C_0) and the probability of energy transfer in solutions of less than 0.001 OD at the excitation wavelength. At these concentrations the probability of energy transfer is less than 0.0003% -meaning energy transfer can be eliminated as a potential cause of our observed elongated red photoluminescence tail and emission wavelength dependent lifetimes.

Table B6: FRET probability in solutions of spheroidal quantum dots at experimental concentrations

	QD Concentration (M)	R_0 (cm)	C_0 (M)	FRET Probability (%)
S4	1.47 E-9	8.81 E-7	5.80 E-4	0.0003
S5	1.01 E-9	9.51 E-7	4.62 E-4	0.0002
S7	1.19 E-10	1.17 E-6	2.48 E-4	0.0001
S12	8.80 E-11	1.49 E-6	1.19 E-4	0.0001

We can also discard size-dependent lifetime changes as the cause of the observed lifetime trends because in that scenario we would expect the S4 and S5 samples to have shorter lifetimes and lower energies.[22]

We find that the observed linear lifetime trends are likely due to a mobility edge at or near the band edge and that the emission energy dependent lifetimes appear to monitor the relative contributions of trap and band-edge emission across the different emission energies. This is supported by Figure B14 which shows the trends in lifetime homogeneity (β value) with emission energy. A completely homogeneous sample would have β = 1. For the spheroidal quantum dots β trends in a U shape, with local maxima at the highest and lowest energies. Starting from the high energy side we see a rapid decrease in β within the first few emission energies indicating that trap emission is contributing to the spectrum even at higher energies. The β value subsequently increases rapidly at low energies as trap emission becomes the dominate component. This mixing of trap and band-edge emission results in the observed lifetime trends and the noted lack of constant lifetime across the band-edge portion of the spectrum. Although, the magnitude of the observed lifetime change is relatively smaller for the S5 and S7 samples, we find that the contrasting β value trends between the spheroidal and cubic samples further indicate that red-edge emission in spheroidal quantum dots is dominated by a slower recombination process and that the second slower recombination process is not present in cubic quantum dots.

The trends in lifetime homogeneity suggesting highly overlapped trap and band-edge emission spectra are self-consistent with the observed overlap between the sub-gap and above-gap excitation spectra in Figure 3.3c where we can consider the spectra as dominated by trap and band-edge recombination respectively.

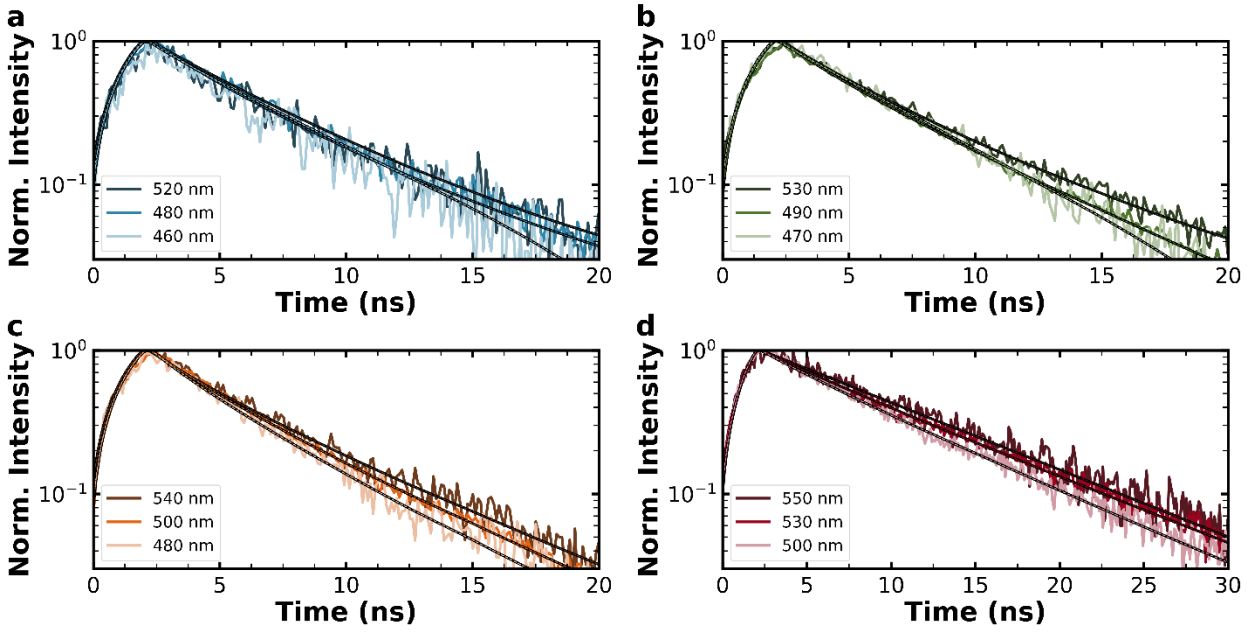

Figure B13: Selected emission energy dependent lifetimes for **a)** S4 quantum dots **b)** S5 quantum dots **c)** S7 quantum dots and **d)** S12 quantum dots

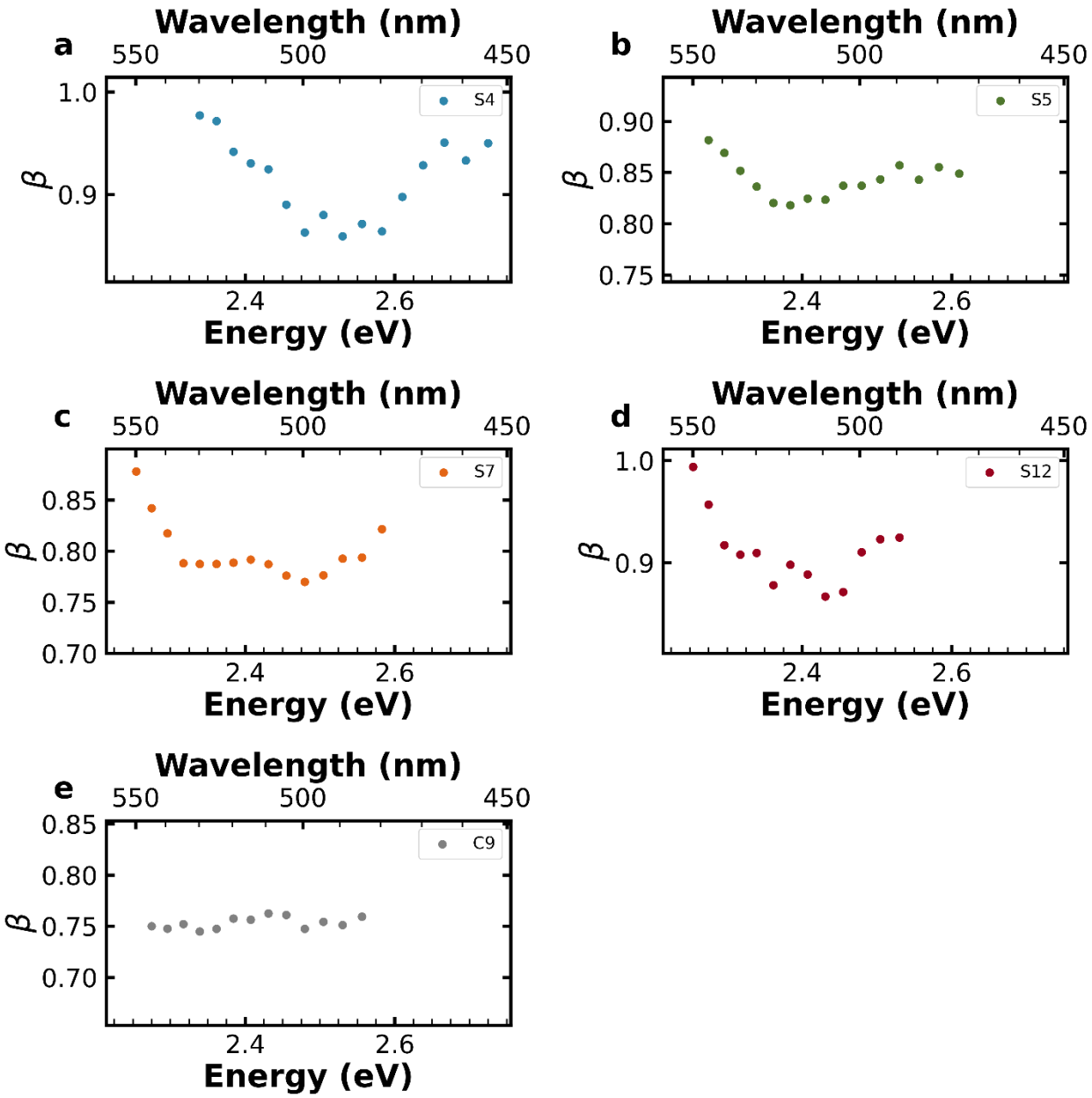

Figure B14: Trends in lifetime homogeneity with emission energy for a) S4 quantum dots **b)** S5 quantum dots **c)** S7 quantum dots **d)** S12 quantum dots **e)** C9 quantum dots. All plots have the y-axis limits set to +/- 0.1 from the mean β value. For the spheroidal quantum dots β trends in a U shape, with local maxima at the highest and lowest energies. Starting from the high energy side we see a rapid decrease in β within the first few emission energies indicating that trap emission is contributing to the spectrum even at higher energies. The β value subsequently increases rapidly at low energies as trap emission becomes the dominate component of the lifetime. This mixing of trap and band-edge emission across nearly the entire photoluminescence spectrum results in the linear lifetime trends observed in Figure 3.3b and explains the lack of sigmoidal lifetime trends typically expected from localized trap emission.

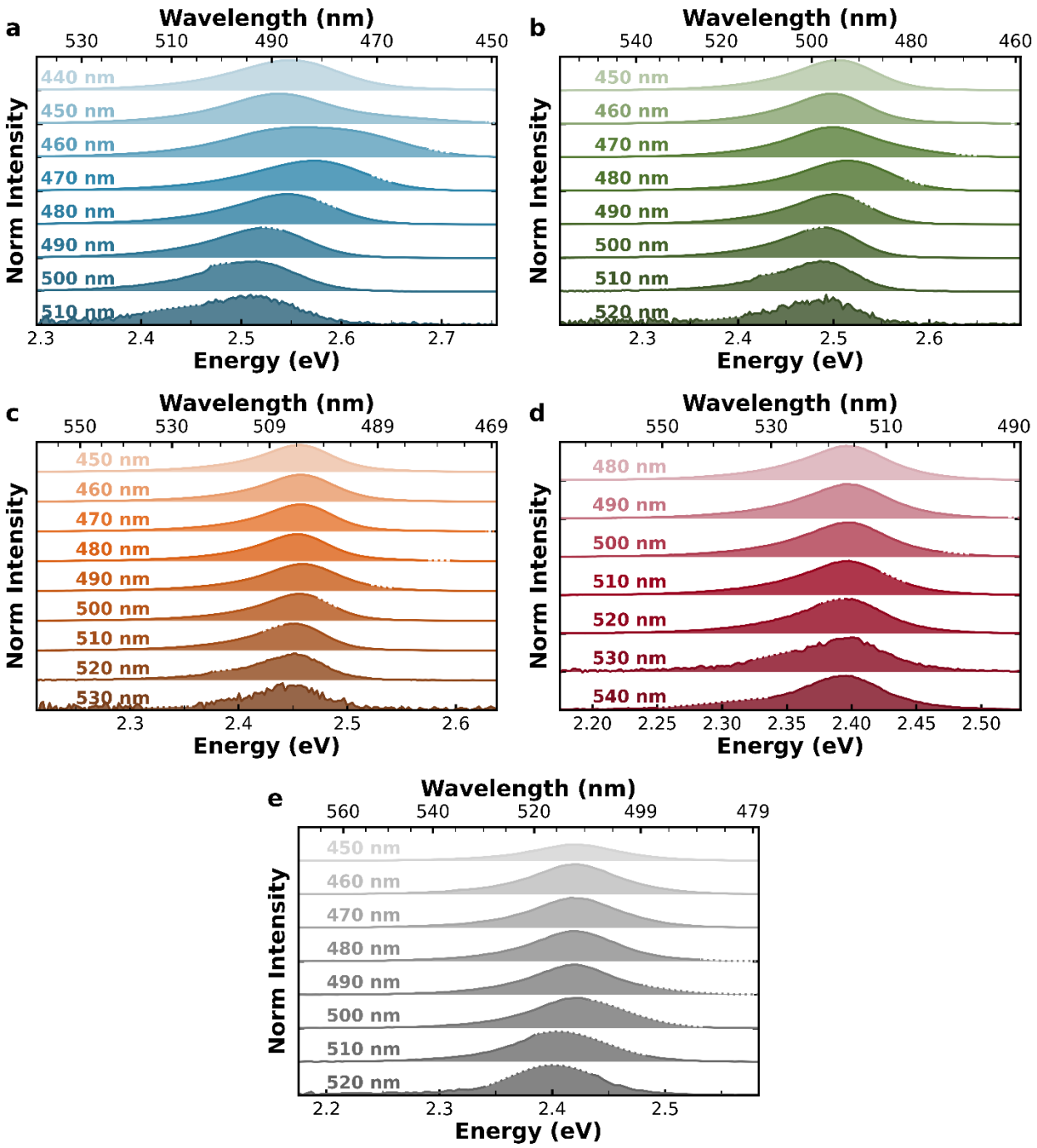

Figure B15: Excitation dependent emission spectra for **a)** S4 quantum dots excited between 440 and 510 nm. Excitation from 450-470 nm exhibits the characteristics of size-selective excitation for smaller quantum dots. Excitation from 480-490 nm shows the characteristics of size-selective excitation for larger quantum dots. Excitation from 500-510 nm shows the characteristics of trap emission **b)** S5 quantum dots between 450 and 520 nm. Excitation from 470-480 nm exhibits the characteristics of size-selective excitation for smaller quantum dots. Excitation from 490-500 nm shows the characteristics of size-selective excitation for larger quantum dots. Excitation from 510-520 nm shows the characteristics of trap emission **c)** S7 quantum dots excited between 450 and 530 nm. Excitation from 480-490 nm exhibits the characteristics of size-selective excitation for smaller quantum dots. Excitation from 500-510 nm shows the characteristics of size-selective excitation for larger quantum dots. Excitation

from 520-530 nm shows the characteristics of trap emission **d)** S12 quantum dots excited between 480 and 540 nm. Excitation from 530-540 nm shows the characteristics of trap emission **e)** C9 quantum dots excited between 450 and 530 nm

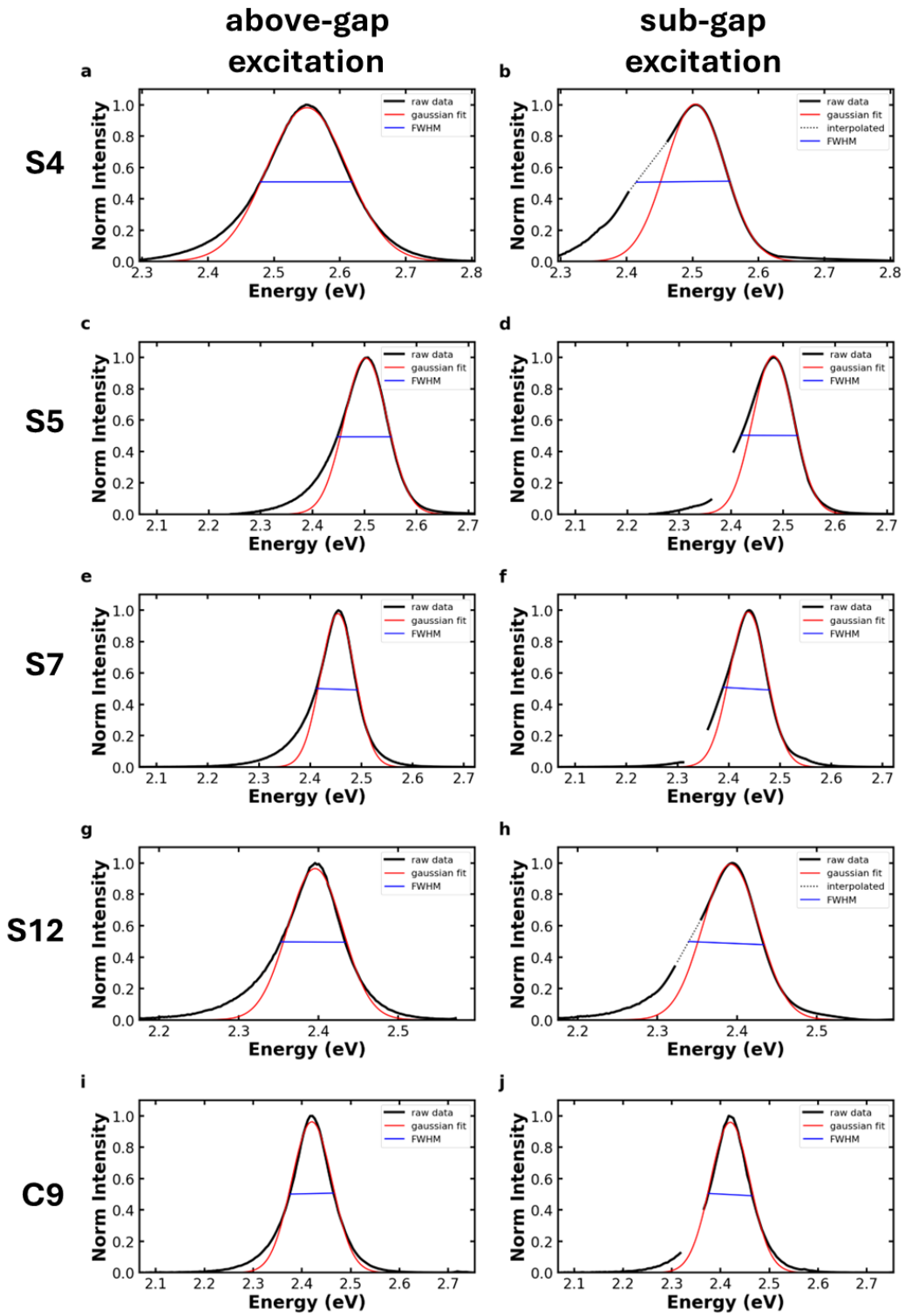

Figure B16: Fitting above-gap and sub-gap excitation spectra for **a)** above-gap S4 **b)** sub-gap S4 **c)** above-gap S5 **d)** sub-gap S5 **e)** above-gap S7 **f)** sub-gap S7 **g)** above-gap S12 **h)** sub-gap S12 **i)** above-gap C9 and **j)** sub-gap C9. We determined the emission maxima by fitting the high energy half of the photoluminescence spectrum to a Gaussian. We consider the center of this Gaussian fit to be the emission maximum. We determined the FWHMs by finding the difference between the two energies where the emission intensity was equal to 0.5. For sub-gap excitation spectra where the low energy 0.5 value occurred underneath the excitation scatter, we applied a linear interpolation to approximate the spectral line shape.

Table B7: Above-gap and sub-gap photoluminescence emission maxima and FWHMs. Theoretical resolution of the spectrometer is approximately 2 meV in the relevant spectral region.

	Above-Gap PL Max (eV)	Sub-Gap PL Max (eV)	Δ PL Max (meV)	Above-Gap FWHM (meV)	Sub-Gap FWHM (meV)	Δ FWHM (meV)
S4	2.550	2.501	-48	138	150	12
S5	2.502	2.480	-22	103	110	7
S7	2.454	2.438	-16	80	91	11
S12	2.396	2.392	-8	81	94	13
C9	2.420	2.420	0	90	90	0

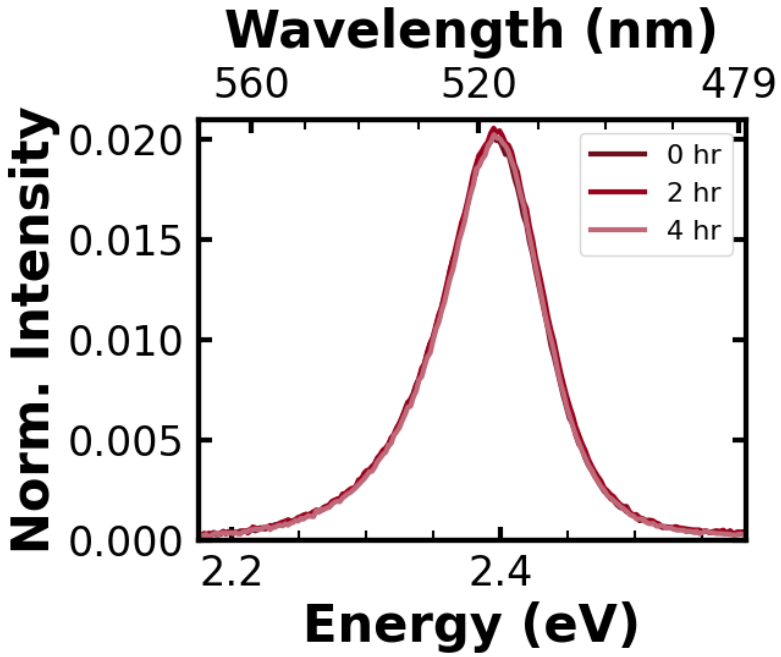

Figure B17: Illumination stability of S12 quantum dots. Quantum dots were left under continuous illumination at 405 nm for 4 hours. Over the course of this time period no change is observed in the photoluminescence intensity, line shape or peak position. Spectra are normalized to the area of the 0 hour spectrum.

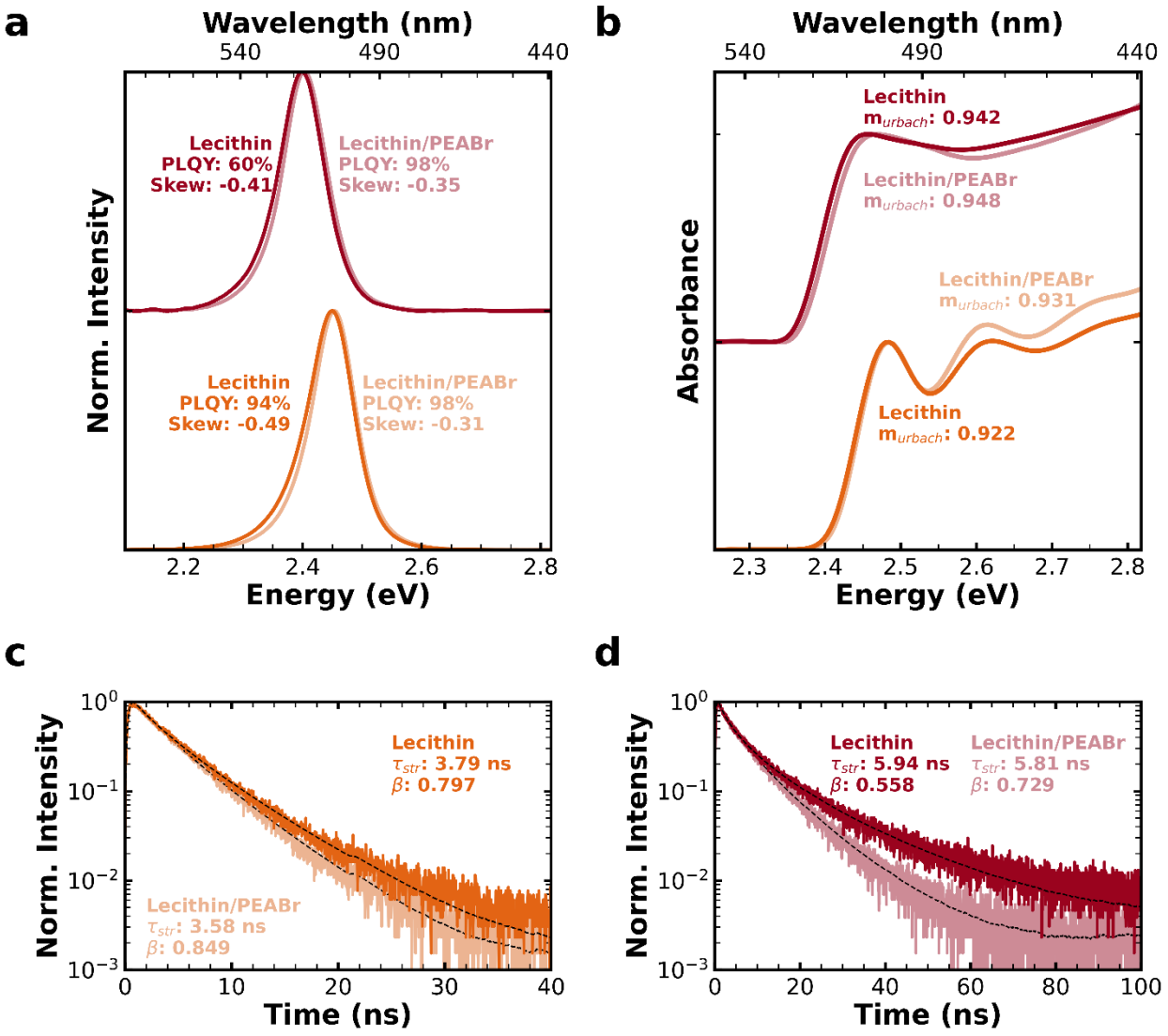

Figure B18: Passivating Emissive Traps on the Spheroidal QD Surface. a) Photoluminescence spectra for S12 (red) and S7 (orange) lecithin- and lecithin/PEABr- capped spheroidal QDs. Capping with lecithin/PEABr results in increasingly symmetric spectra with higher PLQYs, indicating increased passivation. S7 lecithin-capped QD emission is centered at 2.445 ± 0.044 eV, and lecithin/PEABr-capped QD emission is centered at 2.451 ± 0.041 eV. S12 lecithin-capped QD emission is centered at 2.397 ± 0.043 eV and lecithin/PEABr-capped QD emission is centered at 2.403 ± 0.041 eV. The decreased PLQY for lecithin-capped S12 QDs relative to those reported in Figure 3.1f (95% vs 60%) is caused by ligand stripping from additional wash steps before adding PEABr.[37] **b)** Absorbance spectra for S12 (red) and S7 (orange) lecithin- and lecithin/PEABr- capped spheroidal QDs. The Urbach slope is slightly steeper for lecithin/PEABr-capped QDs. Photoluminescence lifetimes for **c)** S7 and **d)** S12 lecithin- and lecithin/PEABr-capped spheroidal QDs. Lecithin/PEABr-capped QDs see reduced lifetimes and increased stretching exponents, indicating the passivation of the emissive traps.

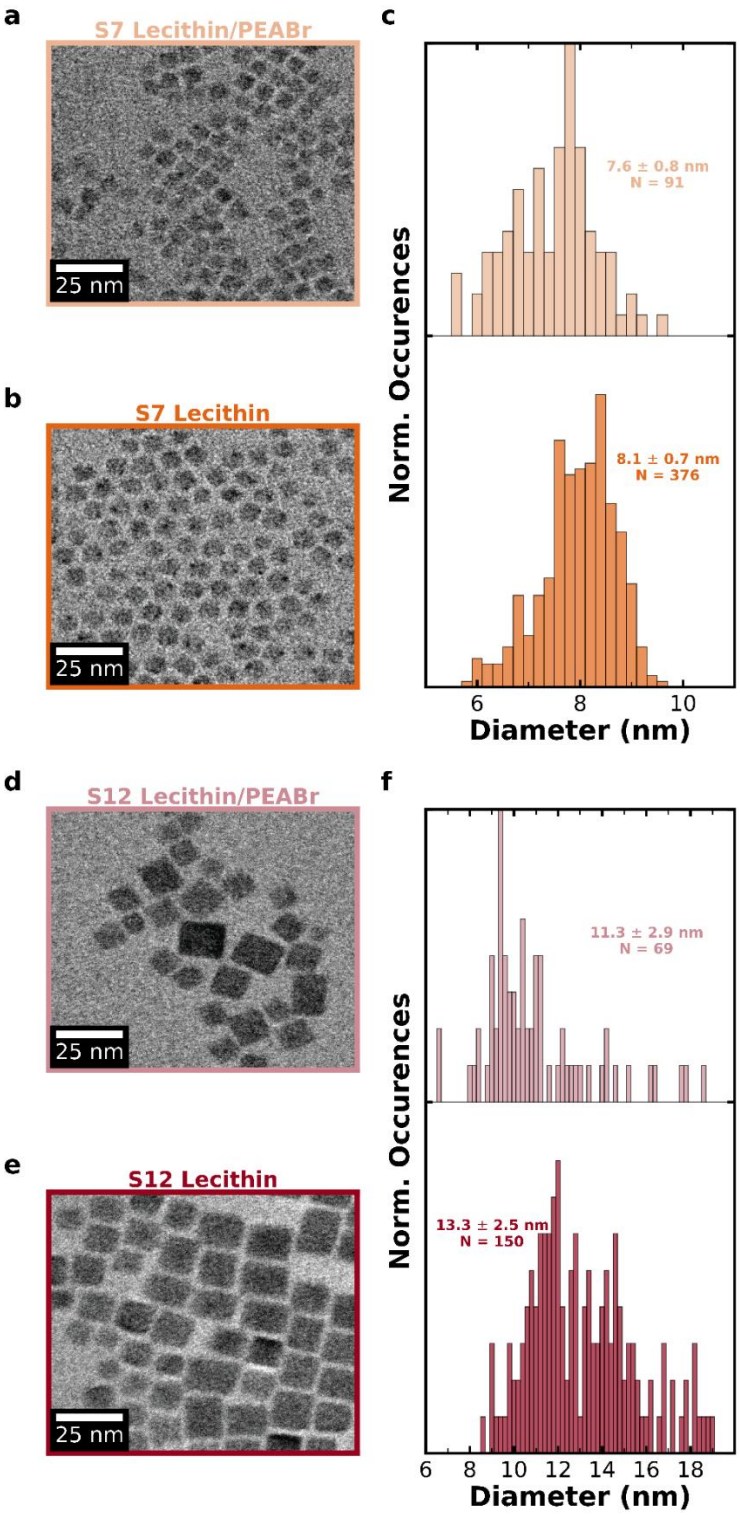

Figure B19: TEMs comparing lecithin- and lecithin/PEABr-capped quantum dots. a) TEM image of S7 lecithin/PEABr-capped quantum dots **b)** TEM image of S7 lecithin-capped quantum dots **c)** TEM measured sizes for S7 lecithin- and lecithin/PEABr-capped quantum dots **d)** TEM image of S12 lecithin/PEABr-capped quantum dots **e)** TEM image of S12 lecithin-capped quantum dots **f)** TEM measured sizes for S12 lecithin- and lecithin/PEABr-capped quantum dots

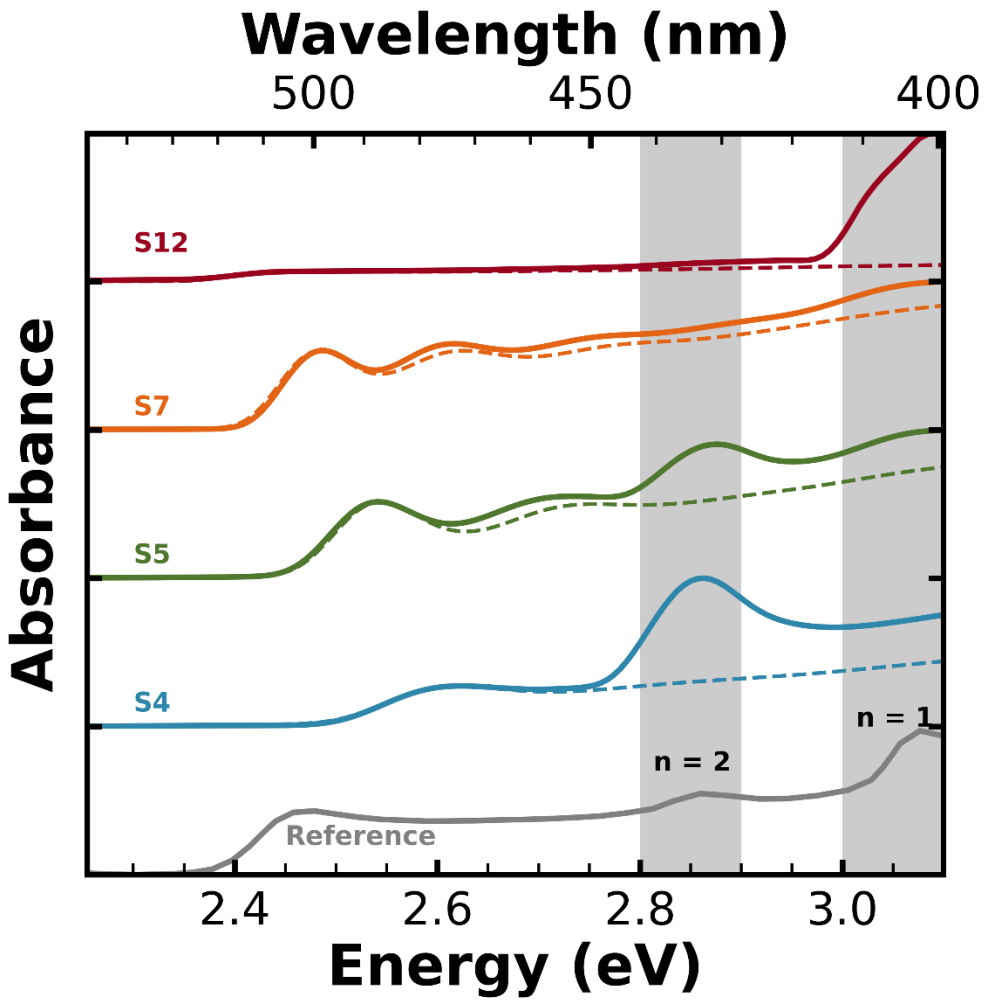

Figure B20: Quasi-2D perovskite formation. Absorbance spectra showing evidence quasi-2D perovskite formation after PEABr treatment (solid lines). Absorbance spectra from the samples prior to PEABr treatment are shown as dashed lines. Quasi-2D perovskite has a formula of $PEA_2Cs_{(n-1)}Pb_nBr_{(3n+1)}$. We see evidence of both n = 2 quasi-2D perovskite which results in a discreet absorbance peak near 2.85 eV and n = 1 quasi-2D perovskite which is responsible for the absorbance peak near 3.05 eV. Reference spectrum is reproduced from [23] copyright 2022 American Chemical Society.

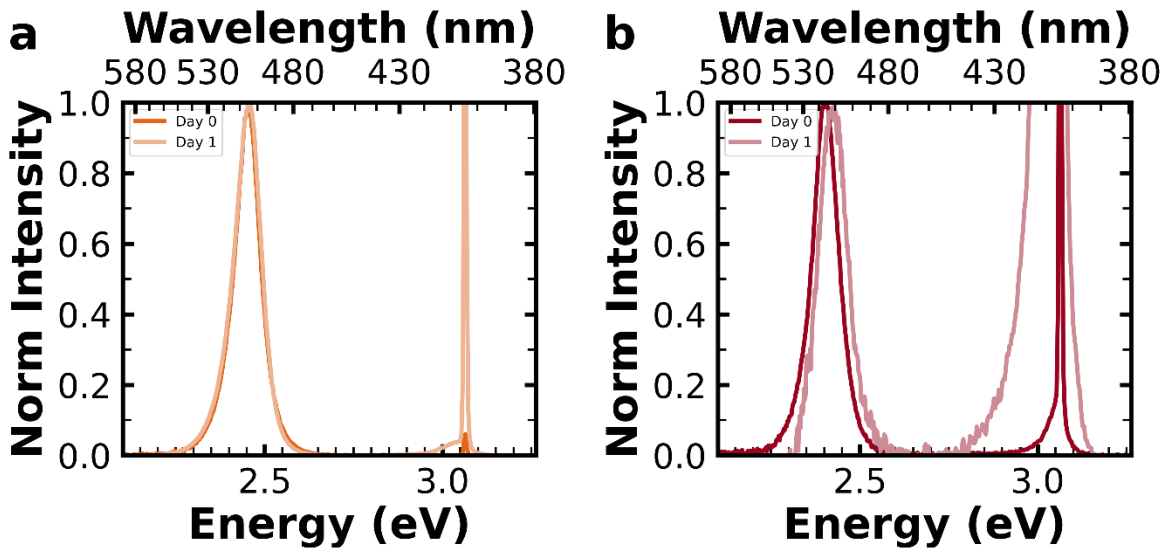

Figure B21: Storage stability of lecithin/PEABr-capped quantum dots for a) S7 and **b)** S12 quantum dots over a 24 hour period. The secondary emission peak near 3.05 eV and corresponds to the convolution of laser scatter from excitation at 405 nm and emission from quasi-2D perovskite. See Figure B20 for more details. Over the course of 24 hours the amount of n = 1 quasi-2D perovskite and other scattering material increases indicating that PEABr treated quantum dots are not colloidally stable.

References

(1) Morad, V.; Stelmakh, A.; Svyrydenko, M.; Feld, L. G.; Boehme, S. C.; Aebli, M.; Affolter, J.; Kaul, C. J.; Schrenker, N. J.; Bals, S.; Sahin, Y.; Dirin, D. N.; Cherniukh, I.; Raino, G.; Baumketner, A.; Kovalenko, M. V. Designer Phospholipid Capping Ligands for Soft Metal Halide Nanocrystals. *Nature 2023 626:7999* **2023**, *626* (7999), 542–548. https://doi.org/10.1038/s41586-023-06932-6.

(2) Ginterseder, M.; Sun, W.; Shcherbakov-Wu, W.; McIsaac, A. R.; Berkinsky, D. B.; Kaplan, A. E. K.; Wang, L.; Krajewska, C.; Šverko, T.; Perkinson, C. F.; Utzat, H.; Tisdale, W. A.; Van Voorhis, T.; Bawendi, M. G. Lead Halide Perovskite Nanocrystals with Low Inhomogeneous Broadening and High Coherent Fraction through Dicationic Ligand Engineering. *Nano Lett* **2023**, *23* (4), 1128–1134. https://doi.org/10.1021/ACS.NANOLETT.2C03354.

(3) Akkerman, Q. A.; Nguyen, T. P. T.; Boehme, S. C.; Montanarella, F.; Dirin, D. N.; Wechsler, P.; Beiglböck, F.; Rainò, G.; Erni, R.; Katan, C.; Even, J.; Kovalenko, M. V. Controlling the Nucleation and Growth Kinetics of Lead Halide Perovskite Quantum Dots. *Science (1979)* **2022**. https://doi.org/10.1126/SCIENCE.ABQ3616.

(4) Krieg, F.; Ong, Q. K.; Burian, M.; Rainò, G.; Naumenko, D.; Amenitsch, H.; Süess, A.; Grotevent, M. J.; Krumeich, F.; Bodnarchuk, M. I.; Shorubalko, I.; Stellacci, F.; Kovalenko, M. V. Stable Ultraconcentrated and Ultradilute Colloids of CsPbX3 (X = Cl, Br) Nanocrystals Using Natural Lecithin as a Capping Ligand. *J Am Chem Soc* **2019**, *141* (50), 19839–19849. https://doi.org/10.1021/JACS.9B09969.

(5) Mooney, J.; Kambhampati, P. Get the Basics Right: Jacobian Conversion of Wavelength and Energy Scales for Quantitative Analysis of Emission Spectra. *Journal of Physical Chemistry Letters* **2013**, *4* (19), 3316–3318. https://doi.org/10.1021/JZ401508T.

(6) Zwillinger, D.; Kokoska, S. *CRC Standard Probability and Statistics Tables and Formulae*; Chapman & Hall: New York, 2000.

(7) Taddei, M.; Smith, J. A.; Gallant, B. M.; Zhou, S.; Westbrook, R. J. E.; Shi, Y.; Wang, J.; Drysdale, J. N.; McCarthy, D. P.; Barlow, S.; Marder, S. R.; Snaith, H. J.; Ginger, D. S. Ethylenediamine Addition Improves Performance and Suppresses Phase Instabilities in Mixed-Halide Perovskites. *ACS Energy Lett* **2022**, *7* (12), 4265–4273. https://doi.org/10.1021/ACSENERGYLETT.2C01998.

(8) Leng, H.; Loy, J.; Amin, V.; Weiss, E. A.; Pelton, M. Electron Transfer from Single Semiconductor Nanocrystals to Individual Acceptor Molecules. *ACS Energy Lett* **2016**, *1* (1), 9–15. https://doi.org/10.1021/ACSENERGYLETT.6B00047.

(9) Gallagher, S.; Kline, J.; Jahanbakhshi, F.; Sadighian, J. C.; Lyons, I.; Shen, G.; Hammel, B. F.; Yazdi, S.; Dukovic, G.; Rappe, A. M.; Ginger, D. S. Ligand Equilibrium Influences Photoluminescence Blinking in CsPbBr3: A Change Point Analysis of Widefield Imaging Data. *ACS Nano* **2024**, *18* (29), 19208–19219. https://doi.org/10.1021/ACSNANO.4C04968.

(10) Schindelin, J.; Arganda-Carreras, I.; Frise, E.; Kaynig, V.; Longair, M.; Pietzsch, T.; Preibisch, S.; Rueden, C.; Saalfeld, S.; Schmid, B.; Tinevez, J. Y.; White, D. J.; Hartenstein, V.; Eliceiri, K.; Tomancak, P.; Cardona, A. Fiji: An Open-Source Platform for Biological-Image Analysis. *Nature Methods 2012 9:7* **2012**, *9* (7), 676–682. https://doi.org/10.1038/nmeth.2019.

(11) Arganda-Carreras, I.; Kaynig, V.; Rueden, C.; Eliceiri, K. W.; Schindelin, J.; Cardona, A.; Seung, H. S. Trainable Weka Segmentation: A Machine Learning Tool for Microscopy Pixel Classification. *Bioinformatics* **2017**, *33* (15), 2424–2426. https://doi.org/10.1093/BIOINFORMATICS/BTX180.

(12) Maes, J.; Castro, N.; De Nolf, K.; Walravens, W.; Abécassis, B.; Hens, Z. Size and Concentration Determination of Colloidal Nanocrystals by Small-Angle x-Ray Scattering. *Chemistry of Materials* **2018**, *30* (12), 3952–3962. https://doi.org/10.1021/ACS.CHEMMATER.8B00903.

(13) Montanarella, F.; Akkerman, Q. A.; Bonatz, D.; Van Der Sluijs, M. M.; Van Der Bok, J. C.; Prins, P. T.; Aebli, M.; Mews, A.; Vanmaekelbergh, D.; Kovalenko, M. V. Growth and Self-Assembly of CsPbBr3Nanocrystals in the TOPO/PbBr2Synthesis as Seen with X-Ray Scattering. *Nano Lett* **2022**, *8*, 28. https://doi.org/10.1021/ACS.NANOLETT.2C04532.

(14) Brennan, M. C.; Forde, A.; Zhukovskyi, M.; Baublis, A. J.; Morozov, Y. V.; Zhang, S.; Zhang, Z.; Kilin, D. S.; Kuno, M. Universal Size-Dependent Stokes Shifts in Lead Halide Perovskite Nanocrystals. *Journal of Physical Chemistry Letters* **2020**, *11* (13), 4937–4944. https://doi.org/10.1021/ACS.JPCLETT.0C01407.

(15) Ryu, J.; Park, S. D.; Baranov, D.; Rreza, I.; Owen, J. S.; Jonas, D. M. Relations between Absorption, Emission, and Excited State Chemical Potentials from Nanocrystal 2D Spectra. *Sci Adv* **2021**, *7* (22), 4741–4769. https://doi.org/10.1126/SCIADV.ABF4741.

(16) Han, Y.; Liang, W.; Lin, X.; Li, Y.; Sun, F.; Zhang, F.; Sercel, P. C.; Wu, K. Lattice Distortion Inducing Exciton Splitting and Coherent Quantum Beating in CsPbI3 Perovskite Quantum Dots. *Nature Materials 2022 21:11* **2022**, *21* (11), 1282–1289. https://doi.org/10.1038/s41563-022-01349-4.

(17) Pejova, B. Optical Absorption of Semiconductor Quantum Dot Solids. *Semicond Sci Technol* **2014**, *29* (4), 045007. https://doi.org/10.1088/0268-1242/29/4/045007.

(18) Li, J.; Gan, L.; Fang, Z.; He, H.; Ye, Z. Bright Tail States in Blue-Emitting Ultrasmall Perovskite Quantum Dots. *Journal of Physical Chemistry Letters* **2017**, *8* (24), 6002–6008. https://doi.org/10.1021/ACS.JPCLETT.7B02786.

(19) He, H.; Yu, Q.; Li, H.; Li, J.; Si, J.; Jin, Y.; Wang, N.; Wang, J.; He, J.; Wang, X.; Zhang, Y.; Ye, Z. Exciton Localization in Solution-Processed Organolead Trihalide Perovskites. *Nature Communications 2016 7:1* **2016**, *7* (1), 1–7. https://doi.org/10.1038/ncomms10896.

(20) Maes, J.; Balcaen, L.; Drijvers, E.; Zhao, Q.; De Roo, J.; Vantomme, A.; Vanhaecke, F.; Geiregat, P.; Hens, Z. Light Absorption Coefficient of CsPbBr3 Perovskite Nanocrystals. *Journal of Physical Chemistry Letters* **2018**, *9* (11), 3093–3097. https://doi.org/10.1021/ACS.JPCLETT.8B01065.

(21) Förster, T. *Biological Physics*; Mielczarek, E. V. ., Greenbaum, E. S. ., Knox, R. S. ., Eds.; American Institute of Physics, 1993.

(22) Oriel, E. H.; Dirin, D. N.; Shcherbak, K.; Bodnarchuk, M. I.; Kovalenko, M. V.; Chen, L. X.; Schaller, R. D. Intraband Cooling and Auger Recombination in Weakly to Strongly Quantum-Confined CsPbBr3 Perovskite Nanocrystals. *Journal of Physical Chemistry Letters* **2024**, *15* (23), 6062–6068. https://doi.org/10.1021/ACS.JPCLETT.4C00941/ASSET/IMAGES/LARGE/JZ4C00941_0004.JPEG.

(23) Xiao, M.; Xiang, T.; Kim, D.; Wang, M.; Zhang, W.; Ahmadi, M.; Li, T.; Wu, X.; Xu, L.; Chen, P. Superior External Quantum Efficiency of LEDs via Quasi-2D Perovskite Crystals Implanted with Phenethylammonium Acetate. *ACS Appl Mater Interfaces* **2022**, *14* (40), 45352–45363. https://doi.org/10.1021/ACSAMI.2C12048.

Appendix C: Supporting Information Trion Formation Hampers Single Quantum Dot Performance in Silane-Coated $FAPbBr_3$ Quantum Dots

Jessica Kline, Shaoni Kar, Benjamin F. Hammel, Yunping Huang, Seth R. Marder, Sadegh Yazdi, Gordana Dukovic, Henry Snaith, David S. Ginger

Table of Contents

Table of Contents

Synthesis

Chemicals

Formamidine acetate (99%), oleic acid (OA, ≥ 99%), octadecene (ODE, 90%), oleylamine (OAm, 70%), trioctylphosphine oxide (TOPO, 99%), hexanes (≥ 95%), toluene (anhydrous 99.8%), octane (anhydrous ≥ 99%), formamidinium bromide (FABr, ≥ 98%), isopropanol (IPA, 90%), ethyl acetate (≥ 99%), acetonitrile (≥ 99%), N-(2-aminoethyl)-3-aminopropyltriethoxysilane (AEAPTES) and Ludox TMA (34 wt.%) were purchased from Millipore Sigma. Lead (II) bromide ($PbBr_2$, 99.998% metals basis) was purchased from Alfa Aesar. All chemicals were used as received. $PEAC_8C_{12}$ was synthesized according to Morad et al.[1]

$PEAC_8C_{12}$-passivated $FAPbBr_3$ synthesis

0.08 M $PbBr_2$-TOPO and 0.12 M FA-OA solutions were prepared according to Morad et al.[1] A 0.05 M solution of $PEAC_8C_{12}$ was prepared by dissolving 42 mg (0.10 mol) $PEAC_8C_{12}$ in 2 mLs of a 1:1 mixture of IPA and toluene. 260 µL of the $PbBr_2$-TOPO solution and 100 µL of the FA-OA solution were added to 5 mLs of hexanes and allowed to react while stirring for 30 s. After 30 s, 240 µL of the $PEAC_8C_{12}$ solution were added and the mixture was allowed to react for another 30s. The quantum dots were then washed with a 2:1 mixture of ethyl acetate and acetonitrile and centrifuged at 10 krpm for 5 minutes. The precipitate was dissolved in 2 mLs hexanes and stored in the glovebox.

Silane-coated $FAPbBr_3$ synthesis

Formamidinium lead bromide ($FAPbBr_3$) nanocrystals were synthesized via a conventional hot-injection method. In a typical procedure, 0.2 mmol of $PbBr_2$ was dissolved in 5 mL of octadecene (ODE) containing 0.5 mL of oleic acid (OA) and 0.5 mL of oleylamine (OAm) under nitrogen atmosphere. The mixture was dried under vacuum at 120 °C for 30 min to remove moisture and oxygen and then heated to 170 °C. A precursor solution of formamidinium bromide (FABr, 0.2 mmol) dissolved in 2 mL of ODE was swiftly injected into the hot $PbBr_2$ solution. The reaction mixture was quenched after 7 s by immersion in an ice–water bath, yielding a bright green colloidal dispersion. The crude solution was centrifuged at 6000 rpm for 5 min after the addition of 10 mL of methyl acetate to precipitate the nanocrystals, which were then redispersed in toluene for further processing.

To improve surface passivation and environmental stability, the as-synthesized $FAPbBr_3$ nanocrystals were subjected to post-synthetic ligand exchange using AEAPTES. In a typical treatment, a 0.1 mL aliquot of AEAPTES was added dropwise to 5 mL of the nanocrystal dispersion in toluene (≈5 mg mL^{-1} concentration) under inert conditions. The mixture was stirred for 30 min at room temperature, and the exchanged nanocrystals were purified by adding acetone (3× volume) to induce precipitation, followed by centrifugation and redispersion in toluene. The resulting AEAPTES-capped $FAPbBr_3$ nanocrystals exhibited enhanced colloidal stability and photoluminescence retention under ambient conditions.

Characterization

Ensemble Optical Characterization

Absorbance spectra of the QD solutions were performed using a Perkin-Elmer Lambda 950 UV/Vis/NIR Spectrometer in a range of 400-600 nm with an integration time of 0.5 s. Absorbance spectra were transformed from wavelength to their Einstein B spectrum according to Equation C1.[2]

$$A(E) \propto {}^{A(\lambda)}/_{\nu} \tag{C1}$$

Steady-state photoluminescence spectra were acquired *via* a home-built fluorescence set up. Dilute solutions (OD of 0.0001 at 405 nm) were excited with a 405 nm laser (CrystaLaser) and spectra were collected on an OceanHDX (Ocean Insight). Spectral correction was performed using a calibrated white light source (Ocean Insight HL-3P-INT-CAL) to correct for the responsivity of the detector. Photoluminescence spectra were converted from wavelength to energy and corrected for line shape analysis according to Equation C2.[2]

$$I(E) \propto {}^{I(\lambda)}/_{\nu^3 E^2} \tag{C2}$$

Photoluminescence quantum yield measurements (PLQY) were performed on a commercial integrating sphere system (Hamamatsu Photonics K.K). PLQY values are determined using a white light source (Hamamatsu Mercury Xenon Lamp) and a monochromator for wavelength selection (405 nm) as the excitation source to illuminate the samples in an integrating sphere (Hamamatsu Photonics K.K). The optical density of samples was kept below 0.1 at the excitation wavelength to minimize reabsorption effects. Spectral correction was performed using a calibrated white light source (Ocean Insight HL-3P-INT-CAL) to correct for the responsivity of the detector.

Time resolved photoluminescence measurements at 470 nm excitation were acquired using a commercial PicoQuant FluorTime 100 system with LDH-470 laser diode, a 470 nm picosecond pulsed diode laser. The repetition rate is controlled by an external trigger input from a PicoHarp PDL 800-B laser driver and was set to 1 MHz. A photomultiplier tube (PMT) detector was used in TCSPC mode with an instrumental response function (IRF) of approximately 400 ps. The instrument response function (IRF) was measured via laser scatter from a solution of Ludox. Lifetimes were fit to a stretch exponential (Equation C3) using a custom IRF-reconvolution python package.

$$I(t) = A \exp\left(-\frac{t}{\tau_k}\right)^{\beta} + C \tag{C3}$$

Where A is the pre-exponential factor, τ_k is the lifetime of the decay, C is the background of the measurement and β is the distribution of decay rates. τ_{str}, the average lifetime of a stretch exponential, is calculated according to Equation C4 where Γ is the gamma function.[3]

$$\tau_{str} = \frac{\tau_k}{\beta}\Gamma\left(\frac{1}{\beta}\right) \tag{C4}$$

Single Quantum Dot Optical Characterization - Widefield

Single quantum dot films were prepared by diluting quantum dot stock solutions by a factor of 1,000 in toluene. 60 µL of this dilute solution was then spun coat onto a clean[4] low fluorescence glass coverslips (VistaVision #1.5 22x22 mm, VWR) at 2,000 rpm for 40 seconds.

Widefield microscopy measurements were performed on a Nikon TE2000 inverted optical microscope using a CFI Super Fluor 40x Oil immersion objective (NA = 1.3), with Olympus F immersion oil. The illumination source was a 415 nm LED (SOLIS-415C, Thor Labs) at a power density of 9 mW/cm^2. The following filters were used for the measurement: ET510/80m (Chroma), FF01-424/SP-25 (Semrock) and ZT442rdc (Chroma) mounted in Chroma Laser TIRF for Nikon TE2000/T filter cube. Videos of the sample photoluminescence in time were collected on a Prime 95B (Photometrics) camera for 6 minutes and 40 seconds (8000 total images) with an integration time of 50 ms per image.

Single Quantum Dot Optical Characterization - Confocal

Single quantum dot films were prepared by diluting quantum dot stock solutions by a factor of 1,000 in toluene. 60 µL of this dilute solution was then spun coat onto a clean [4] 1 mm thick quartz microscope slide (SPI) at 2,000 rpm for 40 seconds.

Single quantum dot optical characterization was carried out on a home-built confocal microscope integrated with a cryostat (AttoDry800, Attocube). Samples were illuminated with a pulsed 472 nm laser (15.647 MHz, 95 W/cm^2, NKT Photonics). The laser is cleaned up by a bandpass filter (ET470/24m, Chroma) and focused (1/e^2 = 1.7 µm) by an objective inside the cryostat (NA = 0.82) onto the sample, and the same objective collects the emitted light. The collected light is passed through a dichroic (Di02-R488, Semrock), a notch filter (ZET473NF, Chroma) and a bandpass (ET520/20m, Chroma) to filter out residual light from the excitation laser and substrate autofluorescence. The collected light is then sent to either a spectrometer and electron-multiplying charge-coupled device camera (Isoplane 320 and Pixis 400, Princeton Instruments) or a Hanbury Brown-Twiss interferometer. The Hanbury Brown-Twiss interferometer consists of a 50/50 beam splitter, two avalanche photodiodes (35 ps IRF, Micro Photon Devices) and photon counting electronics (Swabian) enabling the acquisition of time-tagged time-resolved (TTTR) data. Single quantum-dot measurements were carried out in the weak excitation regime at a fluence of 6.1 µJ/cm^2.

At room temperature quantum dot spectra were obtained with an integration time of 20 seconds on a 600 lines/mm grating. Substrate autofluorescence was subtracted from the spectra and then the spectra were corrected for detector sensitivity using a calibrated white light source (Ocean Insight HL-3P-INT-CAL). Spectra are converted from wavelength to energy (Equation C2) and fit to a single Gaussian of the form:

$$I(E) = {}^{A}/_{\sigma\sqrt{2\pi}} \exp\left[-0.5\left({}^{(E-\mu)}/_{\sigma}\right)^2\right] + b \qquad \text{(C5)}$$

Where A is the amplitude, b is the background, µ is the center of the peak and σ is the standard deviation of the peak. TTTR data was then acquired on the quantum dots for 600 seconds. TTTR data was analyzed using a modified version of the poissonian noise Change Point Analysis (CPA) package from Palstra et al [5] (see **Data Analysis** for more details).

At 4K quantum dot spectra were obtained with an integration time of 1 second on a 600 lines/mm grating. 300 spectra were acquired sequentially after which 600 seconds of TTTR data was acquired followed by the acquisition of another 300 sequential spectra. For each of the 600 spectra substrate autofluorescence was subtracted from the spectra and then the spectra were corrected for detector sensitivity using a calibrated white light source spectra are converted from wavelength to energy

(Equation C2) are fit by a single Gaussian (Equation C5). Spectra with less than 10% of the area of the most intense spectrum are considered OFF and are not factored into the analysis further. The time integrated single quantum dot spectrum is the summation of qualifying single frame spectra.

Scanning Transmission Electron Microscopy (STEM)

STEM was performed with a Thermo Fisher Scientific Titan Themis operated at 300kV. Samples were prepared by drop-casting solutions of $FAPbBr_3$ QDs onto ultrathin carbon film TEM grids (Ted Pella, Prod # 01824, ultrathin carbon film on lacey carbon support film, 400 mesh, Cu). To minimize air exposure, grid prep was performed in a glovebox with an argon atmosphere. After drop-casting, the grids were dried under vacuum in the glovebox antechamber for roughly 30 min, before being transferred back into the glovebox, sealed in an air-tight container, and transported to the microscopy facility.

Size analysis was performed using ImageJ (version 1.54f), specifically the FIJI distribution. Particles were segmented using the Trainable Weka Segmentation plug-in (v3.3.4). The particle areas were measured using the "Analyze Particle" function in ImageJ, with size limits set from 25 – 50 nm2 and shape limits from circularity = 0.5 to 1.0 to exclude noise, secondary, or aggregated particles.

Attenuated Total Reflectance Infrared Spectroscopy (ATR-IR)

ATR-IR was performed in the solid-state on a PerkinElmer Frontier FT-IR spectrometer. Samples were prepared by drop-casting quantum dot solutions on indium tin oxide-coated glass substrates.

Data Analysis

Widefield Blinking Data

The analysis of widefield blinking data is described in detail in Gallagher et al.[4] But in brief we identify individual quantum dots in a video using the Laplacian of Gaussian method and process the blinking data using a version of CPA adapted for a Gaussian-distributed time series as published by Yang et al.[6] . Our particle selection and CPA code is publicly available at: https://github.com/GingerLabUW/Widefield-CPA.

TTTR Data

Single quantum dot lifetimes were fit using a custom IRF-reconvolution python package. At room temperature the lifetimes were fit to a stretch exponential (Equations C3 and S4). At 4K the lifetimes were fit to a biexponential (Equation C6) where τ_{fast} was assumed to capture the lifetime of the bright triplet and τ_{slow} is due to emission from the dark singlet.[7]

$$I(t) = A \exp\left(-\frac{t}{\tau_{fast}}\right) + (1 - A)\exp\left(-\frac{t}{\tau_{slow}}\right) + C \qquad \text{(C6)}$$

Classification of the TTTR blinking traces was performed using a modified version of the poissonian noise CPA package from Palstra et al [5]. Our code is publicly available at: https://github.com/GingerLabUW/Cryostat-Data-Processing. We chose to apply an additional penalty after the "true" number of states was returned by the Bayesian Information Criterion which limited the fit based on the physical constraints of the system. Since three times standard deviation of the dark noise is 150 cps in our system, we reduce the number of "true" states by one until the splitting between all identified intensity levels is at least 150 cps.

As perovskite QDs exhibit multi-level blinking, we find that the traditional ON, OFF and GREY definitions are insufficient to capture the data. Traditionally the ON state is the CPA identified maximum intensity level, the OFF state is anything below the average dark counts + 3 standard deviations, and any other states are GREY. In our data set these definitions result in traces which are classified as around 70% GREY on average, meaning that most of our data is effectively being thrown out. Instead, we choose to treat our GREY states as representing a linear combination of our traditionally defined ON and OFF states. Which can be rationalized as either due to fast blinking events or an instantaneous k_{nr} which is similar to the k_r as in the ON state $k_r >> k_{nr}$ and in the OFF state $k_{nr} >> k_r$. As such we can calculate the weighted ON and OFF fractions for each trace as shown in Equations C7a-c.

$$I_n = a_n I_{ON} + (1 - a_n) I_{OFF} \tag{C7a}$$

$$f_{ON} = \sum_n a_n T_n \tag{C7b}$$

$$f_{OFF} = \sum_n (1 - a_n) T_n \tag{C7c}$$

Where I_{ON} is the CPA identified maximum intensity level, I_{OFF} is the average APD dark counts + 3 standard deviations (300 cps at room temperature, 500 cps at 4K), I_n is any CPA identified intensity level, a_n is the fraction of ON character in an intensity level and T_n is the fraction of total measurement time spent in the intensity level. For example, for the quantum dot shown in Figure C6 our methodology classifies the blinking trace as 37% ON and 63% OFF which we find is a better descriptor than traditional ON/OFF/GREY classification (26% ON, 47% OFF and 27% GREY) or traditional ON/OFF classification (53% ON and 47% OFF).

To fit fluorescence lifetime intensity distributions (FLIDs) we find the lifetime of each CPA identified intensity level. We consider two primary non-radiative decay mechanisms which can be responsible for blinking in these quantum dots.[8] Non-radiative band-carrier (BC) recombination which can occur in a neutral quantum dot and non-radiative Auger recombination which can occur in a photoionized quantum dot. The expected lifetime intensity relationships are described in Equations C8a and b respectively. As individual quantum dots can experience both BC and Auger blinking during a measurement the measured lifetime intensity correlation is fit to a linear combination of BC and Auger blinking (Equation C8c). Single QD FLIDs were not lifetime or intensity normalized before fitting to Equation C8. FLIDs were only normalized to construct the representative average FLIDs shown in Figure 4 in the Main Text. During the normalization process, the lifetime- and intensity- axes were divided by the maximum observed lifetime and intensity respectively.

$$I(\tau)_{Auger} = \frac{I_{ON} I_{OFF,Aug} (\tau_{OFF,Aug} - \tau_{ON})}{I_{OFF,Aug} (\tau_{OFF,Aug} - \tau) + I_{ON} (-\tau_{ON} + \tau)} \tag{C8a}$$

$$I(\tau)_{BC} = \frac{I_{OFF,BC} - I_{ON}}{\tau_{OFF,BC} - \tau_{ON}} \tau \tag{C8b}$$

$$I(\tau) = \alpha I(\tau)_{BC} + (1 - \alpha) I(\tau)_{Auger} \tag{C8c}$$

We use a mono-exponential function to fit the $g^{(2)}(\tau)$ data and determine $g^{(2)}(0)$ (Equations C9a-b).

$$g^{(2)}(\tau) = b + \sum_n A_n \exp\left(^{-|\tau - r_n|}/_{\tau_{TRPL}}\right) \tag{C9a}$$

$$g^{(2)}(0) = {}^{6 * A_4}/_{(A_1 + A_2 + A_3 + A_5 + A_6 + A_7)} \quad \text{(C9b)}$$

Where b is the constant background counts, A_n is the amplitude of the n-th peak, r_n is the peak of the n-th peak (approximately -192, -128, -64, 0, 64, 127 and 192 ns respectively) and τ_{TRPL} is the average lifetime. $g^{(2)}(0)$ is then determined as the ratio between the area of the peak at zero time delay at the averaged area of the side peaks.

Photoluminescence Components

To look at the components of single quantum dot photoluminescence we first correct the short (1s) integration time spectra for spectral variations in time (blue shifting and spectral diffusion) according to Gumbsheimer et al.[9] The 600 short time spectra were then summed into one long time (600 s) spectrum.

To fit single quantum dot photoluminescence components, we consider five contributors – the zero phonon line (ZPL) at 0 meV, optical phonon 1 (OP_1) at -4.9 meV, optical phonon mode 2 (OP_2) at -19.5 meV, trion emission (X*) and biexciton emission (XX). Each component is considered to have a gaussian contribution with equal standard deviations and different emission maxima/heights as described in Equation C10.

$$I(E) = g(a, 0, \sigma)_{zpl} + g(a, -4.9, \sigma)_{op1} + g(a, -19.5, \sigma)_{op2} + g(a, \mu, \sigma)_{x*} + g(a, \mu, \sigma)_{XX} + b \quad \text{(C10)}$$

The emission maxima of the ZPL, OP_1 and OP_2 contributions are fixed to 0, -4.9 and 19.5 meV respectively[10–12] and the emission maxima of the X* and XX contributions are fit. Based on the reported trion and biexciton binding energies in the literature we constrain the emission maxima of the trion between -40 and -20 meV and the biexciton between -60 and -30 meV.[10] The standard deviation of the Gaussians is constrained between 5 and 15 meV. Additionally we constrain the intensity of the optical phonon emission peaks based on the reported strength of these peaks in ~ 6 nm $FAPbBr_3$ quantum dots. OP_1 must be between [0.5, 1]*a_{zpl}, and OP_2 is constrained between [0.01, 0.15]*a_{zpl}.[11,12]

Fluence Dependent PLQY

We estimate the PLQY of the quantum dot thin films by first measuring the PLQY of the quantum dot thin films at room temperature in an integrating sphere. We then measure the intensity of our films on the confocal-integrated cryostat at room temperature using our lowest excitation power (4.5E-4 μJ/cm^2). The film intensities were determined by averaging the intensity of six 29x29 μm scans acquired with a resolution of 0.5 μm. The films were subsequently cooled down to 4K and another series of six 29x29 μm scans were acquired with a resolution of 0.5 μm to determine the average film intensity at 4K. The dwell time at each pixel was less than 50 ms to prevent photobleaching from affecting the measurement. We assume that the absorbance cross section does not change between room temperature and 4K and as such the PLQY at 4K equal to the room temperature PLQY scaled by the change in film intensity.

The absorption cross section of the films were determined by fitting the long-time photoluminescence intensity to:

$$I = q * (1 - e^{-\sigma j}) \quad \text{(C11)}$$

Where q is the quantum yield at a given fluence, σ is the absorption cross section and j is the incident fluence in photons/cm^2.

During the fitting process we constrain the parameters of Equation 1 in the Main Text as follows. $k_{r,X}$ and $k_{nr,X}$ are fixed by measuring the lifetime and quantum yield of the quantum dots at the lowest fluence, where recombination is dominated by the exciton. Selected fluence dependent lifetimes are shown in Figure C15. The radiative rates of the trion and biexciton are constrained by the expected statistical scaling of radiative rates such that $k_{r,X\pm} = [1.5, 2.5]*k_{r,X}$ and $k_{r,XX} = [3.5, 4.5]*k_{r,XX}$.[13] The non-radiative rate of the trion and trapping rate of the biexciton are free parameters, and the non-radiative rate of the biexciton is constrained by the expected statistical scaling of Auger rates such that $k_{nr,XX} = [3.5, 4.5]*k_{nr,X\pm}$.[13]

Before selecting the model depicted in Figure 5a of the Main Text, we considered many potential models to explain fluence dependent quantum yield changes in quantum dots. These potential models and their fits for our fluence dependent quantum yield data are shown in Figure C16. The three models we primarily considered are: (1) QY roll off due to biexciton formation with no trion formation (2) conversion of the exciton to a dark charged state and a subsequent absorption event to generate a trion and (3) a combination of the dark charged and biexciton pathways for trion formation. QY roll off due to biexciton formation with no trion formation (model 1) is discarded because this model can not capture the experimental QY roll-off of silane-coated quantum dots. Even without constraining the biexciton radiative and non-radiative rates, Model 1 always predicts shallower QY roll-off than experimentally observed in the silane-coated quantum dots. Conversion of the exciton to a dark charged state which can then generate a trion (model 2) is discarded because this model predicts a large steady state population (> 80%) of the dark charged state which is inconsistent with the high weighted ON%s observed in both quantum dot samples. A combination of the dark charged and biexciton pathways for trion formation (model 3) is discarded because of the predicated large steady state population of the dark charged state which is inconsistent with the high weighted ON%s observed in both quantum dot samples and trion and biexciton rate constants which do not converge to a unique solution within reasonable physical bounds.

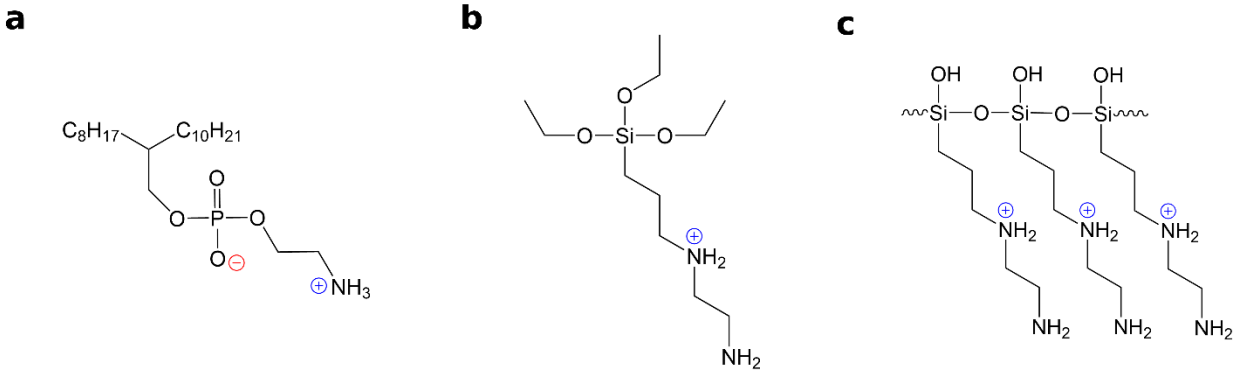

Figure C1. Chemical structures of **a)** $PEAC_8C_{12}$ **b)** mono-protonated N-(2-aminoethyl)-3-aminopropyltriethoxysilane (AEAPTES) and **c)** hydrolyzed mono-protonated AEAPTES. Although AEAPTES is neutral, the acid-base chemistry of our solutions suggests that the functional form of AEAPTES is mono-protonated. Protonation likely occurs via proton transfer from free oleylammonium in solution ($K_{tranfser} \sim 0.3$) and the counterion for mono-protonated AEAPTES takes the form of free oleate or Br-.

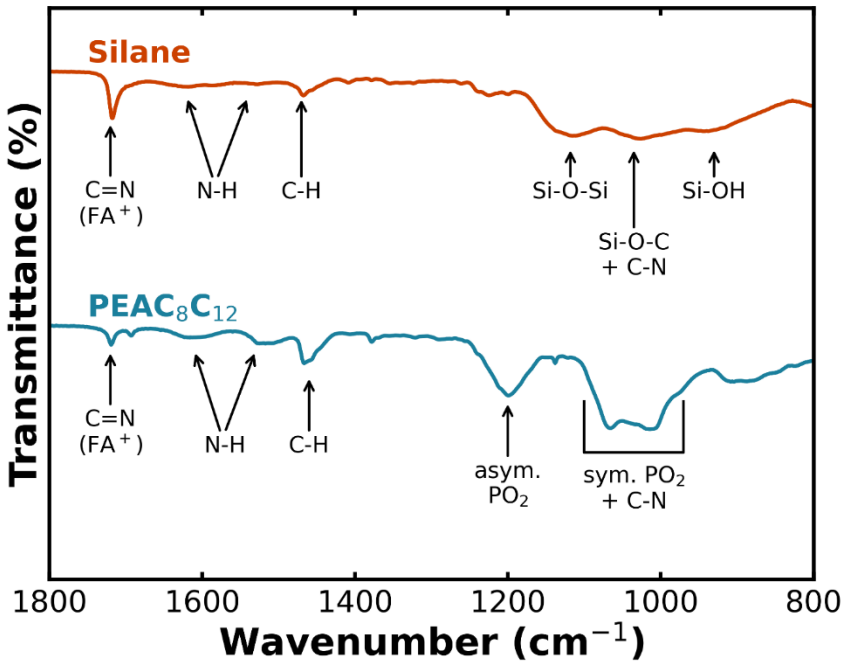

Figure C2. AT-IR characterization of $PEAC_8C_{12}$-passivated (blue) and silane-coated (orange) quantum dot samples. Both samples show C=N stretching from FA^+ and NH and CH bending from the ligands.[1,14,15] $PEAC_8C_{12}$-passivated quantum dots also show PO_2 and C-N stretches.[1] In contrast silane-coated quantum dots show Si-O-Si, Si-O-C, Si-OH and C-N vibrations[1,15] indicating the partial hydrolysis and cross-linking of the triethoxysilane tail.

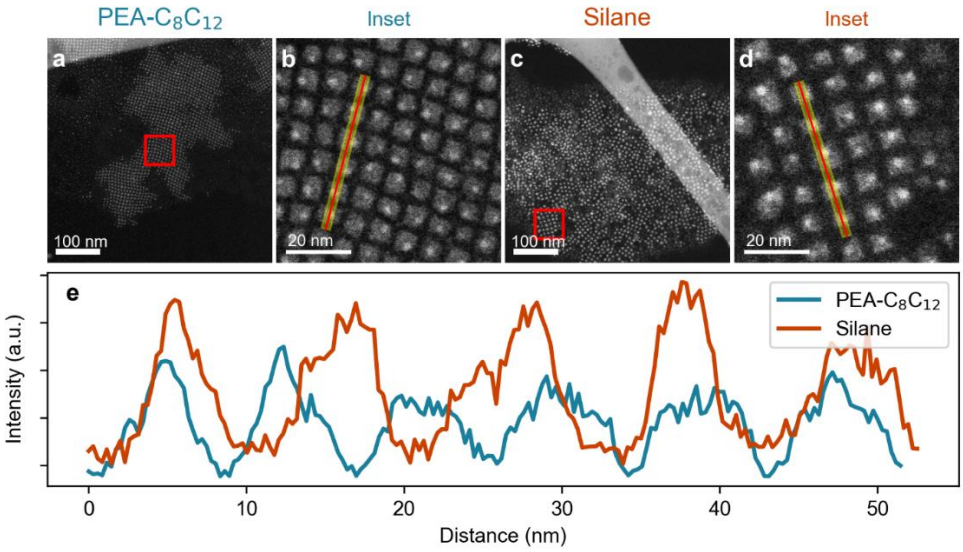

Figure C3. HAADF-STEM images of **a)** $PEAC_8C_{12}$-passivated and **c)** silane-coated $FAPbBr_3$ quantum dots, with insets **b and d)** indicated by the red box in the full image. The red line with yellow highlight illustrates the path and linewidth, respectively, of the line profiles. **e)** Line profiles of HAADF intensity for the $PEAC_8C_{12}$-passivated and silane-coated $FAPbBr_3$ quantum dots. The regular size and shape of the quantum dots encourages the formation of well-ordered regions; line profiles across these regions reveal that the silane-coated quantum dots are slightly larger and have greater distances between particles than the $PEAC_8C_{12}$-passivated quantum dots. This suggests that the silane-coating contributes to the size of the particles as well as the size of the ligand sphere.

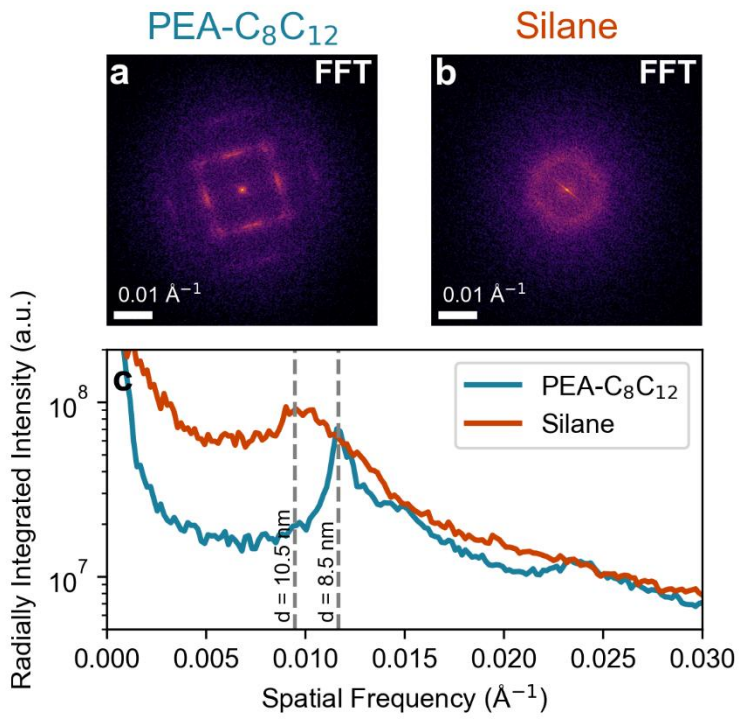

Figure C4. FFTs of HAADF-STEM images of **a)** $PEAC_8C_{12}$-passivated (Figure C2a) and **b)** silane-coated $FAPbBr_3$ quantum dots (Figure C2c). **c)** Radially integrated intensity of the FFTs. To determine the averaging packing distances over the entirety of both HAADF-STEM images, we computed the fast Fourier transformation (FFT). In this case, peaks in the FFT correspond to periodicity in the particle packing. In the image of the $PEAC_8C_{12}$-passivated quantum dots (Figure C2a), the particles are ordered in a large superlattice domains with small orientational mismatches, which results in well-defined peaks. In the image of the silane-coated quantum dots (Figure C2c), there are smaller superlattice domains with different orientations, which results in a less-defined circular pattern. The radial integration of the FFT (Figure C3c) demonstrates that the silane-coated quantum dots are, on average, further spaced than the $PEAC_8C_{12}$-passivated quantum dots. Assuming that the spacing equals the particle size (e.g., the edge length) plus twice the thickness of the ligand sphere, (accounting for the two layers of ligands in the gap between two particles), comparing the spacing (8.5 and 10.5 nm) to the average sizes in Figure 1d (6.2 and 7.3 nm) allows us to estimate ligand sphere thicknesses of 1 nm and 1.5 nm for the $PEAC_8C_{12}$-passivated and silane-coated quantum dots, respectively. Altogether, this suggests that the silane-coating contributes about 0.5 nm to the size of the particles as well as 0.5 nm to the size of the ligand sphere.

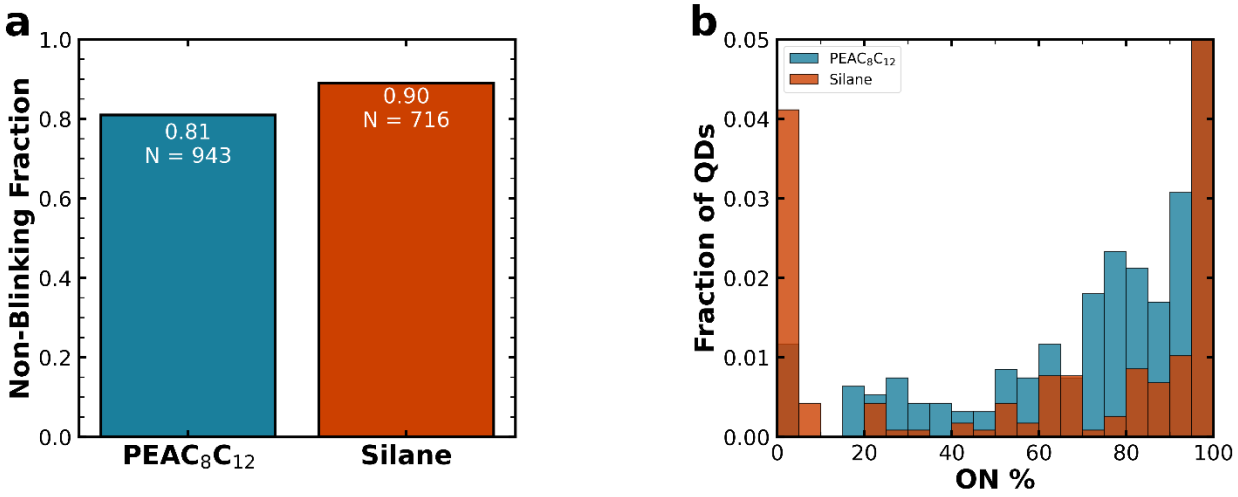

Figure C5. Widefield blinking characterization of single $FAPbBr_3$ quantum dots a) the non-blinking fraction (≥ 95% ON) for both passivation methods **b)** distribution on quantum dot ON% for both passivation methods. In widefield, blinking $PEAC_8C_{12}$-passivated quantum dots tend to blink less than their silane-coated counterparts.

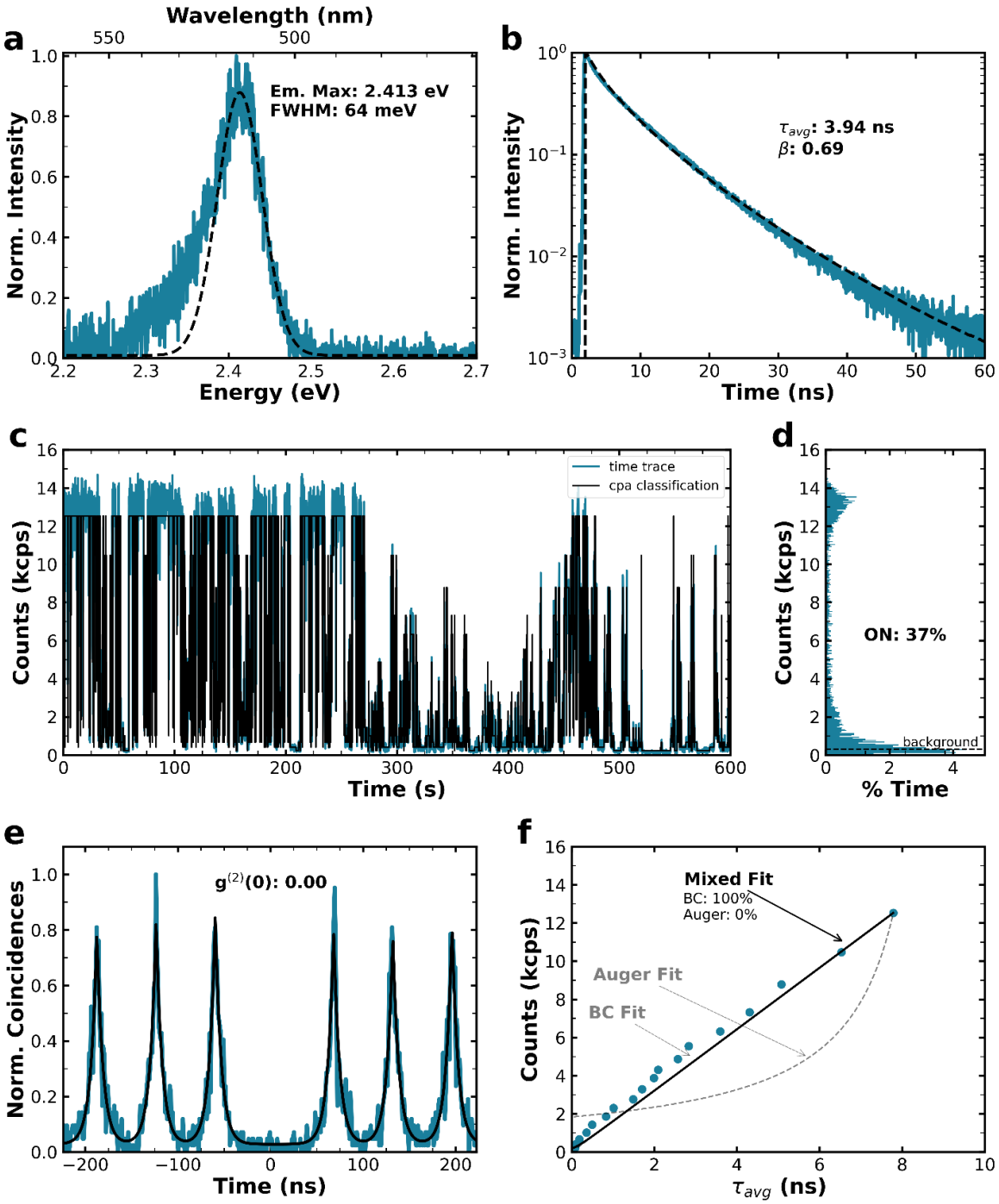

Figure C6. Example room temperature characterization of a single $PEAC_8C_{12}$-passivated $FAPbBr_3$ quantum dot a) the single quantum dot photoluminescence spectrum is shown in blue while the black dashed lines represent the Gaussian fit from which the emission maximum and FWHM are extracted **b)** photoluminescence lifetime (blue) and stretched exponential fit (black dashed line) **c)** experimental blinking trace (blue) and CPA classified blinking trace (black) **d)** photoluminescence intensity histogram **e)** experimental $g^{(2)}(\tau)$ trace (blue) and fit (black) **f)** CPA identified intensity levels correlated to their measure lifetime (blue points). Dashed lines represent the Auger- and BC-type blinking fits (Equations C8a and b) of the data while the solid black line represents the combination of both blinking types.

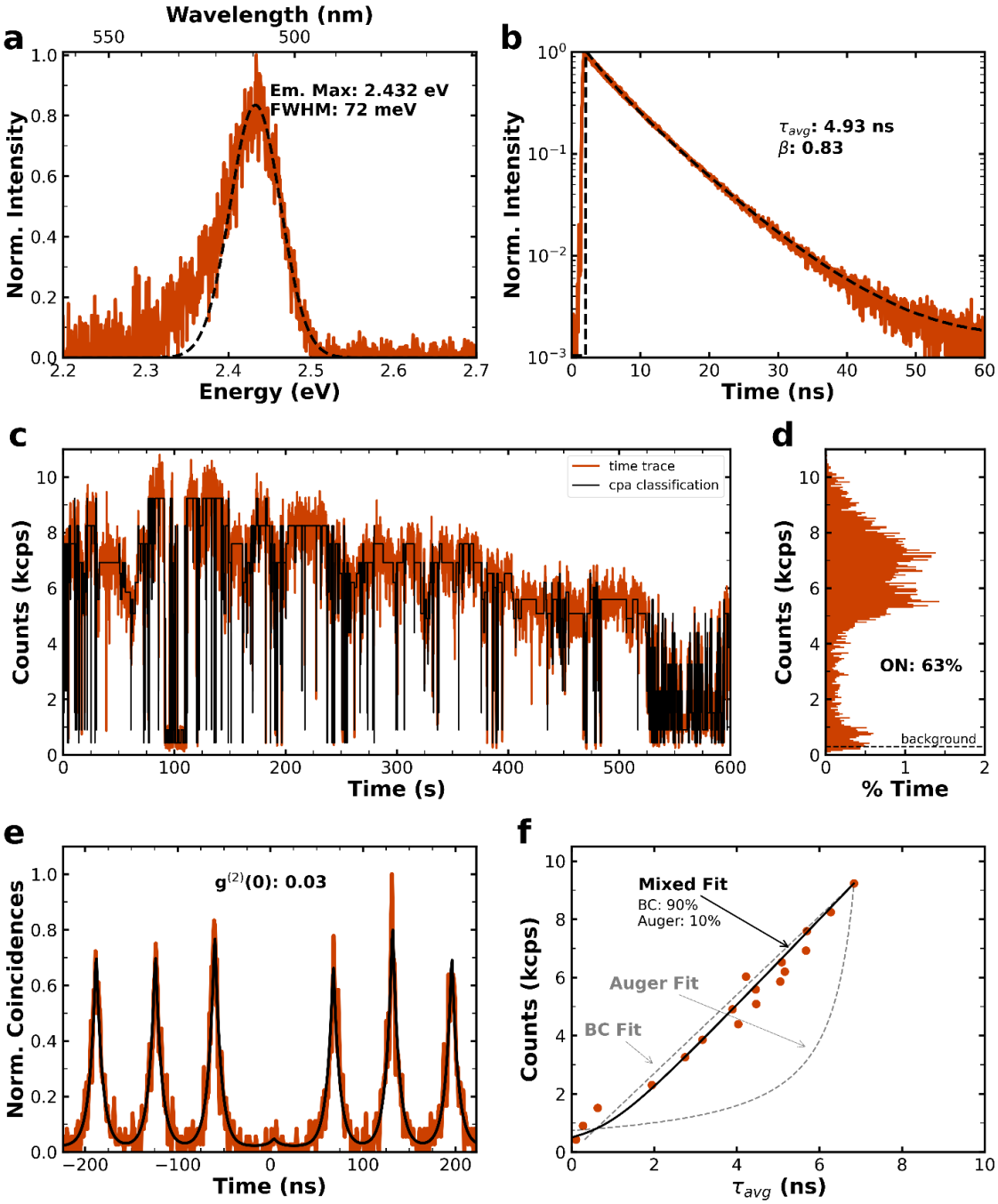

Figure C7. Example room temperature characterization of a single silane-coated $FAPbBr_3$ quantum dot a) the single quantum dot photoluminescence spectrum is shown in orange while the black dashed lines represent the Gaussian fit from which the emission maximum and FWHM are extracted **b)** photoluminescence lifetime (orange) and stretched exponential fit (black dashed line) **c)** experimental blinking trace (orange) and CPA classified blinking trace (black) **d)** photoluminescence intensity histogram **e)** experimental $g^{(2)}(\tau)$ trace (orange) and fit (black) **f)** CPA identified intensity levels correlated to their measure lifetime (orange points). Dashed lines represent the Auger- and BC-type blinking fits (Equations C8a and b) of the data while the solid black line represents the combination of both blinking types.

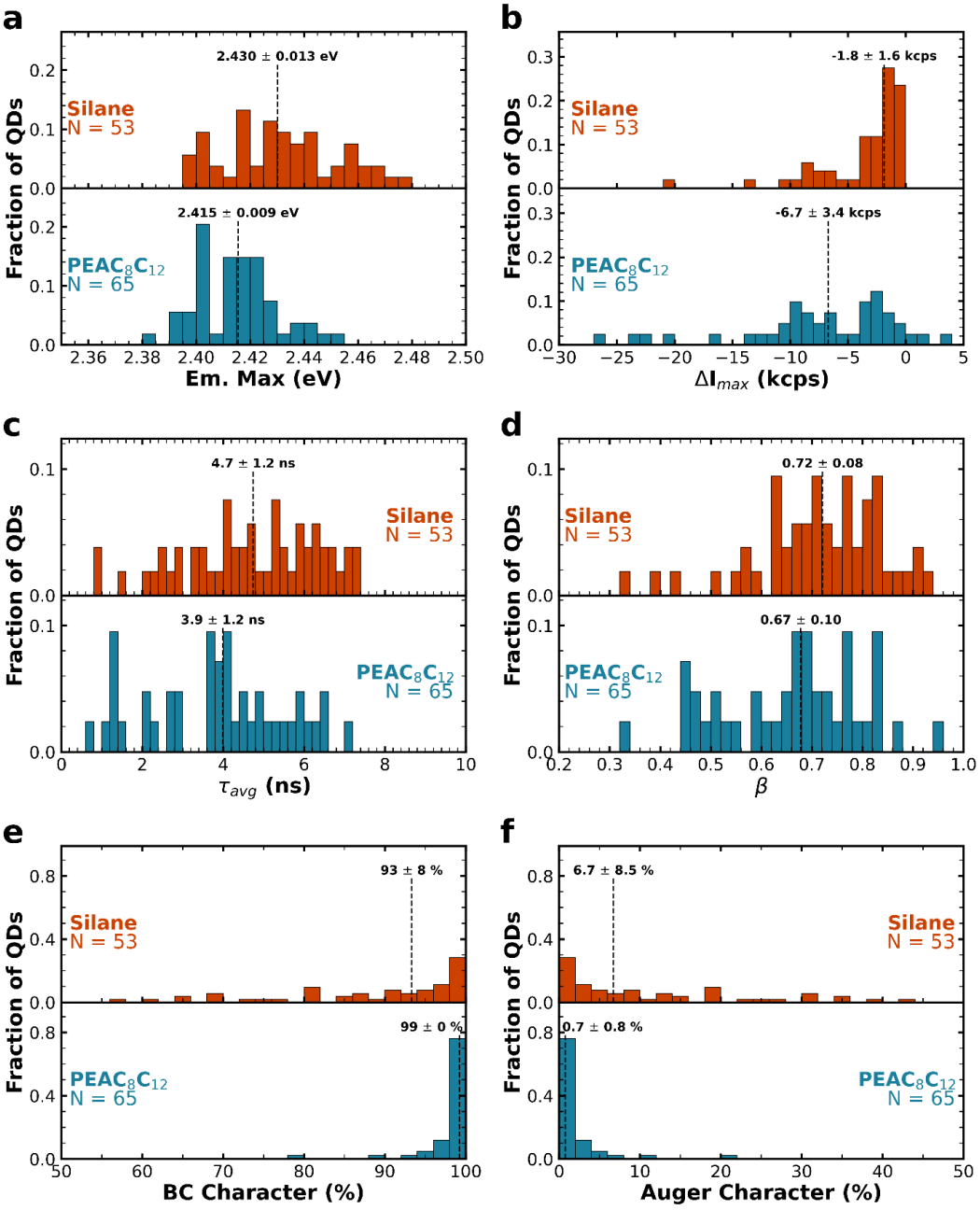

Figure C8. Additional room temperature characterization of single quantum dots a) Distribution of emission maxima. Silane-coated quantum dots have a slightly broader distribution consistent with the broader size distribution seen in TEM. **b)** Distribution of change in maximum intensity over 600 seconds. On average $PEAC_8C_{12}$-passivated quantum dots lose five times more intensity than silane-coated quantum dots. **c)** Distribution of single quantum dot average lifetimes. On average silane-coated quantum dots have a slightly longer lifetime. **d)** Distribution of single quantum dot lifetime homogeneity (beta) factors. On average silane-coated quantum dots tend to have slightly more homogenous lifetimes. Distributions of **e)** BC and **f)** Auger character determined from FLID fitting. Silane-coated quantum dots tend to have more Auger mediated blinking in comparison to $PEAC_8C_{12}$-passivated quantum dots.

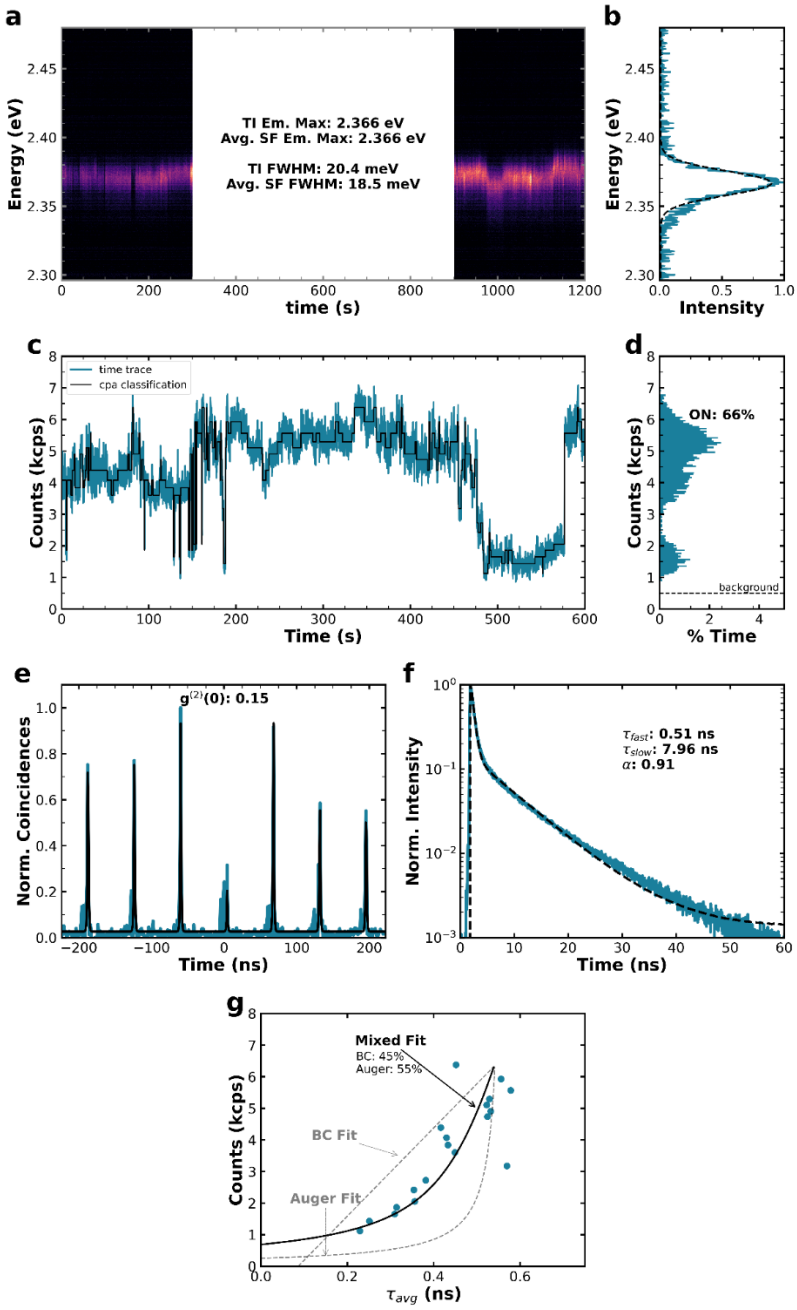

Figure C9. Example 4K characterization of a single PEAC$_8$C$_{12}$-passivated FAPbBr$_3$ quantum dot a) spectral diffusion trace consisting of 600 spectra with a 1s integration time acquired in two batches of 300 with a 600 s period of TTTR data acquisition in between. The average single frame (SF) spectrum has a peak emission energy of 2.366 eV and a FWHM of 18.5 meV **b)** the time integrated (TI) spectrum of the quantum dot which is the sum of the qualifying SF spectra. The TI spectrum has a peak emission energy of 2.366 eV and a FWHM of 20.4 meV **c)** experimental blinking trace (blue) and CPA classified blinking trace (black) **d)** photoluminescence intensity histogram **e)** experimental $g^{(2)}(\tau)$ trace (blue), and fit (black) **f)** photoluminescence lifetime (blue) and biexponential fit (black dashed line) **g)** CPA identified intensity levels correlated to their measure lifetime (blue points). Dashed lines represent the Auger- and BC-type blinking fits (Equations C8a and b) of the data while the solid black line represents the combination of both blinking types.

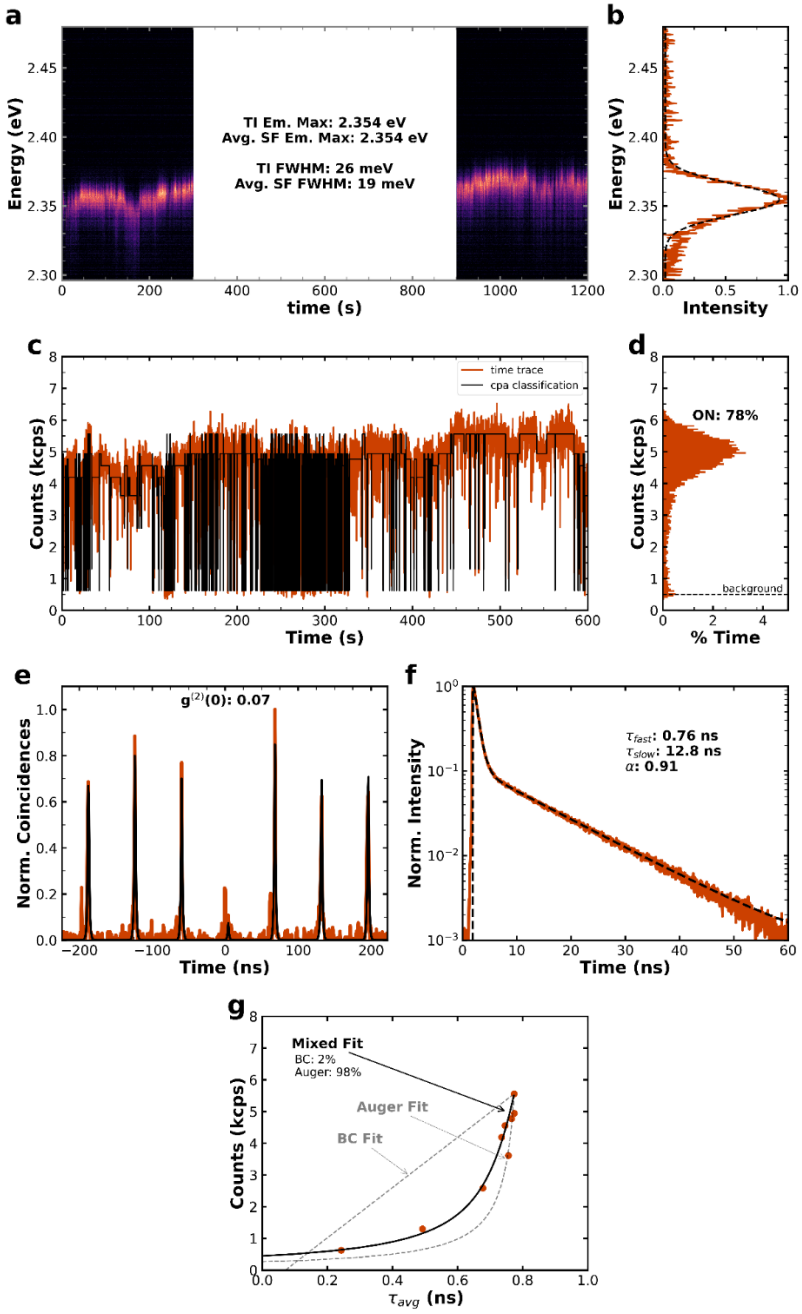

Figure C10. Example 4K characterization of a single silane-coated $FAPbBr_3$ quantum dot a) spectral diffusion trace consisting of 600 spectra with a 1s integration time acquired in two batches of 300 with a 600 s period of TTTR data acquisition in between. The average single frame (SF) spectrum has a peak emission energy of 2.354 eV and a FWHM of 19 meV **b)** the time integrated (TI) spectrum of the quantum dot which is the sum of the qualifying SF spectra. The TI spectrum has a peak emission energy of 2.354 eV and a FWHM of 26 meV **c)** experimental blinking trace (orange) and CPA classified blinking trace (black) **d)** photoluminescence intensity histogram **e)** experimental $g^{(2)}(\tau)$ trace (orange), and fit (black) **f)** photoluminescence lifetime (orange) and biexponential fit (black dashed line) **g)** CPA identified intensity levels correlated to their measure lifetime (orange points). Dashed lines represent the Auger- and BC-type blinking fits (Equations C8a and b) of the data while the solid black line represents the combination of both blinking types.

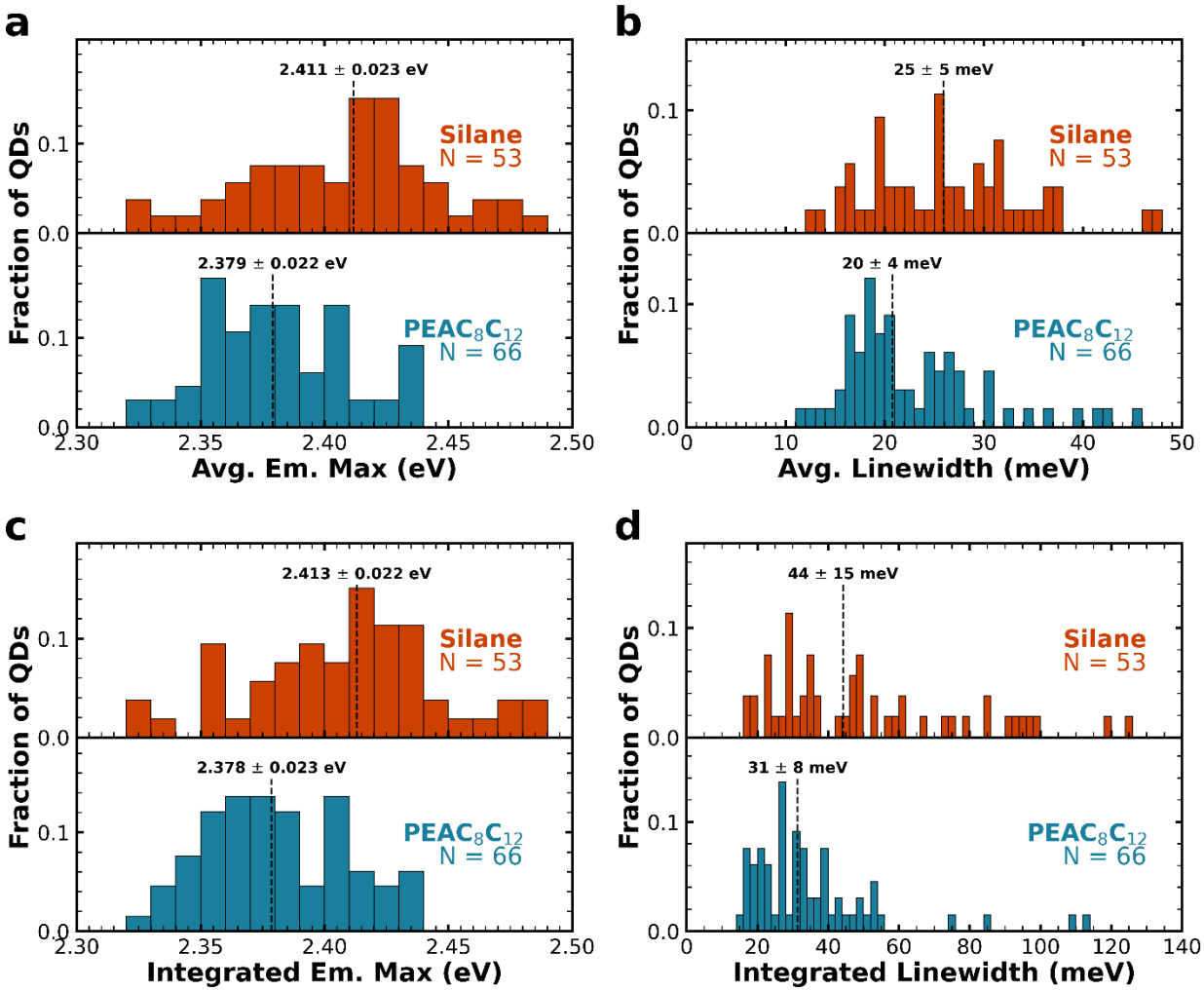

Figure C11. Additional 4K photoluminescence characterization a) Distribution of average single quantum dot emission maximum at short (1s) integration times **b)** Distribution of average single quantum dot linewidths at short (1s) integration times **c)** Distribution of single quantum dot emission maximum at long (600 s) integration times **d)** Distribution single quantum dot linewidths at long (600 s) integration times

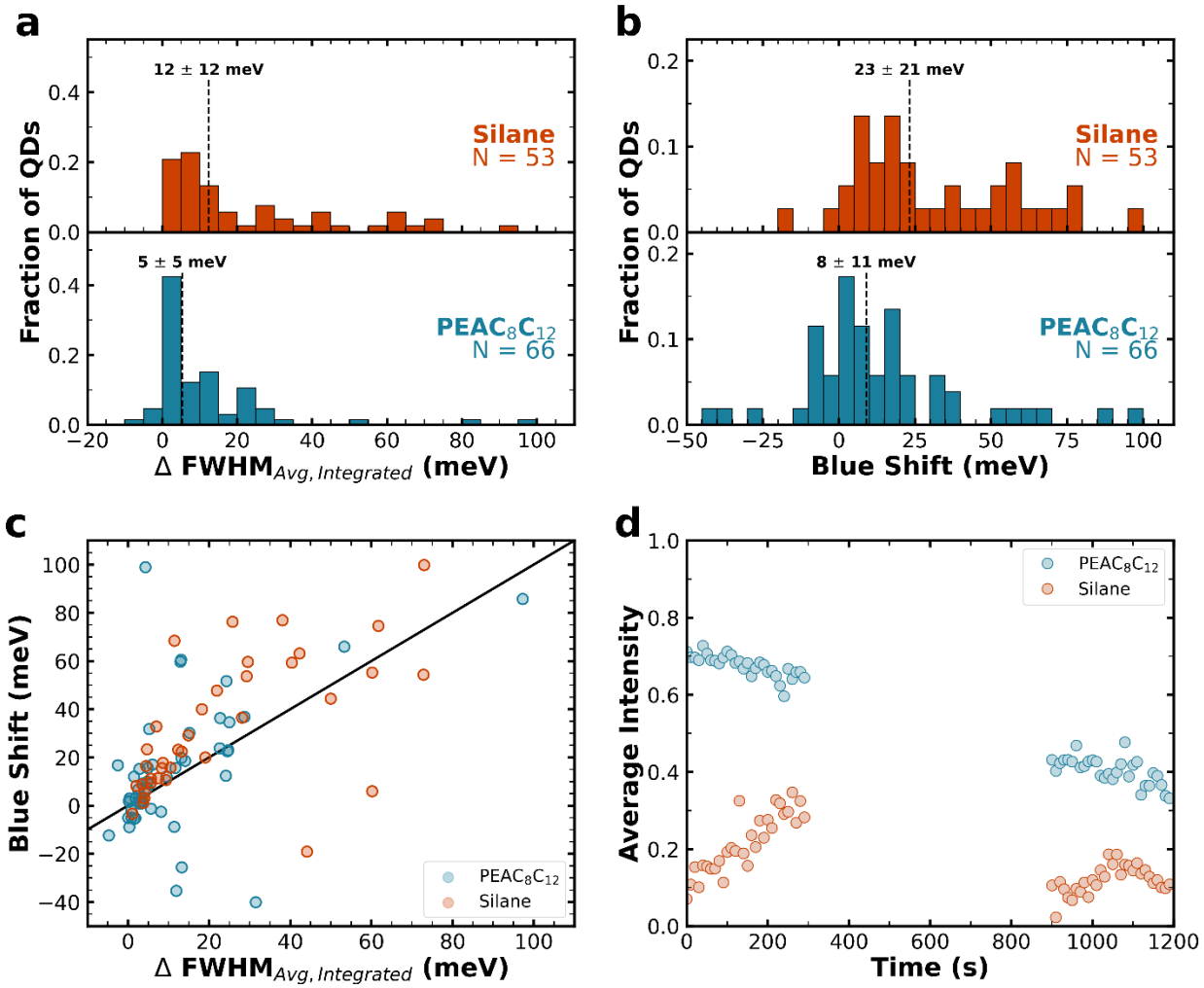

Figure C12. Evidence for Photodegradation at 4K a) Distribution of the change in FWHM between short (1s) and long (600s) integration times. Silane-coated quantum dots FWHMs have broadened twice as much as $PEAC_8C_{12}$-passivated quantum dots. **b)** Distribution of the change in the short integration time emission maximum over twenty minutes of illumination. On average, silane-coated quantum dots have blue shifted three times more than $PEAC_8C_{12}$-passivated quantum dots. **c)** Correlation between changing linewidth and a blue shifting emission maximum. In both samples the broadening of the linewidth with long integration times is strongly correlated with blue shifting emission. **d)** Average intensity of single quantum dot emission in time extracted from photoluminescence spectra. On average, $PEAC_8C_{12}$-passivated quantum dots have higher intensities and less variation in time. Silane-coated quantum dots see both photobrightening and photobleaching during the measurement time and have much larger variations in emission intensity.

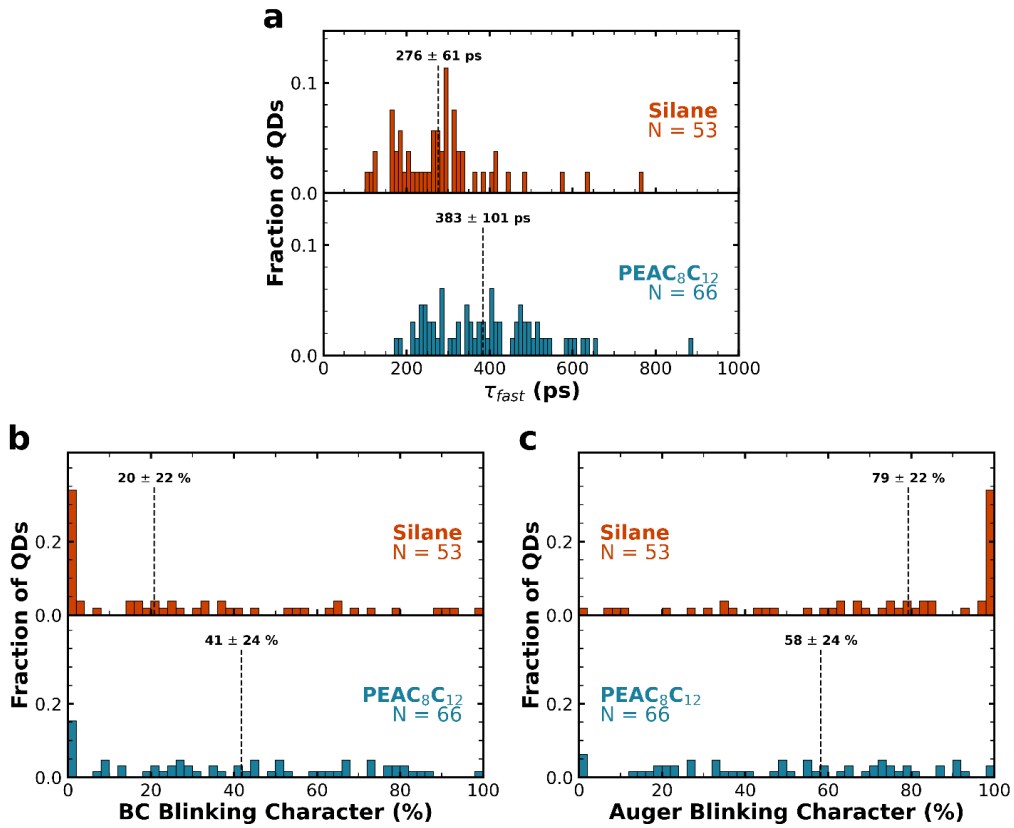

Figure C13. Additional 4K blinking characterization a) Distribution over average lifetimes for single quantum dots over ten minutes. On average $PEAC_8C_{12}$-passivated quantum dots have lifetimes 100 ps longer than silane-coated quantum dots indicating better surface passivation by $PEAC_8C_{12}$ at 4K. Distributions of **b)** BC and **c)** Auger character determined from FLID fitting. Silane-coated quantum dots tend to have more Auger mediated blinking in comparison to $PEAC_8C_{12}$-passivated quantum dots.

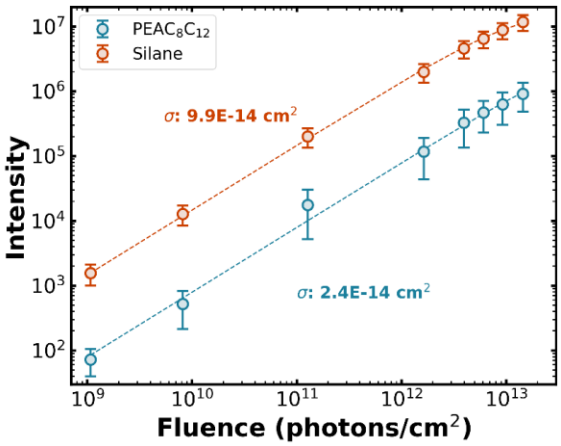

Figure C14. Absorption cross sections determined by fitting the fluence dependent intensity to Equation C11. Silane-coated quantum dots have an absorption cross section of 9.9E-14 cm^2 and $PEAC_8C_{12}$-passivated quantum dots have an absorption cross section of 2.4E-14 cm^2.

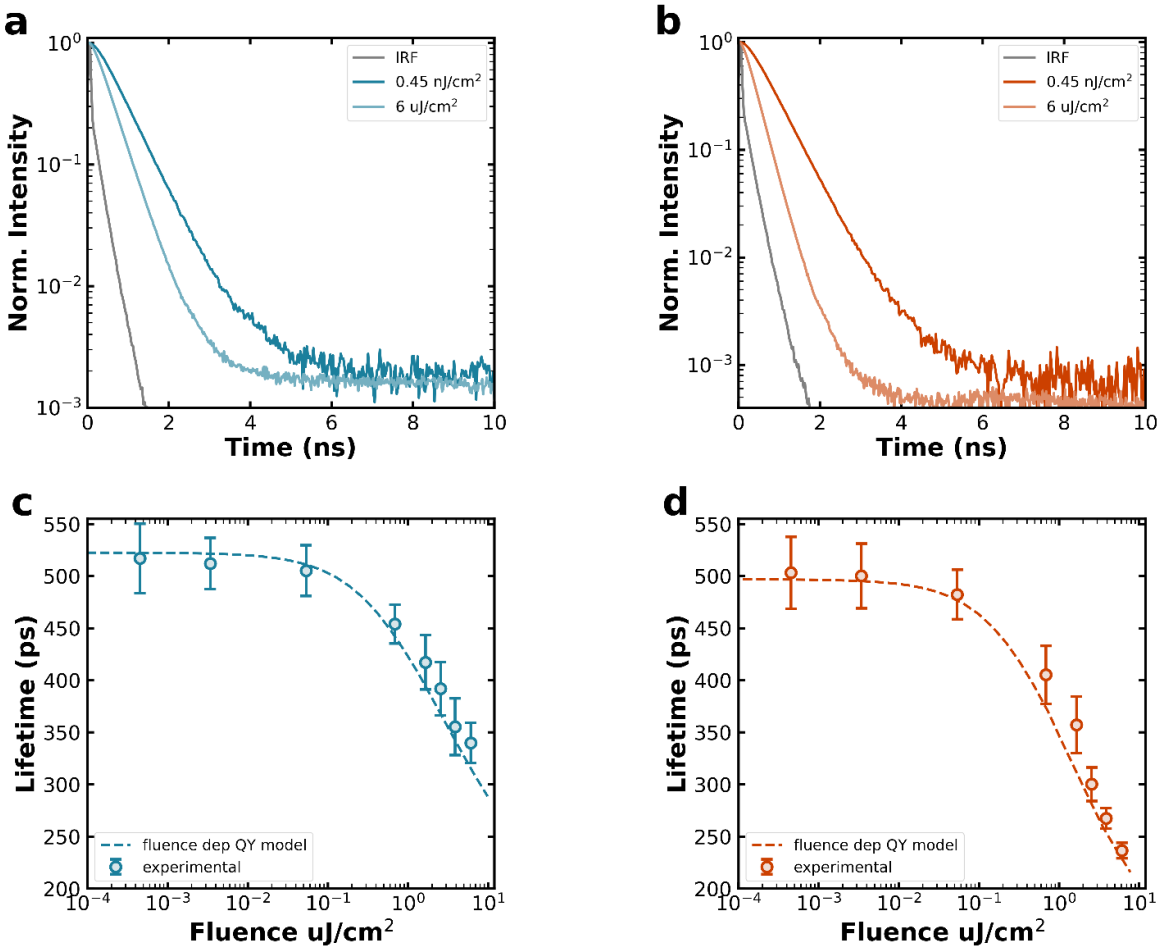

Figure C15. 4K fluence dependent lifetimes. Selected lifetimes for **a)** $PEAC_8C_{12}$-passivated and **b)** silane-coated quantum dots at minimum (0.45 nJ/cm^2) and maximum (6 uJ/cm^2) excitation densities. $k_{r,X}$ and $k_{nr,X}$ of the fluence dependent quantum yield model are extracted from the lifetimes acquired at 0.45 nJ/cm^2. Experimental fluence dependent lifetime for **c)** $PEAC_8C_{12}$-passivated and **d)** silane-coated quantum dots compared to the lifetime predicted from the fit fluence dependent quantum yield.

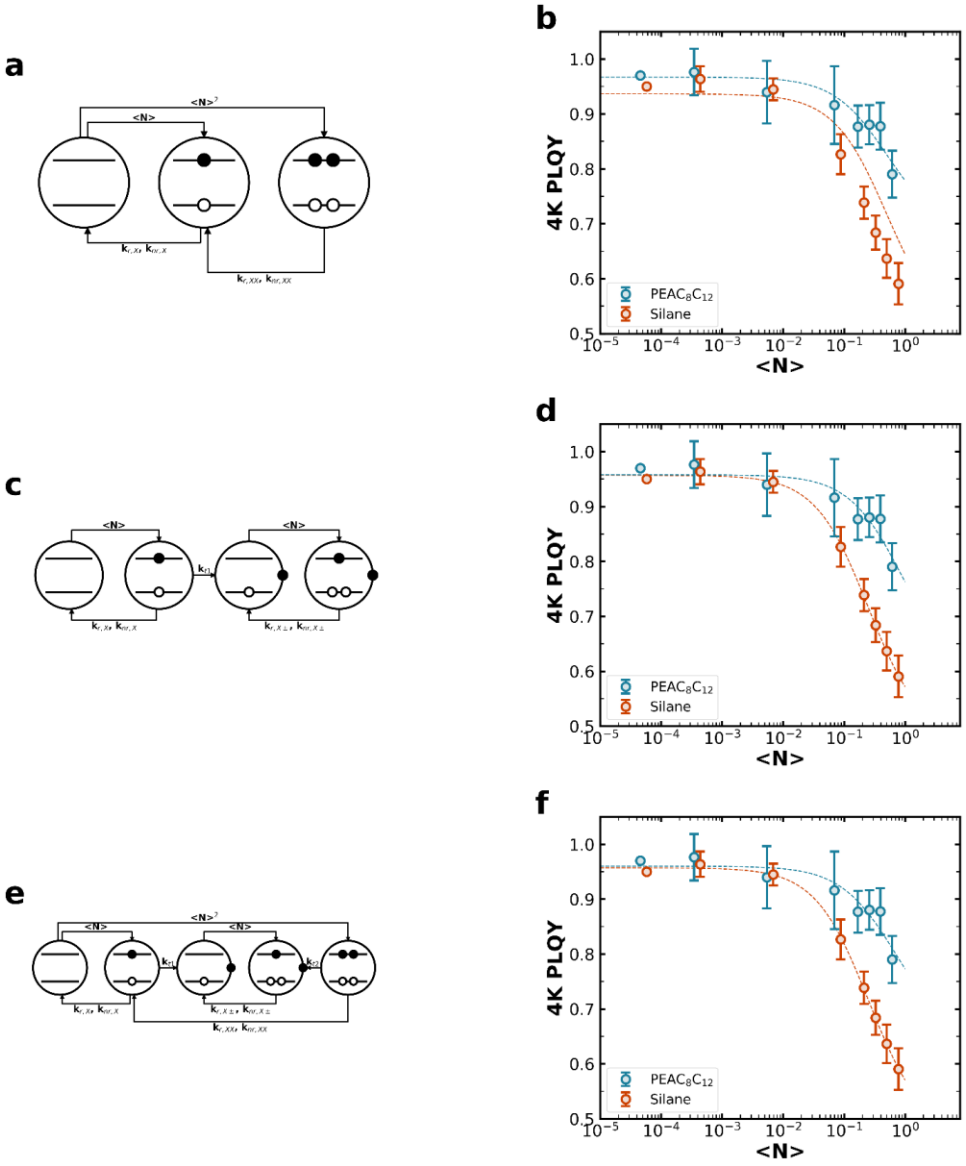

Figure C16. Models for fluence dependent quantum yield in quantum dots a) model for quantum yield changing only based on biexciton formation **b)** fit of biexciton only model to experimental data. This model fails to capture the experimental quantum yield dynamics for silane-coated quantum dots and even with unconstrained biexciton recombination rates the fit roll off is always too shallow. **c)** model for quantum yield changing based on the formation of a dark charged state which can generate trions after a second absorption. **d)** fit of dark charged only model to experimental data. While this model captures the experimental quantum yield dynamics, it predicts a large steady-state population (> 80%) of the dark charged state which is inconsistent with the single quantum characterization of these materials. **e)** model for quantum yield changing based on the formation of a dark charged state which can generate trions after a second absorption and a biexciton which can convert to a trion. **f)** fit of mixed model to experimental data. While this model captures the experimental quantum yield dynamics, it predicts a large steady-state population (> 80%) of the dark charged state which is inconsistent with the single quantum characterization of these materials. Additionally, there is no unique solution for the trion and biexciton rate constants with this fit.

Table C1. Comparison of exciton and biexciton state parameters extracted from fluence dependent PLQY fit (QY) and single quantum dot blinking traces (TRPL)

		Exciton		Biexciton	
		QY	***τ (ps)***	***QY***	***τ (ps)***
$PEAC_8C_{12}$	***QY***	0.96	523 ± 62	0.68	144 ± 27
	TRPL	1	534 ± 140	0.73 ± 0.19	196 ± 51
Silane	***QY***	0.95	500 ± 45	0.39	103 ± 13
	TRPL	1	525 ± 120	0.60 ± 0.13	157 ± 34

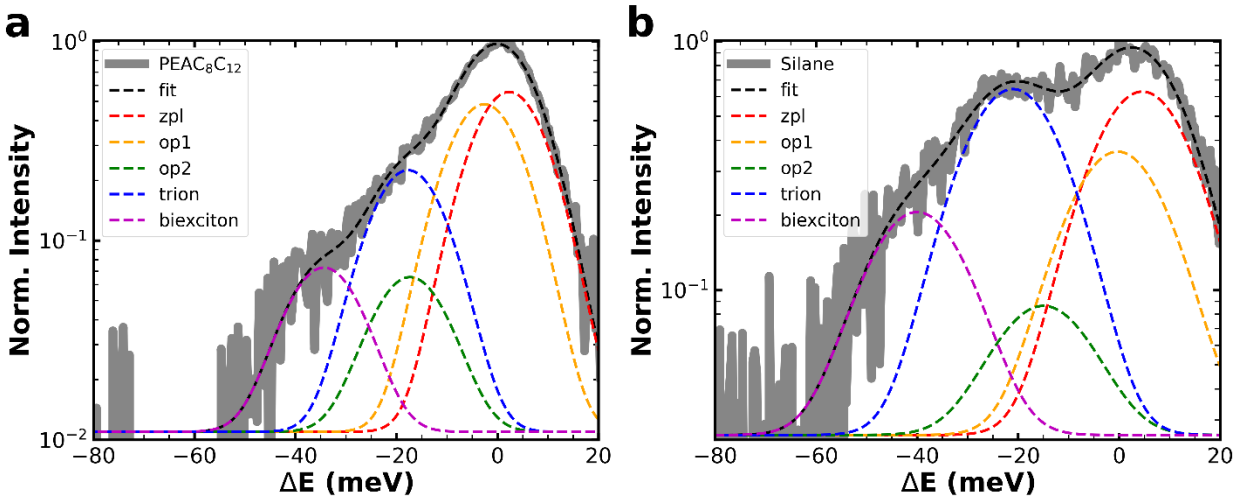

Figure C17. Components of single quantum dot 4K photoluminescence spectra for **a)** $PEAC_8C_{12}$-passivated quantum dots. ZPL (A = 9.2, μ = 0 meV, σ = 6.7 meV), OP1 (A = 7.9, μ = -4.9 meV, σ = 6.7 meV) , OP2 (A = 0.9, μ = -19.6 meV, σ = 6.7 meV) , trion (A = 3.6, μ = -20 meV, σ = 6.7 meV) , biexciton (A = 1.0, μ = -36 meV, σ = 6.7 meV) **b)** silane-coated quantum dots. ZPL (A = 13.2, μ = 0 meV, σ = 8.8 meV), OP1 (A = 7.4, μ = -4.9 meV, σ = 8.8 meV) , OP2 (A = 1.2, μ = -19.6 meV, σ = 8.8 meV) , trion (A = 13.6, μ = -20 meV, σ = 8.8 meV) , biexciton (A = 4.0, μ = -44 meV, σ = 8.8 meV) Silane-coated quantum dots see more emission from the trion state (blue dashed line) than $PEAC_8C_{12}$-passivated quantum dots.

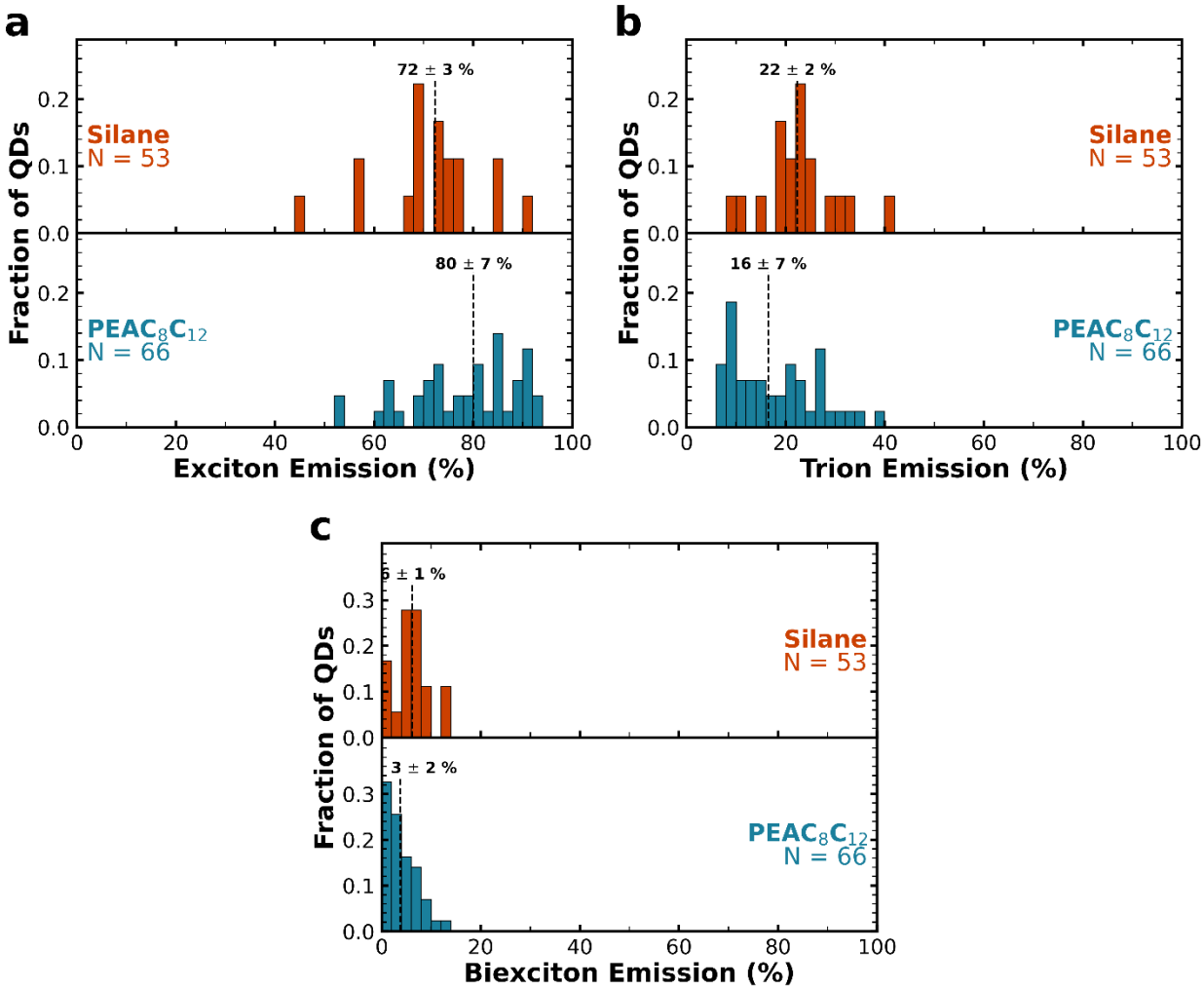

Figure C18. Photoluminescence spectra composition of single quantum dots at 4K a) exciton emission **b)** trion emission and **c)** biexciton emission

References

(1) Morad, V.; Stelmakh, A.; Svyrydenko, M.; Feld, L. G.; Boehme, S. C.; Aebli, M.; Affolter, J.; Kaul, C. J.; Schrenker, N. J.; Bals, S.; Sahin, Y.; Dirin, D. N.; Cherniukh, I.; Raino, G.; Baumketner, A.; Kovalenko, M. V. Designer Phospholipid Capping Ligands for Soft Metal Halide Nanocrystals. *Nature 2023 626:7999* **2023**, *626* (7999), 542–548. https://doi.org/10.1038/s41586-023-06932-6.

(2) Mooney, J.; Kambhampati, P. Get the Basics Right: Jacobian Conversion of Wavelength and Energy Scales for Quantitative Analysis of Emission Spectra. *Journal of Physical Chemistry Letters* **2013**, *4* (19), 3316–3318. https://doi.org/10.1021/JZ401508T.

(3) Taddei, M.; Smith, J. A.; Gallant, B. M.; Zhou, S.; Westbrook, R. J. E.; Shi, Y.; Wang, J.; Drysdale, J. N.; McCarthy, D. P.; Barlow, S.; Marder, S. R.; Snaith, H. J.; Ginger, D. S. Ethylenediamine Addition Improves Performance and Suppresses Phase Instabilities in Mixed-Halide Perovskites. *ACS Energy Lett* **2022**, *7* (12), 4265–4273. https://doi.org/10.1021/ACSENERGYLETT.2C01998.

(4) Gallagher, S.; Kline, J.; Jahanbakhshi, F.; Sadighian, J. C.; Lyons, I.; Shen, G.; Hammel, B. F.; Yazdi, S.; Dukovic, G.; Rappe, A. M.; Ginger, D. S. Ligand Equilibrium Influences Photoluminescence Blinking in CsPbBr3: A Change Point Analysis of Widefield Imaging Data. *ACS Nano* **2024**, *18* (29), 19208–19219. https://doi.org/10.1021/ACSNANO.4C04968.

(5) Palstra, I. M.; Koenderink, A. F. A Python Toolbox for Unbiased Statistical Analysis of Fluorescence Intermittency of Multilevel Emitters. *Journal of Physical Chemistry C* **2021**, *125* (22), 12050–12060. https://doi.org/10.1021/ACS.JPCC.1C01670.

(6) Li, H.; Yang, H. Statistical Learning of Discrete States in Time Series. *Journal of Physical Chemistry B* **2019**, *123* (3), 689–701. https://doi.org/10.1021/ACS.JPCB.8B10561.

(7) Tang, X.; Khurana, M.; Rossi, D.; Luo, L.; Akimov, A. V.; Son, D. H. Exciton Photoluminescence of Strongly Quantum-Confined Formamidinium Lead Bromide (FAPbBr3) Quantum Dots. *Journal of Physical Chemistry C* **2022**, *126* (43), 18366–18373. https://doi.org/10.1021/ACS.JPCC.2C05661.

(8) Yuan, G.; Gómez, D. E.; Kirkwood, N.; Boldt, K.; Mulvaney, P. Two Mechanisms Determine Quantum Dot Blinking. *ACS Nano* **2018**, *12* (4), 3397–3405. https://doi.org/10.1021/ACSNANO.7B09052.

(9) Gumbsheimer, P.; Conradt, F.; Behovits, Y.; Huber, S.; Hinz, C.; Negele, C.; Mecking, S.; Seletskiy, D. V.; Leitenstorfer, A. Enhanced Determination of Emission Fine Structure and Orientation of Individual Quantum Dots Based on Correction Algorithm for Spectral Diffusion. *J Phys D Appl Phys* **2021**, *54* (15), 155106. https://doi.org/10.1088/1361-6463/ABDA83.

(10) Cho, K.; Sato, T.; Yamada, T.; Sato, R.; Saruyama, M.; Teranishi, T.; Suzuura, H.; Kanemitsu, Y. Size Dependence of Trion and Biexciton Binding Energies in Lead Halide Perovskite Nanocrystals. *ACS Nano* **2023**, *18*, 45. https://doi.org/10.1021/ACSNANO.3C11842.

(11) Cho, K.; Yamada, T.; Tahara, H.; Tadano, T.; Suzuura, H.; Saruyama, M.; Sato, R.; Teranishi, T.; Kanemitsu, Y. Luminescence Fine Structures in Single Lead Halide Perovskite Nanocrystals: Size Dependence of the Exciton-Phonon Coupling. *Nano Lett* **2021**, *21* (17), 7206–7212. https://doi.org/10.1021/ACS.NANOLETT.1C02122.

(12) Zhu, C.; Feld, L. G.; Svyrydenko, M.; Cherniukh, I.; Dirin, D. N.; Bodnarchuk, M. I.; Wood, V.; Yazdani, N.; Boehme, S. C.; Kovalenko, M. V; Rainò, G.; Zhu, C.; Feld, L. G.; Svyrydenko, M.; Cherniukh, I.; Dirin, D. N.; Bodnarchuk, M. I.; Boehme, S. C.; Kovalenko, M. V; Rainò, G. Quantifying the Size-Dependent Exciton-Phonon Coupling Strength in Single Lead-Halide Perovskite Quantum Dots. *Adv Opt Mater* **2024**, 2301534. https://doi.org/10.1002/ADOM.202301534.

(13) Sampat, S.; Karan, N. S.; Guo, T.; Htoon, H.; Hollingsworth, J. A.; Malko, A. V. Multistate Blinking and Scaling of Recombination Rates in Individual Silica-Coated CdSe/CdS Nanocrystals. *ACS Photonics* **2015**, *2* (10), 1505–1512. https://doi.org/10.1021/ACSPHOTONICS.5B00423.

(14) Pan, A.; He, B.; Fan, X.; Liu, Z.; Urban, J. J.; Alivisatos, A. P.; He, L.; Liu, Y. Insight into the Ligand-Mediated Synthesis of Colloidal CsPbBr3 Perovskite Nanocrystals: The Role of Organic Acid, Base, and Cesium Precursors. *ACS Nano* **2016**, *10* (8), 7943–7954. https://doi.org/10.1021/ACSNANO.6B03863.

(15) Meng, C.; Yang, D.; Wu, Y.; Zhang, X.; Zeng, H.; Li, X. Synthesis of Single CsPbBr3@SiO2 Core–Shell Particles via Surface Activation. *J Mater Chem C Mater* **2020**, *8* (48), 17403–17409. https://doi.org/10.1039/D0TC03932B.